Plastic Solar Cells: Where the Current Begins

Ultrafast Exciton-to-Charge Conversion in Organic Photovoltaics

Oleg Kozlov

2017

Plastic Solar Cells: Where the Current Begins
Ultrafast Exciton-to-Charge Conversion in Organic Photovoltaics

Oleg Kozlov PhD thesis
University of Groningen

Stratingh Institute PhD thesis series
Zernike Institute PhD thesis series

ISBN: 978-94-034-0043-3 (Printed version)
ISBN: 978-94-034-0042-6 (Electronic version)

The research presented in this Thesis was performed in the groups of Chemistry of (Bio)Organic Materials and Devices, Stratingh Institute for Chemistry, and Optical Condensed Matter Science, Zernike Institute for Advanced Materials, both at University of Groningen. The work was supported by Aurora – Towards Modern and Innovative Higher Education program and the Faculty of Science and Engineering.

university of groningen
faculty of science and engineering
stratingh institute for chemistry

university of groningen
faculty of science and engineering
zernike institute for advanced materials

university of groningen

Plastic Solar Cells: Where the Current Begins

Ultrafast Exciton-to-Charge Conversion in Organic Photovoltaics

PhD thesis

to obtain the degree of PhD at the
University of Groningen
on the authority of the
Rector Magnificus Prof. E. Sterken
and in accordance with
the decision by the College of Deans.

This thesis will be defended in public on

Friday 15 September 2017 at 14.30 hours

by

Oleg Kozlov

born on 18 January 1990
in Cheboksary, Russia

Supervisor
Prof. J.C. Hummelen

Co-supervisor
Dr. M.S. Pchenitchnikov

Assessment Committee
Prof. M.A. Loi
Prof. L.D.A. Siebbeles
Prof. V. Dyakonov

Table of Contents

Chapter 1. Introduction **1**
1.1 Basics of Organic Electronics 2
1.2 Excitations in Organic Semiconductors 3
1.3 Organic Solar Cells 8
1.4 Charge Generation in Organic Solar Cells 11
1.5 Goals and Objectives of the Thesis 15
1.6 Photoluminescence and Photoinduced Absorption Spectroscopies 16
1.7 Overview of the Thesis 21
References 23
Chapter 2. Real-Time Tracking of Singlet Exciton Diffusion in Organic Semiconductors **33**
2.1 Introduction 34
2.2 Experimental Results 36
2.3 Conclusions 40
2.4 Methods 40
2.5 Supporting Information 42
Author Contributions 62
References 62
Chapter 3. Ultrafast Spectroscopy Reveals Bulk Heterojuction Morphology **65**
3.1 Introduction 66
3.2 Experimental Results 68
3.3 Conclusions 75
3.4 Methods 76
3.5 Supporting Information 78
Author Contributions 91
References 91
Chapter 4. Ultrafast Exciton-to-Polaron Conversion in Densely-Packed Small Organic Semiconducting Molecules **97**
4.1 Introduction 98
4.2 Experimental Results 100
4.3 Conclusions 106
4.4 Methods 107
4.5 Supporting Information 108
Author Contributions 110
References 110

Chapter 5. Ultrafast Charge Generation Pathways in Photovoltaic Blends Based on Novel Star-Shaped Conjugated Molecules 115
5.1 Introduction 116
5.2 Experimental Results 118
5.3 Conclusions 129
5.4 Methods 130
5.5 Supporting Information 132
Author Contributions 142
References 142
Chapter 6. Triplet Exciton Harvesting in Singlet Fission Solar Cells 147
6.1 Introduction 148
6.2 Experimental Results 149
6.3 Conclusions 157
6.4 Methods 157
Author Contributions 158
References 158
Summary 160
Samenvatting 163
Summary for General Public 167
List of Journal Publications 168
Acknowledgements 170

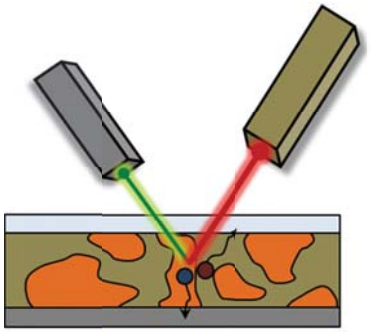

Chapter 1

Introduction

Organic photovoltaics is a field of organic electronics with a great potential for e.g. wearable or built-in applications. Organic solar cells employ organic semiconductors to convert Sun photons to electricity. Photon-to-charge conversion in organic solar cells is a multistep process that includes exciton photogeneration, their diffusion and dissociation, and geminate charge recombination – the processes that occur at ultrafast (femtosecond to nanosecond) timescales, and directly affect the efficiency of devices.

In this Chapter, the basic concepts of operation of organic solar cells are described. The photon-to-charge conversion is broken down to substeps, and the physics of each substep is explained. Spectroscopic approaches to track the ultrafast exciton and charge dynamics are introduced. Finally, the research goals and objectives of this Thesis are formulated.

1.1 Basics of Organic Electronics

In the modern world, life is impossible without a huge variety of electronics. Every day people use hundreds and thousands of different electronic devices – from smartphones and PCs to "smart" trackable dog collars[1] or electronic slippers with fall prevention[2]. The heart and foundation of modern electronics are semiconductors – the majority of the modern electronic devices would be impossible without e.g. semiconducting transistors. The most widely-used semiconductors are Group IV elements (like silicon or germanium) or binary compounds of group III-V elements (e.g. gallium arsenide), but in principle an electronic device can be manufactured from any semiconductor.[3]

Semiconducting properties and conductivity in organic materials have been intensively studied since 19th century; the first organic conductive material – polyaniline – was described in 1862.[4] However, manufacturing of the real organic electronic devices was not reported until the second half of 20th century. In 1977 a breakthrough discovery happened: Alan G. MacDiarmid, Alan J. Heeger and Hideki Shirakawa with co-workers synthesized semiconducting organic polymer polyacetylene[5], which immediately triggered development of the field of polymer-based "plastic" organic electronics. The potential of organic electronic devices are really astonishing because of possibility to supplement an electronic circuit with advantages of organic material such as light weight, flexibility, room-temperature solution processability and so on.[6,7]

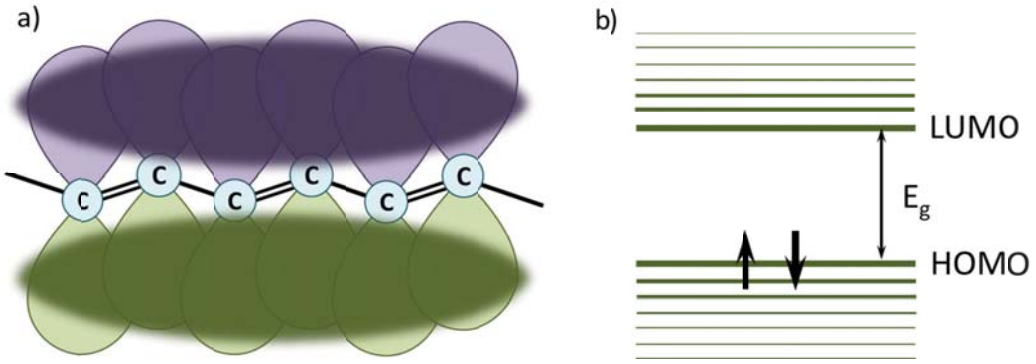

Figure 1.1 (a) Schematic representation of a conjugated chain with π-orbitals (purple/green ovals) formed by overlapping *p*-orbitals of individual carbon atoms (shown as purple-green eights). (b) Energy band diagram of an organic semiconductor. Black arrows represent spins of electrons located at the Highest Occupied Molecular Orbital (HOMO). The molecule is in the ground state, so that the Lowest Unoccupied Molecular Orbital (LUMO) is empty.

Since then, the field organic electronics started to expand rapidly. The first organic electronic device emerged in early 1980s as a single-layer organic solar cell (OSC) with efficiency well below 0.1%[8] (to compare, efficiency of modern OSCs exceeds 13%[9]). In 1983, the first organic

thin-film transistor was proposed[10], and in 1987 organic light emitting diode (OLED) was introduced[11]. Nowadays, organic electronics is an advanced and mature field of science and technology with organic electronic devices (mainly OLEDs) commercially available and widely used.

As follows from the name, organic semiconductors are carbon-based (organic) materials. They demonstrate ability to conduct electricity due to the so-called π-conjugation: overlapping of the *p*-orbitals along the molecular backbone leads to formation of delocalized molecular π–orbitals (Figure 1.1a); as a result, electrons in these orbitals are delocalized along the conjugated chain.[12-14] Manifold of the π-orbitals form a band-like structure with frontier orbitals called HOMO (Highest Occupied Molecular Orbital) and LUMO (Lowest Unoccupied Molecular Orbital), respectively. The HOMO acts as an analogue of the valence band edge in a conventional inorganic semiconductor while the LUMO is analogous to the conduction band edge; the difference between HOMO and LUMO energy levels is a bandgap E_g of the organic semiconductor (Figure 1.1b).[12]

Nowadays, the most widely-used organic semiconductors are conjugated polymers[15] and small molecules[16,17]. Those materials demonstrate extremely high flexibility of the molecular design and outstanding tunability of chemical, physical and optical properties.[18] Such parameters as a bandgap and the exact position of energy levels, absorption spectrum and extinction coefficient, charge mobility, stability and many others can be tuned by careful chemical engineering of the material. Variety of conjugated moieties (e.g. phenyl, thiophene, carbazole, benzothiadiazole and many more) can be connected in many different ways, resulting eventually in hundreds and thousands structures with unique properties.[19,20] This ensures endless possibilities for organic semiconductors.

1.2 Excitations in Organic Semiconductors

Essential difference between organic and inorganic semiconductors is their dielectric constants ε. While ε of silicon amounts to 11.7[21], the dielectric constant of organic semiconductors is typically lower than 4[22]. This results in essentially different photophysics of organic semiconductors compared to their inorganic counterparts. In the latter absorption of the photon results in direct generation of a free electron-hole pair, while in organic materials the so-called excitons (bound electron-hole pair) are formed upon photoexcitation.[23] Additionally, because of complex and often intrinsically heterogeneous structure of organic semiconductors, such excited states as inter- and intramolecular charge-transfer (CT) excitons[24-27] and/or polaron pairs[28,29] may be formed upon photoexcitation along with the excitons. This makes photophysics of pristine organic semiconductors quite challenging.

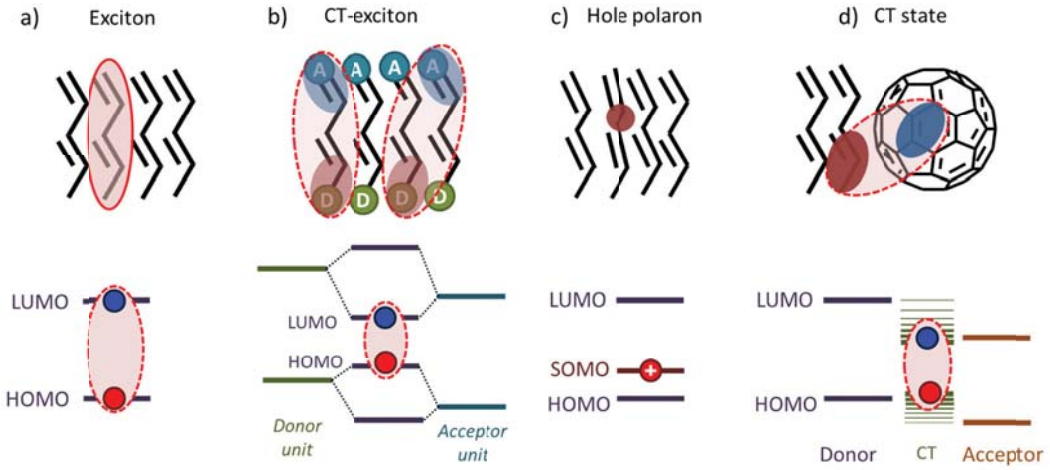

Figure 1.2 Schematic drawings (top) and energetics (bottom) of (a) a Frenkel exciton[30], (b) intra- and intermolecular charge-transfer excitons in push-pull materials[31], (c) hole polaron[32] and (d) interfacial charge-transfer state[33]. Excitons are shown by pink ovals, while electrons (holes) are depicted as blue (red) ovals/circles. In (b), intramolecular donor and acceptor units are shown by green and cyan circles, respectively. Note distortions of the conjugated chains in (c) which, together with a charge, form a polaron.

1.2.1 Singlet excitons

When an organic semiconductor absorbs a photon with energy higher than the bandgap, one electron is promoted from an occupied to an unoccupied molecular orbital, forming a bound electron-hole pair: an exciton. Note that exciton as a quasi-particle exists only in solid state of organic semiconductor; in the case of e.g. diluted solution of organic molecules no excitons are formed but the molecule is simply promoted to its excited state.

For simplicity, we will assume further on that the electron in the excited state is located in the LUMO, while the hole is created in the HOMO (Figure 1.2a), i.e. the exciton has the lowest possible energy. In soft organic semiconductors, excitons are usually fairly localized within several conjugated segments and are called Frenkel excitons[34] (in contrast with highly delocalized Wannier-Mott excitons[35] found in inorganic semiconductors at low temperatures[36]). The binding energy of an exciton depends on the dielectric constant of the material and a particular configuration of the electron and hole wavefunctions (which depends on the chemical structure of the material), and in organic materials typically amounts to ~0.3-1 eV.[37-40]

Selection rules require the electron photoexcitation to occur without change of spin. Thus, the spins of the electron in the LUMO and the hole in the HOMO are opposite, and the total spin of the generated exciton is zero. In this case, the multiplicity of such excited state is one and

therefore it is called “singlet excited state” and the respective quasi-particle is called a “singlet exciton”.

Singlet excitons are major and most important energy carriers in organic electronics.[41-43] Because of the opposite spins, recombination of the electron and hole of the exciton is dipole allowed; therefore, the lifetime of singlet excitons typically does not exceed several nanoseconds.[44] Another consequence of the singlet multiplicity is the ability of singlet excitons to be transferred within the semiconductor via the Förster resonant energy transfer mechanism (FRET)[45] which relies on dipole-dipole interactions. Förster energy transfer is relatively fast and long-range (the transfer rate scales with the distance as r^{-6})[46] and, therefore, the singlet excitons are quite mobile. Singlet excitons can also be transported via the short-range Dexter mechanism[47] (where the transfer rate decreases exponentially with the distance)[48], and a combination of the two mechanisms determines diffusivity of the exciton.

1.2.2 Triplet excitons

In the ground state, the neutral molecule has a net spin zero due to the Pauli Exclusion Principle. If the molecule is excited, the electron and hole are in different energy levels, so that they can have the same spins without violating the Pauli Exclusion Principle. The multiplicity of such an excited state is three[49], so that it is called “triplet state”, and the electron-hole pair form a triplet exciton[50]. Triplet states are “dark” states: they cannot be directly excited by photon absorption as such a transition would require spin flipping which is forbidden in the electric-dipole approximation.[51] Thus, the triplet excitons are not formed directly via photoexcitation, but they are created from singlet excitons via singlet-to-triplet conversion processes[50] or after merging an electron and hole (e.g. after injecting from electrodes in an OLED) with same spins[52,53].

The most common mechanism of singlet-to-triplet conversion is intersystem crossing[50,54-56] (ISC, Figure 1.3a). For ISC to occur, the transition to the triplet state must be energetically favorable, and the singlet and triplet states must be spin-orbit coupled.[57,58] Because of the second requirement, efficient ISC occurs in a number of fullerenes (e.g. C_{60}, C_{70}, C_{76} and C_{92})[59] and fullerene derivatives (e.g. PCBM and $PC_{71}BM$)[60]. Additionally, efficient ISC is observed in organic materials with heavy atoms in the structure as the heavy atom promotes spin-orbit coupling.[61-63] Another possible route to singlet-to-triplet conversion is singlet fission[50,64-66] (SF, Figure 1.3b). Via SF, one singlet is converted to a correlated triplet pair[67-70] which further separates to a pair of free triplet excitons. To make this process possible, doubled energy of triplet state should be somehow lower than the singlet state energy[64,71], and the neighboring chromophores must be electronically coupled[72,73] to each other to accommodate the generated triples at different molecules. Singlet fission is of great interest in organic photovoltaics as it

produces two electron-hole pairs from a single photon which potentially allows overcoming the Shockley-Queisser limit.[74,75]

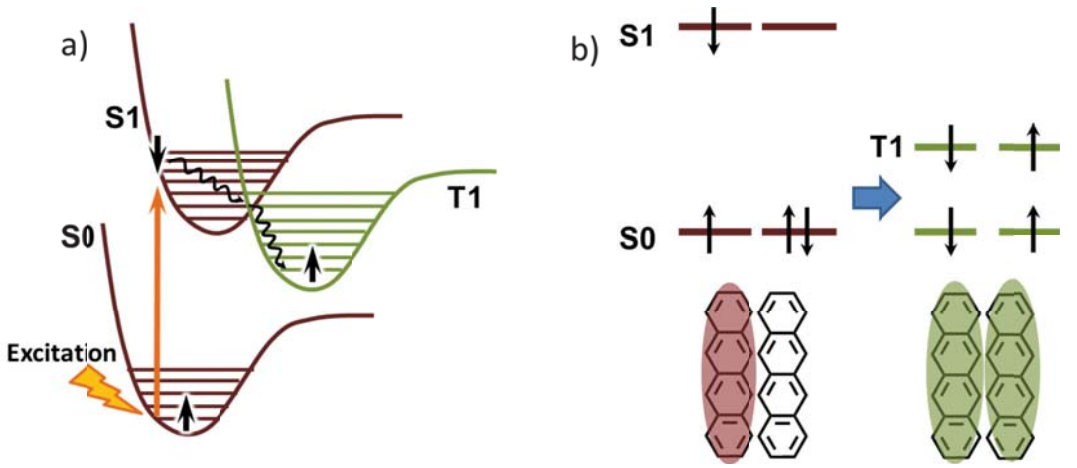

Figure 1.3 Schematics of (a) intersystem crossing and (b) singlet fission. Spin direction of the electrons are shown by black arrows. Vibrational relaxation is shown by wiggled arrow. In (b), the singlet and triplet excitons are shown by brown and green ovals, respectively.

Because the transition from the triplet excited state to the ground state requires change of spin orientation, the lifetime of triplet excitons is orders of magnitude longer compared to that of singlet excitons.[50,76] As the FRET rate is in inverse proportion to the excited state lifetime, FRET is extremely inefficient for the triplet excitons (which is also a consequence of the spin-forbidden relaxation of the triplet exciton to the singled ground state); thus the main transport mechanism for the triplets is Dexter transfer.[53,77] Triplet dynamics are extremely important for OLED operation, as due to the basic quantum statistics, 75% of electrons and holes injected to the device form triplet excitons.[53,78] In OSCs the triplet dynamics are of lower importance as typically timescales of singlet exciton collection (<100 ps) are much faster compared to the singlet-to-triplet conversion time (~1 ns) and therefore the triplet contribution to the separated charges is typically low.[60] Triplet dynamics become important in SF solar cells, where the charge collection from triplet excitons is the ultimate goal[74,79] (see Chapter 6 for discussion of triplet harvesting in SF solar cells).

1.2.3 Charge-transfer excitons

One of the goals in designing new materials for organic photovoltaics is to optimize the amount of absorbed solar photons by manipulating the bandgap of the organic semiconductor.[80-82] Nowadays the most common way to achieve this goal is in designing the so-called push-pull (donor-acceptor) molecules[20,83]. A push-pull molecule (either a polymer or a small molecule)

comprises conjugated donor and acceptor units[19,84] (Figure 1.2b, top). Because of different energetics of the donor and acceptor units, a ground state charge-transfer occurs within the molecule[85], with orbital reorganization and narrowing of the bandgap (Figure 1.2b, bottom).

In addition to the narrow bandgap, push-pull molecules typically demonstrate lower exciton binding energy compared to classical conjugated materials.[38,86] This is due to the intramolecular charge transfer which occurs after photoexcitation of the molecule. Because the accepting moiety has lower lying orbital energies with respect to the donating one[87], the electron density is shifted to the acceptor unit after the photon absorption[19,88,89]. Thus, the positions of electron and hole in space do not coincide any longer (unlike in a Frenkel exciton), which results in a larger delocalization length of the electron-hole pair and lower Coulomb attraction. The bound electron-hole pair formed after charge transfer is called the charge-transfer exciton (CT-exciton). In densely packed films of push-pull molecules not only intramolecular charge transfer can occur, but the electron can also be transferred to an acceptor unit of the neighboring molecule, therefore forming intermolecular CT-exciton.[27,90]

1.2.4 Polarons

Eventually, electronics deal with electrical current – or, in other words, with flow of charges (electrons). Thus, organic semiconductors in organic electronic devices are often populated not only with excitons, but also with free (or weekly bound) charges. Because organic semiconductors are “soft” materials, a free charge is coupled to the induced deformation of the conjugated chain which results in change of electronic configuration of the surrounding.[30] Such a quasiparticle which consists of a charge and charge-induced deformation of the surrounding is called a polaron.[91-95] Depending on the charge sign, the electron polaron and the hole polaron (Figure 1.2c, top) are distinguished.

Reorganization of surrounding and respective change in local polarization of the environment affects the energetics of the material.[30] In the case of a hole (electron) polaron the energy level of singly occupied molecular orbital (SOMO, former HOMO or LUMO) shifts up (down) in the energy (an example for hole polaron is shown in Figure 1.2c, bottom). This, in turn, results in changed optical properties of the material (namely, appearance of additional absorption bands)[91].

Polaron dynamics are of great importance for organic electronics. In the case of OSCs, charges are to be collected at the electrodes creating photocurrent; in OLEDs polarons are injected into the recombination layer, where they form excitons and, eventually, electroluminescence.

1.3 Organic Solar Cells

Solar cells are optoelectronic devices which convert incident light to electricity. A typical solar cell consists of a semiconductor-based active layer and conductive electrodes. The active layer collects incoming solar photons and converts them into charges, which are further collected by the electrodes. The power conversion efficiency (PCE) of a solar cell depends on the number of collected photons, photon-to-charge conversion ratio, charge recombination and charge collection efficiencies and so on.[96]

As any semiconductor-based device, a solar cell may be based on organic semiconductors.[37,82] Organic solar cells combine the ability of photon-to-charge conversion with advantages of organic-based devices such as light weight, flexibility, solution processability, etc.[12,97] Efficiency of OSCs has steadily overcome the 10% threshold[98] and keeps on increasing every year[99], which makes them attractive for niche applications. In this section, the basic working principles of OSCs are described.

1.3.1 Heterojunction Concept

The exciton binding energy in organic semiconductors is estimated as 0.3-1 eV[100] so that the fraction of thermally generated free charges is negligibly low. Not surprisingly that the first OSCs made of a single layer of organic semiconductor demonstrated PCE as low as 0.1% due to extremely low exciton-to-charge conversion efficiencies of <1%[8]. Despite this discouraging figure, manufacturing of the first OSCs had a great proof-of-concept value and promoted further development of organic photovoltaics.

Because of suboptimal quantum efficiencies of single-layer OSCs, it became clear that the exciton dissociation was the bottleneck in the device operation. As thermal dissociation of photogenerated excitons in organic materials is quite improbable, a driving force is needed to be applied to the exciton in order to dissociate it to the charges. A simple and elegant solution of this issue was found by creating a *heterojunction* of two organic semiconductors.[82,84] In a heterojunction, two semiconductors with different energy levels are placed together to create an interface.[101] If the exciton dissociation is energetically favorable (i.e. if the total energy of separated charges is lower than that of the exciton), the electron is transferred from the *donor* material to the *acceptor* material, thereby promoting the exciton dissociation (Figure 1.4a). Similarly, if the exciton is initially located in the acceptor material, the exciton can be dissociated via *hole transfer process* if the energy alignment allows for it (Figure 1.4b).

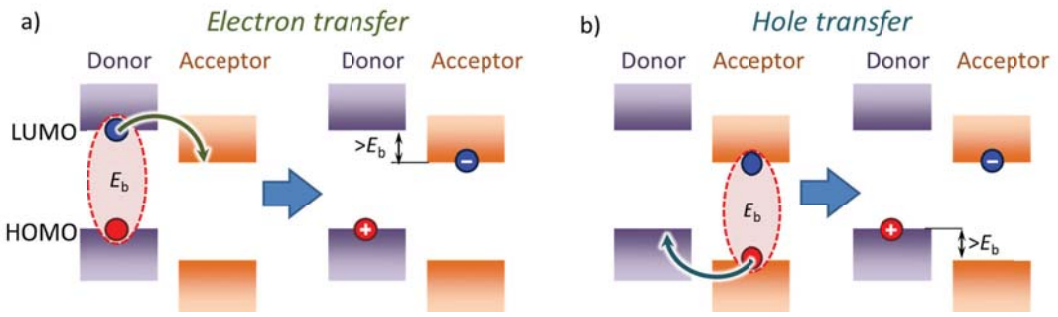

Figure 1.4 Schematic representation of (a) electron transfer and (b) hole transfer processes in heterojunction of donor-type (purple) and acceptor-type (orange) organic semiconductors. Excitons with binding energy E_b are shown by the shaded ovals.

1.3.2 Planar Heterojunction

The most straightforward realization of heterojunction concept is the so-called planar (layered) heterojunction of donor-type and acceptor-type materials. This concept was first realized by Tang in 1986 and demonstrated the overwhelming advantage over the single-layer devices: a PCE of ~1% was readily achieved[102]. Thirty years after this invention, layered solar cells reached >8% efficiency in multilayer devices with several absorbers which ensure efficient photon absorption and cascade energy transfer.[103,104]

The planar heterojunction OSCs have two major advantages. First, the device structure is very simple in principle – two layers of organic semiconductors are needed to create a simplest active layer. Second, because of the layered structure, the interface area between the two materials is relatively small, and the pathways for the charges to the electrodes are well-defined, which leads to negligible non-geminate recombination and, consequently, to a high fill factor.[105,106]

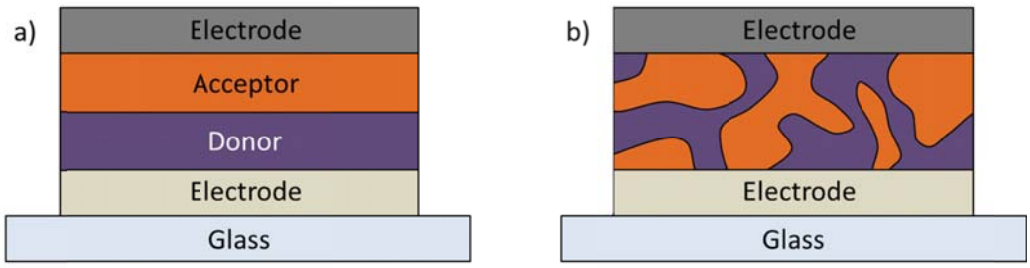

Figure 1.5 Schematic drawings of (a) planar heterojunction and (b) bulk heterojunction organic solar cells.

On the other hand, the major drawback of such a structure is mismatch between the light penetration depth of ~100 nm[12] and the exciton diffusion length of ~10 nm[107-111]. This creates a

conflict: to ensure efficient photon collection, the active layer must be thick (as the least, comparable to the light penetration depth), which inevitably results in low exciton harvesting and therefore low device efficiency. The reversed situation is the thin absorber (~10 nm) and close-to-unity exciton harvesting – but in this case the fraction of absorbed photons is extremely low with an apparent consequence of low efficiency. Because of this contradiction, it is almost impossible to design an efficient bilayer device based on widely-used organic semiconductors. Thus, the best layered heterojunction solar cells[103,104] consist of multiple absorbing layers with carefully tuned energetics to ensure efficient exciton/charge transport, and a lot of efforts in chemical and device engineering are required to fully exploit the potential of this seems-to-be-simple concept.

1.3.3 Bulk Heterojunction

A simple and elegant way to balance the exciton and charge harvesting efficiencies in the OSC active layer was discovered in 1995 by introducing the so-called "bulk heterojunction" (BHJ) concept.[112] In BHJ OSC, donor and acceptor semiconductors are mixed together during the film casting. The mixing is typically done either by co-evaporating the donor and acceptor compounds (in the case of vacuum-deposited OSC) or by casting from a pre-mixed donor:acceptor solution. As the two materials are mixed together, the active layer may be made thick enough to ensure sufficient absorption (typically, the thickness of the active layer of BHJ OSCs is in order of hundreds nanometers[12]).

During the film deposition, donor and acceptor materials self-organize in a phase-segregated network. The particular structure (also called morphology) of the donor-acceptor mixture in the active layer largely determines the efficiency of the resulting OSC.[113-116] Generally, there are several factors in the active layer morphology which influence the exciton and charge collection efficiency: the scale and the type of phase separation, the number of phases, and the area of the interface between the phases. Apparently, these factors are not independent: very intimate mixing with fine phase separation results in a large interface area while in a well-separated mixture the interface area is smaller.

Fine intermixing of the two phases ensures close-to-unity charge generation efficiency (for simplicity, we will consider ideal phase separation without intermixed region which is often present in real BHJs). However, extremely large interfacial area leads to high bimolecular recombination rate of charges. As a consequence, the two fully separated phases do not form enough pathways for the free charges to the electrodes, which eventually results in low charge collection efficiency. This is not a problem in BHJs with coarse morphology (large phase separation): due to the relatively small interfacial area, the probability of the separated electron

and hole to meet each other is fairly low, and bimolecular recombination is inefficient. Unfortunately, coarse morphology cannot ensure efficient exciton harvesting: phase-separated domains may be larger than the exciton diffusion length, and the excitons generated in such domains will be wasted.[117,118]

Therefore, the interfacial area and phase separation scale must be carefully balanced in order to achieve both efficient exciton harvesting and charge collection. As there are no solid methods to predict or to control the morphology (see Chapter 3 for details), efficiency optimization requires a lot of efforts on a trial-and-error basis. One of the most promising and straightforward ways to simplify the device optimization (both planar and bulk heterojunction – based) is developing the materials with increased exciton diffusion length.[119]

1.4 Charge Generation in Organic Solar Cells

In any heterojunction OSC, the current photogeneration process may be broken down to the following steps[120]:

1. Photon absorption and exciton generation
2. Exciton diffusion to the interface
3. Exciton dissociation at the interface
4. Charge drift to the electrodes, charge collection

Each step is subject to losses, which have to be minimized in order to achieve maximal efficiency of the device. As was discussed, the requirements for optimizing different steps may be contradictive (for example, there is interplay between exciton harvesting and non-geminate recombination). Therefore, the design of efficient OSCs is quite complex and well-thought, and requires not only optimizing of the active layer, but also wise choosing of the electrodes[121], using of buffer layers[122] and so on.

1.4.1 Photon absorption and exciton photogeneration

The very first step of OSC operation is absorption of the solar photons and generation of excitons. In modern OSCs, push-pull polymers and small molecules are typically used as a donor material[120,123], while highly absorptive C_{70} fullerene or its soluble derivatives (e.g. $PC_{71}BM$) act as an acceptor[120]. Typically, the donor material collects photons from near-IR and green/red regions of the solar spectrum while the fullerene acceptor is responsible for the photon harvesting in the blue/near-UV range.

At this step, there might be losses of two kinds: i). transmission of photons through the active layer due to the low absorbance of the device, and ii). poor energy management due to the non-optimal bandgap of the absorbers.

The first issue may be resolved straightforwardly by increasing the absorber thickness. However, this might be not an optimal solution as in the case of planar heterojunction OSC increasing the absorber thickness would reduce the exciton harvesting while for the BHJ device non-geminate recombination will be increased. A more optimal way is to design materials with high extinction coefficient to ensure sufficient photon absorption in a relatively thin (<100 nm) layer[124] or to increase the exciton diffusion length in the materials[119].

The second loss channel takes place if the bandgap of the absorber(s) is too wide or too low. In the case of a wide-bandgap absorber, a significant fraction of low-energy photons is lost, which leads to decreased photocurrent. A too narrow bandgap results in thermalization losses of high-energy photons and to decreased voltage. To achieve the best energy management, the bandgaps, the LUMO-LUMO offset (and the HOMO-HOMO offset) of the donor and acceptor compounds have to be carefully tuned.[80,125] Depending on the LUMO-LUMO offset, optimal bandgap of the donor material (which is considered to be the main absorber) varies in 1.1 eV – 2 eV region[126]. Another approach to maximize the photon harvesting is using multi-cell devices with absorber layers tuned for the particular wavelength range.[127-130]

1.4.2 Exciton diffusion

In the next step, the photogenerated excitons need to reach the interface in order to dissociate into a pair of charges. As excitons are neutral species with zero net charge, they cannot be driven and guided by an external electric field of an OSC; in the first approximation, the exciton motion is random. Such random motion is described as diffusion – the process of spreading of neutral particles from areas of high concentration to areas of low concentration.[131,132]

In organic semiconductors, the exciton diffusion is often considered as random hopping between the molecules/conjugated segments, occurring either via Förster-like or Dexter energy transfer mechanisms. In the simplest case of fully random hopping with constant rate, the exciton diffusion in three-dimensional medium is described by the well-known diffusion equation[133,134]:

$$\frac{\partial n(\boldsymbol{r},t)}{\partial t} = -\frac{n(\boldsymbol{r},t)}{T_1} + D\nabla^2 n(\boldsymbol{r},t) + G(\boldsymbol{r},t), \tag{1.1}$$

where $n(r,t)$ is the exciton concentration, T_1 is the exciton lifetime, D is the exciton diffusion constant and G is the exciton generation rate. In the case of normal diffusion (i.e. if the mean squared displacement of the exciton is a linear function of time), the exciton diffusion length is readily calculated as:

$$L_d = \sqrt{2ZDT_1}, \tag{1.2}$$

where Z is dimensionality of the diffusion process. Typical values for L_d in organics amount to 3-10 nm[107-111,134], which essentially limits the phase separation scale in heterojunction OSC: if the spatial separation between the donor and the acceptor phases is large than L_d, a significant fraction of the excitons is lost[117,135].

Equation (1.1) is written with important assumptions: (i) no interactions between the excitons (e.g. exciton-exciton annihilation) occur, and (ii) the diffusion coefficient D is constant in space and time. In the real organic semiconductors only the first condition can be fulfilled by minimizing the flux of the incoming light to ensure low density of photogenerated excitons.

The second condition is challenged by the fact that "soft" organic semiconductors are often characterized by significant energetic disorder with a Gaussian density of states (DOS)[45,136,137]. This inevitably leads to time-dependent diffusion dynamics: photogenerated excitons undergo downhill migration within the DOS until they reach the equilibrium energy level of $-\sigma^2/kT$ (assuming that the DOS is centered at 0 eV)[137,138], where σ is the width of the Gaussian DOS, k is the Boltzmann constant, and T is the ambient temperature (Figure 1.6). In a disordered medium, the hopping process is thermally activated and the hopping probability depends on the energies of the initial and host sites[45,139,140]:

$$p_{ij} = \begin{cases} 1 & if\ E_i \geq E_j \\ exp\left(-\frac{E_j - E_i}{kT}\right) & if\ E_i < E_j' \end{cases} \tag{1.3}$$

where p_{ij} is the hopping probability and E_i and E_j are energies of initial and host sites, respectively.

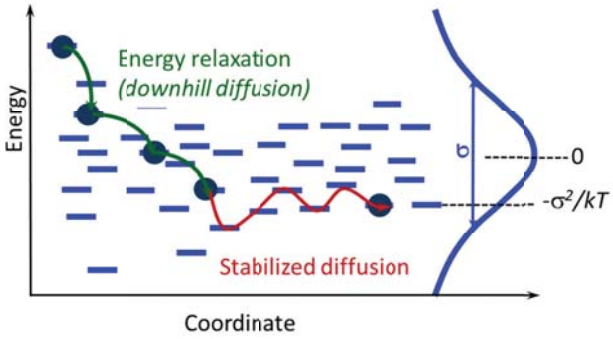

Figure 1.6 Schematic representation of exciton diffusion in a disordered medium. Exciton downhill migration (green arrows) is followed by the stabilized diffusion (red arrow) around equilibrium energy level of $-\sigma^2/kT$.

Because of the presence of different diffusion regimes in a disordered material, the diffusion process cannot be considered as normal anymore. During the downhill migration, the excitons

tend to “choose” the sites with the lowest energy among the neighboring sites and therefore the direction of the exciton diffusion is largely pre-defined by the energetic landscape.[141] This makes the whole exciton diffusion process essentially anomalous[142] and, generally speaking, it cannot be described with the Equations (1.1) and (1.2). In the extreme of very fast exciton cooling in comparison with the exciton lifetime, the diffusion length still can be estimated from Equation (1.2) with the stabilized value of *D* taken. However, typically the singlet exciton lifetime in organic semiconductors is shorter that 1 ns while the cooling time may be as long as several hundreds of picoseconds.[143] In this case, the stabilized diffusion does not dominate, and the diffusion length has to be calculated from the average displacement of the excitons.

It should be noted that the diffusion coefficient decreases dramatically during the exciton cooling: the difference between initial *D* and stabilized *D* can exceed an order of magnitude[142,143]. This leads to significant shortening of the diffusion length. Thus, increasing the exciton lifetime and decreasing the material disorder are winning strategies for maximizing the exciton diffusion length and, therefore, the exciton harvesting. Exciton diffusion in ordered and disordered semiconductors is considered in detail in Chapters 2-3 of this Thesis.

1.4.3 Exciton dissociation

After having reached the donor-acceptor interface, photogenerated excitons must be dissociated to a pair of free (separated) charges. To make the dissociation process efficient, the donor-acceptor interface should meet a number of requirements. First of all, the exciton dissociation must be energetically favorable, i.e. the LUMO-LUMO (HOMO-HOMO) offset between the donor and acceptor materials must be large enough to ensure efficient electron (hole) transfer.[97] Secondly, the orbital overlap between the donor and acceptor molecules at the interface should be large enough[144]; otherwise the charge transfer would not be possible even if the energetics allows for it.

If the donor-acceptor pair meets the aforementioned requirements, the exciton dissociates at the interface via electron or hole transfer. However, exciton dissociation *per se* does not guarantee formation of free charges. After charge transfer, the electron and hole which reside at different materials are still Coulombically bound.[145] This interfacial bound electron-hole pair is called the charge-transfer (CT) state (Figure 1.2d).[146,147] The filling of CT states via electron or hole transfer processes occurs at ultrafast (<100 fs) timescales.[148-152]

Eventually, the electron and hole in the CT state either overcome their Coulomb attraction and form a separated pair of free charges[153], recombine back to ground state[147], or form a singlet or triplet exciton (with triplet excitons prevailing both due to the spin statistics and favorable energetics) via back electron (hole) transfer[154-157]. Apparently, in a good working photovoltaic blend the first route must be dominating, while the latter two have to be suppressed in order to

achieve maximal efficiencies. Thus, the donor-acceptor system should be designed in such way to promote the CT state separation and minimize geminate recombination.[33,158]

Typically, the energy of the CT state is lower than the energy of the exciton, thus the CT state is formed in a "hot" state with some excess energy present which depends on the LUMO-LUMO (HOMO-HOMO) offset of the donor-acceptor pair. Even though the role of this excess energy of hot excitons by itself for CT state dissociation is questionable[33,159], it was shown that it promotes direct formation of separated charge pairs bypassing the bound CT state[160] because of effective delocalization of the electron and hole densities in "hot" states, which facilitates long-range charge separation. Delocalization of the state depends on the state energy[160], materials used[33] and blend morphology[158]. After initial separation, the distance between the electron and hole increases due to the disorder-assistant[161,162] fast motion of not-yet-cooled charges (mainly electrons)[163], until it reaches ~10-15 nm where the charges can be considered free. Thus, extending the wavefunctions delocalization of separated charges and charge mobility by material and device engineering is a route to efficiency optimization by reducing geminate recombination of CT states (see Chapter 5 for detailed discussion of charge separation in BHJ OSCs).

1.4.4 Charge collection

The last step of photon-to-electricity conversion in OSCs is collection of separated charges. At this step, the separated charges have to find their way to the electrodes. As charges can be guided by the external field, their motion is not random: electrons drift to the anode while the holes move to the cathode. The important loss mechanism at this state is non-geminate recombination of the charges.[164]

In the layered OSCs, the probability of electron and hole to meet each other and recombine is very low[106] as the charges transport from the interface to the electrodes within different material phases. This fact explains high fill factors of the layered devices.[105,165] In BHJ OSCs, however, this is not the case. As BHJs form a percolated random structure, no direct and straight pathways to the electrodes are present. Thus, the charges must travel along the entangled channels of the corresponding phases. In such a system, the probability of electron and hole to meet each other at the interface is considerably higher.[166,167] Additionally, in the BHJ solar cells low-energy traps for the carriers or isolated clusters of either of the materials can be formed which also reduces the charge collection.[168] To minimize the non-geminate recombination and the number of traps, material ordering and morphology optimization are required.

1.5 Goals and Objectives of the Thesis

This Thesis is devoted to ultrafast charge generation and recombination channels in organic photovoltaics, and provides comprehensive studies of early-time photoinduced dynamics in

modern organic photovoltaics along with suggestions for further improvement of OSC efficiency.

The Thesis aims at answering the following questions: What are the initial steps of photon-to-current conversion? What are the fundamental processes which determine the efficiency of charge generation in organic solar cells? How could the exciton dynamics in organic semiconductors be controlled and observed? What are the possible ways to increase the quantum efficiency of OSCs?

To answer these questions, the following objectives are posed:

1) To develop a direct technique to track the exciton diffusion in real time (Chapter 2) and to apply the technique to monitor the exciton dissociation dynamics in bulk heterojunction solar cells (Chapters 3)
2) To examine the dynamics of primary photoexcitations in organic semiconductors (Chapter 4)
3) To identify main charge generation and recombination channels in bulk heterojunction solar cells at ultrafast timescales and suggest the routes for device optimization (Chapter 5)
4) To demonstrate a possibility to control the triplet harvesting from singlet fission material by e.g. changing the active layer morphology (Chapter 6)

To fulfill the objectives, time-resolved photoinduced absorption spectroscopy in combination with time-resolved photoluminescence and steady-state spectroscopy techniques was used.

1.6 Photoluminescence and Photoinduced Absorption Spectroscopies

A convenient and most straightforward approach to study the photophysical processes in organic semiconductors is optical spectroscopy.[30,97] The simplest spectroscopic technique is linear absorption spectroscopy. Even this simplest experimental approach provides tremendous amount of useful information about the system[169] such as the optical bandgap, vibrational frequencies, presence of ground-state charge-transfer complexes and so on. However, linear absorption spectroscopy lacks the dynamical aspect: it is impossible to track the evolution of the photoexcitations. To study the dynamics of excited states, it is necessary to employ non-linear time-resolved spectroscopies.

1.6.1 Time-resolved photoluminescence

After the system is excited to some high-energy state after photon absorption, the processes lowering the potential energy of the system will start. A most straightforward process is to return back to the ground state. If the relaxation to the ground state is accompanied by photon emission, such a process is called photoluminescence (PL). To examine the dynamics of the excitation, the

PL must be measured in a time-resolved manner. In organic semiconductors and photovoltaic blends, PL provides important information about material properties, excitons and CT states.

The primary photoexcitations in organic materials – singlet excitons – can relax to the ground state with a photon emission within relatively short times (typically in order of nanoseconds). Not surprisingly that time-resolved photoluminescence is one of the most popular approaches to study the exciton dynamics in organic semiconductors.[99,100,109,110,157,158]

The most straightforward results obtained from the time-resolved PL measurements are exciton lifetime[44,170] and the singlet quantum yield[63,171]. The former is important to know, as the exciton lifetime must be large enough to ensure the possibility for the excitons to reach the interface; generally, a longer lifetime results in simplified device optimization.[44,119]

Knowing the PL quantum yield is crucial as it is directly related to the presence of non-radiative relaxation channels. The pathways of non-radiative decay are typically triplet-to-singlet conversion, non-radiative relaxation and exciton trapping in "dark" states.[172] In some exceptional cases, exciton-to-polaron conversion may occur, which also lead to decreased PL lifetime (and, consequently, quantum yield)[173], see Chapter 4 for details. For each individual material, the exact pathways of non-radiative decay suggest the routes to device optimization.

Using time- and frequency-resolved PL measurements, one can estimate the energetic disorder of the material. Right after photoexcitation above the bandgap, the excitons uniformly occupy the DOS, and then the excitons start to lose their energy due to the downhill migration within the DOS (see Section 1.4.2 "Exciton diffusion"). Finally, the diffusion process stabilizes at the energy level of $-\sigma^2/kT$ below the center of DOS.[126,127]

The process of downhill exciton migration affects the PL energy. Obviously, the excitons which occupy higher energy levels in the DOS also emit photons with higher energy compared to the excitons which reside at lower energy levels. Therefore, right after photoexcitation the PL spectrum peaks at the center of DOS. During the exciton cooling, the PL spectrum shifts to the red and stabilizes when the excitons reach the equilibrium level.[142,143,174,175] The width of energetic disorder σ is calculated from the difference in PL spectrum at the early times and stabilized PL spectrum.

In principle, any emitting species can be studied with time-resolved PL. If the charge separation in a BHJ blend occurs via interfacial CT state, there is a finite probability of CT state to recombine to the ground state producing a PL.[176-178] In this case, PL can provide important information about CT state dynamics.[179]

Typically, PL of the CT state is red-shifted compared to the PL of singlet excitons[176,180]. This fact can be used to separate these PL channels and to calculate the branching ratio between the PL of singlet excitons (i.e. the number of excitons which relax before reaching the interface) and CT-state PL (which is proportional to the number of dissociated excitons). This branching ratio

was shown to be correlated with the OSC efficiency[177] and can be used as a tool for blend optimization. Additionally, the fact that the CT state emission occurs only from the donor-acceptor interface can be used to study the morphology of donor-acceptor blends[181], diffusion of the interfacial charge pairs[182] or reveal the low-energy trap states from which efficient bimolecular recombination occurs[179,183].

1.6.2 Photoinduced absorption

Photoluminescence-based techniques are extremely convenient for measuring the dynamics of emitting species; however, photoexcitations that do not produce light (e.g. free charges) are not observable by PL means. As dynamics of free charges are extremely important for OSC operation, it is necessary to be able to detect them.

As it was mentioned in Section 1.2.4 "Polarons", formation of free charges in organic semiconductor leads to deformation of the molecule and, eventually, formation of energy levels within the bandgap (the so-called Singly Occupied Molecular Orbital – SOMO)[30]. HOMO-SOMO and SOMO-LUMO transitions form two additional polaron-induced absorption bands[94] (Figure 1.7, red curve). Typically, in time-resolved photoinduced absorption experiments (PIA) on organic photovoltaic blends, hole polarons at the donor phase are detected.

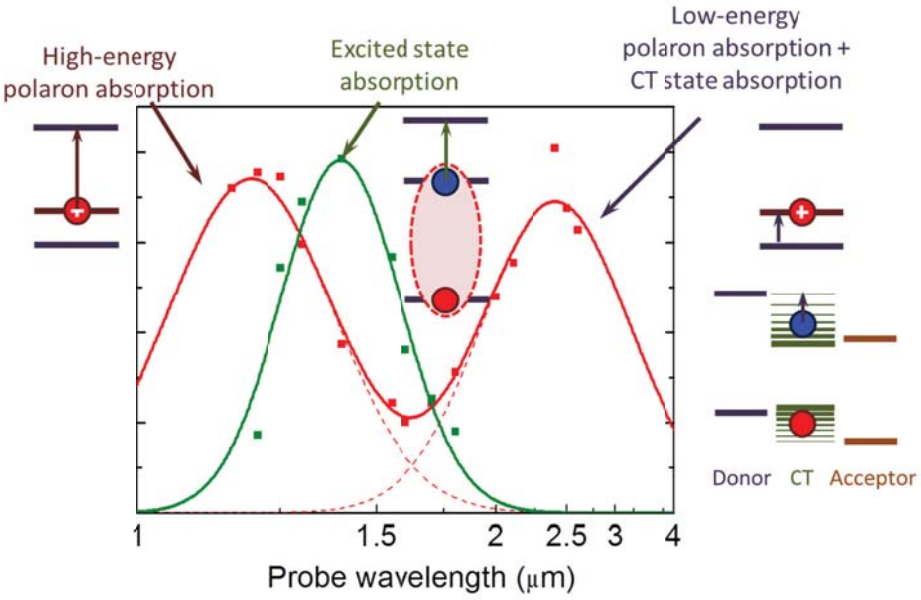

Figure 1.7 Representative PIA spectrum of a BHJ blend (adopted from Ref. [184]). Experimental points are shown by symbols while lines are the best fits with Gaussian functions. The exciton response and combined polaron/CT state responses are shown by the green and red, respectively. The transitions are schematically shown next to the respective bands.

As a rule-of-thumb, there is inverse proportionality between the polaron absorption energy and the conjugated length of the molecule[32]:

$$P_1 = \frac{A}{L} + C, \tag{1.4}$$

where P_1 is the photoinduced absorption band energy, C and A are constants (which depend on the particular system), and L is the conjugation length. In conjugated polymers, the high-energy and low energy bands are usually located around ~1 μm and ~3 μm, respectively[185-187]. As in polymers the conjugation length can be long, the positions of polaron absorption peaks depend mainly on the polymer structure (i.e. they are determined by constant C in Equation (1.4)), while the dependence on the conjugation length is not that prominent.

In contrast, in small molecular semiconductors, the positions of polaron bands strongly depend both on the chemical structure and conjugation length of the molecule. Typically, the low-energy band is located in 1-3 μm region, with the high-energy band position in the visible region[188-191].

Along with polaron detection, PIA can be also used to detect other excitations - excitons and CT states. Excitons are detected via the excited state absorption – after absorbing a photon, the exciton can be excited to a higher excited state (S_1-S_n transition)[54,160,192,193]. The excited state absorption spectrum is typically red-shifted from the linear absorption spectrum and located in the near-IR region (Figure 1.7, green curve). Because of this, the exciton spectrum often (partially) overlaps with the high-energy polaron absorption band. Luckily, the dynamics of the two species can be easily separated due to i). different cross-sections of polaron and exciton absorptions, ii). different time behavior of the two species (excitons undergo fast dissociation in BHJ, while the lifetime of polarons is typically long), and iii). possibility to isolate the exciton response in a pure film without external acceptor.

Detection of CT state dynamics by PIA is more complicated than polaron and exciton detection and it is also less straightforward. The spectral signature of the CT states may combine exciton-like excited state absorption with polaron-like absorption, and the CT state PIA spectrum typically overlaps with the low-energy polaron band[33,194]. As it is essentially impossible to isolate the CT state response, it is often a non-trivial task to distinguish between the CT state and low-energy polaron absorption.

1.6.3 Time-resolved pump-probe technique

The photoinduced absorption is proportional to the number of photoexcited species present in the material (be that polarons, excitons or CT states):

$$\Delta A \sim \Delta \alpha z \sim N, \tag{1.5}$$

where ΔA is the change of the sample absorption caused by excited species, α is the extinction coefficient, z is the sample's thickness and N is a number of photoexcited species. Thus, to measure the concentration of photogenerated excitations, one can compare the absorption of the sample in the ground state and after photoexcitation.

A typical way to do this is the so-called pump-probe approach. First, the system is excited to a non-equilibrium state by a laser pulse (the so-called "pump" or "excitation" pulse). After that, the absorption of the system is measured with a second "probe" pulse, which intensity is weak in order to prevent re-excitation of the sample. By comparing the absorptions of the sample with and without the excitation pulse, one can estimate the concentration of photogenerated species (see Equation (1.5)). By varying the delay between the two pulses, the dynamics of the photoexcitations can be easily followed. Also the excitation and probe pulses must be tunable (or have broad spectrum) to ensure freedom in exciting/probing different species.

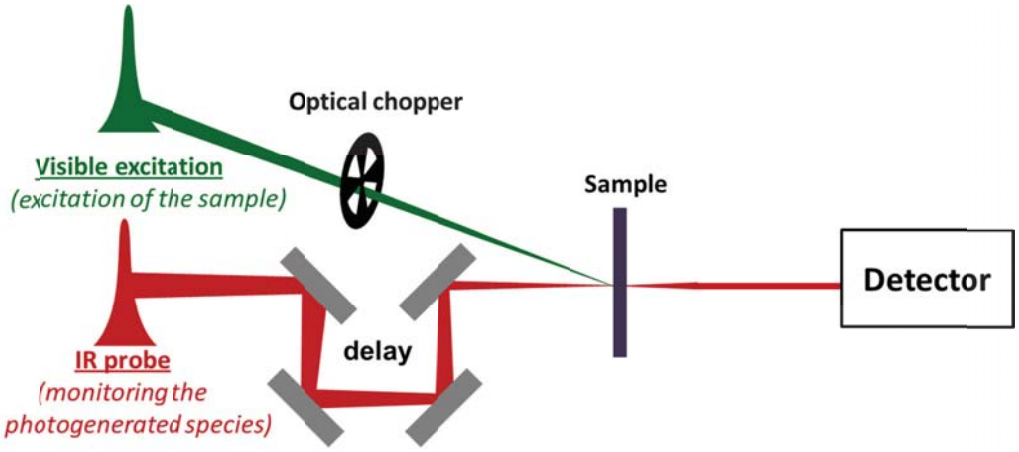

Figure 1.8 Schematic representation of a typical two-color pump-probe setup.

A schematic representation of a pump-probe setup is shown in Figure 1.8. The excitation and probe laser pulses are focused into the sample, and the intensity of transmitted IR probe pulse is measured by a detector. The excitation pulse passes an optical chopper in order to ensure momentarily comparison of the intensities of the probe pulse with the excitation pulse open/closed.

Experimentally, not the absorption but the intensity of transmitted light I is detected. The intensity of transmitted light is directly related to the transmittance T of the sample as:

$$T = \frac{I}{I_0}, \tag{1.6}$$

where I and I_0 are intensities of transmitted and incident light, respectively. If the induced change of the extinction coefficient is low ($\Delta\alpha z \ll 1$), the normalized difference in transmittance is:

$$-\frac{\Delta T}{T} = \frac{T - T'}{T} = \frac{I - I'}{I} = \frac{I_0 e^{-\alpha z} - I_0 e^{-\alpha' z}}{I_0 e^{-\alpha z}} = 1 - e^{-\Delta\alpha z} \approx \Delta\alpha z \sim N, \tag{1.7}$$

where T and T' are transmissions and I and I' are intensities of transmitted light with and without excitation, respectively. Thus, the normalized change in sample's transmission is also proportional to the number of excitations. Note that the results of PIA experiments in this Thesis are denoted as $-\Delta T/T$ as it corresponds to the real experimental conditions.

1.7 Overview of the Thesis

This Thesis focuses on revealing the early steps of photon-to-charge conversion in organic solar cells using ultrafast spectroscopy as a tool. Early-time photophysics is extremely important in organic optoelectronics, as any losses occurring at ultrafast timescales cannot be recovered further on, which necessarily results in non-optimal efficiencies. Thus, each process of photon-to-charge conversion (see Section 1.4 "Charge Generation in Organic Solar Cells") has to be carefully observed and monitored, and the Thesis aims to fulfill this mission step-by-step.

In Chapter 2, a direct spectroscopic technique to track the singlet exciton diffusion process in real time with femtosecond accuracy is introduced. With this new technique, extremely fast exciton diffusion in vacuum-deposited C_{70} fullerene was demonstrated, which results in efficient exciton harvesting from a 70 nm thick layer. The diffusion coefficient was shown to be 10 times higher than in common organics because of extremely low material disorder. The proposed noninvasive time-of-flight technique is a powerful tool for further development of organic optoelectronic components, such as e.g. layered and bulk heterojunction solar cells.

In Chapter 3, the novel technique is applied for morphology characterization of bulk heterojunction solar cells. Diffusion-delayed exciton dissociation from phase-separated domains of fullerene acceptor allows for capturing the essential morphology features with ~1 nm spatial resolution. The morphology is modelled as spherical fullerene domains of two types and sizes ("mixed phase" and "large domains") dispersed in the polymer matrix, and the sizes of the clusters are retrieved from Monte-Carlo simulations of the fullerene exciton dissociation dynamics. The validity of this approach is demonstrated using mixtures of three well-known polymers (MDMO-PPV, RRa-P3HT and RRe-P3HT) with $PC_{71}BM$ acceptor, and the possibility to expand the technique to modern low-bandgap donors was demonstrated. From the simulations,

it was shown that energetic disorder is a major factor limiting the exciton diffusion length in organics, and promoting the material ordering is a winning strategy to maximize the exciton collection.

In Chapter 4, exciton dynamics preceding intermolecular charge separation are discussed. Using small star-shaped push-pull molecules with different donor and acceptor units, it was shown that efficient exciton-to-polaron conversion occurs in thin films even without external acceptor. Exciton-to-polaron conversion takes place at tens of picoseconds timescales and results in populating the film with quasi-free electron-hole pairs with low Coulomb binding. These findings suggest that promoting intermolecular interactions in films of small organic molecules is one of the pathways to highly efficient organic solar cells.

In Chapter 5, the processes following exciton diffusion – charge separation and recombination – are discussed. Using bulk heterojunction blends of three novel star-shaped push-pull molecules with $PC_{71}BM$ acceptor as model system, dynamics of charge generation and recombination were revealed. It was demonstrated, that both electron and hole transfers contribute to the separated charges with comparable efficiencies. Geminate charge recombination via interfacial charge-transfer states competes with charge separation, decreasing the overall fraction of separated charges to ~60% at the optimal donor:acceptor ratio, limiting the quantum efficiency of the resulted device. Thus, any charge losses at ultrafast timescale must be suppressed by material and/or device design to maximize the efficiency of the device.

Chapter 6 addresses the question of triplet harvesting in organic photovoltaics. Possibility of the triplet harvesting in organic photovoltaics is a burning issue as it allows developing of singlet fission solar cells with up to 200% quantum efficiency for certain spectral regions. In this Chapter, the possibility of triplet harvesting from a SF material (rubrene) combined with C_{60} acceptor is demonstrated using time-resolved PL. It was shown that the efficiency of triplet harvesting depends strongly on the rubrene morphology: triplet excitons are efficiently harvested in crystalline rubrene/C_{60} while in an amorphous rubrene/C_{60} bilayer no triplet harvesting occurs due to unfortunate energy alignment. The results presented in this chapter demonstrate the importance of fine tuning of the active layer energetics for the exciton harvesting, which can be achieved by morphology control.

Overall, the Thesis covers all initial steps of photon-to-charge conversion in both singlet- and triplet- driven modern organic photovoltaics revealing the ultrafast processes which eventually lead to the generation of photocurrent. Charge generation processes and loss mechanisms are revealed by time-resolved PIA and PL spectroscopies, which proves them as powerful and indispensable tools for understanding the photophysics of organic optoelectronic devices.

References

1 www.getwuf.com.

2 *AT&T develops "smart slippers" for fall prevention*, www.mobihealthnews.com/5675/att-develops-smart-slippers-for-fall-prevention.

3 T. Floyd. *Electronic Devices (Conventional Current Version) (9th Edition)*. (Pearson Education, 2011).

4 H. Letheby. XXIX.-On the Production of a Blue Substance by the Electrolysis of Sulphate of Aniline. *J. Chem. Soc.* **15**, 1862, p. 161.

5 H. Shirakawa, E. J. Louis, A. G. MacDiarmid, C. K. Chiang, and A. J. Heeger. Synthesis of Electrically Conducting Organic Polymers: Halogen Derivatives of Polyacetylene, $(CH)_x$. *Journal of the Chemical Society, Chemical Communications* no. 16, 1977, p. 578.

6 M. Jacob. Organic Semiconductors: Past, Present and Future. *Electronics* **3** no. 4, 2014, p. 594.

7 S. Ahmad. in *J. Polym. Eng.* Vol. 34 279 (2014).

8 H. Spanggaard and F. C. Krebs. A Brief History of the Development of Organic and Polymeric Photovoltaics. *Sol. Energy Mater. Sol. Cells* **83** no. 2–3, 2004, p. 125.

9 *Heliatek sets new Organic Photovoltaic world record efficiency of 13.2%*, www.heliatek.com/en/press/press-releases/details/heliatek-sets-new-organic-photovoltaic-world-record-efficiency-of-13-2 (2016).

10 F. Ebisawa, T. Kurokawa, and S. Nara. Electrical Properties of Polyacetylene/Polysiloxane Interface. *J. Appl. Phys.* **54** no. 6, 1983, p. 3255.

11 C. W. Tang and S. A. VanSlyke. Organic Electroluminescent Diodes. *Appl. Phys. Lett.* **51** no. 12, 1987, p. 913.

12 C. Brabec, U. Scherf, and V. Dyakonov. *Organic Photovoltaics: Materials, Device Physics, and Manufacturing Technologies*. (Wiley-VCH Verlag GmbH & Co. KGaA, Weinheim, Germany, 2011).

13 J. D. Myers and J. Xue. Organic Semiconductors and their Applications in Photovoltaic Devices. *Polym. Rev.* **52** no. 1, 2012, p. 1.

14 A. Moliton and R. C. Hiorns. Review of Electronic and Optical Properties of Semiconducting π-Conjugated Polymers: Applications in Optoelectronics. *Polym. Int.* **53** no. 10, 2004, p. 1397.

15 A. Facchetti. π-Conjugated Polymers for Organic Electronics and Photovoltaic Cell Applications. *Chem. Mater.* **23** no. 3, 2011, p. 733.

16 Y. Lin, Y. Li, and X. Zhan. Small Molecule Semiconductors for High-Efficiency Organic Photovoltaics. *Chem. Soc. Rev.* **41** no. 11, 2012, p. 4245.

17 A. Mishra and P. Bäuerle. Small Molecule Organic Semiconductors on the Move: Promises for Future Solar Energy Technology. *Angewandte Chemie International Edition* **51** no. 9, 2012, p. 2020.

18 P.-O. Morin, T. Bura, and M. Leclerc. Realizing the Full Potential of Conjugated Polymers: Innovation in Polymer Synthesis. *Materials Horizons* **3** no. 1, 2016, p. 11.

19 F. Bures. Fundamental Aspects of Property Tuning in Push-Pull Molecules. *RSC Adv.* **4** no. 102, 2014, p. 58826.

20 D. Chunhui, H. Fei, and C. Yong. Recent Development of Push-Pull Conjugated Polymers for Bulk-Heterojunction Photovoltaics: Rational Design and Fine Tailoring of Molecular Structures. *J. Mater. Chem.* **22** no. 21, 2012, p. 10416.

21 W. C. Dunlap and R. L. Watters. Direct Measurement of the Dielectric Constants of Silicon and Germanium. *Physical Review* **92** no. 6, 1953, p. 1396.

22 S. Torabi, F. Jahani, I. Van Severen, C. Kanimozhi, S. Patil, R. W. A. Havenith, R. C. Chiechi, L. Lutsen, D. J. M. Vanderzande, T. J. Cleij *et al.* Strategy for Enhancing the Dielectric Constant of Organic Semiconductors Without Sacrificing Charge Carrier Mobility and Solubility. *Adv. Funct. Mater.* **25** no. 1, 2015, p. 150.

23 P. W. M. Blom, V. D. Mihailetchi, L. J. A. Koster, and D. E. Markov. Device Physics of Polymer:Fullerene Bulk Heterojunction Solar Cells. *Adv. Mater.* **19** no. 12, 2007, p. 1551.

24 M. A. Loi, S. Toffanin, M. Muccini, M. Forster, U. Scherf, and M. Scharber. Charge Transfer Excitons in Bulk Heterojunctions of a Polyfluorene Copolymer and a Fullerene Derivative. *Adv. Funct. Mater.* **17** no. 13, 2007, p. 2111.

25 X. Y. Zhu, Q. Yang, and M. Muntwiler. Charge-Transfer Excitons at Organic Semiconductor Surfaces and Interfaces. *Acc. Chem. Res.* **42** no. 11, 2009, p. 1779.

26 A. E. Jailaubekov, A. P. Willard, J. R. Tritsch, W.-L. Chan, N. Sai, R. Gearba, L. G. Kaake, K. J. Williams, K. Leung, P. J. Rossky *et al.* Hot Charge-Transfer Excitons Set the Time Limit for Charge Separation at Donor/Acceptor Interfaces in Organic Photovoltaics. *Nat. Mater.* **12** no. 1, 2013, p. 66.

27 D. Qi, H. Su, M. Bastjan, O. D. Jurchescu, T. M. Palstra, A. T. S. Wee, M. Rübhausen, and A. Rusydi. Observation of Frenkel and Charge Transfer Excitons in Pentacene Single Crystals Using Spectroscopic Generalized Ellipsometry. *Appl. Phys. Lett.* **103** no. 11, 2013, p. 113303.

28 P. A. Lane, X. Wei, and Z. V. Vardeny. Spin and Spectral Signatures of Polaron Pairs in π-Conjugated Polymers. *Physical Review B* **56** no. 8, 1997, p. 4626.

29 R. Tautz, E. Da Como, T. Limmer, J. Feldmann, H.-J. Egelhaaf, E. von Hauff, V. Lemaur, D. Beljonne, S. Yilmaz, I. Dumsch *et al.* Structural Correlations in the Generation of Polaron Pairs in Low-Bandgap Polymers for Photovoltaics. *Nat. Commun.* **3**, 2012, p. 970.

30 G. Lanzani. *The Photophysics behind Photovoltaics and Photonics.* (Wiley-VCH, Weinheim, Germany, 2012).

31 Y.-J. Cheng, S.-H. Yang, and C.-S. Hsu. Synthesis of Conjugated Polymers for Organic Solar Cell Applications. *Chemical Reviews* **109** no. 11, 2009, p. 5868.

32 G. Lanzani. *Photophysics of Molecular Materials: From Single Molecules to Single Crystals.* (Wiley-VCH Verlag GmbH & Co. KGaA, 2006).

33 A. A. Bakulin, A. Rao, V. G. Pavelyev, P. H. M. van Loosdrecht, M. S. Pshenichnikov, D. Niedzialek, J. Cornil, D. Beljonne, and R. H. Friend. The Role of Driving Energy and Delocalized States for Charge Separation in Organic Semiconductors. *Science* **335** no. 6074, 2012, p. 1340.

34 A. Kohler and H. Bassler. *Electronic Processes in Organic Semiconductors: An Introduction*. (Wiley-VCH Verlag GmbH & Co. KGaA, Weinheim, Germany, 2015).

35 G. H. Wannier. The Structure of Electronic Excitation Levels in Insulating Crystals. *Physical Review* **52** no. 3, 1937, p. 191.

36 E. F. Gross. Optical Spectrum and Magneto-Optical Properties of Excitons. *J. Phys. Chem. Solids* **8**, 1959, p. 172.

37 P. Würfel. Photovoltaic Principles and Organic Solar Cells. *CHIMIA International Journal for Chemistry* **61** no. 12, 2007, p. 770.

38 H.-W. Li, Z. Guan, Y. Cheng, T. Lui, Q. Yang, C.-S. Lee, S. Chen, and S.-W. Tsang. On the Study of Exciton Binding Energy with Direct Charge Generation in Photovoltaic Polymers. *Advanced Electronic Materials*, 2016, p. 1600200.

39 S. Y. Leblebici, T. L. Chen, P. Olalde-Velasco, W. Yang, and B. Ma. Reducing Exciton Binding Energy by Increasing Thin Film Permittivity: An Effective Approach To Enhance Exciton Separation Efficiency in Organic Solar Cells. *ACS Appl. Mater. Interfaces* **5** no. 20, 2013, p. 10105.

40 J. E. Donaghey, A. Armin, P. L. Burn, and P. Meredith. Dielectric Constant Enhancement of Non-Fullerene Acceptors via Side-Chain Modification. *Chemical Communications* **51** no. 74, 2015, p. 14115.

41 R. C. Powell and Z. G. Soos. Singlet Exciton Energy Transfer in Organic Solids. *J. Lumin.* **11** no. 1, 1975, p. 1.

42 Z. Xu and B. Hu. Photovoltaic Processes of Singlet and Triplet Excited States in Organic Solar Cells. *Adv. Funct. Mater.* **18** no. 17, 2008, p. 2611.

43 R. Osterbacka, M. Wohlgenannt, M. Shkunov, D. Chinn, and Z. V. Vardeny. Excitons, Polarons, and Laser Action in Poly(p-phenylene vinylene) Films. *J. Chem. Phys.* **118** no. 19, 2003, p. 8905.

44 S. Dimitrov, B. Schroeder, C. Nielsen, H. Bronstein, Z. Fei, I. McCulloch, M. Heeney, and J. Durrant. Singlet Exciton Lifetimes in Conjugated Polymer Films for Organic Solar Cells. *Polymers* **8** no. 1, 2016, p. 14.

45 K. Feron, W. Belcher, C. Fell, and P. Dastoor. Organic Solar Cells: Understanding the Role of Förster Resonance Energy Transfer. *Int. J. Mol. Sci.* **13** no. 12, 2012, p. 17019.

46 T. Förster. Transfer Mechanisms of Electronic Excitation Energy. *Radiation Research Supplement* **2**, 1960, p. 326.

47 S. Hofmann, T. C. Rosenow, M. C. Gather, B. Lüssem, and K. Leo. Singlet Exciton Diffusion Length in Organic Light-Emitting Diodes. *Physical Review B* **85** no. 24, 2012, p. 245209.

48 D. L. Dexter. A Theory of Sensitized Luminescence in Solids. *The Journal of Chemical Physics* **21** no. 5, 1953, p. 836.

49 M. A. Baldo, M. E. Thompson, and S. R. Forrest. High-Efficiency Fluorescent Organic Light-Emitting Devices Using a Phosphorescent Sensitizer. *Nature* **403** no. 6771, 2000, p. 750.

50 A. Köhler and H. Bässler. Triplet States in Organic Semiconductors. *Materials Science and Engineering: R: Reports* **66** no. 4–6, 2009, p. 71.

51 *Quantum Physics (UCSD Physics 130)* quantummechanics.ucsd.edu/ph130a/130_notes/node422.html (2003).

52 M. Wohlgenannt, K. Tandon, S. Mazumdar, S. Ramasesha, and Z. V. Vardeny. Formation Cross-Sections of Singlet and Triplet Excitons in π-conjugated Polymers. *Nature* **409** no. 6819, 2001, p. 494.

53 M. A. Baldo, D. F. O'Brien, M. E. Thompson, and S. R. Forrest. Excitonic Singlet-Triplet Ratio in a Semiconducting Organic Thin Film. *Physical Review B* **60** no. 20, 1999, p. 14422.

54 S. Reindl, A. Penzkofer, and H. Gratz. Intersystem-Crossing and Excited-State Absorption of C_{70} Studied by Picosecond Pump and Probe Absorption and Fluorescence Measurements. *J. Photochem. Photobiol. A* **115** no. 2, 1998, p. 89.

55 H. D. Burrows, J. S. d. Melo, C. Serpa, L. G. Arnaut, A. P. Monkman, I. Hamblett, and S. Navaratnam. S_1~>T_1 Intersystem Crossing in π-Conjugated Organic Polymers. *The Journal of Chemical Physics* **115** no. 20, 2001, p. 9601.

56 A. Watanabe, O. Ito, M. Watanabe, H. Saito, and M. Koishi. Excited States of C_{70} and the Intersystem Crossing Process Studied by Picosecond Time-Resolved Spectroscopy in the Visible and Near-IR Region. *The Journal of Physical Chemistry* **100** no. 25, 1996, p. 10518.

57 C. M. Marian. Spin–Orbit Coupling and Intersystem Crossing in Molecules. *Wiley Interdisciplinary Reviews: Computational Molecular Science* **2** no. 2, 2012, p. 187.

58 D. Beljonne, Z. Shuai, G. Pourtois, and J. L. Bredas. Spin−Orbit Coupling and Intersystem Crossing in Conjugated Polymers: A Configuration Interaction Description. *J. Phys. Chem. A* **105** no. 15, 2001, p. 3899.

59 Y. Liu, M. Lin, and Y. Zhao. Intersystem Crossing Rates of Isolated Fullerenes: Theoretical Calculations. *J. Phys. Chem. A*, 2017, p. 1145.

60 P. C. Y. Chow, S. Albert-Seifried, S. Gélinas, and R. H. Friend. Nanosecond Intersystem Crossing Times in Fullerene Acceptors: Implications for Organic Photovoltaic Diodes. *Adv. Mater.* **26** no. 28, 2014, p. 4851.

61 S. P. McGlynn, J. Daigre, and F. J. Smith. External Heavy-Atom Spin—Orbital Coupling Effect. IV. Intersystem Crossing. *The Journal of Chemical Physics* **39** no. 3, 1963, p. 675.

62 H. Saigusa, T. Azumi, M. Sumitani, and K. Yoshihara. Internal Heavy Atom Effect on the Triplet Spin Sublevels of the Lowest Triplet State of Naphthalene. II. Intersystem Crossing Processes from the Singlet Excited State to the Individual Spin Sublevels of the Lowest Triplet State. *The Journal of Chemical Physics* **72** no. 3, 1980, p. 1713.

63 A. Harriman. Luminescence of Porphyrins and Metalloporphyrins. Part 3.-Heavy-Atom Effects. *Journal of the Chemical Society, Faraday Transactions 2: Molecular and Chemical Physics* **77** no. 7, 1981, p. 1281.

64 M. B. Smith and J. Michl. Singlet Fission. *Chemical Reviews* **110** no. 11, 2010, p. 6891.

65 L. Ma, K. Zhang, C. Kloc, H. Sun, M. E. Michel-Beyerle, and G. G. Gurzadyan. Singlet Fission in Rubrene Single Crystal: Direct Observation by Femtosecond Pump-Probe Spectroscopy. *Phys. Chem. Chem. Phys.* **14** no. 23, 2012, p. 8307.

66 Y. Kasai, Y. Tamai, H. Ohkita, H. Benten, and S. Ito. Ultrafast Singlet Fission in a Push–Pull Low-Bandgap Polymer Film. *J. Am. Chem. Soc.* **137** no. 51, 2015, p. 15980.

67 R. D. Pensack, E. E. Ostroumov, A. J. Tilley, S. Mazza, C. Grieco, K. J. Thorley, J. B. Asbury, D. S. Seferos, J. E. Anthony, and G. D. Scholes. Observation of Two Triplet-Pair Intermediates in Singlet Exciton Fission. *J. Phys. Chem. Lett.* **7** no. 13, 2016, p. 2370.

68 G. D. Scholes. Correlated Pair States Formed by Singlet Fission and Exciton–Exciton Annihilation. *J. Phys. Chem. A* **119** no. 51, 2015, p. 12699.

69 N. R. Monahan, D. Sun, H. Tamura, K. W. Williams, B. Xu, Y. Zhong, B. Kumar, C. Nuckolls, A. R. Harutyunyan, G. Chen *et al.* Dynamics of the Triplet-Pair State Reveals the Likely Coexistence of Coherent and Incoherent Singlet Fission in Crystalline Hexacene. *Nat Chem* **9**, 2017, p. 341.

70 A. A. Bakulin, S. E. Morgan, T. B. Kehoe, M. W. B. Wilson, A. W. Chin, D. Zigmantas, D. Egorova, and A. Rao. Real-Time Observation of Multiexcitonic States in Ultrafast Singlet Fission Using Coherent 2D Electronic Spectroscopy. *Nat Chem* **8** no. 1, 2016, p. 16.

71 Y.-D. Zhang, Y. Wu, Y. Xu, Q. Wang, K. Liu, J.-W. Chen, J.-J. Cao, C. Zhang, H. Fu, and H.-L. Zhang. Excessive Exoergicity Reduces Singlet Exciton Fission Efficiency of Heteroacenes in Solutions. *J. Am. Chem. Soc.* **138** no. 21, 2016, p. 6739.

72 J. C. Johnson, A. J. Nozik, and J. Michl. The Role of Chromophore Coupling in Singlet Fission. *Acc. Chem. Res.* **46** no. 6, 2013, p. 1290.

73 P. M. Zimmerman, F. Bell, D. Casanova, and M. Head-Gordon. Mechanism for Singlet Fission in Pentacene and Tetracene: From Single Exciton to Two Triplets. *J. Am. Chem. Soc.* **133** no. 49, 2011, p. 19944.

74 D. N. Congreve, J. Lee, N. J. Thompson, E. Hontz, S. R. Yost, P. D. Reusswig, M. E. Bahlke, S. Reineke, T. Van Voorhis, and M. A. Baldo. External Quantum Efficiency Above 100% in a Singlet-Exciton-Fission–Based Organic Photovoltaic Cell. *Science* **340** no. 6130, 2013, p. 334.

75 P. D. Reusswig, D. N. Congreve, N. J. Thompson, and M. A. Baldo. Enhanced External Quantum Efficiency in an Organic Photovoltaic Cell via Singlet Fission Exciton Sensitizer. *Appl. Phys. Lett.* **101** no. 11, 2012, p. 113304.

76 D. S. McClure. Triplet-Singlet Transitions in Organic Molecules. Lifetime Measurements of the Triplet State. *The Journal of Chemical Physics* **17** no. 10, 1949, p. 905.

77 V. Cleave, G. Yahioglu, P. L. Barny, R. H. Friend, and N. Tessler. Harvesting Singlet and Triplet Energy in Polymer LEDs. *Adv. Mater.* **11** no. 4, 1999, p. 285.

78 J. S. Wilson, A. S. Dhoot, A. J. A. B. Seeley, M. S. Khan, A. Kohler, and R. H. Friend. Spin-Dependent Exciton Formation in π-Conjugated Compounds. *Nature* **413** no. 6858, 2001, p. 828.

79 Y. L. Lin, M. A. Fusella, O. V. Kozlov, X. Lin, A. Kahn, M. S. Pshenichnikov, and B. P. Rand. Morphological Tuning of the Energetics in Singlet Fission Organic Solar Cells. *Adv. Funct. Mater.* **26** no. 35, 2016, p. 6489.

80 M. C. Scharber, D. Mühlbacher, M. Koppe, P. Denk, C. Waldauf, A. J. Heeger, and C. J. Brabec. Design Rules for Donors in Bulk-Heterojunction Solar Cells - Towards 10 % Energy-Conversion Efficiency. *Adv. Mater.* **18** no. 6, 2006, p. 789.

81 R. Kroon, M. Lenes, J. C. Hummelen, P. W. M. Blom, and B. de Boer. Small Bandgap Polymers for Organic Solar Cells (Polymer Material Development in the Last 5 Years). *Polym. Rev.* **48** no. 3, 2008, p. 531.

82 S. Günes, H. Neugebauer, and N. S. Sariciftci. Conjugated Polymer-Based Organic Solar Cells. *Chemical Reviews* **107** no. 4, 2007, p. 1324.

83 J. Roncali. Molecular Engineering of the Band Gap of π-Conjugated Systems: Facing Technological Applications. *Macromol. Rapid Commun.* **28** no. 17, 2007, p. 1761.

84 Y.-W. Su, S.-C. Lan, and K.-H. Wei. Organic Photovoltaics. *Mater. Today* **15** no. 12, 2012, p. 554.

85 R. S. Mulliken. Molecular Compounds and their Spectra. 3. The Interaction of Electron Donors and Acceptors. *J. Phys. Chem.* **56** no. 7, 1952, p. 801.

86 H. D. de Gier, B. J. Rietberg, R. Broer, and R. W. A. Havenith. Influence of Push–Pull Group Substitution Patterns on Excited State Properties of Donor–Acceptor Co-monomers and Their Trimers. *Computational and Theoretical Chemistry* **1040–1041**, 2014, p. 202.

87 W. Tress. *Organic Solar Cells: Theory, Experiment, and Device Simulation*. (Springer International Publishing, 2014).

88 E. Ripaud, Y. Olivier, P. Leriche, J. Cornil, and J. Roncali. Polarizability and Internal Charge Transfer in Thiophene-Triphenylamine Hybrid π-Conjugated Systems. *J. Phys. Chem. B* **115** no. 30, 2011, p. 9379.

89 D. Demeter, V. Jeux, P. Leriche, P. Blanchard, Y. Olivier, J. Cornil, R. Po, and J. Roncali. Tuning of the Photovoltaic Parameters of Molecular Donors by Covalent Bridging. *Adv. Funct. Mater.* **23** no. 38, 2013, p. 4854.

90 N. J. Hestand, R. V. Kazantsev, A. S. Weingarten, L. C. Palmer, S. I. Stupp, and F. C. Spano. Extended-Charge-Transfer Excitons in Crystalline Supramolecular Photocatalytic Scaffolds. *J. Am. Chem. Soc.* **138** no. 36, 2016, p. 11762.

91 X. Wei, Z. V. Vardeny, N. S. Sariciftci, and A. J. Heeger. Absorption-Detected Magnetic-Resonance Studies Of Photoexcitations In Conjugated-Polymer/C_{60} Composites. *Physical Review B* **53** no. 5, 1996, p. 2187.

92 P. B. Miranda, D. Moses, and A. J. Heeger. Ultrafast Photogeneration of Charged Polarons in Conjugated Polymers. *Physical Review B* **64** no. 8, 2001, p. 081201.

93 J. L. Bredas and G. B. Street. Polarons, Bipolarons, and Solitons in Conducting Polymers. *Acc. Chem. Res.* **18** no. 10, 1985, p. 309.

94 Z. V. Vardeny, X. Wei, and D. Dick. Optical Probes of Photoexcitations in Fullerene Thin Films from Femtoseconds to Milliseconds in *SPIE*. 100 (1995).

95 N. S. Sariciftci, L. Smilowitz, A. J. Heeger, and F. Wudl. Photoinduced Electron Transfer from a Conducting Polymer to Buckminsterfullerene. *Science* **258** no. 5087, 1992, p. 1474.

96 P. Würfel. *Physics of Solar Cells: From Basic Principles to Advanced Concepts.* (Wiley-VCH Verlag GmbH & Co. KGaA, 2009).

97 B. P. Rand and H. Richter. *Organic Solar Cells: Fundamentals, Devices, and Upscaling.* (Pan Stanford Publishing, Stanford, USA, 2014).

98 M. A. Green, K. Emery, Y. Hishikawa, W. Warta, and E. D. Dunlop. Solar Cell Efficiency Tables (Version 48). *Prog. Photovoltaics Res. Appl.* **24** no. 7, 2016, p. 905.

99 *NREL Efficiency Chart*, www.nrel.gov/pv/ (2017).

100 V. Agranovich. *Excitations in Organic Solids.* (Oxford University Press, 2009).

101 K. A. Mazzio and C. K. Luscombe. The Future of Organic Photovoltaics. *Chem. Soc. Rev.* **44** no. 1, 2015, p. 78.

102 C. W. Tang. Two-Layer Organic Photovoltaic Cell. *Appl. Phys. Lett.* **48** no. 2, 1986, p. 183.

103 K. Cnops, B. P. Rand, D. Cheyns, B. Verreet, M. A. Empl, and P. Heremans. 8.4% Efficient Fullerene-Free Organic Solar Cells Exploiting Long-Range Exciton Energy Transfer. *Nat. Commun.* **5**, 2014, p. 3406.

104 O. L. Griffith and S. R. Forrest. Exciton Management in Organic Photovoltaic Multidonor Energy Cascades. *Nano Lett.* **14** no. 5, 2014, p. 2353.

105 V. A. Trukhanov, V. V. Bruevich, and D. Y. Paraschuk. Fill Factor in Organic Solar Cells Can Exceed the Shockley-Queisser Limit. *Sci. Rep.* **5**, 2015, p. 11478.

106 T. Hahn, S. Tscheuschner, F.-J. Kahle, M. Reichenberger, S. Athanasopoulos, C. Saller, G. C. Bazan, T.-Q. Nguyen, P. Strohriegl, H. Bässler *et al.* Monomolecular and Bimolecular Recombination of Electron–Hole Pairs at the Interface of a Bilayer Organic Solar Cell. *Adv. Funct. Mater.* **27** no. 1, 2017, p. 1604906.

107 S. Cook, A. Furube, R. Katoh, and L. Han. Estimate of Singlet Diffusion Lengths in PCBM Films by Time-Resolved Emission Studies. *Chem. Phys. Lett.* **478** no. 1–3, 2009, p. 33.

108 G. J. Hedley, A. J. Ward, A. Alekseev, C. T. Howells, E. R. Martins, L. A. Serrano, G. Cooke, A. Ruseckas, and I. D. W. Samuel. Determining the Optimum Morphology in High-Performance Polymer-Fullerene Organic Photovoltaic Cells. *Nat. Commun.* **4**, 2013, p. 2867.

109 O. V. Mikhnenko, M. Kuik, J. Lin, N. van der Kaap, T.-Q. Nguyen, and P. W. M. Blom. Trap-Limited Exciton Diffusion in Organic Semiconductors. *Adv. Mater.* **26** no. 12, 2014, p. 1912.

110 J. J. M. Halls, K. Pichler, R. H. Friend, S. C. Moratti, and A. B. Holmes. Exciton Diffusion and Dissociation in a Poly(p-phenylenevinylene)/C_{60} Heterojunction Photovoltaic Cell. *Appl. Phys. Lett.* **68** no. 22, 1996, p. 3120.

111 O. V. Mikhnenko, H. Azimi, M. Scharber, M. Morana, P. W. M. Blom, and M. A. Loi. Exciton Diffusion Length in Narrow Bandgap Polymers. *Energ. Environ. Sci.* **5** no. 5, 2012, p. 6960.

112 G. Yu, J. Gao, J. C. Hummelen, F. Wudl, and A. J. Heeger. Polymer Photovoltaic Cells: Enhanced Efficiencies via a Network of Internal Donor-Acceptor Heterojunctions. *Science* **270** no. 5243, 1995, p. 1789.

113 D. Chirvase, J. Parisi, J. C. Hummelen, and V. Dyakonov. Influence of Nanomorphology on the Photovoltaic Action of Polymer-Fullerene Composites. *Nanotechnology* **15** no. 9, 2004, p. 1317.

114 V. Dyakonov. Mechanisms Controlling the Efficiency of Polymer Solar Cells. *Applied Physics a-Materials Science & Processing* **79** no. 1, 2004, p. 21.

115 H. Hoppe, M. Niggemann, C. Winder, J. Kraut, R. Hiesgen, A. Hinsch, D. Meissner, and N. S. Sariciftci. Nanoscale Morphology of Conjugated Polymer/Fullerene-Based Bulk-Heterojunction Solar Cells. *Adv. Funct. Mater.* **14** no. 10, 2004, p. 1005.

116 M. A. Brady, G. M. Su, and M. L. Chabinyc. Recent Progress in The Morphology of Bulk Heterojunction Photovoltaics. *Soft Matter* **7** no. 23, 2011, p. 11065.

117 G. F. Burkhard, E. T. Hoke, S. R. Scully, and M. D. McGehee. Incomplete Exciton Harvesting from Fullerenes in Bulk Heterojunction Solar Cells. *Nano Lett* **9** no. 12, 2009, p. 4037.

118 Z. Li, J. D. A. Lin, H. Phan, A. Sharenko, C. M. Proctor, P. Zalar, Z. Chen, A. Facchetti, and T.-Q. Nguyen. Competitive Absorption and Inefficient Exciton Harvesting: Lessons Learned from Bulk Heterojunction Organic Photovoltaics Utilizing the Polymer Acceptor P(NDI2OD-T2). *Adv. Funct. Mater.* **24** no. 44, 2014, p. 6989.

119 S. M. Menke, W. A. Luhman, and R. J. Holmes. Tailored Exciton Diffusion in Organic Photovoltaic Cells for Enhanced Power Conversion Efficiency. *Nat. Mater.* **12** no. 2, 2013, p. 152.

120 D. Carsten and D. Vladimir. Polymer–Fullerene Bulk Heterojunction Solar Cells. *Rep. Prog. Phys.* **73** no. 9, 2010, p. 096401.

121 Z. A. Page, Y. Liu, V. V. Duzhko, T. P. Russell, and T. Emrick. Fulleropyrrolidine Interlayers: Tailoring Electrodes to Raise Organic Solar Cell Efficiency. *Science* **346** no. 6208, 2014, p. 441.

122 R. Po, C. Carbonera, A. Bernardi, and N. Camaioni. The Role of Buffer Layers in Polymer Solar Cells. *Energy Environ. Sci.* **4** no. 2, 2011, p. 285.

123 B. Walker, C. Kim, and T.-Q. Nguyen. Small Molecule Solution-Processed Bulk Heterojunction Solar Cells. *Chem. Mater.* **23** no. 3, 2010, p. 470.

124 C. Wetzel, A. Mishra, E. Mena-Osteritz, K. Walzer, M. Pfeiffer, and P. Bauerle. Development of Strongly Absorbing S,N-heterohexacene-based Donor Materials for Efficient Vacuum-Processed Organic Solar Cells. *J. Mater. Chem. C* **4** no. 17, 2016, p. 3715.

125 K. Kawashima, Y. Tamai, H. Ohkita, I. Osaka, and K. Takimiya. High-Efficiency Polymer Solar Cells With Small Photon Energy Loss. *Nat. Commun.* **6**, 2015, p. 10085.

126 M. C. Scharber and N. S. Sariciftci. Efficiency of Bulk-Heterojunction Organic Solar Cells. *Prog. Polym. Sci.* **38** no. 12, 2013, p. 1929.

127 X. Che, X. Xiao, J. D. Zimmerman, D. Fan, and S. R. Forrest. High-Efficiency, Vacuum-Deposited, Small-Molecule Organic Tandem and Triple-Junction Photovoltaic Cells. *Adv. Energy Mater.* **4** no. 18, 2014, p. 1400568.

128 D. Cheyns, M. Kim, B. Verreet, and B. P. Rand. Accurate Spectral Response Measurements of a Complementary Absorbing Organic Tandem Cell with Fill Factor Exceeding the Subcells. *Appl. Phys. Lett.* **104** no. 9, 2014, p. 093302.

129 C.-C. Chen, W.-H. Chang, K. Yoshimura, K. Ohya, J. You, J. Gao, Z. Hong, and Y. Yang. An Efficient Triple-Junction Polymer Solar Cell Having a Power Conversion Efficiency Exceeding 11%. *Adv. Mater.* **26** no. 32, 2014, p. 5670.

130 J. You, L. Dou, K. Yoshimura, T. Kato, K. Ohya, T. Moriarty, K. Emery, C.-C. Chen, J. Gao, G. Li *et al.* A Polymer Tandem Solar Cell with 10.6% Power Conversion Efficiency. *Nat. Commun.* **4**, 2013, p. 1446.

131 S. M. Menke and R. J. Holmes. Exciton Diffusion in Organic Photovoltaic Cells. *Energy Environ. Sci.* **7** no. 2, 2014, p. 499.

132 O. V. Mikhnenko, P. W. M. Blom, and T.-Q. Nguyen. Exciton Diffusion in Organic Semiconductors. *Energy Environ. Sci.* **8**, 2015, p. 1867.

133 S.-S. Sun and N. S. Sariciftci. *Organic Photovoltaics: Mechanisms, Materials, and Devices.* (CRC Press0, 2005).

134 Y. Tamai, H. Ohkita, H. Benten, and S. Ito. Exciton Diffusion in Conjugated Polymers: From Fundamental Understanding to Improvement in Photovoltaic Conversion Efficiency. *J. Phys. Chem. Lett.* **6** no. 17, 2015, p. 3417.

135 S. D. Dimitrov, Z. Huang, F. Deledalle, C. B. Nielsen, B. C. Schroeder, R. S. Ashraf, S. Shoaee, I. McCulloch, and J. R. Durrant. Towards Optimisation of Photocurrent from Fullerene Excitons in Organic Solar Cells. *Energy Environ. Sci.* **7** no. 3, 2014, p. 1037.

136 J. C. Blakesley and D. Neher. Relationship Between Energetic Disorder and Open-Circuit Voltage in Bulk Heterojunction Organic Solar Cells. *Physical Review B* **84** no. 7, 2011, p. 075210.

137 H. Bässler. Charge Transport in Disordered Organic Photoconductors a Monte Carlo Simulation Study. *physica status solidi (b)* **175** no. 1, 1993, p. 15.

138 S. D. Baranovskii. Theoretical Description of Charge Transport in Disordered Organic Semiconductors. *physica status solidi (b)* **251** no. 3, 2014, p. 487.

139 S. Westenhoff, I. A. Howard, and R. H. Friend. Probing the Morphology and Energy Landscape of Blends of Conjugated Polymers with Sub-10 nm Resolution. *Phys. Rev. Lett.* **101** no. 1, 2008, p. 016102.

140 S. Athanasopoulos, S. T. Hoffmann, H. Bässler, A. Köhler, and D. Beljonne. To Hop or Not to Hop? Understanding the Temperature Dependence of Spectral Diffusion in Organic Semiconductors. *J. Phys. Chem. Lett.* **4** no. 10, 2013, p. 1694.

141 L. M. Herz, C. Silva, A. C. Grimsdale, K. Müllen, and R. T. Phillips. Time-Dependent Energy Transfer Rates in a Conjugated Polymer Guest-Host System. *Physical Review B* **70** no. 16, 2004, p. 165207.

142 G. M. Akselrod, F. Prins, L. V. Poulikakos, E. M. Y. Lee, M. C. Weidman, A. J. Mork, A. P. Willard, V. Bulović, and W. A. Tisdale. Subdiffusive Exciton Transport in Quantum Dot Solids. *Nano Lett.* **14** no. 6, 2014, p. 3556.

143 A. Serbenta, O. V. Kozlov, G. Portale, P. H. M. van Loosdrecht, and M. S. Pshenichnikov. Bulk Heterojunction Morphology of Polymer:Fullerene Blends Revealed by Ultrafast Spectroscopy. *Sci. Rep.* **6**, 2016, p. 36236.

144 Q. L. Song, H. B. Yang, and C. M. Li. Long-Range Exciton Dissociation in Layered Organic Solar Cells. *J. Renewable Sustainable Energy* **1** no. 6, 2009, p. 063105.

145 C. Deibel, T. Strobel, and V. Dyakonov. Role of the Charge Transfer State in Organic Donor–Acceptor Solar Cells. *Adv. Mater.* **22** no. 37, 2010, p. 4097.

146 K. Vandewal, K. Tvingstedt, A. Gadisa, O. Inganas, and J. V. Manca. On the Origin of the Open-Circuit Voltage of Polymer-Fullerene Solar Cells. *Nat. Mater.* **8** no. 11, 2009, p. 904.

147 D. Veldman, S. C. J. Meskers, and R. A. J. Janssen. The Energy of Charge-Transfer States in Electron Donor-Acceptor Blends: Insight into the Energy Losses in Organic Solar Cells. *Adv. Funct. Mater.* **19** no. 12, 2009, p. 1939.

148 L. W. Barbour, M. Hegadorn, and J. B. Asbury. Watching Electrons Move in Real Time: Ultrafast Infrared Spectroscopy of a Polymer Blend Photovoltaic Material. *J. Am. Chem. Soc.* **129** no. 51, 2007, p. 15884.

149 J. Piris, T. E. Dykstra, A. A. Bakulin, P. H. M. v. Loosdrecht, W. Knulst, M. T. Trinh, J. M. Schins, and L. D. A. Siebbeles. Photogeneration and Ultrafast Dynamics of Excitons and Charges in P3HT/PCBM Blends. *J. Phys. Chem. C* **113** no. 32, 2009, p. 14500.

150 A. A. Bakulin, J. C. Hummelen, M. S. Pshenichnikov, and P. H. M. van Loosdrecht. Ultrafast Hole-Transfer Dynamics in Polymer/PCBM Bulk Heterojunctions. *Adv. Funct. Mater.* **20** no. 10, 2010, p. 1653.

151 I.-W. Hwang, D. Moses, and A. J. Heeger. Photoinduced Carrier Generation in P3HT/PCBM Bulk Heterojunction Materials. *J. Phys. Chem. C* **112** no. 11, 2008, p. 4350.

152 S. Cook, R. Katoh, and A. Furube. Ultrafast Studies of Charge Generation in PCBM:P3HT Blend Films following Excitation of the Fullerene PCBM. *J. Phys. Chem. C* **113** no. 6, 2009, p. 2547.

153 S. R. Cowan, N. Banerji, W. L. Leong, and A. J. Heeger. Charge Formation, Recombination, and Sweep-Out Dynamics in Organic Solar Cells. *Adv. Funct. Mater.* **22** no. 6, 2012, p. 1116.

154 H. Kraus, M. C. Heiber, S. Väth, J. Kern, C. Deibel, A. Sperlich, and V. Dyakonov. Analysis of Triplet Exciton Loss Pathways in PTB7:$PC_{71}BM$ Bulk Heterojunction Solar Cells. *Sci. Rep.* **6**, 2016, p. 29158.

155 B. Z. Tedlla, F. Zhu, M. Cox, J. Drijkoningen, J. Manca, B. Koopmans, and E. Goovaerts. Understanding Triplet Formation Pathways in Bulk Heterojunction Polymer:Fullerene Photovoltaic Devices. *Adv. Energy Mater.* **5** no. 2, 2015, p. 1401109.

156 M. Liedtke, A. Sperlich, H. Kraus, A. Baumann, C. Deibel, M. J. M. Wirix, J. Loos, C. M. Cardona, and V. Dyakonov. Triplet Exciton Generation in Bulk-Heterojunction Solar Cells Based on Endohedral Fullerenes. *J. Am. Chem. Soc.* **133** no. 23, 2011, p. 9088.

157 M. K. Etherington, J. Wang, P. C. Y. Chow, and N. C. Greenham. Recombination Pathways in Polymer:Fullerene Photovoltaics Observed Through Spin Polarization Measurements. *Appl. Phys. Lett.* **104** no. 6, 2014, p. 063304.

158 A. C. Jakowetz, M. L. Böhm, J. Zhang, A. Sadhanala, S. Huettner, A. A. Bakulin, A. Rao, and R. H. Friend. What Controls the Rate of Ultrafast Charge Transfer and Charge Separation Efficiency in Organic Photovoltaic Blends. *J. Am. Chem. Soc.* **138** no. 36, 2016, p. 11672.

159 J. Lee, K. Vandewal, S. R. Yost, M. E. Bahlke, L. Goris, M. A. Baldo, J. V. Manca, and T. V. Voorhis. Charge Transfer State Versus Hot Exciton Dissociation in Polymer−Fullerene Blended Solar Cells. *J. Am. Chem. Soc.* **132** no. 34, 2010, p. 11878.

160 G. Grancini, M. Maiuri, D. Fazzi, A. Petrozza, H. J. Egelhaaf, D. Brida, G. Cerullo, and G. Lanzani. Hot Exciton Dissociation in Polymer Solar Cells. *Nat. Mater.* **12** no. 1, 2013, p. 29.

161 D. A. Vithanage, A. Devižis, V. Abramavičius, Y. Infahsaeng, D. Abramavičius, R. C. I. MacKenzie, P. E. Keivanidis, A. Yartsev, D. Hertel, J. Nelson *et al.* Visualizing Charge Separation in Bulk Heterojunction Organic Solar Cells. *Nat. Commun.* **4**, 2013, p. 2334

162 S. N. Hood and I. Kassal. Entropy and Disorder Enable Charge Separation in Organic Solar Cells. *J. Phys. Chem. Lett.* **7** no. 22, 2016, p. 4495.

163 A. Devižis, J. De Jonghe-Risse, R. Hany, F. Nüesch, S. Jenatsch, V. Gulbinas, and J.-E. Moser. Dissociation of Charge Transfer States and Carrier Separation in Bilayer Organic Solar Cells: A Time-Resolved Electroabsorption Spectroscopy Study. *J. Am. Chem. Soc.* **137** no. 25, 2015, p. 8192.

164 D. Bartesaghi, I. d. C. Perez, J. Kniepert, S. Roland, M. Turbiez, D. Neher, and L. J. A. Koster. Competition Between Recombination and Extraction of Free Charges Determines the Fill Factor of Organic Solar Cells. *Nat. Commun.* **6**, 2015, p. 7083.

165 B. Ray and M. A. Alam. Achieving Fill Factor Above 80% in Organic Solar Cells by Charged Interface in *2012 IEEE 38th Photovoltaic Specialists Conference (PVSC) PART 2.* 1.

166 D. Bartesaghi, M. Turbiez, and L. J. A. Koster. Charge Transport and Recombination in PDPP5T:[70]PCBM Organic Solar Cells: The Influence of Morphology. *Org. Electron.* **15** no. 11, 2014, p. 3191.

167 J. Guo, H. Ohkita, H. Benten, and S. Ito. Charge Generation and Recombination Dynamics in Poly(3-hexylthiophene)/Fullerene Blend Films with Different Regioregularities and Morphologies. *J. Am. Chem. Soc.* **132** no. 17, 2010, p. 6154.

168 A. Baumann, T. J. Savenije, D. H. K. Murthy, M. Heeney, V. Dyakonov, and C. Deibel. Influence of Phase Segregation on Recombination Dynamics in Organic Bulk-Heterojunction Solar Cells. *Adv. Funct. Mater.* **21** no. 9, 2011, p. 1687.

169 S. W. Koch, M. Kira, G. Khitrova, and H. M. Gibbs. Semiconductor Excitons in New Light. *Nat. Mater.* **5** no. 7, 2006, p. 523.

170 J. Song, F.-m. Li, S.-x. Qian, Y.-f. Li, W.-j. Peng, J.-y. Zhou, and Z.-x. Yu. Time Decay Behavior of Fullerene-C_{60} Studied by Time-Resolved Photoluminescence. *Acta Physica Sinica (Overseas Edition)* **4** no. 3, 1995, p. 175.

171 H.-Y. Wang, J.-J. Shi, C. Wang, X.-X. Zhang, Y. Wan, and H. Wu. Novel Fluorescence Dyes Based on Entirely New Chromeno[4,3,2-de][1,6]naphthyridine Framework. *Dyes Pigm.* **95** no. 2, 2012, p. 268.

172 G. D. Scholes and G. Rumbles. Excitons in Nanoscale Systems. *Nat. Mater.* **5** no. 9, 2006, p. 683.

173 O. V. Kozlov, Y. N. Luponosov, A. N. Solodukhin, B. Flament, Y. Olivier, R. Lazzaroni, J. Cornil, S. A. Ponomarenko, and M. S. Pshenichnikov. Ultrafast Exciton-to-Polaron Conversion in Densely-Packed Small Organic Semiconducting Molecules. *Advanced Optical Materials* **5** no. 7, 2017, p. 1700024.

174 C. Madigan and V. Bulović. Modeling of Exciton Diffusion in Amorphous Organic Thin Films. *Phys. Rev. Lett.* **96** no. 4, 2006, p. 046404.

175 S. T. Hoffmann, H. Bässler, J.-M. Koenen, M. Forster, U. Scherf, E. Scheler, P. Strohriegl, and A. Köhler. Spectral Diffusion in Poly(para-phenylene)-type Polymers with Different Energetic Disorder. *Physical Review B* **81** no. 11, 2010, p. 115103.

176 K. Tvingstedt, K. Vandewal, F. Zhang, and O. Inganäs. On the Dissociation Efficiency of Charge Transfer Excitons and Frenkel Excitons in Organic Solar Cells: A Luminescence Quenching Study. *J. Phys. Chem. C* **114** no. 49, 2010, p. 21824.

177 D. Baran, N. Li, A.-C. Breton, A. Osvet, T. Ameri, M. Leclerc, and C. J. Brabec. Qualitative Analysis of Bulk-Heterojunction Solar Cells without Device Fabrication: An Elegant and Contactless Method. *J. Am. Chem. Soc.* **136** no. 31, 2014, p. 10949.

178 M. Gerhard, A. P. Arndt, I. A. Howard, A. Rahimi-Iman, U. Lemmer, and M. Koch. Temperature- and Energy-Dependent Separation of Charge-Transfer States in PTB7-Based Organic Solar Cells. *J. Phys. Chem. C* **119** no. 51, 2015, p. 28309.

179 A. P. Arndt, M. Gerhard, A. Quintilla, I. A. Howard, M. Koch, and U. Lemmer. Time-Resolved Charge-Transfer State Emission in Organic Solar Cells: Temperature and Blend Composition Dependences of Interfacial Traps. *J. Phys. Chem. C* **119** no. 24, 2015, p. 13516.

180 N. A. Ran, M. Kuik, J. A. Love, C. M. Proctor, I. Nagao, G. C. Bazan, and T.-Q. Nguyen. Understanding the Charge-Transfer State and Singlet Exciton Emission from Solution-Processed Small-Molecule Organic Solar Cells. *Adv. Mater.* **26** no. 43, 2014, p. 7405.

181 M. Manca, C. Piliego, E. Wang, M. R. Andersson, A. Mura, and M. A. Loi. Tracing Charge Transfer States in Polymer:Fullerene Bulk-Heterojunctions. *J. Mater. Chem. A* **1** no. 25, 2013, p. 7321.

182 P. B. Deotare, W. Chang, E. Hontz, D. N. Congreve, L. Shi, P. D. Reusswig, B. Modtland, M. E. Bahlke, C. K. Lee, A. P. Willard *et al.* Nanoscale Transport of Charge-Transfer States in Organic Donor-Acceptor Blends. *Nat. Mater.* **14** no. 11, 2015, p. 1130.

183 G.-J. A. H. Wetzelaer, M. Kuik, and P. W. M. Blom. Identifying the Nature of Charge Recombination in Organic Solar Cells from Charge-Transfer State Electroluminescence. *Adv. Energy Mater.* **2** no. 10, 2012, p. 1232.

184 A. V. Akkuratov, D. K. Susarova, O. V. Kozlov, D. V. Novikov, A. V. Chernyak, Y. L. Moskvin, L. A. Frolova, M. S. Pshenichnikov, and P. A. Troshin. Design of $(X\text{-}DADAD)_n$ Type Copolymers with Improved Optoelectronic Properties for Bulk Heterojunction Organic Solar Cells. *Macromolecules* **48** no. 7, 2015, p. 2013.

185 A. A. Bakulin, D. S. Martyanov, D. Y. Paraschuk, M. S. Pshenichnikov, and P. H. M. van Loosdrecht. Ultrafast Charge Photogeneration Dynamics in Ground-State Charge-Transfer Complexes Based on Conjugated Polymers. *J. Phys. Chem. B* **112** no. 44, 2008, p. 13730.

186 C. X. Sheng, M. Tong, S. Singh, and Z. V. Vardeny. Experimental Determination of the Charge/Neutral Branching Ratio η in the Photoexcitation of π-Conjugated Polymers by Broadband Ultrafast Spectroscopy. *Physical Review B* **75** no. 8, 2007, p. 085206.

187 A. Serbenta. *Organic Donor-Acceptor Systems: Charge Generation and Morphology* PhD thesis, University of Groningen, (2016).

188 X. He, G. Zhu, J. Yang, H. Chang, Q. Meng, H. Zhao, X. Zhou, S. Yue, Z. Wang, J. Shi *et al.* Photogenerated Intrinsic Free Carriers in Small-molecule Organic Semiconductors Visualized by Ultrafast Spectroscopy. *Sci. Rep.* **5**, 2015, p. 17076.

189 O. V. Kozlov, Y. N. Luponosov, S. A. Ponomarenko, N. Kausch-Busies, D. Y. Paraschuk, Y. Olivier, D. Beljonne, J. Cornil, and M. S. Pshenichnikov. Ultrafast Charge Generation Pathways in Photovoltaic Blends Based on Novel Star-Shaped Conjugated Molecules. *Adv. Energy Mater.* **5** no. 7, 2015, p. 1401657.

190 O. V. Kozlov, F. de Haan, R. A. Kerner, B. P. Rand, D. Cheyns, and M. S. Pshenichnikov. Real-Time Tracking of Singlet Exciton Diffusion in Organic Semiconductors. *Phys. Rev. Lett.* **116** no. 5, 2016, p. 057402.

191 Y. N. Luponosov, J. Min, A. N. Solodukhin, O. V. Kozlov, M. A. Obrezkova, S. M. Peregudova, T. Ameri, S. N. Chvalun, M. S. Pshenichnikov, C. J. Brabec *et al.* Effects of Electron-Withdrawing Group and Electron-Donating Core Combinations on Physical Properties and Photovoltaic Performance in D-π-A Star-Shaped Small Molecules. *Org. Electron.* **32**, 2016, p. 157.

192 C. Silva, D. M. Russell, M. A. Stevens, J. D. Mackenzie, S. Setayesh, K. Müllen, and R. H. Friend. Excited-State Absorption in Luminescent Conjugated Polymer Thin Films: Ultrafast Studies of Processable Polyindenofluorene Derivatives. *Chem. Phys. Lett.* **319** no. 5–6, 2000, p. 494.

193 S. Ling, S. Schumacher, I. Galbraith, and M. J. Paterson. Excited-State Absorption of Conjugated Polymers in the Near-Infrared and Visible: A Computational Study of Oligofluorenes. *J. Phys. Chem. C* **117** no. 13, 2013, p. 6889.

194 A. A. Bakulin, S. D. Dimitrov, A. Rao, P. C. Y. Chow, C. B. Nielsen, B. C. Schroeder, I. McCulloch, H. J. Bakker, J. R. Durrant, and R. H. Friend. Charge-Transfer State Dynamics Following Hole and Electron Transfer in Organic Photovoltaic Devices. *J. Phys. Chem. Lett.* **4** no. 1, 2013, p. 209.

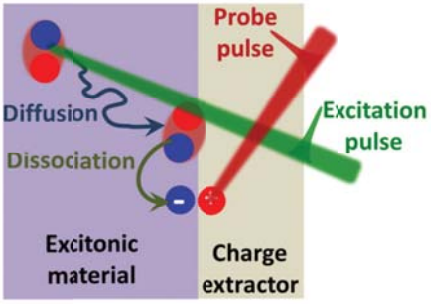

Chapter 2

Real-Time Tracking of Singlet Exciton Diffusion in Organic Semiconductors

Exciton diffusion in organic materials provides the operational basis for functioning of such devices as organic solar cells and light-emitting diodes. Here we track the exciton diffusion process in organic semiconductors in real time with a novel technique based on femtosecond photoinduced absorption spectroscopy. Using vacuum-deposited C_{70} layers as a model system, we demonstrate an extremely high diffusion coefficient of $D \approx 3.5 \cdot 10^{-3}$ cm^2/s that originates from surprisingly low energetic disorder of <5 meV. The experimental results are well-described by the analytical model and supported by extensive Monte-Carlo simulations. The proposed noninvasive time-of-flight technique is deemed as a powerful tool for further development of organic opto-electronic components, such as simple layered solar cells, light-emitting diodes, and electrically pumped lasers.

This Chapter is based on the following publication:
Oleg V. Kozlov, Foppe de Haan, Ross A. Kerner, Barry P. Rand, David Cheyns and Maxim S. Pshenichnikov, *Phys. Rev. Lett.* **116**, 057402 (2016)

2.1 Introduction

Electronic devices based on organic semiconductors have attracted much interest over the last decades as an alternative to conventional inorganic electronics[1], largely due to their chemically-tunable optical properties[2]. Organic electronic devices, such as organic solar cells (OSCs) and light-emitting diodes (OLEDs) rely on the ability of Frenkel excitons either to dissociate at the interface between *p*- and *n*-type materials to produce separated charges or to recombine within the recombination layer to produce photon emission[3,4]. The efficiency of the aforementioned devices directly depends on the exciton diffusion within the active layer. In general, there are three parameters characterizing the exciton diffusion in the semiconducting layer: the exciton lifetime T_1, the diffusion coefficient D and the diffusion length L_d, interconnected via the relation $L_d \sim \sqrt{DT_1}$.[4] The singlet exciton lifetime $T_1$is relatively easy to measure by e.g. the time-resolved fluorescence[5], while obtaining either D or L_d is much more challenging because of the tens-nm length scale over which the Frenkel excitons diffuse.

Various techniques to measure L_d and/or D have been proposed and utilized to date[3,4,6-10] which roughly fall into the following two categories. Spectroscopic techniques rely on photoluminescence quenching[9,11,12], or on a highly non-equilibrium process of exciton-exciton annihilation[13]. Charge carrier techniques observe time-averaged charge yield after exciton dissociation and as a consequence necessitate either the modeling of the external quantum efficiency of the operating device[14,15] or microwave/photoconductivity measurements[16,17]. Spectroscopic methods provide high temporal resolution; however, they require strongly photoluminescent (PL) materials[6], while the charge yield does not necessary correlate with the efficiency of PL quenching[18]. In turn, charge carrier techniques do not possess time resolution and therefore miss dynamical aspects of exciton dynamics[4].

The advantages of both approaches can be combined in a new technique that provides a direct handle on the exciton diffusion coefficient. Similarly to the spectroscopic techniques, the material of interest (absorber) with known thickness is covered by an exciton quencher, the hole (or electron) accepting layer (Figure 2.1). After spectrally-selective photoexcitation of the absorber by the ultrashort visible pulse, the photogenerated excitons diffuse to the interface with the quencher where they dissociate into pairs of charges. The concentration of charges (holes) in the quencher is measured - similarly to the charge carrier techniques - but now in the time-resolved fashion via photoinduced polaron absorption (PIA)[19] (Figure 2.1b). The resulting transient alone yields the exciton diffusion coefficient; therefore, only a single sample of well-defined thickness is required.

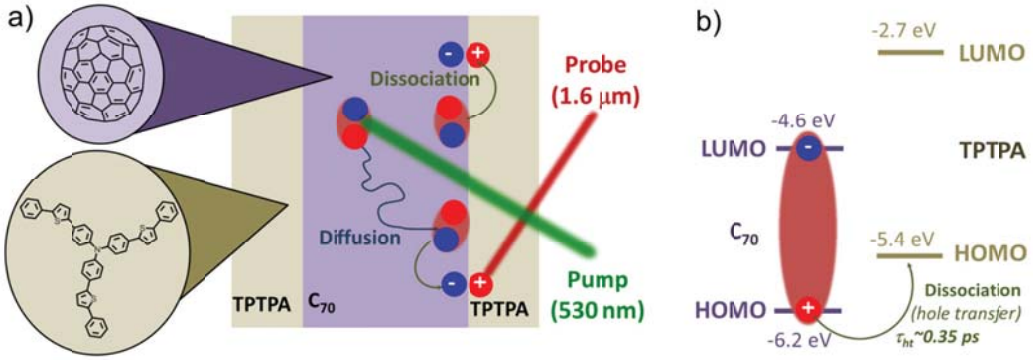

Figure 2.1 Experimental concept. (a) Schematic of the time-of-flight experiment, and molecular structures of TPTPA (donor) and C_{70} (acceptor). (b) Energetics of C_{70} exciton (shown as the brown oval) dissociation via hole transfer process[20]. Energy levels of C_{70} and TPTPA are taken from Refs. [21,22].

Here we apply the new method for real-time tracking of singlet exciton diffusion to vacuum-deposited layers of the well-known OSC acceptor, C_{70} fullerene. We demonstrate efficient singlet exciton harvesting from C_{70} layers up to 70 nm in thickness. The exciton diffusion process is temperature-independent down to 77 K, which implies extremely low energetic disorder of <5 meV. The experimental findings are excellently described by a simple analytical model and also supported by extensive Monte-Carlo simulations.

In our experiments, vacuum-deposited C_{70} layers of different thicknesses from 6 nm to 196 nm (absorber) are sandwiched between 10 nm thick layers of tris[4-(5-phenylthiophen-2-yl)phenyl]amine (TPTPA) which acts as a quencher and hole acceptor (for compete sample set, refer to Supporting Information (SI), Figure S2.1 and Table S2.1). All the TPTPA/C_{70} and C_{70}/TPTPA interfaces are measured to be abrupt in the limit of molecular roughness[11,23], see Ref. [24] for details.

PIA measurements were performed in a standard pump-probe arrangement at a visible-pump, IR-probe setup based on a Spectra-Physics Hurricane system (~120 fs, 800 nm, 1 KHz repetition rate) and two optical parametrical amplifiers (Light Conversion TOPAS). The polarization of the probe pulse was set at the magic angle of 54.7° with respect to the polarization of excitation pulse to observe the population signal only[25]. After the sample, the IR signal was detected by nitrogen-cooled InSb detectors, transmission change ΔT of the sample with and without the excitation pulse was calculated and normalized on the sample transmission T as $\Delta T/T$. To minimize the biexciton recombination and ensure linearity of the response at all delay times the energy density of the excitation pulse was decreased to ~1.3 μJ/cm^2, which corresponds to the average photon density of $3 \cdot 10^{-4}$ nm^{-3}. For a more detailed description of the experiment, see Section 2.4 “Methods”.

2.2 Experimental Results

2.2.1 Linear and Polaron Absorption Spectra

Figure 2.2a shows absorption spectra of TPTPA and C_{70} layers (for other spectra, see Figure S2.2). C_{70} exhibits strong absorption below 700 nm while the TPTPA film absorption peaks at 400 nm so that the excitation wavelength of 530 nm was chosen to selectively excite C_{70}; lower-energy excitation yielded similar results (Figure S2.3). To evaluate the position of the polaron absorption peak in the TPTPA molecule, the dependence of the response on the probe wavelength was measured at different delay times (Figure 2.2b). The polaron spectra show a broad peak in the near-IR region centered around 1.5 μm, consistent with previous data on similar star-shaped molecules[26]. The position of the absorption peak remains unchanged with the pump-probe delay which indicates an absence of spectral diffusion due to, for instance, polaron relaxation. Therefore, the hole polarons are monitored at the constant probe wavelength of 1.55 μm. At this wavelength, maximal IR response of pure C_{70} films (due to excited state absorption of singlet and/or triplet excitons C_{70}) is by a factor of ~6 weaker than the resonant TPTPA response, and is readily accounted for (see SI, Figure S2.4 and Section 2.5.5 ”Separation of C_{70} and TPTPA IR responses”).

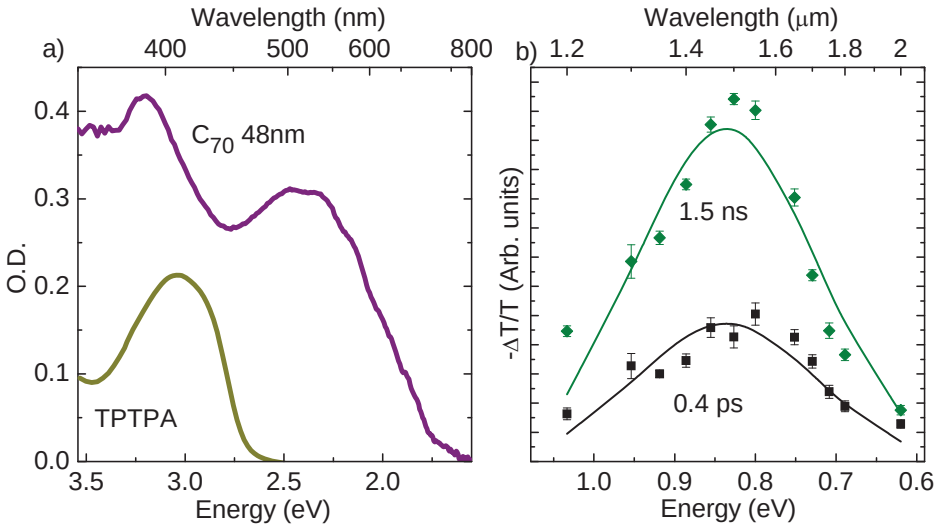

Figure 2.2 (a) Absorption spectra of 48 nm C_{70} (purple) and 12 nm TPTPA (yellow) samples. (b) Polaron absorption spectra for the 6 nm sample at 0.4 ps (black squares) and 1.5 ns (green diamonds) delays; for other polaron spectra, see Figure S2.4 in SI. Solid lines are fits with Gaussian functions. The excitation wavelength is 530 nm.

2.2.2 Exciton Harvesting

The time-of-flight dynamics of exciton harvesting from C_{70} layers of different thicknesses from 6 nm to 192 nm, are shown in Figure 2.3 (for raw experimental data see Figure S2.6). The transients represent the accumulated number of generated TPTPA holes via C_{70} exciton dissociation and therefore their amplitudes are proportional to the amount of split excitons (i.e. those which have made it to the interfaces). All signals are normalized by the number of the photons absorbed so that harvesting efficiencies in different samples can be compared directly. At short times (<1 ps), the signal rises due to interfacial excitons (i.e. excitons formed at the donor/acceptor interface) splitting into charges via the hole-transfer process[20]. This development is the most apparent in samples with thin C_{70} layers where the share of interfacial excitons is statistically higher. At longer times, the signals increase gradually at a much slower timescale (up to ns) that is strongly dependent on the C_{70} thickness. This time region is attributed to diffusion-delayed splitting of excitons generated within the C_{70} layer.

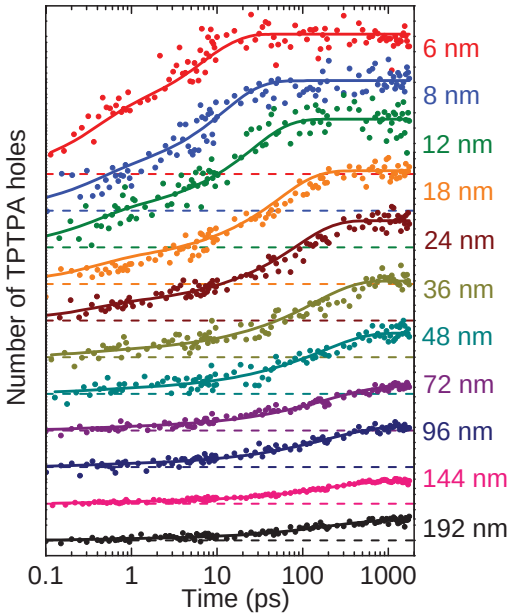

Figure 2.3 Measured (dots) and fitted with analytical model (solid lines) transients for different samples. Each transient is offset by $\Delta T/T=2\cdot10^{-4}$ to the corresponding dashed line; the thickness of each C_{70} layer is indicated to the right. All transients are normalized by the number of absorbed photons and corrected for the C_{70} contribution (see SI for details).

The total number of diffusion-delayed excitons split at the interface by time t (i.e. the number of accumulated holes) is readily obtained (see SI, Section 2.5.6 “Analytical model” for details) by solving the 1D exciton diffusion equation with the zero Dirichlet boundary conditions[4]:

$$H_b(t) = \frac{DT_1}{L}\sum_{m=1}^{\infty}[P(0) - (-1)^m P(L)]B_m\left(\frac{\pi m}{L}\right)\frac{1 - e^{-t\left(\frac{1}{T_1}+\left(\frac{\pi m}{L}\right)^2 D\right)}}{1 + \left(\frac{\pi m}{L}\right)^2 DT_1}, \quad (2.1)$$

where D is the diffusion coefficient, L is the thickness of the C_{70} layer, $P(0)$ and $P(L)$ are the (relative) intensity of the probe at the two interfaces, T_1 is C_{70} exciton effective lifetime of 500 ps obtained from time-resolved photoluminescence (PL) measurements (Figure S2.7) and

$$B_m = \frac{2}{L}\int_0^L I(z)\sin(\omega_m z)dz, \quad (2.2)$$

where $I(z)$ is the initial distribution of the exciton density along the z-axis. Because of optical interference in the thin layered samples[27-30], $P(z)$ and $I(z)$ were calculated separately using a transfer-matrix method[31].

In Eq. (2.1), the only unknown parameter is the diffusion coefficient D, which can be directly obtained by fitting each individual transient (Figure 2.3, solid lines). The diffusion coefficients are grouped around $D \approx 3.5 \cdot 10^{-3}$ cm^2/s (Figure 2.4a) so that a single sample could be used to obtain the diffusion coefficient. The obtained diffusion coefficient is a factor of 15 higher than for the prototypical solution-processed organic solar cell acceptor material, $PC_{71}BM$[32]. For the thin samples (<12 nm), the diffusion coefficients are somewhat higher due to a relatively high share of interfacial excitons (~20% for 12 nm sample) which are generated directly at the C_{70}/TPTPA interface and therefore do not undergo the diffusion process (Eq. (2.1)).

An alternative way to obtain the diffusional coefficient is to examine the efficiency η of exciton harvesting (i.e. the maximal amplitudes of the transients) as a function of C_{70} layer thickness (Figure 2.4b) and fit it with the well-known equation [33]:

$$\eta(L) = \frac{2\sqrt{DT_1} * tanh(\frac{L}{2\sqrt{DT_1}})}{L} \quad (2.3)$$

The fit resulted in $D \approx 3 \cdot 10^{-3}$ cm^2/s which is in excellent agreement with the single-transient approach (Figure 2.4a). Exciton harvesting efficiency decreases with increasing layer thickness because of the finite C_{70} singlet exciton effective lifetime of ~500 ps (Figure S2.7), mainly due to intersystem crossing to the triplet state[5,34]. The excitons are efficiently harvested from the 70 nm layer if we define it as a thickness at which the harvesting efficiency falls to the e^{-1} level for direct comparison with the light penetration depth of ~80 nm at 530 nm in C_{70} films (Figure S2.8). Previously, L_d ranging from 7 to 40 nm has been reported for the C_{60} fullerene[27,35] but recently attributed to triplets[16]; the results for C_{70} are also widely spread from 7 to 29 nm[36,37]. We note that wide spread of these numbers most probably originates from indirect measurements

relying on modeling of the external quantum efficiency; in contrast, our measurements directly demonstrate the long exciton harvesting distances in C_{70}.

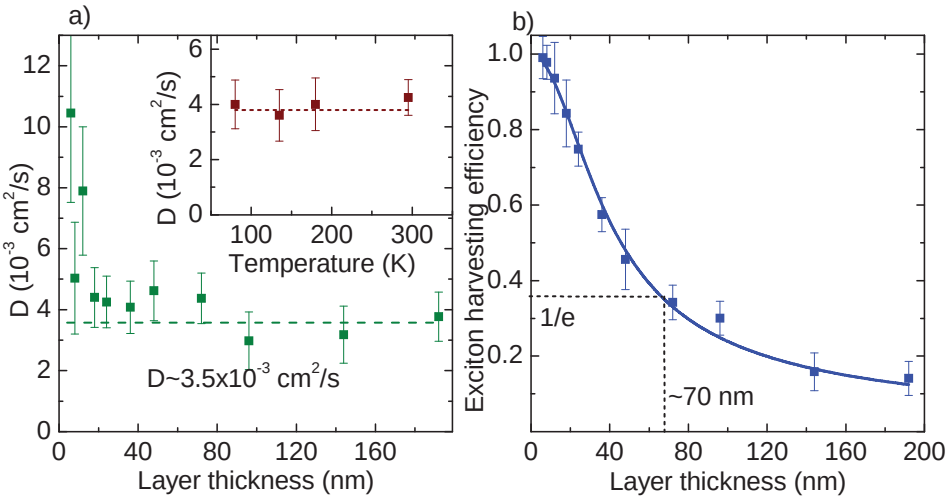

Figure 2.4 (a) Exciton diffusion coefficients obtained from independent fits of each transient. The inset shows the temperature dependence of the diffusion coefficient for the 24 nm thick sample. (b) Exciton harvesting efficiency vs. C70 layer thickness. The experimental values are shown by symbols while the solid line is obtained from a fit to Eq. (2.3). The data are corrected for the exciton annihilation. For the thinnest sample (6 nm), a 100% exciton harvesting efficiency is assumed.

As C_{70} produces weak but nonetheless detectable PL, our results can be benchmarked against conventional time-resolved PL quenching method[4,6,33,38,39] (Figure S2.9). It turns out that a single-transient approach (similar to the one depicted Figure 2.4a) does not produce stable results especially for thick samples (Figure S2.10). Nonetheless, from the combined dependence of quenching efficiency on the C_{70} layer thickness (i.e. from essentially multisampling approach as opposed to single-sample PIA), we obtained the diffusion coefficient of $D \approx 4 \cdot 10^{-3}$ cm^2/s, which is fairly close to the values cited above.

The analytical model makes several implicit assumptions (such as a flat energy landscape, localized excitons, negligible exciton annihilation) that in general are not granted. To verify their significance, Monte-Carlo simulations were performed to model exciton motion in a 3D random walk within a cubic disordered grid (Figure S2.11, Figure S2.12). It appears that the excitons are delocalized within approximately four C_{70} molecules, which is in good agreement with previous findings on delocalization effects in fullerenes[40], and the share of annihilated excitons is relatively low (<10% even for the thickest samples). The energetic Gaussian disorder resulting from simulations is ~5 meV, i.e. negligibly low compared to kT ~26 meV at 297 K. This implies that the diffusion process should not change substantially down to nitrogen temperatures of 77 K which was confirmed to be the case (Figure 2.4a, inset; SI, Figure S2.13). The low disorder (and,

as a result, high diffusion rate) most probably sources from the symmetry of the C_{70} molecule and vacuum deposition process used to prepare the films.

2.3 Conclusions

In summary, we have demonstrated efficient exciton harvesting from vacuum-deposited C_{70} layers up to 70 nm thick with the unique time-of-flight spectroscopic approach that allows obtaining the diffusion coefficient and exciton harvesting distances from a single sample. The experimental data are perfectly described by a simple analytical model, allowing us to obtain the diffusion rate of $D \approx 3.5 \cdot 10^{-3}$ cm^2/s from a single sample. We foresee the proposed noninvasive time-of-flight technique as a powerful tool for further development of organic opto-electronic components, such as simple layered solar cells[41], thin-film light-emitting transistors, and electrically pumped lasers.

2.4 Methods

Samples preparation

The samples were fabricated as layered structures of C_{70} fullerene and TPTPA star-shaped conjugated molecule in a "sandwich" arrangement (Figure 2.1a, Figure S2.1) by D. Cheyns, *imec*, Belgium. The C_{70} layer thickness varies between 6 and 192 nm (Table S2.1). For the thin (<48 nm) C_{70} layers, the "repeated sandwich" architecture was implemented to boost overall optical density of C_{70}. As a result, the samples consist of a number (1 to 8) of C_{70} layers with total thickness of 48 nm, 72 nm, 96 nm, 144 nm or 192 nm, with 10-nm TPTPA hole-detection layers sandwiched between them (Figure S2.1). Absorption spectra of the samples are depicted in Figure S2.2. To prevent degradation, the samples were encapsulated in an inert N_2 atmosphere. No sample degradation was observed in a year of storage and experimenting under ambient conditions. The quality of the interfaces between TPTPA and C_{70} were characterized by X-ray reflectometry by R. Kerner, Princeton University, USA. The measurements confirm that the interfaces are molecularly smooth (no intermixed region).

For control of the C_{70} absorption and its IR response (Figure S2.4), the 12 nm, 24 nm, 48 nm, 72 nm, and 96 nm thick C_{70} layers with no TPTPA layers were used. For blank experiments, the sample with a single 12 nm thick TPTPA layer was also fabricated; no IR response was observed from this sample even at excitation intensities of a factor of 10 higher than experimentally used. To ensure that signals does not depend on the TPTPA layers thickness, the 24 nm thick C_{70} samples with 2 nm and 20 nm TPTPA layers were fabricated and measured (Figure S2.14); no TPTPA thickness dependence was observed.

For details on the sample preparation and X-ray measurements, refer to Ref. [24].

Optical

Absorption spectra of the samples were recorded with a Perkin-Elmer Lambda 900 spectrophotometer. Photo-induced absorption (PIA) measurements were performed at a VIS-pump, IR-probe setup based on a Spectra-Physics Hurricane system (~120 fs, 800 nm, 1 KHz repetition rate) and two optical parametrical amplifiers (Light Conversion TOPAS) operating in the visible (400-2400 nm) and IR (1.2-12 μm) regions. The wavelength of the excitation pulse was chosen in the region of TPTPA transparency near a maximum at the C_{70} absorption spectrum at 530 nm. The wavelength of the IR probe pulse was varied in the 1.2-2.6 μm range to record the TPTPA polaron spectra and the non-resonant C_{70} response. The exciton dynamics were measured at 1.55 μm and at 1.3 μm probe wavelengths to separate TPTPA hole and C_{70} exciton responses. The polarization of the probe pulse was set at the magic angle of 54.7° with respect to the polarization of excitation pulse to observe the population signal only[25]. After the sample, the IR signal was detected by nitrogen-cooled InSb detectors, transmission change ΔT of the sample with and without the excitation pulse was calculated and normalized on the sample transmission T: $\Delta T/T$. To minimize the biexciton recombination and ensure linearity of the response at all delay times (Figure S2.15), the energy density of the excitation pulse was decreased to ~1.3 μJ/cm^2, which corresponds to ~1 absorbed photon per 15 nm. The experiments were performed under room temperature of 297 K, if not indicated otherwise. The low-temperature measurements were performed in a nitrogen-cooled Oxford CF204 cryostat.

Time-resolved photoluminescence (PL) measurements were performed with a Hamamatsu C5680 streak-camera system with time resolution of ~10 ps. The excitation wavelength of 560 nm was produced by selecting a 10-nm wide portion of the supercontinuum generated form the Ti:sapphire laser (Mira) output in a Newport SCG-800 hollow fiber. The time-resolved PL was collected in a 90° geometry with respect to the excitation beam. The color glass longpass filter OG570 was placed before the polychromator to filter the excitation stray light.

Monte-Carlo simulations

Monte-Carlo simulations were performed to model exciton motion in a 3D random walk within a cubic C_{70} grid. Each C_{70} molecule was assigned its own energy gap, randomly generated from a Gaussian distribution with standard deviation σ. The (delocalized) exciton hops between neighboring C_{70} molecules with the hopping time τ_j. Once the exciton reaches the interface, it dissociates into charges with the hole transfer time τ_{ht} and from this moment contributes to the observed signal. If two excitons meet each other, one of them immediately annihilates. Hole transfer time τ_{ht} and hopping time τ_j are global (i.e. identical for all samples) fit parameters. See more detailed description and simulated results in SI, Section 2.5.12 “Monte-Carlo simulations”.

2.5 Supporting Information

2.5.1 List of samples

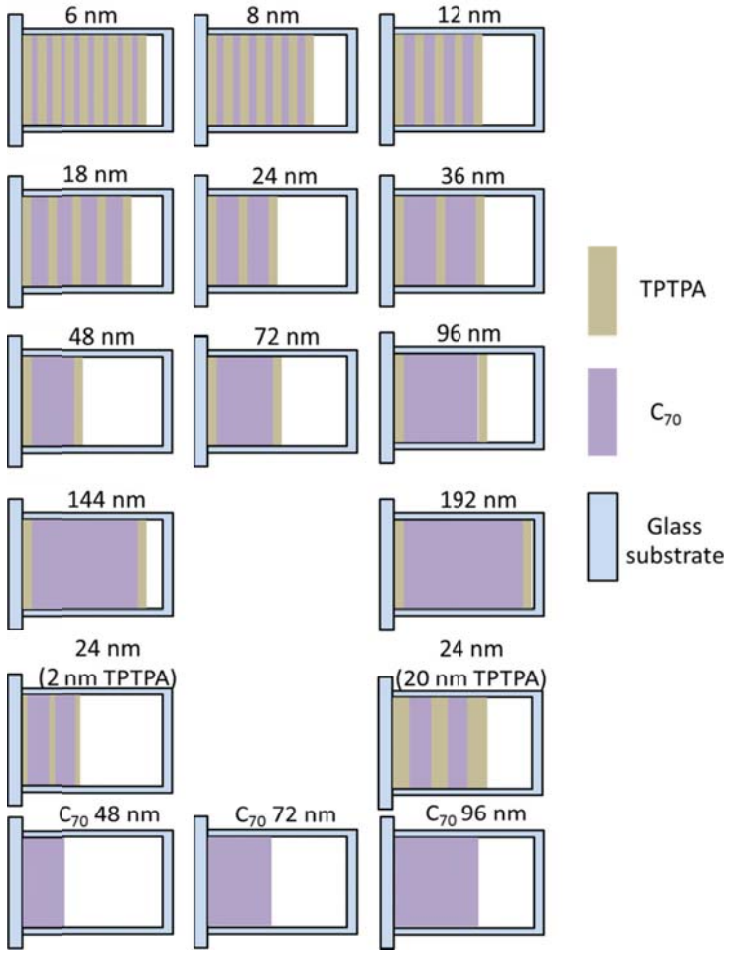

Figure S2.1 Schematic drawings of all investigated layered samples.

Table S2.1 List of the samples studied

C_{70} thickness	Number of C_{70} layers	TPTPA thickness	C_{70} total thickness
6 nm	8	10 nm	48 nm
8 nm	6		
12 nm	4		
18 nm	4		72 nm
24 nm	2		48 nm
36 nm	2		72 nm
48 nm	1		48 nm
72 nm	1		72 nm
96 nm	1		96 nm
144 nm	1		144 nm
192 nm	1		192 nm
24 nm	2	2 nm	48 nm
24 nm	2	20 nm	
12 nm	1	--	12 nm
24 nm	1		24 nm
48 nm	1		48 nm
72 nm	1		72 nm
96 nm	1		96 nm

2.5.2 Linear absorption spectra

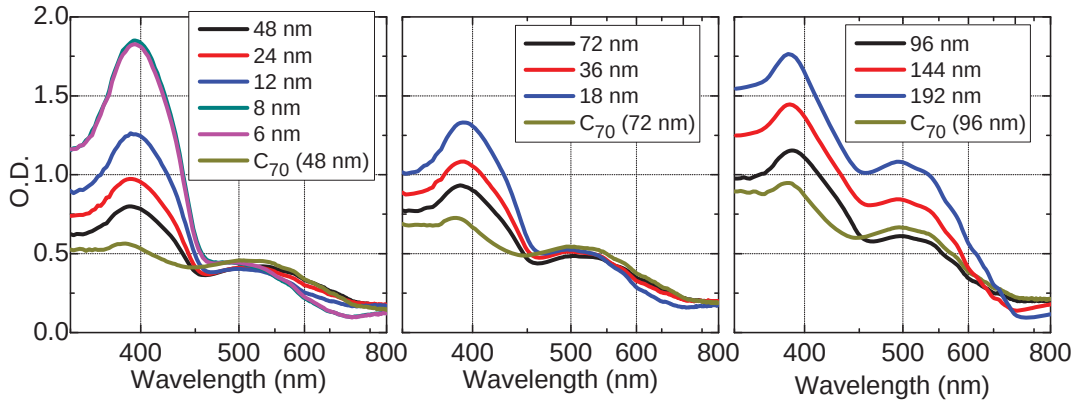

Figure S2.2 Absorption spectra of all samples as measured by an absorption spectrometer (Perkin-Elmer Lambda 900). Thickness of each C_{70} layer is shown in the legend, for the exact structure of the samples refer to Figure S2.1 and Table S2.1.

2.5.3 Excitation wavelength dependence

To insure that the exciton cooling does not affect the diffusion dynamics, we measured the transients at the excitation wavelength of 650 nm at which the photon energy is 0.43 eV lower than at 530 nm. The resulting transients are very similar (Figure S2.3), so that there is no difference between "hot" and "cold" exciton dynamics.

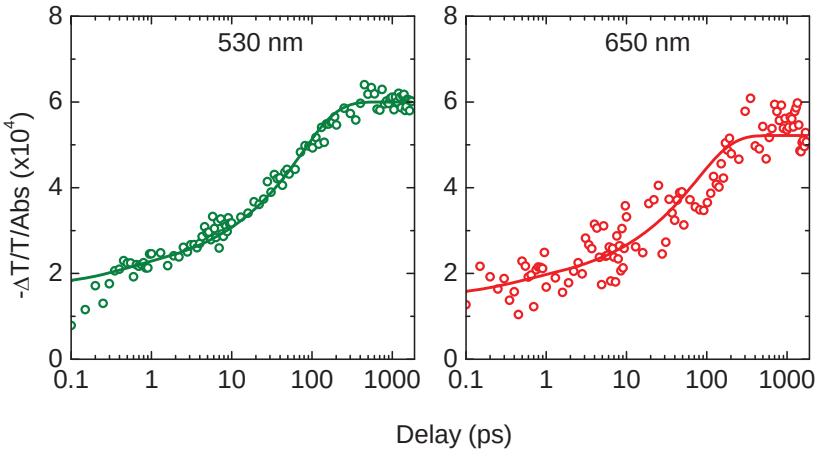

Figure S2.3 Measured (dots) and fitted (solid lines) PIA transients at two excitation wavelengths (indicated) for the 24 nm sample.

2.5.4 C_{70} and TPTPA IR responses

To evaluate the possible contribution of C_{70} to the TPTPA polaron response (Figure S2.4a), the IR response of the pure C_{70} film was also measured (Figure S2.4b). The PIA transients (insets in Figure S2.4b) indicate two different processes involved, occurring at the 500 ps and >2 ns timescales. To find spectral signatures of these processes, the C_{70} spectral response was decomposed into two Gaussian-shaped bands. The first Gaussian is centered around 1.7 μm and decays with a timescale of about 500 ps, which perfectly corresponds to the intersystem crossing time in C_{70} (see also Section 2.5.9 "C_{70} exciton lifetime"**).** Therefore, we attribute this band to C_{70} singlet exciton absorption. The second band peaks below 1 μm and does not decay at an experimentally accessible time basis. It is well-known that the triplet-triplet absorption in C_{70} is located mainly in the visible region with a relatively weak shoulder into the near-IR region[34,42]. Taking all of this into account, this time-independent spectroscopic feature is assigned to the triplet-triplet absorption in C_{70}.

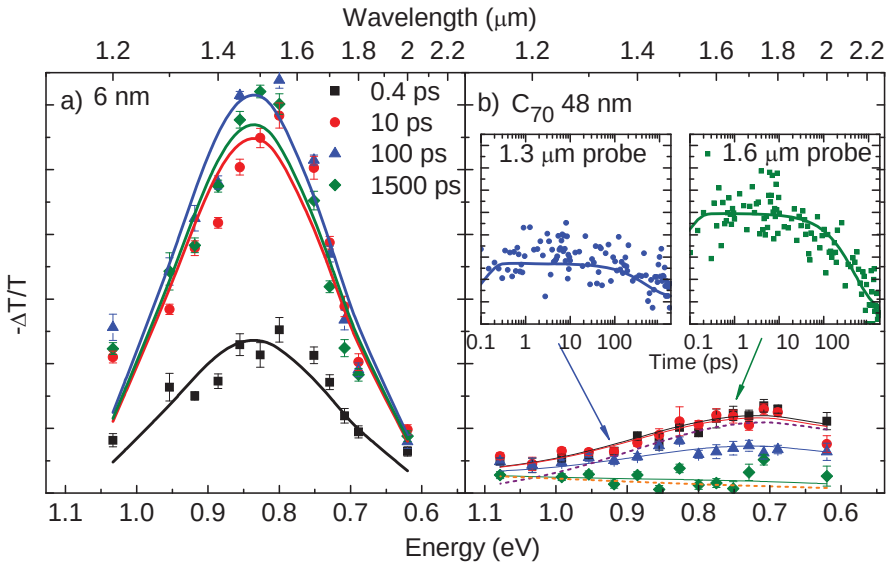

Figure S2.4 (a) Polaron absorption spectra for the 6 nm sample and (b) exciton response of the 48 nm C_{70} film. Solid lines are fits with a single Gaussian function in (a) and with two Gaussian functions in (b) (shown by the dotted lines). The excitation wavelength is 530 nm; the delays are indicated in the legend. The insets in (b) show the PIA transient response at two probe wavelengths of 1.3 μm (left) and 1.6 μm (right) for the 48 nm C_{70} layer. Solid dots and lines represent experimental data and fits with a single-exponential decay function (500 ps decay time) and a constant offset, convoluted with Gaussian (σ~0.1 ps) apparatus function, respectively.

Despite relatively low amplitude of the C_{70} contribution to the TPTPA polaron response, it is expected to contribute to the signals from thick (i.e. 96-192 nm) C_{70} layers at early times when

the majority of C_{70} excitons have not arrived at the TPTPA interface. Therefore, the procedure of subtraction of the unwanted C_{70} response from the signals to isolate the TPTPA response was developed (see detailed description below).

2.5.5 Separation of C_{70} and TPTPA IR responses

The C_{70} response has a step-wise behavior at early times and decreases in time due to (i) the exciton lifetime and (ii) exciton splitting at the interface (Figure S2.4b, inset). The latter precludes the straightforward subtraction of the independently measured C_{70} response from the overall PIA response: the C_{70} response in the layered samples is always shorter than the exciton lifetime because of an extra channel of exciton decay (i.e. splitting into a hole and an electron).

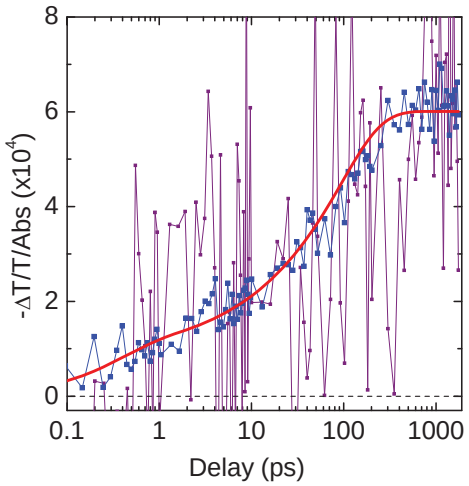

Figure S2.5 TPTPA hole dynamics calculated by subtraction simulated C70 exciton response from the transients (blue symbols/lines), calculated by using equation S3 (purple symbols/lines) and obtained from simulation (red solid line) for the 24 nm sample.

However, taking into consideration the fact that the TPTPA response is strongly-resonant (Figure S2.4a), while the C_{70} response is almost non-resonant (Figure S2.4b), the TPTPA response can be extracted from two measurements at different IR probe wavelengths: close to the TPTPA response maximum (~1.55 μm) and at a detuned wavelength (~1.3 μm). At 1.3 μm probe TPTPA response drops significantly (with a factor of β) compared to 1.55 μm while the C_{70} response changes weakly. Therefore, signals at two probe wavelengths are:

$$\Delta T_{1.6\mu}(t) = \Delta T_{TPTPA}(t) + \Delta T_{C70}(t) \qquad \text{(S2.1)}$$

$$\Delta T_{1.3\mu}(t) = \Delta T_{TPTPA}(t) \cdot \beta + \Delta T_{C70}(t) \tag{S2.2}$$

Taking the difference of the two, the TPTPA response is readily factorized:

$$\Delta T_{TPTPA}(t) = \frac{1}{1-\beta}\left[\Delta T_{1.6\mu}(t) - \Delta T_{1.3\mu}(t)\right] \tag{S2.3}$$

In practice, however, the difference is affected by the noise (originating mainly from weaker 1.3 μm signal, Figure S2.5). Hence, it is more advantageous first to fit the overall responses at both wavelengths globally (i.e. with all fitting parameters identical for both sets of transients for all samples) with either analytical model or Monte-Carlo simulation (see below), and then to subtract the calculated C_{70} contribution, thereby extracting the TPTPA response. The resulted transients are in perfect agreement with those obtained using Eq. (S2.3) directly but have a much higher signal-to-noise ratio (Figure S2.5).

2.5.6 Analytical model

The number of excitons within the C_{70} film is known[33] to be described as:

$$n(z,t) = e^{-t/T_1} \sum_{m=1}^{\infty} B_m e^{-\omega_m^2 Dt} \sin(\omega_m z), \tag{S2.4}$$

with

$$B_m = \frac{2}{L}\int_0^L I(z)\sin(\omega_m z)dz, \omega_m = \frac{\pi m}{L}, \tag{S2.5}$$

where T_1 is the effective exciton lifetime, D is the diffusion coefficient, $I(z)$ is the initial distribution of the exciton density along the z-axis (aligned along the light propagation direction), and L is the thickness of the layer.
At the interfaces, the flux of holes is described by the following boundary conditions:

$$J_h(t)|_{z=0,L} = \pm D \frac{dn(z,t)}{dz}\Big|_{z=0,L} \tag{S2.6}$$

Therefore, the density of holes in the quencher by the time t is

$$h(t) = -\int_0^t \left(D \frac{dn(z,t)}{dz}\Big|_{z=0} - D \frac{dn(z,t)}{dz}\Big|_{z=L} \right) dt \tag{S2.7}$$

Taking into consideration the probe intensity distribution $P(z)$, the bulk exciton response is

$$N_b(t) = \frac{e^{-t/T_1}}{L}\int_0^L \sum_{m=1}^{\infty} B_m e^{-\omega_m^2 Dt}\sin(\omega_m z)\,P(z)dz \tag{S2.8}$$

while the hole response is given by

$$H_b(t) = \frac{DT_1}{L}\sum_{m=1}^{\infty}[P(0)-(-1)^m P(L)]B_m\omega_{km}\frac{1-e^{-t\left(\frac{1}{T_1}+\omega_m^2 D\right)}}{1+\omega_m^2 DT_1} \tag{S2.9}$$

Note that the equations S2.8 and S2.9 do not include the interfacial excitons (i.e. those in the C_{70} layer adjacent to the TPTPA layer) that dissociate without any precluding diffusion within the hole-transfer time τ_{ht}. This process is included *ad hoc* as an exponential decay added to the exciton response:

$$N(t) = \gamma * e^{-\frac{t}{\tau_{ht}}}N_b(0) + N_b(t) \tag{S2.10}$$

where γ is share of interfacial excitons calculated as

$$\gamma = \frac{\int_0^{L_{int}} I(z)dz + \int_{L-L_{int}}^{L} I(z)dz}{\int_0^L I(z)dz}, \tag{S2.11}$$

where L_{int} is the thickness of the interfacial layer (in case of localized excitons L_{int} =1 nm).

The hole response consist of responses of interfacial holes with relative fraction γ and of bulk holes:

$$H(t) = \gamma * \left(1 - e^{-\frac{t}{\tau_{ht}}}\right)H_0 + H_b(t), \tag{S2.12}$$

where H_0 is the concentration of holes assuming 100% harvesting efficiency.

Finally, the measured signal consists of both TPTPA and C_{70} exciton responses with the relative cross-section α:

$$S(t) = S * [\alpha H(t) + (1-\alpha)N(t)] \tag{S2.13}$$

Equation (S2.13) was used to fit the experimental transients taken at two probe wavelengths (Figure S2.6). Hole transfer time τ_{ht}, amplitude S and exciton diffusion coefficient D were set global for all transients, the relative cross-section α was set global for the set of transients with the same probe wavelength, while the effective exciton lifetime T_1 =500 ps was taken from time-resolved PL experiments (see below). The PIA transients as measured at the two probe

wavelengths together with fit results are shown in Figure S2.6. To obtain the exciton dissociation dynamics (Figure 2.3, Main Text), the C_{70} responses with the already determined parameters are separately calculated for each transient (green solid lines in Figure S2.6), and subtracted then from the transients. Note the strong dependence of the C_{70} decay time on the sample: thinner the C_{70} layer (and therefore faster exciton dissociation at the TPTPA interface), faster the decay. Secondly, the contribution of the C_{70} response can hardly be neglected at short times in thick samples.

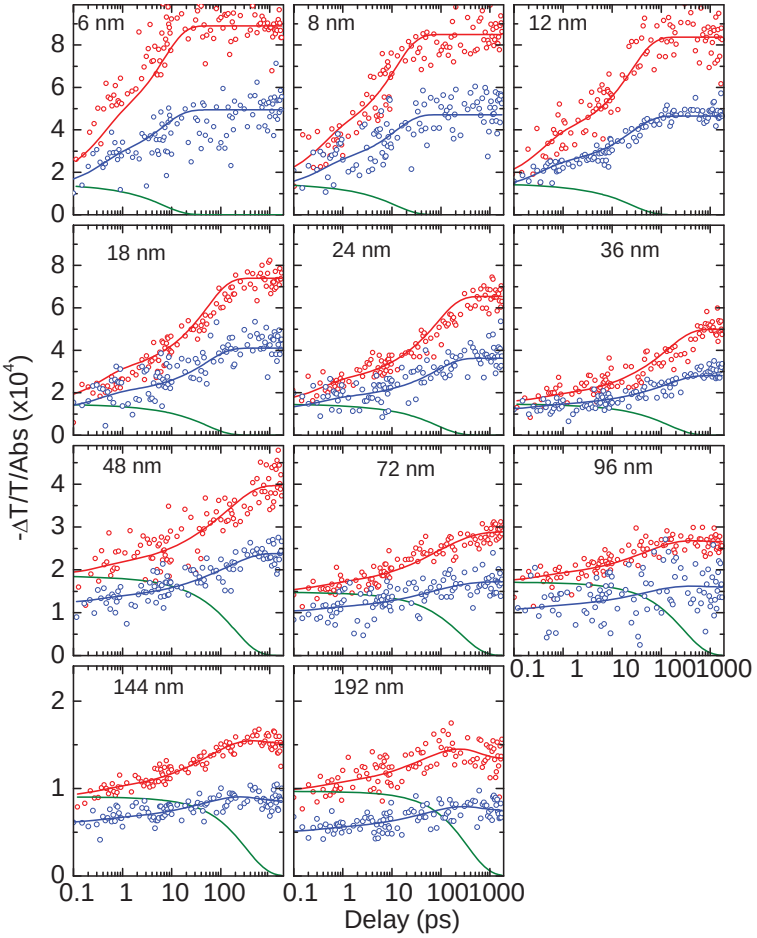

Figure S2.6 Measured (dots) and fitted (solid lines) PIA transients at 1.55 μm (red) and 1.3 μm (blue) probe wavelengths, and calculated C_{70} contributions at the 1.55 μm probe (green solid lines) for all samples. The transient amplitudes are normalized by the sample absorption. Note change in the vertical scale in the two lowest rows.

2.5.7 Exciton harvesting efficiency vs. the layer thickness

The diffusion coefficient *D* can also be obtained by fitting the exciton harvesting efficiency dependence on the sample thickness *L* with *D* as the only fitting parameter. The dependence of exciton harvesting efficiency on the layer thickness *η(L)* is directly calculated from equation S9 as:

$$\eta(L) = \frac{H_b(t=\infty, L)}{H_b(t=\infty, L=0)} \tag{S2.14}$$

Here we assumed 100% harvesting of interfacial excitons, so that the exciton harvesting efficiency decreases only due to the incomplete harvesting of the bulk excitons. In the case of uniform excitation and probe intensity distributions, equation S14 is simplified to the well-known result[33]:

$$\eta(L) = \frac{2\sqrt{DT_1} * tanh(\frac{L}{2\sqrt{DT_1}})}{L} \tag{S2.15}$$

To ensure a stable fit, the harvesting efficiencies from a series of samples (~5-10, Ref. [4]) should be measured. The fit of the exciton harvesting efficiency dependence on the layer thickness (Figure 2.4, Main Text) with Eq. (S2.15) resulted in diffusion coefficient $D \approx 3 \cdot 10^{-3}$ cm^2/s.

2.5.8 Connection between PL and PIA signals

In the simplest case of uniform excitation and probe intensities distributions, the number of holes at the interface (measured by PIA) and the number of excitons in the layer (measured by time-resolved PL) are inherently connected. In this case, the number of excitons can be derived from Eq. (S2.8) (see also Ref. [33]) as

$$N_b(t) = \frac{8N_0}{L} e^{-t/T_1} \sum_{m=1}^{\infty} \frac{e^{-\omega_{2m-1}^2 Dt}}{\omega_{2m-1}^2}, \tag{S2.16}$$

where N_0 is the initial exciton density. The number of holes is calculated according to Eq. (S2.9) as:

$$H_b(t) = -\frac{8N_0 D}{L} \int_0^t e^{-t/T_1} \sum_{m=1}^{\infty} e^{-\omega_{2m-1}^2 Dt} \tag{S2.17}$$

Therefore, the number of holes and the number of excitons are connected as

$$H_b(t) = -\int_0^t e^{-t/T_1} \frac{d\left(N_b(t)/e^{-t/T_1}\right)}{dt} dt \quad \text{(S2.18)}$$

which is simplified to

$$H_b(t) = N_0 - N_b(t) - \frac{1}{T_1}\int_0^t N_b(t)dt \quad \text{(S2.19)}$$

Eqs.(S2.18)-(S2.19) present inherent connection between time-resolved PIA and PL measurements. In practice, however, the conversion is mere involved due to (i) convolution with the apparatus functions, (ii) substantial fraction of the interfacial excitons in thin samples, and (iii) the assumption of uniform excitation and probe intensity distributions.

2.5.9 C_{70} exciton lifetime

C_{70} exciton lifetime in 48-nm film was measured by both time-resolved PL (Hamamatsu C5680 streak camera system, 560 nm excitation) and PIA (530 nm excitation, 1.55 μm probe) experiments (Figure S2.7). The PL decay was also measured in C_{70} diluted in ortho-dichlorobenzene to exclude packing effects, if any. The solution was placed in 1-mm quartz cuvette and its concentration was adjusted to OD= 0.3 at 560 nm to match C_{70} absorption.

The resulting transients are shown in Figure S2.7. In the solution, the PL signal decays with a timescale of 500±50 ps, while PIA signal decays at 600±100 ps. We attribute this to the effective lifetime of singlet excitons in the C_{70} layer. In the film, both PL and PIA signal decay with similar timescales of ~500 ps (520±40 ps for PL and 500±100 ps for PIA). Note that the effective lifetime measured herein is not the natural singlet lifetime but is mainly determined by the intersystem crossing time to the triplet state[5,43].

2.5.10 C_{70} absorption

To calculate the light penetration depth in C_{70} at the excitation wavelength, we measured the transmission of the single-layer samples at 530 nm (Figure S2.8). To eliminate the effects of reflections and/or interference, we carefully measured the transmitted and reflected light for each sample, and recalculated transmission of the layers. The dependence was fit with an exponential decay function with a zero baseline, and the light penetration depth at 530 nm wavelength was obtained as 80 nm.

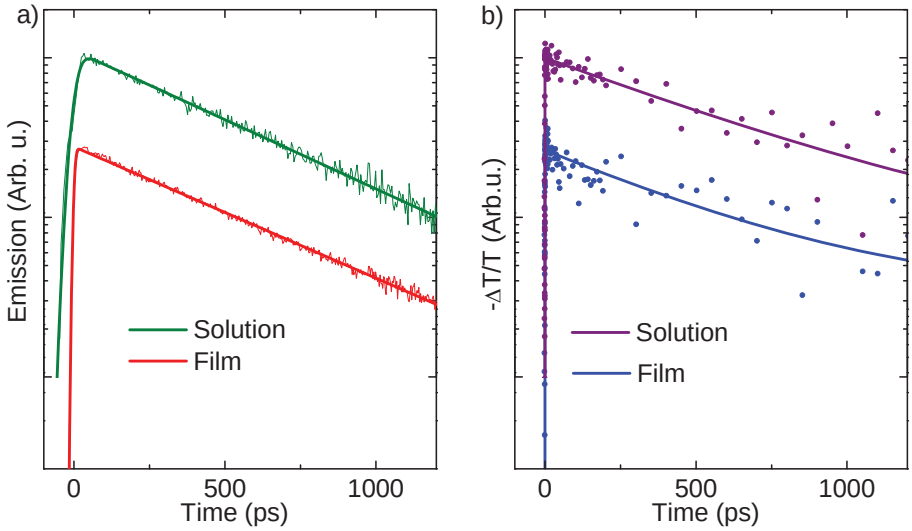

Figure S2.7 (a) PL decay of C_{70} 96 nm layer (red) and C_{70} solution in ortho-dichlorobenzene (green) and (b) PIA response of C_{70} 48 nm layer (blue) and C_{70} solution in ortho-dichlorobenzene (brown). Dots show the measured values while the thick lines represent the best exponential fit convoluted with the Gaussian apparatus function with σ~20 ps for PL and σ~100 fs for PIA. The PL was recorded with a 560 nm excitation and integrated in the 600-800 nm region. The PIA signal in b was measured at 530 nm excitation and 1.55 μm probe wavelengths. The data in each panel are vertically offset for clarity.

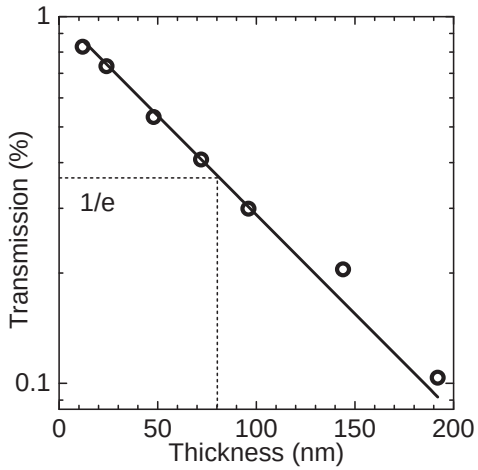

Figure S2.8 Dependence of C_{70} transmission on thickness for different samples at the wavelength of 530 nm. Experimental data are shown by open circles, while the solid line shows the exponential fit.

2.5.11 Time-resolved photoluminescence (PL) measurements

In order to validate the proposed technique, we measured the diffusion coefficient with a widely-used method of time-resolved PL quenching[4,6,33,38,39]. This was possible owing to weak but

nonetheless detectable PL from C_{70}. The time-resolved PL for all layered samples is shown in Figure S2.9a, together with the PL of the 96 nm C_{70} layer as a reference (Figure S2.9b shows the corresponding time-integrated spectra). PL transients were individually fit (solid lines) with the equation S16 (convoluted with a Gaussian apparatus function with σ~7 ps), with diffusion coefficient *D* as the only fit parameter.

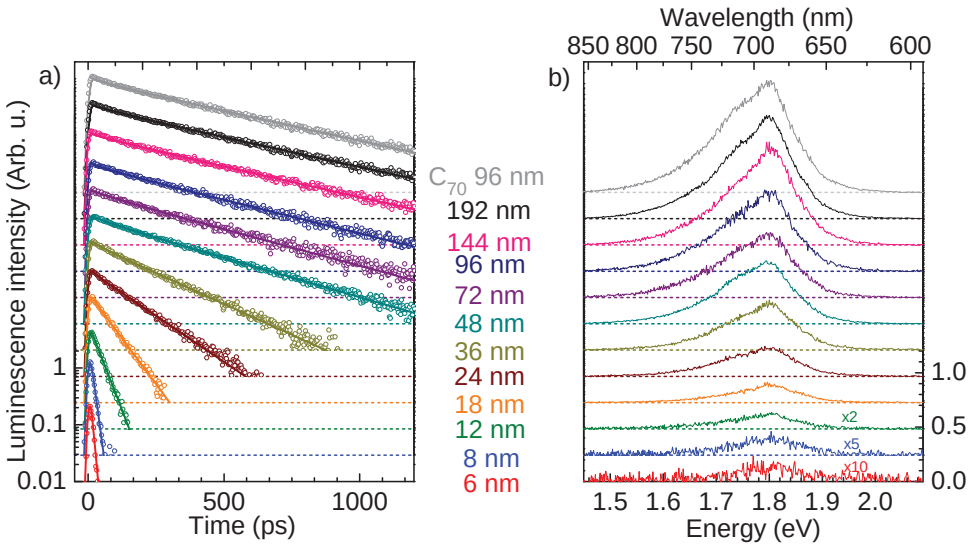

Figure S2.9 (a) Measured (dots) and fitted with Eq. (S2.18) time-resolved PL transients. Each transient is offset to the corresponding dashed line at 10-2 level; the thickness of each C70 layer is indicated to the right. All transients are normalized by the number of absorbed photons and integrated in 630-850 nm spectral range. The relative PL intensity of unity was assigned to the PL maximum of 96 nm unquenched C70 layer. (b) Time-integrated PL spectra. Each spectrum is offset to the corresponding dashed line; the thickness of each C70 layer is indicated to the left. All spectra are normalized by the number of absorbed photons. The relative PL intensity of unity was assigned to the maximum of 96 nm unquenched C70 layer.

The resulting diffusion coefficients are shown in Figure S2.10a. It is evident that the fits give reasonable results only for the samples with thicknesses close to the diffusion length. For thin samples, the diffusion coefficient is overestimated due to the relatively high fraction of interfacial excitons (compare with Figure 2.4b in the main text). For thick samples, fits becomes increasingly unstable because the decay time in this case is close to that in the unquenched sample. This can be readily seen from Eq. (S2.18) where the pre-sum exponential function which corresponds to the exciton effective lifetime, is accelerated by the quencher-related part (under the sum) which depends on the diffusion coefficient. Therefore, uncertainty in the exciton lifetime of 10% causes huge variations in *D* (error bars in Figure S2.10b). Therefore, time-resolved PL quenching cannot be used for obtaining the diffusion coefficient from a single sample, in a sharp contrast to the proposed time-resolved PIA technique.

To overcome this issue, we followed the standard procedure [4,33] of obtaining the diffusion coefficient from quenching efficiencies for the whole ensemble of samples. The quenching efficiencies were calculated as $\eta(L) = 1 - Q(L)/Q(C_{70})$, where *Q(L)* and *Q(C70)* are time-integrated PL of the sample with thickness *L* and the reference (unquenched) C_{70} sample, respectively [33]. Then we fit the resulted dependence (Figure S2.10a) with Eq. (S2.15) to obtain the diffusion coefficient. The fit results in $D \approx 4.3 \cdot 10^{-3}$ cm^2/s, which is fairly close to the PIA result of $D = 3.5 \cdot 10^{-3}$ cm^2/s.

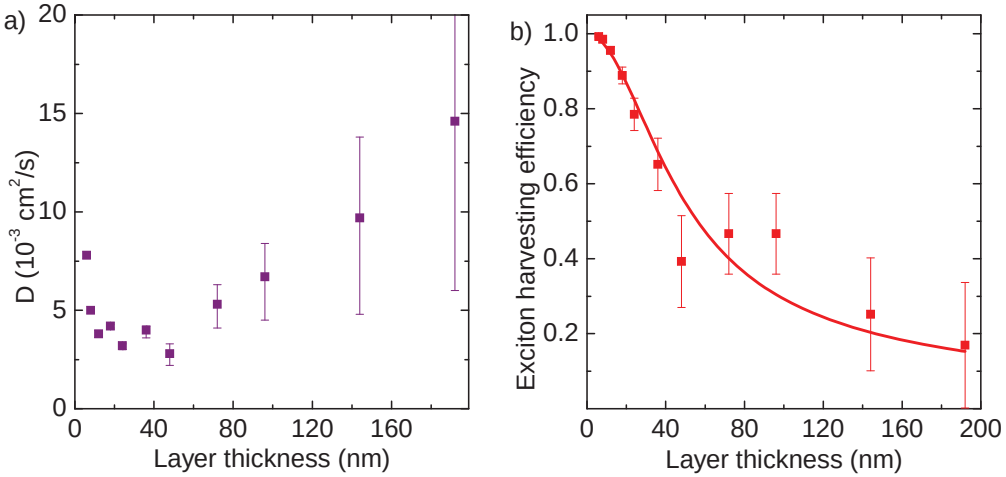

Figure S2.10 (a) Exciton diffusion coefficients obtained from independent fits of each transient in Figure S2.9 with Eq. (S2.18). The error bars show variations of *D* for exciton effective lifetime T_1 variations of 10% (from 450 ps to 550 ps). (b) PL quenching efficiency vs. C70 layer thickness, obtained from PL quenching. The experimental values are shown by symbols while the solid line is the best fit with Eq. (S2.15).

2.5.12 Monte-Carlo simulations

The Monte-Carlo simulations are performed by modeling an exciton random walk in the C_{70} layer. The C_{70} layer is modeled as a cubic grid with typical lateral dimensions of 400x400 grid points and the longitudinal dimension of *N* grid points, where *N* is the layer thickness. The lateral dimensions were chosen larger than the longest sample thickness, and periodic boundary conditions are applied (i.e. if the exciton leaves one side of the grid it appears from the opposite side). TPTPA layers are placed on both sides of the C_{70} layer along the lateral plane.

Each Monte-Carlo realization began with generation of the energy landscape of the grid. For each grid point, the site energy value is randomly chosen according to a Gaussian distribution with the standard deviation σ [44]. At time zero, the excitons finite effective lifetime T_1 are randomly placed into the grid with the given profile along the *z*-axis to account for the longitudinal excitation intensity distribution (see Figure S2.16), and the averaged exciton density

(i.e. the number of excitons per grid point) that corresponds to the experimental conditions (~$3 \cdot 10^{-4}$ nm^{-3}). The possible exciton delocalization was accounted for by assigning each exciton the delocalization radius of r grid points, i.e. each exciton effectively occupied a sphere with the radius r centered in the given grid point (the fully localized excitons had the delocalization radius of r=0). At each time step, an exciton migrates by one grid point to a random direction (Figure S2.11a) with a hopping time τ_j. The probability p_{if} of hopping depends on the energies of the starting and target grid points. If the energy of the target grid point is lower than the energy of starting point, the exciton always hops (p_{if}=1). If the energy of the target grid point is higher than the energy of starting point, the probability of hopping scales according to the Boltzmann factor, i.e:

$$p_{if} = \begin{cases} 1, & E_f < E_i \\ e^{-\frac{E_f - E_i}{kT}}, & E_f > E_i \end{cases} \qquad \text{(S2.20)}$$

where E_i and E_f are the energies of starting and target grid point, respectively, k is the Boltzmann constant and T is the ambient temperature (Figure S2.11c).

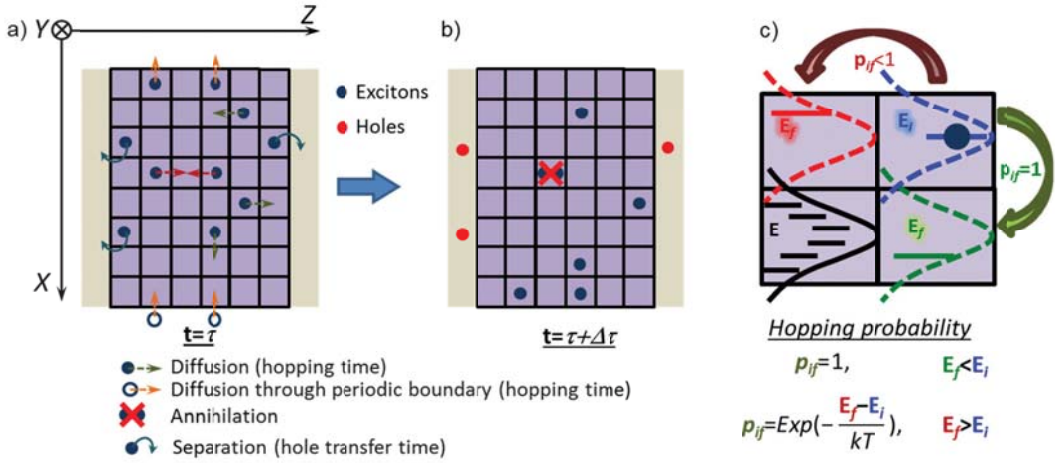

Figure S2.11 Schematics of the Monte-Carlo simulations: (a) Exciton distribution at times τ and (b) $\tau+\Delta\tau$ (the next step). The next-step processes of hopping diffusion, exciton-exciton annihilation and charge separation are shown in a by colored arrows. The electrons are not shown. The excitation and probe beams propagate along the z-axis. (c) Grid energy landscape and hopping probability

If two excitons meet each other (i.e. their delocalization volumes overlap), one of them immediately annihilates. If the exciton approaches the interface within proximity of its delocalization radius, it contributes to the signal with the hole transfer time τ_{ht} and excluded from the simulations. To match the real experiment conditions, the C_{70} excitons also contribute to the

signal with their own relative cross-section α, and the total signal is convoluted with a Gaussian apparatus function of σ~80 fs width.

As adjustable parameters, the time τ_j per step (the hopping time), the hole transfer time τ_{ht} and the exciton delocalization radius r and the standard deviation of the energy distribution σ are used while the exciton effective lifetime T_1 =500 ps was taken from time-resolved PL experiments, and kT was equal to 25.6 meV (297K, room temperature). For multi-layered structures, only a single C_{70} layer was considered as the excitation intensity distributions inside each layer are reasonably homogeneous and therefore not affecting the dynamics. For the single-layer samples (i.e. 48, 72, 96, 144 and 192 nm layers), the pre-calculated exciton distribution along the longitudinal direction was implemented. For the thickest samples (i.e. 96, 144 and 192 nm) the inhomogeneous distribution of the probe pulse within the C_{70} layer also was taken into account by introducing the probe distribution profile (Figure S2.16), as obtained by an optical model using the transfer matrix method. The exciton response at each longitudinal point was scaled according the probe intensity while the hole responses for the front and back TPTPA layers were scaled according to the intensity at the respective interfaces. To narrow the parameter landscape, the global fit procedure was performed for all transients at both probe wavelengths of 1.55 and 1.3 μm. The exciton harvesting efficiency, derived from the experiment (Figure 2.4, Main Text), was used as a constraining parameter (the fraction of split excitons from the simulation had to match the experimental values). Times τ_j and τ_{ht} and the standard deviation σ of the energy distribution were set as global parameters for all transients, the relative cross-section α was set global for the set of transients with the same probe wavelength. To maintain the simulation noise constant, the number of realizations was in the inverse ratio to the thickness of the layer (from 1 for 192 nm to 30 for 3 nm).

The simulated transients are shown in Figure S2.12 by red and blue solid lines (the simulated C_{70} response is shown by green solid lines). The excitons appear to be delocalized over ~4 C_{70} molecules, which is in good agreement with previous findings on delocalization effects in fullerenes[40]. The hole transfer time is derived from the simulations as $\tau_{ht} \approx 0.35 \pm 0.1$ ps, while the C_{70} exciton hopping time is $\tau_j \approx 0.5 \pm 0.1$ps. The share of annihilated excitons did not exceed 10% even for the thickest samples. The energy disorder emerged from simulations is lower than σ≈5 meV, i.e. negligibly low compared to kT ~26 meV at 297 K. From the hopping time, the diffusion coefficient is calculated as

$$D = \frac{a^2}{6\tau_j}, \qquad \text{(S2.21)}$$

where a is the hopping distance (equal to the distance between the centers of neighboring C_{70} molecules, $a \approx 1$ nm). The exciton diffusion coefficient is $D \approx 3.3 \cdot 10^{-3}$ cm^2/s, which is in perfect agreement with that obtained from the analytical model.

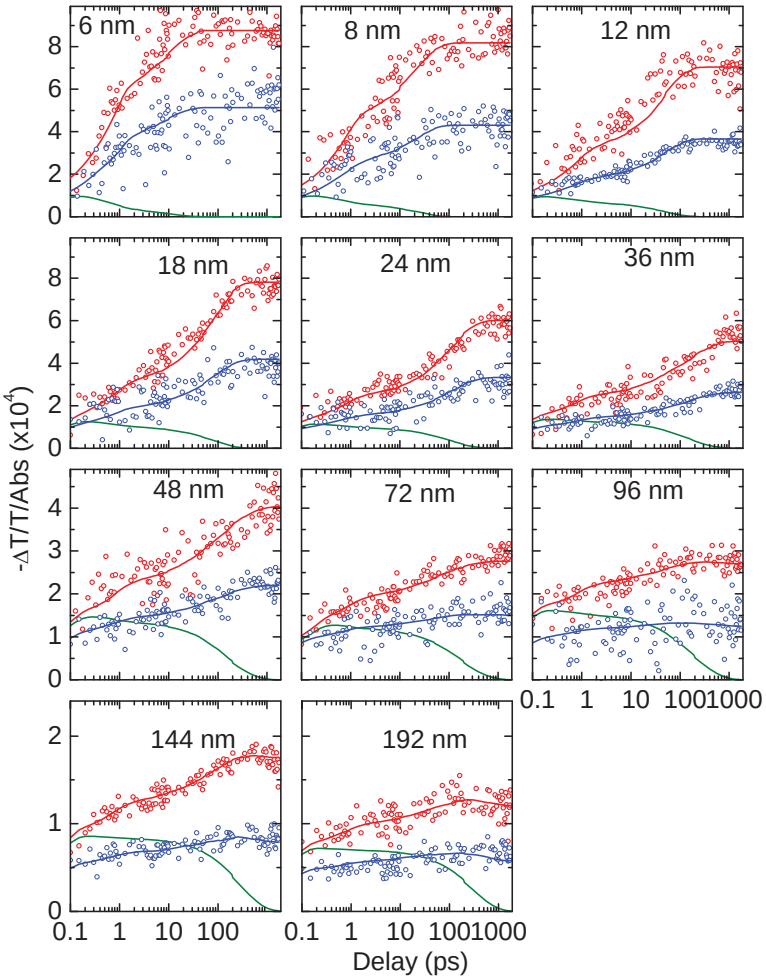

Figure S2.12 Measured (dots) and simulated (solid lines) PIA transients at 1.55 μm (red) and 1.3 μm (blue) probe wavelengths, and calculated C_{70} contributions at the 1.55 μm probe (green solid lines) for all samples. The transient amplitudes are normalized by the sample absorption. Note change in the vertical scale in the two lowest rows.

2.5.13 Temperature dependence

To evaluate the energy disorder, the 24 nm sample was measured in a wide range of temperatures (from 80 K to 297 K), and the 96 nm samples at two extreme temperatures (80 K and 297 K). The former sample was chosen because it combines prominent diffusion with high

exciton harvesting efficiency while in the later the exciton lifetime is more dominant. No differences neither in dynamics nor in transient amplitudes are observed (Figure S2.13). This confirms that energy disorder is lower than 5 meV rms.

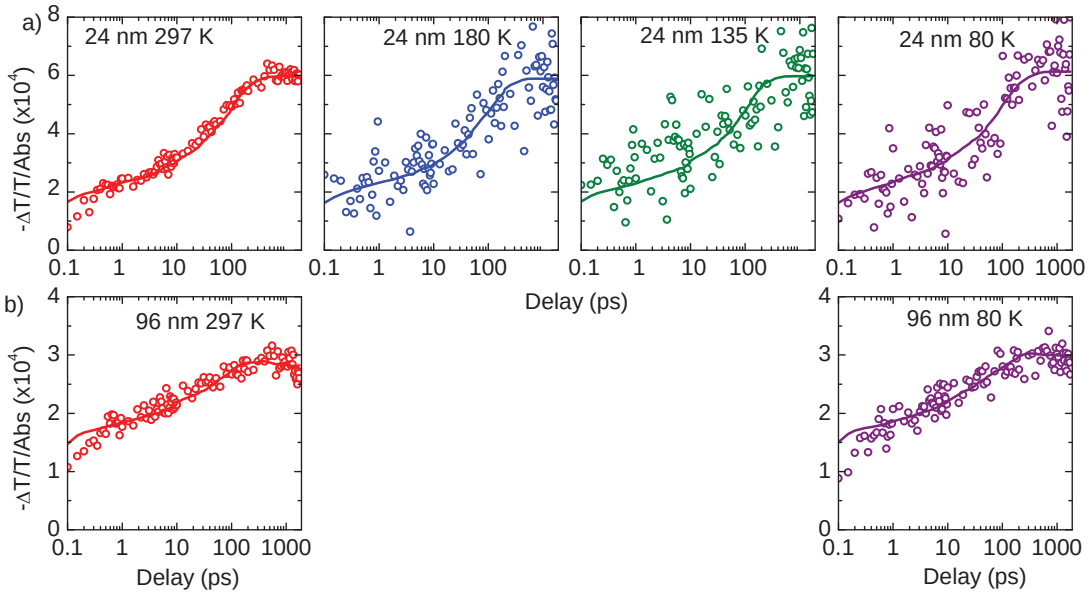

Figure S2.13 Measured (dots) and fitted with Eq. (2.1), main text (solid lines) PIA transients obtained at different temperatures (indicated) for (a) the 24 nm and (b) 96 nm samples.

2.5.14 TPTPA thickness dependence

Since the signal is proportional to the number of TPTPA holes produced, which in turn depends on the number of dissociated excitons, the signal should not be susceptible to the TPTPA layer thickness (as long as there are enough TPTPA molecules to accept the newcoming holes). To verify if this is the case, the responses from the 24 nm C_{70} samples with TPTPA layers of 20 nm, 10 nm and 2 nm in thickness were measured under identical conditions. The observed transients are indeed identical (Figure S2.14) so that the possible dependence on TPTPA thickness can be safely ruled out.

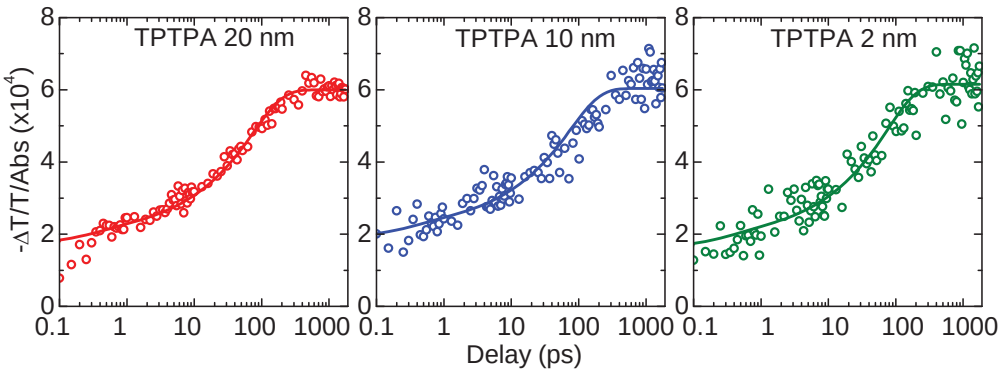

Figure S2.14 Measured (dots) and fitted (solid lines) PIA transients for 24 nm C_{70} samples with intermediate TPTPA layers of 20 nm (red), 10 nm (blue) and 2 nm (green).

2.5.15 Excitation intensity dependence

To ensure the linearity of the PIA response at all delays, the excitation intensity dependences of the PIA signals were measured (Figure S2.15). Figure S2.15 shows such dependences for the 6 nm (a) and 96 nm (b) samples on excitation energy density varied in the range 1.3-170 μJ/cm^2 at several representative delays. These particular samples were chosen as the least and the most susceptible to exciton annihilation, respectively, due to their thickness. The signals at 1 ps are linear for both samples in the whole intensity region which demonstrates the linearity of the number of the excitons on the incoming light intensity. In contrast, at longer delays the signal becomes increasingly saturated at high intensities.

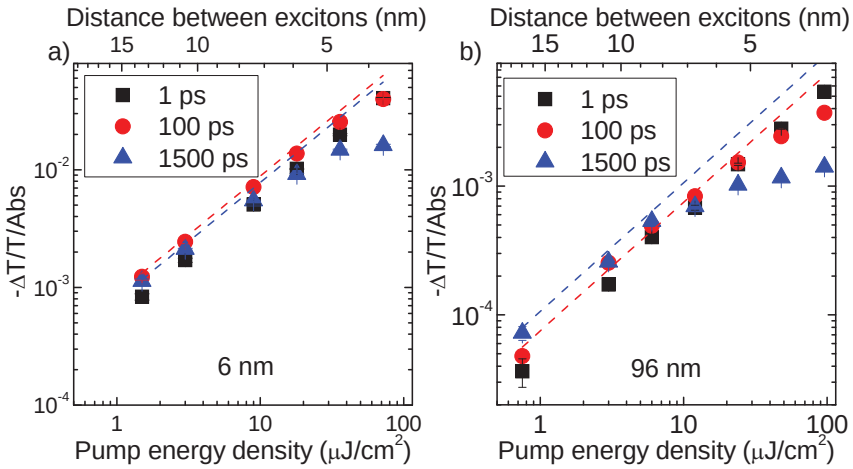

Figure S2.15 Dependences of PIA response for (a) 6 nm and (b) 96 nm samples on the excitation intensity at representative delays (as indicated in the legend). The experimental and simulated data are shown by solid symbols and solid lines, respectively. As the charge recombination is not included in the model, the simulated values at 1500 ps are not shown.

For the 6 nm sample, all excitons dissociate within ~50 ps (Figure 2.3, Main Text) so that nonlinearity at long times is attributed to the recombination of the separated charges due to their high density at the TPTPA/C_{70} interface. In the 96 nm sample, excitons dissociate over a longer period of time (~500 ps). Therefore, the nonlinearity at 100 ps delay is assigned to the exciton annihilation in the C_{70}, while at 1.5 ns delay the signal saturates due to both exciton annihilation and charge recombination. Nonetheless, the response at all times is fairly linear for excitation flux below ~3 $\mu J/cm^2$. Therefore, to minimize exciton annihilation, the excitation flux as low as 1.3 $\mu J/cm^2$ was chosen (~1 absorbed photon per 15 nm length to each side).

2.5.16 Intensity distribution

Optical interference[27-31] in the thin layered samples cannot be neglected due to i). the reflection at the TPTPA/air or substrate interface, ii). the difference in the complex index of refraction for C_{70} and TPTPA[24]. To take this effect into account, we modeled the transmission of all samples using a transfer-matrix method[31] (modelling was performed by D. Cheyns, IMEC). Using the same model, the excitation and probe intensity distributions within the samples are determined (Figure S2.16). For the 72-192 nm samples, a strong inhomogeneity of the excitation intensity is observed: the field is mostly localized near one of the two TPTPA layers, thereby skewing the density of photogenerated excitons towards one of them. Also, the probe intensity inhomogeneity in the 96-192 nm samples results in different sensitivity to the holes at both interfaces and excitons within the C_{70} layer.

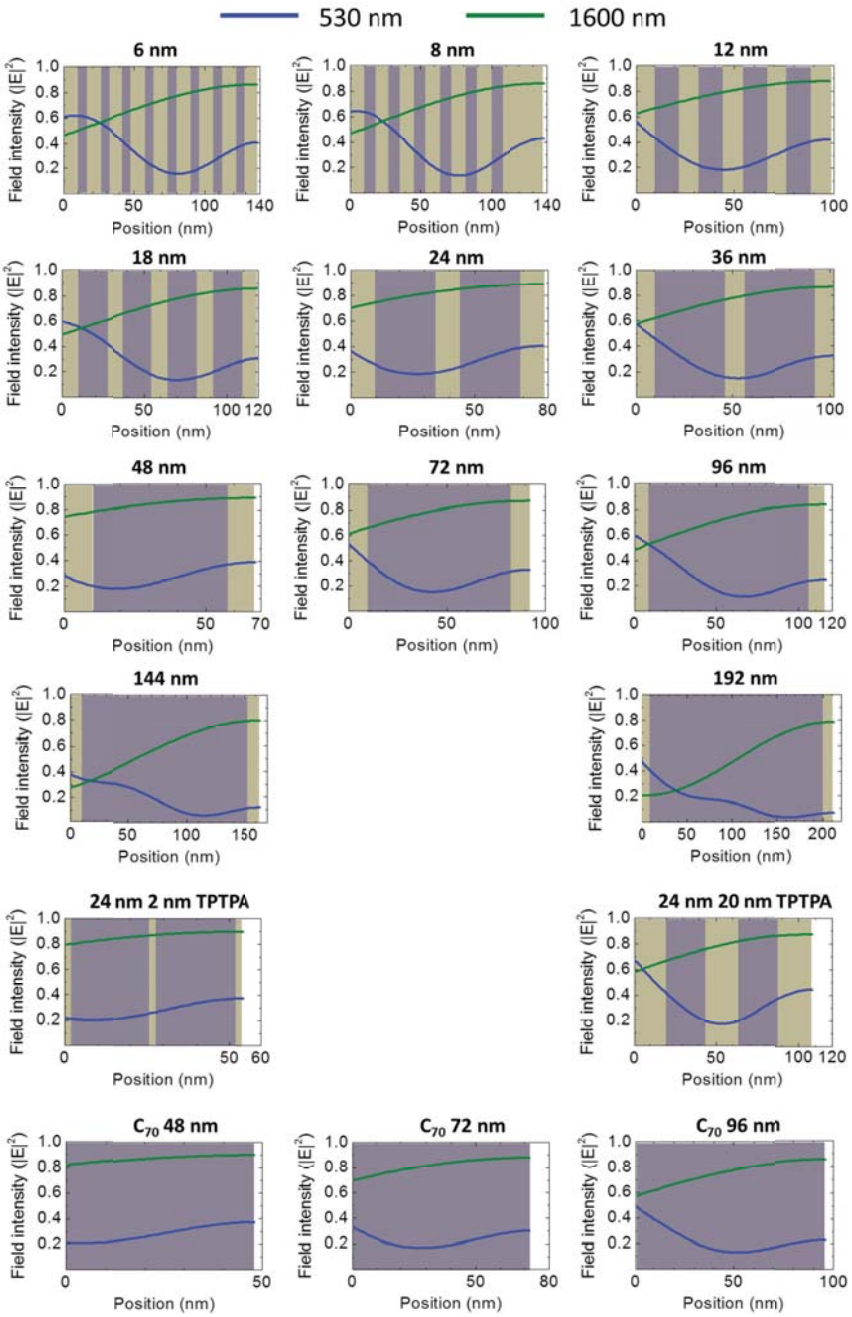

Figure S2.16 Intensity distributions in the samples at excitation (530 nm, blue solid lines) and probe (1600 nm, green lines) wavelengths, as obtained by an optical model using the transfer matrix method (see Ref. [24] for details).

Author Contributions

OVK performed PIA, PL and linear absorption measurements and the data processing, and developed the analytical and the Monte-Carlo models; FdH wrote the Monte-Carlo simulations code; RAK performed the X-Ray measurements; DC manufactured the samples, performed the ellipsometry measurements, and conducted transfer-matrix intensity distribution calculations (see Ref. [24] for details), BPR and MSP conceived the concept and supervised the research.

References

1 T. W. Kelley, P. F. Baude, C. Gerlach, D. E. Ender, D. Muyres, M. A. Haase, D. E. Vogel, and S. D. Theiss. Recent Progress in Organic Electronics: Materials, Devices, and Processes. *Chem. Mater.* **16** no. 23, 2004, p. 4413.

2 R. R. Lunt and V. Bulovic. Transparent, Near-Infrared Organic Photovoltaic Solar Cells for Window and Energy-Scavenging Applications. *Appl. Phys. Lett.* **98** no. 11, 2011, p. 113305.

3 A. Kohler and H. Bassler. *Electronic Processes in Organic Semiconductors: An Introduction*. (Wiley-VCH Verlag GmbH & Co. KGaA, Weinheim, Germany, 2015).

4 O. V. Mikhnenko, P. W. M. Blom, and T.-Q. Nguyen. Exciton Diffusion in Organic Semiconductors. *Energy Environ. Sci.* **8**, 2015, p. 1867.

5 S. Reindl, A. Penzkofer, and H. Gratz. Intersystem-Crossing and Excited-State Absorption of C_{70} Studied by Picosecond Pump and Probe Absorption and Fluorescence Measurements. *J. Photochem. Photobiol. A* **115** no. 2, 1998, p. 89.

6 S. M. Menke and R. J. Holmes. Exciton Diffusion in Organic Photovoltaic Cells. *Energy Environ. Sci.* **7** no. 2, 2014, p. 499.

7 O. V. Mikhnenko, R. Ruiter, P. W. M. Blom, and M. A. Loi. Direct Measurement of the Triplet Exciton Diffusion Length in Organic Semiconductors. *Phys. Rev. Lett.* **108** no. 13, 2012, p. 137401.

8 S. Westenhoff, I. A. Howard, and R. H. Friend. Probing the Morphology and Energy Landscape of Blends of Conjugated Polymers with Sub-10 nm Resolution. *Phys. Rev. Lett.* **101** no. 1, 2008, p. 016102.

9 A. Haugeneder, M. Neges, C. Kallinger, W. Spirkl, U. Lemmer, J. Feldmann, U. Scherf, E. Harth, A. Gügel, and K. Müllen. Exciton Diffusion and Dissociation in Conjugated Polymer/Fullerene Blends and Heterostructures. *Physical Review B* **59** no. 23, 1999, p. 15346.

10 D. E. Markov, J. C. Hummelen, P. W. M. Blom, and A. B. Sieval. Dynamics of Exciton Diffusion in Poly(p-phenylene vinylene)/Fullerene Heterostructures. *Physical Review B* **72** no. 4, 2005, p. 045216.

11 D. E. Markov, E. Amsterdam, P. W. M. Blom, A. B. Sieval, and J. C. Hummelen. Accurate Measurement of the Exciton Diffusion Length in a Conjugated Polymer Using a Heterostructure with a Side-Chain Cross-Linked Fullerene Layer. *J. Phys. Chem. A* **109** no. 24, 2005, p. 5266.

12 O. V. Mikhnenko, M. Kuik, J. Lin, N. van der Kaap, T.-Q. Nguyen, and P. W. M. Blom. Trap-Limited Exciton Diffusion in Organic Semiconductors. *Adv. Mater.* **26** no. 12, 2014, p. 1912.

13 A. J. Lewis, A. Ruseckas, O. P. M. Gaudin, G. R. Webster, P. L. Burn, and I. D. W. Samuel. Singlet Exciton Diffusion in MEH-PPV Films Studied by Exciton–Exciton Annihilation. *Org. Electron.* **7** no. 6, 2006, p. 452.

14 Y. Terao, H. Sasabe, and C. Adachi. Correlation of Hole Mobility, Exciton Diffusion Length, and Solar Cell Characteristics in Phthalocyanine/Fullerene Organic Solar Cells. *Appl. Phys. Lett.* **90** no. 10, 2007, p. 103515.

15 S. Banerjee, A. P. Parhi, S. S. K. Iyer, and S. Kumar. Method of Determining the Exciton Diffusion Length Using Optical Interference Effect in Schottky Diode. *Appl. Phys. Lett.* **94** no. 22, 2009, p. 223303.

16 M. C. Fravventura, J. Hwang, J. W. A. Suijkerbuijk, P. Erk, L. D. A. Siebbeles, and T. J. Savenije. Determination of Singlet Exciton Diffusion Length in Thin Evaporated C_{60} Films for Photovoltaics. *J. Phys. Chem. Lett.* **3** no. 17, 2012, p. 2367.

17 H. Najafov, B. Lee, Q. Zhou, L. C. Feldman, and V. Podzorov. Observation of Long-Range Exciton Diffusion in Highly Ordered Organic Semiconductors. *Nat. Mater.* **9** no. 11, 2010, p. 938.

18 S. D. Dimitrov and J. R. Durrant. Materials Design Considerations for Charge Generation in Organic Solar Cells. *Chem. Mater.* **26** no. 1, 2014, p. 616.

19 X. Wei, Z. V. Vardeny, N. S. Sariciftci, and A. J. Heeger. Absorption-Detected Magnetic-Resonance Studies Of Photoexcitations In Conjugated-Polymer/C_{60} Composites. *Physical Review B* **53** no. 5, 1996, p. 2187.

20 A. A. Bakulin, J. C. Hummelen, M. S. Pshenichnikov, and P. H. M. van Loosdrecht. Ultrafast Hole-Transfer Dynamics in Polymer/PCBM Bulk Heterojunctions. *Adv. Funct. Mater.* **20** no. 10, 2010, p. 1653.

21 D. Kekuda, J.-S. Huang, M. Velusamy, J. T. Lin, and C.-W. Chu. Dibenzo[f,h]thieno[3,4-b] Quinoxaline–Fullerene Heterojunction Bilayer Solar Cells with Complementary Spectrum Coverage. *Sol. Energy Mater. Sol. Cells* **94** no. 10, 2010, p. 1767.

22 P. D. Reusswig, D. N. Congreve, N. J. Thompson, and M. A. Baldo. Enhanced External Quantum Efficiency in an Organic Photovoltaic Cell via Singlet Fission Exciton Sensitizer. *Appl. Phys. Lett.* **101** no. 11, 2012, p. 113304.

23 A. Neuhold, H. Brandner, S. J. Ausserlechner, S. Lorbek, M. Neuschitzer, E. Zojer, C. Teichert, and R. Resel. X-Ray Based Tools for The Investigation of Buried Interfaces in Organic Electronic Devices. *Org. Electron.* **14** no. 2, 2013, p. 479.

24 O. V. Kozlov, F. de Haan, R. A. Kerner, B. P. Rand, D. Cheyns, and M. S. Pshenichnikov. Real-Time Tracking of Singlet Exciton Diffusion in Organic Semiconductors. *Phys. Rev. Lett.* **116** no. 5, 2016, p. 057402.

25 R. G. Gordon. Molecular Collisions and Depolarization of Fluorescence in Gases. *J. Chem. Phys.* **45** no. 5, 1966, p. 1643.

26 O. V. Kozlov, Y. N. Luponosov, S. A. Ponomarenko, N. Kausch-Busies, D. Y. Paraschuk, Y. Olivier, D. Beljonne, J. Cornil, and M. S. Pshenichnikov. Ultrafast Charge Generation Pathways in Photovoltaic Blends Based on Novel Star-Shaped Conjugated Molecules. *Adv. Energy Mater.* **5** no. 7, 2015, p. 1401657.

27 P. Peumans, A. Yakimov, and S. R. Forrest. Small Molecular Weight Organic Thin-Film Photodetectors and Solar Cells. *J. Appl. Phys.* **93** no. 7, 2003, p. 3693.

28 D. Qin, P. Gu, R. S. Dhar, S. G. Razavipour, and D. Ban. Measuring the Exciton Diffusion Length of C_{60} in Organic Planar Heterojunction Solar Cells. *physica status solidi (a)* **208** no. 8, 2011, p. 1967.

29 F. Monestier, J.-J. Simon, P. Torchio, L. Escoubas, B. Ratier, W. Hojeij, B. Lucas, A. Moliton, M. Cathelinaud, C. Defranoux *et al.* Optical Modeling of Organic Solar Cells Based on CuPc and C_{60}. *Appl. Opt.* **47** no. 13, 2008, p. C251.

30 T. Stübinger and W. Brütting. Exciton Diffusion and Optical Interference in Organic Donor–Acceptor Photovoltaic Cells. *J. Appl. Phys.* **90** no. 7, 2001, p. 3632.

31 L. A. A. Pettersson, L. S. Roman, and O. Inganäs. Modeling Photocurrent Action Spectra of Photovoltaic Devices Based on Organic Thin Films. *J. Appl. Phys.* **86** no. 1, 1999, p. 487.

32 G. J. Hedley, A. J. Ward, A. Alekseev, C. T. Howells, E. R. Martins, L. A. Serrano, G. Cooke, A. Ruseckas, and I. D. W. Samuel. Determining the Optimum Morphology in High-Performance Polymer-Fullerene Organic Photovoltaic Cells. *Nat. Commun.* **4**, 2013, p. 2867.

33 O. V. Mikhnenko, F. Cordella, A. B. Sieval, J. C. Hummelen, P. W. M. Blom, and M. A. Loi. Temperature Dependence of Exciton Diffusion in Conjugated Polymers. *The Journal of Physical Chemistry B* **112** no. 37, 2008, p. 11601.

34 J. W. Arbogast and C. S. Foote. Photophysical Properties of C_{70}. *J. Am. Chem. Soc.* **113** no. 23, 1991, p. 8886.

35 O. Runquing, R. A. Gerhardt, and R. J. Samuels. Structure and Electrical Properties of Undoped Oriented Poly(phenylene vinylene) Films. *Journal of Polymer Science: Part B: Polymer Physics* **42**, 2004, p. 98.

36 B. Verreet, P. E. Malinowski, B. Niesen, D. Cheyns, P. Heremans, A. Stesmans, and B. P. Rand. Improved Cathode Buffer Layer to Decrease Exciton Recombination in Organic Planar Heterojunction Solar Cells. *Appl. Phys. Lett.* **102** no. 4, 2013, p. 043301.

37 T.-M. Kim, H.-S. Shim, M.-S. Choi, H. J. Kim, and J.-J. Kim. Multilayer Epitaxial Growth of Lead Phthalocyanine and C_{70} Using CuBr as a Templating Layer for Enhancing the Efficiency of Organic Photovoltaic Cells. *ACS Appl. Mater. Interfaces* **6** no. 6, 2014, p. 4286.

38 J. D. A. Lin, O. V. Mikhnenko, J. Chen, Z. Masri, A. Ruseckas, A. Mikhailovsky, R. P. Raab, J. Liu, P. W. M. Blom, M. A. Loi *et al.* Systematic Study of Exciton Diffusion Length in Organic Semiconductors by Six Experimental Methods. *Materials Horizons* **1** no. 2, 2014, p. 280.

39 E. M. Y. Lee and W. A. Tisdale. Determination of Exciton Diffusion Length by Transient Photoluminescence Quenching and Its Application to Quantum Dot Films. *J. Phys. Chem. C* **119** no. 17, 2015, p. 9005.

40 B. Bernardo, D. Cheyns, B. Verreet, R. D. Schaller, B. P. Rand, and N. C. Giebink. Delocalization and Dielectric Screening of Charge Transfer States in Organic Photovoltaic Cells. *Nat. Commun.* **5**, 2014, p. 3245.

41 D. Cheyns, M. Kim, B. Verreet, and B. P. Rand. Accurate Spectral Response Measurements of a Complementary Absorbing Organic Tandem Cell with Fill Factor Exceeding the Subcells. *Appl. Phys. Lett.* **104** no. 9, 2014, p. 093302.

42 R. V. Bensasson, T. Hill, C. Lambert, E. J. Land, S. Leach, and T. G. Truscott. Triplet State Absorption Studies of C_{70} in Benzene Solution. *Chem. Phys. Lett.* **206** no. 1–4, 1993, p. 197.

43 A. Watanabe, O. Ito, M. Watanabe, H. Saito, and M. Koishi. Excited States of C_{70} and the Intersystem Crossing Process Studied by Picosecond Time-Resolved Spectroscopy in the Visible and Near-IR Region. *The Journal of Physical Chemistry* **100** no. 25, 1996, p. 10518.

44 K. Feron, W. Belcher, C. Fell, and P. Dastoor. Organic Solar Cells: Understanding the Role of Förster Resonance Energy Transfer. *Int. J. Mol. Sci.* **13** no. 12, 2012, p. 17019.

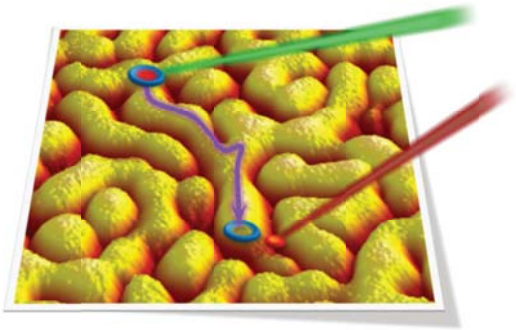

Chapter 3

Ultrafast Spectroscopy Reveals Bulk Heterojuction Morphology

Morphology of organic photovoltaic bulk heterojunctions BHJs – a nanoscale texture of the donor and acceptor phases – is one of the key factors influencing efficiency of organic solar cells. Detailed knowledge of the morphology is hampered by the fact that it is notoriously difficult to investigate by microscopic methods. Here we track the exciton harvesting dynamics in the fullerene acceptor phase from which subdivision of the fullerene domain sizes into the mixed phase (2-15 nm) and large (>50 nm) domains is readily obtained via the Monte-Carlo simulations. These results were independently confirmed by a combination of x-ray scattering, electron and atomic-force microscopies, and time-resolved photoluminescence spectroscopy. In the large domains, the excitons are lost due to the high energy disorder while in the ordered materials the excitons are harvested with high efficiency even from the domains as large as 100 nm due to the absence of low-energy traps. Therefore, optimizing of blend nanomorphology together with increasing the material order are deemed as winning strategies in the exciton harvesting optimization.

This Chapter is based on the following publication:
Almis Serbenta*, Oleg V. Kozlov*, Giuseppe Portale, Paul H.M. van Loosdrecht and Maxim S. Pshenichnikov, *Sci Rep* **6**, 36236 (2017); *denotes equal contribution

3.1 Introduction

Organic solar cells (OSCs) have steadily overcome the important threshold of 10% efficiency[1,2], which makes them a promising alternative to conventional silicon-based solar cells, in particular for niche applications. A typical OSC relies on the ability of strongly-bound photogenerated Frenkel excitons to diffuse to the interface between donor- and acceptor-type materials which provide a driving energy for the exciton splitting[3]. Due to the limited exciton diffusion length in organic materials (~10 nm)[3-5], there is a compelled compromise between the photon harvesting efficiency that requires 100-nm thick absorber layers, and exciton harvesting efficiency that necessitates relatively short exciton diffusion distances. Different approaches were utilized to maximize the exciton and photon harvesting efficiencies in organic devices, e.g. employing multi-layered structures with light-harvesting and charge-transport layers (*p-i-n* devices)[6] or creating interpenetrated polymer network[7]. Eventually, this paradox has been triumphantly resolved by utilizing the bulk heterojunction (BHJ) donor-acceptor architecture[8], which is the most widely used active layer for the OSCs nowadays.

BHJ is basically a nano-textured mixture of organic donor and acceptor materials. To maximize the efficiency of the OSC, the BHJ has to fulfill a number of requirements: i). sufficient thickness (~100 nm) for efficient photon harvesting, ii).fine intermixing (~10 nm) of the ingredients to ensure close-to-unity exciton harvesting, and iii). intercalated pathways to deliver the charges to the electrodes. The particular nanostructure of the BHJ, the BHJ morphology, is a crucial factor which decisively influences the efficiency of OSCs, and as such it has to be carefully optimized and characterized. So far, there is no solid theory to predict nor a systematic method to control the self-organization of BHJs, except for a few cases where general self-organization patterns were qualitatively computed[9,10]. These challenges have driven the development of morphology characterization techniques.

Standard BHJ characterization methods such as electron or X-ray microscopy/spectroscopy potentially provide an adequate spatial resolution and even the possibility to reconstruct the three-dimensional BHJ structure[11,12] by contrast enhancement techniques[13] such as energy filtering[14] and special sample preparation, including selective staining of one of the materials[15]. Sub-10 nm spatial resolution, however, is not always easily achieved due to the typically low-contrast combinations of donor:acceptor materials used in organic photovoltaics. Another powerful method to characterize the morphology is atomic force microscopy (AFM) with typical 10 nm spatial resolution.[16] However, AFM provides information only about the surface topography, which is not necessarily representative for the bulk morphology[17].

Aiming to overcome these limitations, complementary methods to control and optimize the morphology have been developed based on spectroscopic approaches, e.g. monitoring

photoluminescence (PL) of interfacial charge-transfer states[18], or measuring exciton diffusion by PL quenching[19] or pump-probe spectroscopy[20-22]. These methods are mainly focused on diffusion of the excitons in the polymer domains, which has been shown to provide valuable information on the polymer and/or fullerene domain sizes[19,21]. The sensitivity of these methods to determine the domain sizes is essentially limited to the delocalization size of polymer excitons, i.e. several repeating polymer units, or 5-10 nm[23,24].

Modern OSCs comprise high loadings of highly absorptive C_{70}-based fullerene acceptors (up to 98%)[25], which makes the fullerene absorption comparable or even higher than the absorption of the polymer. Consequently, a significant fraction of separated charges is generated after dissociation of the fullerene excitons via hole-transfer (HT) process[26,27]. Large fullerene domains readily observable with AFM[10,28] exceed by far the fullerene exciton diffusion length (<10 nm)[29,30] which results in significant losses in exciton harvesting. On the other hand, too fine polymer-fullerene intermixing (which is hard to observe by conventional characterization techniques) leads to increased non-geminate recombination of charges and lack of pathways to the electrodes for charge extraction[31,32]. Therefore, the fullerene phase morphology is as decisive for high efficiency OSCs as the polymer one, thereby calling for simple yet reliable characterization methods.

In the fullerene domains, the excitons are delocalized very moderately[33,34]. Therefore, the averaged time needed for the exciton to reach the donor/acceptor interface is determined by the fullerene domain size. The information about blend morphology can be extracted by excitation of the fullerene acceptor (e.g. soluble C_{70} derivative $PC_{71}BM$), and detecting the time that is taken for the exciton to diffuse to the fullerene:polymer interface where it dissociates into separated charges[34,35] (Figure 3.1). The latter are detected by e.g. the charge-induced (polaron) photo-induced absorption (PIA)[36] caused by the presence of positive charges (holes) at the polymer backbone. A number of previous studies[15,27,37-41] have reported correlations between fullerene exciton dynamics and blend morphology; however, no attempt has been made to extract information on the fullerene domain size.

In this paper, we use PIA for characterization of the nanoscale morphology of the fullerene domains in organic BHJs. We show for three polymers, regiorandom (RRa) P3HT, regioregular (RRe) P3HT and MDMO-PPV, selected as benchmark materials for exemplary cases of BHJ morphologies, that their blends with $PC_{71}BM$ contain the mixed phase with $PC_{71}BM$ domains typically up to 15 nm in size. The presence of large (>50 nm) $PC_{71}BM$ domains is also evidenced by a reduction of the efficiency of photon-to-charge harvesting. The blend composition was independently verified by GISAXS/GIWAXS, AFM, TEM/SEM and time-resolved photoluminescence (PL) techniques, with perfect matching of all the results. Unique spectroscopic signatures of subtle changes in BHJ morphology observed herein hold great

promise for applications of the proposed technique for on-the-fly characterization of fully functional devices.

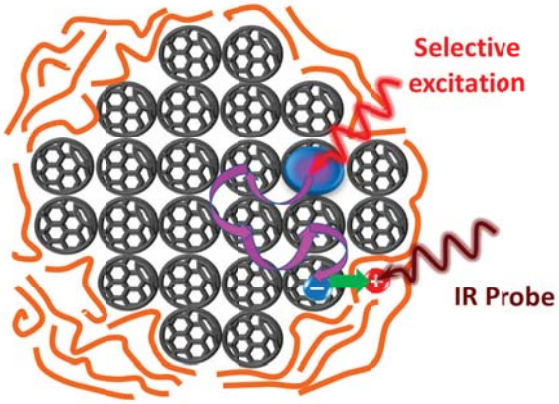

Figure 3.1 Conceptual representation of the spectroscopic technique used. The $PC_{71}BM$ phase is selectively excited by the ultrafast laser pulse (red). The photogenerated exciton (the blue-purple circle) diffuses to the interface where it dissociates into charges via hole transfer (green straight arrow) to the polymer phase (orange spaghetti). The number of accumulated holes at the polymer phase is probed by a delayed IR probe pulse via polaron-induced absorption.

3.2 Experimental Results

3.2.1 Exciton Dissociation Dynamics

Spectrally-selective excitation of $PC_{71}BM$ followed by spectrally-selective probing of the polymer allows spatial decoupling of the excitation and the probing processes and therefore obtaining the exciton travelling time. Selective photoexcitation of $PC_{71}BM$ was achieved by tuning the excitation wavelength below the bandgap of the polymer where $PC_{71}BM$ has a significantly higher absorption coefficient (680 nm for RRa-P3HT and RRe-P3HT, and 630 nm for MDMO-PPV, see Supporting Information (SI), Figure S3.1).

$PC_{71}BM$ exciton dissociation into charges was monitored by probing the charge-induced (polaron) PIA of the polymers in the mid-IR region[42,43]. For this, the wavelength of the probe IR pulse was set close to the maximum of the low-energy polaron band at ~3 μm for all three polymers (the polaron spectra for the polymers can be found elsewhere[43-45]). As the exciton is harvested (i.e. reaches the interface), the polaron absorption increases proportionally to the amount of charges (holes) at the polymer. By changing the delay between the excitation and the probe pulses, exciton diffusion preceding exciton dissociation is monitored in the real time[34,35]. Note that after having reached the interface, the excitons do not necessary produce long-lived separated charges but also the charge-transfer (CT) states which eventually either dissociate into

free charges or geminately recombine within a nanosecond timescale[38,46-49]. However, from the point of view of the PIA response, the exact route of the exciton dissociation makes no difference as even the (interfacially) bound charges produce a similar PIA signal[50]. Therefore, in both cases the gradual build-up of the PIA signal reflects the diffusion time needed for the $PC_{71}BM$ excitons to reach the interface.

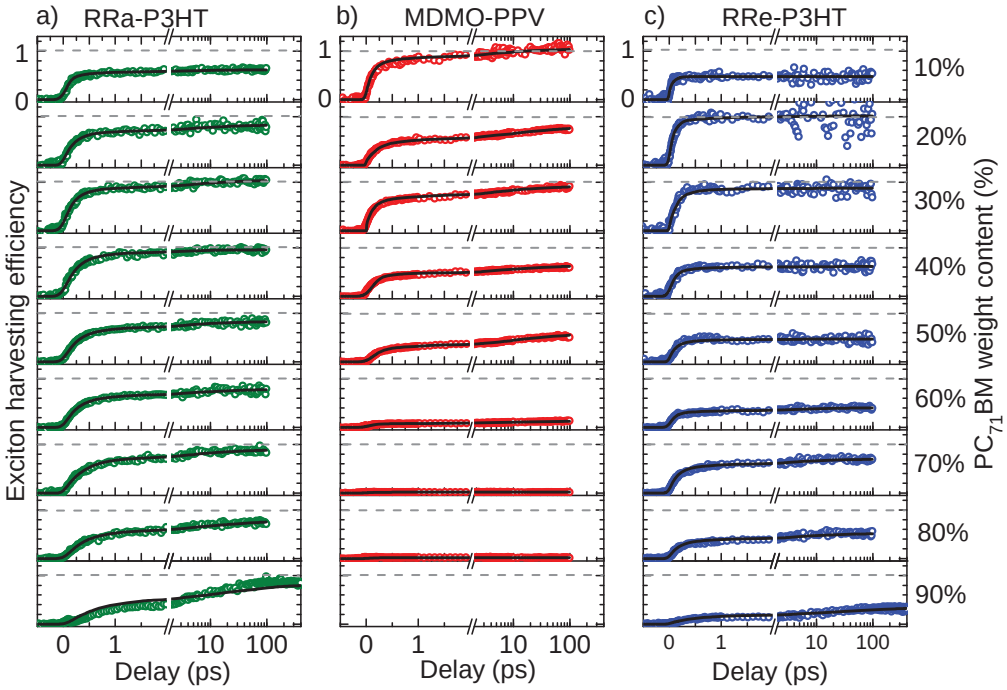

Figure 3.2 Normalized exciton harvesting efficiency as a function of excitation-probe delay for blends with different $PC_{71}BM$ weight fractions with (a) RRa-P3HT, (b) MDMO-PPV, and (c) RRe-P3HT. Symbols represent experimental data points after the polymer and $PC_{71}BM$ background subtraction and normalization to the $PC_{71}BM$ absorption at the excitation wavelength; the lines show the results of Monte-Carlo simulations. For each series, the charge yield was scaled to the maximal amplitude where unity relative efficiency of exciton harvesting was assumed (dashed grey lines, see Ref. [45] for details and unprocessed data). The 90% MDMO-PPV sample produced no polaron response and therefore the respective transient is not shown.

Dynamics of the exciton dissociation into charges are depicted in Figure 3.2 for the blends with different $PC_{71}BM$ weight ratios. The transients at low and high $PC_{71}BM$ loads were corrected for the weak pristine polymer response due to the finite excitation contrast, and IR response of the $PC_{71}BM$ excitons, respectively (see Ref. [45] for details and unprocessed data). All transients were also normalized to the $PC_{71}BM$ absorption at the excitation wavelength so that the transient amplitudes represent the charge yield per absorbed photon (i.e. exciton

harvesting efficiency) to allow for direct comparison of the transient amplitudes at different $PC_{71}BM$ loads.

The exciton harvesting dynamics for the blends with the three polymers have a number of similar features that can be summarized as follows: for the blends with low $PC_{71}BM$ content, the transients exhibit a large amplitude and a rapid rise time (<1 ps), whereas for the blends with high $PC_{71}BM$ content the amplitudes are decreased (except of the RRa-P3HT blends) while the rise of the response becomes substantially slower, up to 100 ps. The latter dynamics are assigned to the $PC_{71}BM$ exciton diffusion followed by the dissociation to charges at the $PC_{71}BM$:polymer interface via hole-transfer process[26,39,40]. We attribute increasing rise time to variations in the $PC_{71}BM$ domain size: the larger the $PC_{71}BM$ domains, the longer it takes for excitons to reach an interface and more excitons are lost.

The exciton harvesting dynamics are quite analogous in MDMO-PPV- and RRa-P3HT-based blends with low $PC_{71}BM$ content (<40%). The similar timescale of the initial signal build-up combined with the close-to-unity amplitudes point to the nanomorphology of the mixed phase with a phase separation of ~10 nm. At higher $PC_{71}BM$ concentrations a dramatic drop of the signal amplitude is observed with the signal reducing to naught at >70% $PC_{71}BM$ concentration. This indicates the formation of large $PC_{71}BM$ domains[51] with the size much larger that the exciton diffusion length (i.e. >>10 nm) separated from the mixed phase. The sharp decrease of the signal amplitude points to an increase of the volume fraction of the large domains, which reaches almost 100% in blends with >70% $PC_{71}BM$ content (i.e. the polymer and fullerene phases are fully separated).This is consistent with the known property of the MDMO-PPV-based blends to form large fullerene domains above a certain acceptor weight fraction[52-54].

For the RRe-P3HT-based blends, the exciton dissociation dynamics are different. For low $PC_{71}BM$ content (<40%), the initial build-up of the signal is significantly faster as compared to RRa-P3HT- and MDMO-PPV-based blends. This indicates extremely fine intermixing of polymer and $PC_{71}BM$ in the mixed phase, probably even isolated $PC_{71}BM$ molecules dispersed in the polymer matrix. At higher $PC_{71}BM$ loadings, the initial build-up slows down indicating the coarser intermixing within the mixed phase. Simultaneously, the decrease of the exciton harvesting is observed, similarly to the MDMO-PPV blends, but to a significantly smaller extent. The observed difference in dynamics between the RRa-P3HT and the RRe-P3HT originates from the different morphology: the blends with RRa-P3HT are completely amorphous while in blends with RRe-P3HT semi-crystalline domains of RRe-P3HT are formed prior to the aggregation of $PC_{71}BM$[55]. Hence, the $PC_{71}BM$ molecules are pushed outside the RRe-P3HT nanocrystals[56] to aggregate into the domains. Therefore, we assign exciton losses (Figure 3.2c) in the blends of RRe-P3HT with 40-60% of $PC_{71}BM$ to the formation of the $PC_{71}BM$ domains with sizes much larger than the exciton diffusion length.

At 70% of $PC_{71}BM$, the exciton harvesting suddenly increases which indicates an abrupt change in the RRe-P3HT:$PC_{71}BM$ nanostructure. Simultaneously, around these blend compositions the absorption shoulder in the red spectral region, which is associated with the absorption by the RRe-P3HT nanocrystals, vanishes (SI, Figure S3.2). Additionally, the GIWAXS data show a significant change of the blend morphology at 70% $PC_{71}BM$ contents (SI, Figure S3.3). All these point to disruption of the RRe-P3HT nanocrystals[57,58] for high $PC_{71}BM$ load[57].

The results of PIA measurements were independently verified with the time-resolved PL quenching technique[19,29]. Due to intrinsic limitations of the PL technique such as spectral overlap of PL from $PC_{71}BM$, polymers and CT states, and limited time resolution (~5 ps), it is nearly impossible to quantitatively characterize the $PC_{71}BM$ domain sizes. Nonetheless, the case of MDMO-PPV-based blends allows the direct comparison of PL quenching efficiency with exciton PIA harvesting efficiency, to produce an excellent match (Figure S3.7). This lends additional support to the proposed PIA method.

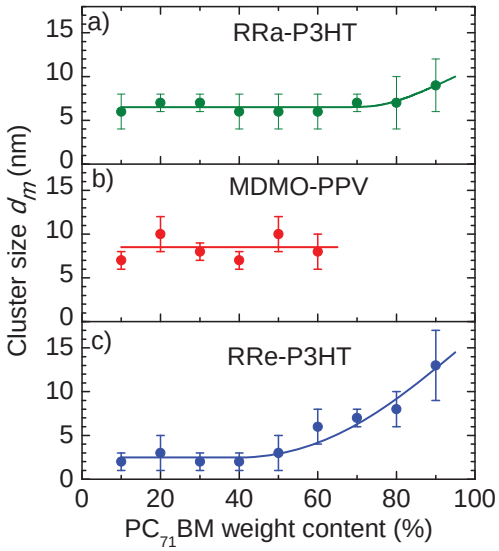

Figure 3.3 Domain size d_m of the mixed $PC_{71}BM$:polymer phase as a function of the blend composition for (a) RRa-P3HT, (b) MDMO-PPV and (c) RRe-P3HT blends. Symbols are results of Monte-Carlo simulations while the solid lines are guides to the eyes. Error bars are derived from uncertainty of the Monte-Carlo simulations.

Summarizing the discussion above: despite some similarities, the three $PC_{71}BM$:polymer blends exhibit very different exciton harvesting dynamics as a function of the blend composition. Interestingly, the exciton harvesting is sensitive to subtle changes in the morphology as is for instance shown by the changes of the dynamics upon disappearance of nanocrystals in

RRe-P3HT. This clearly indicates that a more detailed insight in the characteristic sizes of the mixed phases and the $PC_{71}BM$ domains can be obtained through extensive modeling of the experimental data.

3.2.2 Characterization of the Nanomorphology from Monte Carlo Simulations

Monte Carlo (MC) simulations for modeling exciton dynamics have the important advantage over analytical description[4,5,29,59] that they allow for inclusion of energetic disorder[60,61], which cannot be neglected for the solvent-processed materials and blends. We modeled the exciton diffusion as random hopping in disordered $PC_{71}BM$ domains of a mixed phase of spherical domains with diameter d_m and large domains with larger diameter d_c and a volume fraction f (see section 3.4 "Methods" for details).

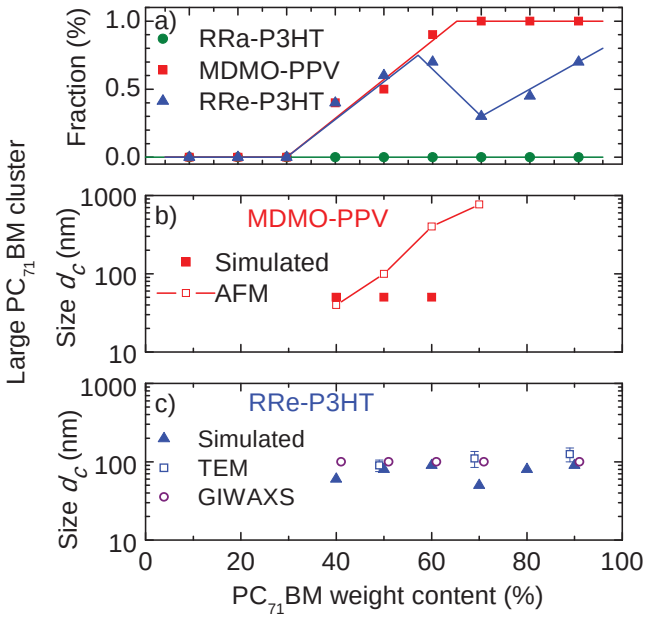

Figure 3.4 (a) Volume fraction of the $PC_{71}BM$ domains and (b,c) sizes of the $PC_{71}BM$ large domains for MDMO-PPV and RRe-P3HT as obtained from the MC simulations (solid symbols). The solid symbols represent the minimal values obtained from MC simulations while the open symbols represent experimental data obtained from the AFM (red squares), TEM (blue triangles) and GIWAXS (purple circles) measurements. The GIWAXS data represent the minimal size of the $PC_{71}BM$ domains. Solid lines are guides to the eye. The data in (c) were slightly displaced from the exact concentration for clarity. AFM and TEM results are taken from Ref. [45].

The MC simulations reproduce the experimental data fairly well (Figure 3.2, solid lines). The estimated domain size in the mixed phase varies from 2 nm to 15 nm depending on the blend composition and the particular polymer (Figure 3.3). In the low (<40%) $PC_{71}BM$ load blends

only the mixed phase is present with typical $PC_{71}BM$ domain sizes of 6-8 nm in amorphous RRa-P3HT and MDMO-PPV polymers, and 2-3 nm in RRe-P3HT-based blends. With the increase of $PC_{71}BM$ load, coarsening of the mixed phase is observed in RRa-P3HT and RRe-P3HT based blends. In contrast, in MDMO-PPV blends higher $PC_{71}BM$ load does not result in any significant change in domain sizes of the mixed phase but leads to explosive growth of extremely large $PC_{71}BM$ domains (up to 1 μm, Figure 3.4), which results in dramatic decrease of the PIA signal (Figure 3.2b). Interestingly, the typical domain size of the mixed phase does not significantly increase with increasing of $PC_{71}BM$ even when the large domains begin to form. In contrast, in MDMO-PPV blends with high $PC_{71}BM$ contents the fine mixed phase coexists with the separated $PC_{71}BM$ domains, which volume share depends on $PC_{71}BM$ concentration (Figure 3.4a).

The sizes of large $PC_{71}BM$ domains obtained from the MC simulations and independently from AFM for the MDMO-PPV blends and from TEM for the RRe-P3HT blends (see Ref. [45] for details) are summarized in Figure 3.4b. MC simulations yield only the minimal sizes of the large $PC_{71}BM$ domains from the long-time exciton harvesting dynamics, while the volume fraction is straightforwardly obtained from decrease of the signal amplitude. The sizes of the large domains derived from the MC simulations match reasonably well the independently measured values for the RRe-P3HT based blends. In the MDMO-PPV case the deviations are quite substantial because for the proposed technique 0.1 and 1 μm size domains look identical as no excitons are harvested from either of them. Note, however, that the $PC_{71}BM$ domain sizes in the mixed phase (Figure 3.3) lay below either attainable resolution (AFM) or contrast (TEM) of the conventional methods but are readily captured by spectroscopic means.

For the P3HT:$PC_{71}BM$ blends with high $PC_{71}BM$ loadings (>40%), the blend composition was also independently verified by GISAXS and GIWAXS (SI, Figure S3.3)[62]. For the mixed phase, the domain sizes of 2 nm and 15 nm with different shares were observed which is in good agreement with the current two-domain model (Figure 3.3c). The sizes of large domains were estimated from GISAXS as >100 nm which matches perfectly both results obtained by TEM and from MC simulations (Figure 3.4b).

3.2.3 Influence of Energetic Disorder

With the MC machinery in hand, we studied the influence of energetic disorder on the exciton losses in large $PC_{71}BM$ domains, by performing simulations of exciton harvesting from 1-100 nm domains (Figure 3.5a, red line) with and without disorder. If the phase intermixing is fine (<15 nm, i.e. similar to the mixed phase), almost 100% of excitons are harvested in both cases, i.e. the disorder does not play any crucial role. The reason is two-fold. First, with such small domain sizes, the significant fraction of excitons is generated in the close proximity to the

interface and dissociate into charged immediately with 100% efficiency. Second, even those excitons that are generated deeper in the $PC_{71}BM$ domains, reach the interface faster (in ~400 ps for 15 nm domain size, Figure 3.5b) than the exciton lifetime of 650 ps.

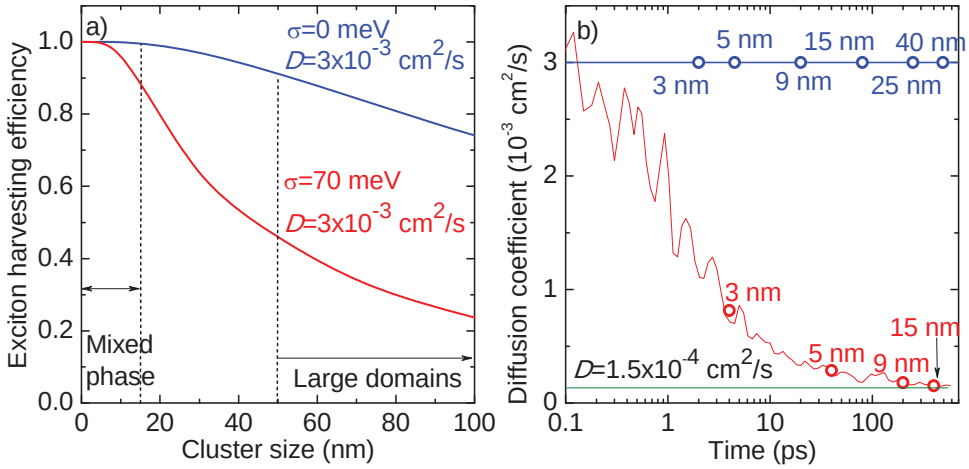

Figure 3.5 (a) Simulated exciton harvesting efficiency *vs.* domain size at room temperature. The harvesting efficiencies for $D_0=3\cdot10^{-3}$ cm^2/s (which corresponds to the initial diffusion coefficient in $PC_{71}BM$ obtained from simulations) with and without energetic disorder are shown in red in blue, respectively. The areas of the mixed phase and large domains are also indicated. (b) Simulated exciton diffusion coefficient dependence on time for energy disorder of σ=70 meV (red line) and without energy disorder (blue line). In the case of disorder, the diffusion coefficient decreases due to the exciton energy downhill migration as subsequent trapping. Stabilized diffusion coefficient of $D=1.5\cdot10^{-4}$ cm^2/s is shown by green line. Open circles indicate the domain size from which the excitons are extracted at the given time.

In contrast, the exciton harvesting efficiency rapidly decreases in the large domains (>50 nm), because the exciton diffusion time needed to reach the interface becomes comparable with the exciton lifetime. This is a direct consequence of ten-fold decrease of the exciton diffusion coefficient within 100 ps (Figure 3.5b). The diffusion coefficient at long times (>100 ps) changes only insignificantly and amounts to $D\sim1.5\cdot10^{-4}$ cm^2/s, which is consistent with the earlier report[29]. This value can be safely used to estimate the exciton diffusion length since the exciton lifetime (650 ps) is much larger than the time needed for diffusion coefficient equilibration (~100 ps). However, the exciton dynamics at the early times (<10 ps) are determined by the highly non-equilibrium D (Figure 3.5b) which explains fast exciton harvesting from the mixed phase (<10 ps for 3 nm domain size).

In materials with negligible energy disorder, where the diffusion coefficient does not depend on time, the excitons are harvested extremely efficiently (>75%) even from the $PC_{71}BM$ domains as large as 100 nm (Figure 3.5a, blue line). This fact explains high efficiency of vacuum-deposited TPTPA/C_{70} solar cells with >95% content of C_{70} with extremely low disorder of 5

meV[25,34]. Interestingly, in the disordered medium exciton harvesting is limited not only by dynamical decrease of *D*, but also by the presence of low-energy trap sites. As the result, the exciton is trapped for a long time, which significantly decreases the diffusion length (SI, Figure S3.8). Thus, even though the excitons can be effectively harvested in a BHJ based on disordered medium with fine phase intermixing, decreasing of the energy disorder seems to be more favorable for the blend optimization as in this case larger domain sizes lead to smaller interface area and, therefore, decreased non-geminate charge recombination.

3.3 Conclusions

The exciton harvesting dynamics from the $PC_{71}BM$ phase have been successfully obtained by a PIA technique and modeled by the Monte-Carlo simulations to yield valuable information on the BHJ morphology. The BHJ blends studied herein contain mixed-phase $PC_{71}BM$ domains of the size of several nanometers (up to 15 nm) as well as the large $PC_{71}BM$ domains with sizes exceeding 50 nm. These findings are fully consistent with the paradigm of a hierarchical BHJ morphology[56,63,64] and were independently confirmed by GISAXS/GIWAXS, AFM, TEM/SEM and time-resolved PL measurements. Note that due to a number of fundamental limitations, the PL technique is not capable to deliver similar quantitative information.

Significant differences of BHJ morphology in terms of formation of the mixed phase and the large (> 50 nm) $PC_{71}BM$ domains have been observed for the blends with donor polymers of RRa-P3HT, MDMO-PPV, and RRe-P3HT. The phase separation of the mixed phase varies from 2 to 15 nm in $PC_{71}BM$:RRa/RRe-P3HT blends and is ~7 nm in $PC_{71}BM$:MDMO-PPV blends. RRa-P3HT based blends demonstrate fine intermixing without large $PC_{71}BM$ domains within the whole range of $PC_{71}BM$ loads investigated. In contrast, the MDMO-PPV and RRe-P3HT based blends exhibit the formation of large $PC_{71}BM$ domains. Observed disruption of the RRe-P3HT nanocrystals at the $PC_{71}BM$ load from 60% to 70%, verified by GIWAXS, underlines the high sensitivity of the technique used. We have also demonstrated that the exciton losses in the large $PC_{71}BM$ domains are related to a high energetic disorder of ~70 meV and in particular to the low-energy trap sites. Decreasing the energetic disorder (e.g. by applying vacuum deposition techniques)[34] dramatically improves the harvesting efficiency from the fullerene domains. This suggests that increasing the material order is a winning strategy in the exciton harvesting optimization.

The main simplification in the MC simulations is an assumption of two types of the spherically shaped domains. Although realistic morphology is much more complex[29,52], this simple model captures the essential aspects of the $PC_{71}BM$ morphology, with two different kinds of domains being among them. Modern computational methods of predicting more realistic BHJ patterns[9,10] could readily incorporate the MC approach used herein. Next, the domain size of the

mixed phase can be slightly underestimated due to the exciton delocalization among 4-5 $PC_{71}BM$ molecules[33,34]. Additionally, the possibility of the long-range hole transfer from next to the outer layer of $PC_{71}BM$ domains[65,66] cannot be ruled out. The observed increase of hole transfer time with increasing of $PC_{71}BM$ content and therefore domain size (SI, Figure S3.10) is in line with this supposition. Nevertheless, all latter effects do not have serious influence on the results and could be readily accounted for in the MC simulations.

Another concern is the possible dependence of the kinetic parameters (i.e. exciton lifetime, hopping time and the disorder) on the $PC_{71}BM$ domain size. We thoroughly tested stability of domain sizes retrieval for both mixed phase and large domains with respect to the kinetic parameters of the model (SI, Figure S3.11, Figure S3.12) and found that vast variations of them do not result in substantial changes of the $PC_{71}BM$ domain sizes. This is attributed to extremely fast extraction of the excitons from the mixed phase. Therefore, the obtained domain sizes for the mixed phase are reliable even if the kinetic parameters are different from the bulk $PC_{71}BM$. On the other hand, the large $PC_{71}BM$ domains behave as the bulk material so that the parameters derived from the PL measurements can be safely used.

The charge generation after excitation of $PC_{71}BM$ is especially important for modern solar cells involving narrow bandgap polymers, where high $PC_{71}BM$ loadings are used and the fullerene becomes the main absorber in the green-blue region of the spectrum. In this work, we used the polymers with relatively wide bandgap to selectively excite $PC_{71}BM$ and therefore to simplify the analysis to demonstrate the proof of concept. In the case of modern low-bandgap donors, selective excitation of $PC_{71}BM$ is hardly achievable even in the blue where $PC_{71}BM$ absorption increases, and both donor and $PC_{71}BM$ PIA responses have to be considered. As the excitons from donor phase dissociate at a 100-fs timescale[39,40,46,50,67,68], i.e. significantly faster than any diffusion-delayed exciton dissociation, the donor PIA response can be considered as step-like function (SI, Figure S3.13). In addition, transient anisotropy might be used as an extra contrast parameter to distinguish between the donor and acceptor PIA responses[26,47]. Overall, the proposed method constitutes a first step towards PIA spectroscopy as a tool that provides a valuable feedback on optimization of BHJ morphology and can be expanded to modern donor materials such as more efficient polymers[1,40,69] and small organic molecules[38,70,71].

3.4 Methods

For detailed description of sample preparation, PIA and TEM measurements (performed by A. Serbenta, University of Groningen, the Netherlands) and X-ray measurements (performed by G. Portale, University of Groningen, the Netherlands) see Ref. [45].

PL Measurements

Time-resolved PL transients were measured by a Hamamatsu C5680 streak-camera system after 650 nm excitation (selected from the white light supercontinuum generated from a Mira Ti:sapphire laser output in a Newport SCG-800 hollow fiber), with time resolution of ~10 ps. The color glass longpass filter RG695 was placed before the polychromator to filter the stray excitation light.

Monte-Carlo simulations

In the MC simulations, the mixed phase was modelled as spherical $PC_{71}BM$ domains surrounded by the polymer (Figure 3.1). The coexistence of the mixed phase and large $PC_{71}BM$ domains[72] was taken into account by including two types of domains with different sizes. Exciton diffusion was simulated as random hopping between discreet $PC_{71}BM$ molecules in the cubic grid cells. The boundaries of the domains were determined as spheres of variable diameters d_m(for the mixed phase)and d_c (for the large $PC_{71}BM$ domains), $d_m<d_c$.

Energetic disorder of the potential energy landscape of $PC_{71}BM$ was taken into account by a Gaussian disorder model[73]. Energies within the Gaussian distribution, with standard deviation σ, were randomly assigned to the $PC_{71}BM$ molecules. Initially, an exciton with finite effective lifetime $T_1$is randomly placed in one of the two domains with probability f which reflects the volume ratio of the mixed phase to the large domains. At each step, the exciton hops into a random direction by one grid point with hopping time τ and hopping probability p_{ij} which depends on the energies of the starting E_i and target E_j grid points:

$$p_{ij} = \begin{cases} 1 & if\ E_i \geq E_j \\ exp\left(-\frac{E_j - E_i}{kT}\right) & if\ E_i < E_j \end{cases} \tag{3.1}$$

where kT is the Boltzmann factor. Finally, exciton dissociation into charges at the surface of $PC_{71}BM$ domain occurs with a finite HT time τ_{ht}[26], after which the resulting hole begins to contribute to the PIA signal. The total PIA signal was convoluted with a Gaussian apparatus function of 70-100 fs width.

The exciton lifetime T_1, hopping time τ and energy disorder parameter σ were obtained independently from the photoluminescence data of $PC_{71}BM$ films with TPTPA quenchers as T_1=650 ps, τ=0.3 ps, and σ=70 meV (see Figure S3.14, Figure S3.15). The fact that a single set of kinetic parameters is needed to describe as high range of quencher concentrations as 0.0125-50%, signifies similar exciton diffusion in $PC_{71}BM$ domains of different sizes. Therefore, the remaining fit parameters for each sample are the $PC_{71}BM$ domain sizes d_m and d_c, the hole transfer time τ_{ht} and the volume fraction of the large domains f. Each of the four fit parameters is

responsible for the particular feature of the PIA transients which makes them independent in the fitting procedure. The early-time dynamics (<0.5 ps) are mainly driven by the HT process characterized by the hole transfer time τ_{ht} (SI, Figure S3.10). The intermediate time window (1-10 ps) accounts for exciton dissociation from the mixed phase and is determined by the size of small domains d_m. Size of the large domains d_c is responsible for the later dynamics (>10 ps), while the volume fraction f determines the PIA transient amplitude. To collect the necessary statistics, each simulation was run 1000 times for each sample (3000 times for MDMO-PPV:$PC_{71}BM$ blend with 60% $PC_{71}BM$ content). The dependence of the three-dimensional exciton diffusion coefficient on time was obtained from the exciton displacement as:

$$D(t) = \frac{1}{6}\frac{\partial\langle L^2(t)\rangle}{\partial t}, \tag{3.2}$$

where L(t) is the exciton displacement and <> denotes averaging over the whole exciton ensemble.

3.5 Supporting Information

3.5.1 Absortpion Spectra

Figure S3.1 shows the red flanks of the absorption spectra of the three pristine polymers (orange curves) and $PC_{71}BM$ (brown curves). Based on the highest contrast between $PC_{71}BM$/polymer excitations (i.e. the ratio of the absorption spectra of the $PC_{71}BM$ and the polymer, green lines), the excitation wavelength was selected as 680 nm for both RRa-P3HT and RRe-P3HT mixed with $PC_{71}BM$, and 630 nm for $PC_{71}BM$:MDMO-PPV.

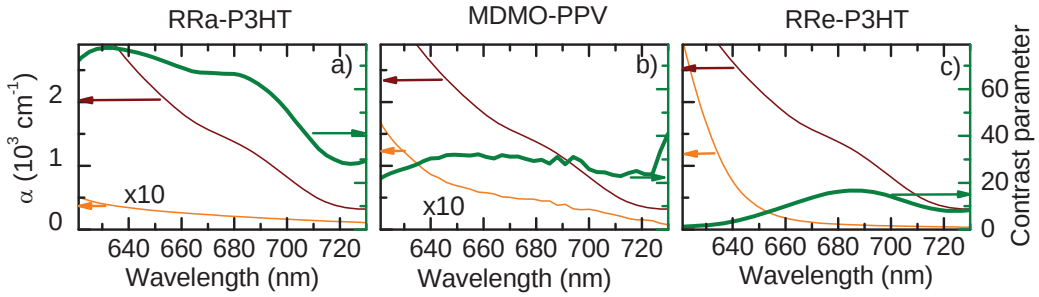

Figure S3.1 Absorption coefficient of $PC_{71}BM$ (brown lines) and polymers (orange lines), and the ratio (contrast parameter) between $PC_{71}BM$ and polymer absorption (green lines) for the three polymers studied: (a) RRa-P3HT, (b) MDMO-PPV, (c) RRe-P3HT. Absorption coefficients of RRa-P3HT and MDMO-PPV are multiplied by a factor of 10.

Figure S3.2 shows the red flank of absorption spectra of RRe-P3HT blends. The disappearance of RRe-P3HT absorption shoulder at 620 nm due to the broken crystallinity[57,58] when the $PC_{71}BM$ content changes from 60% to 70% is observable.

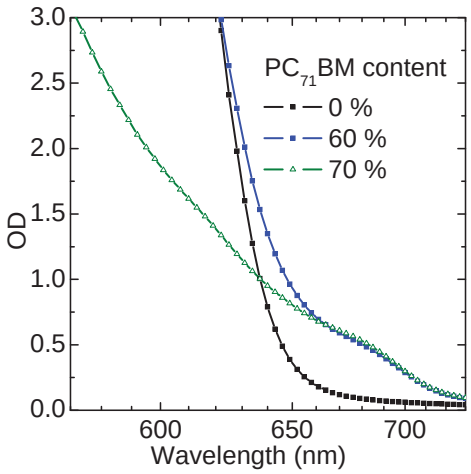

Figure S3.2 Linear absorption of RRe-P3HT:$PC_{71}BM$ blends with different fullerene content (indicated). Note the disappearance of RRe-P3HT absorption shoulder at ~620 nm when $PC_{71}BM$ load changes from 60% to 70%.

3.5.2 X-Ray Measurements

Morphology of RRe-P3HT-based samples with $PC_{71}BM$ loadings of >40% was independently verified by grazing-incidence small-angle X-ray scattering (GISAXS) and grazing-incidence wide-angle X-ray scattering (GIWAXS*)* measurements (performed by G. Portale, University of Groningen, the Netherlands). The results are summarized in Table S3.1.

Table S3.1 Summary of the RRe-P3HT:$PC_{71}BM$ film internal structures extracted from the GISAXS and GIWAXS analysis.

$PC_{71}BM$ content (%)	Mixed phase size 1 (nm)	Mixed phase size 2 (nm)	Mixed phase size 3 (nm)	Large domain size (nm)
40	1.8	15	-	>100
50	1.9	15	-	
60	1.9	14.5	-	
70	2.1	14	23.8	
90	2.1	-	-	

Both the P3HT crystalline content and the fraction of small 2 nm $PC_{71}BM$ domains show a linear behavior with increasing the $PC_{71}BM$ content up to 60% (Figure S3.3). Above 70%, a

strong deviation from the linearity occurs. This deviation is assigned to the broken crystallinity of P3HT domains and formation of amorphous P3HT phase (see also Figure S3.2), in accordance with the literature [57,58]. For the $PC_{71}BM$ 2 nm fraction, a slight deviation from linearity occurs for blends with >60% $PC_{71}BM$ content, which indicates gradual formation of large $PC_{71}BM$ domains (be that 15 nm or >100 nm in size). For the 90% $PC_{71}BM$ blend, the fraction of 2 nm domains drop significantly indicating sufficient amount of the large domains formed, which is in line with dramatic decrease of PIA signal (Figure 2c in the Main Text).

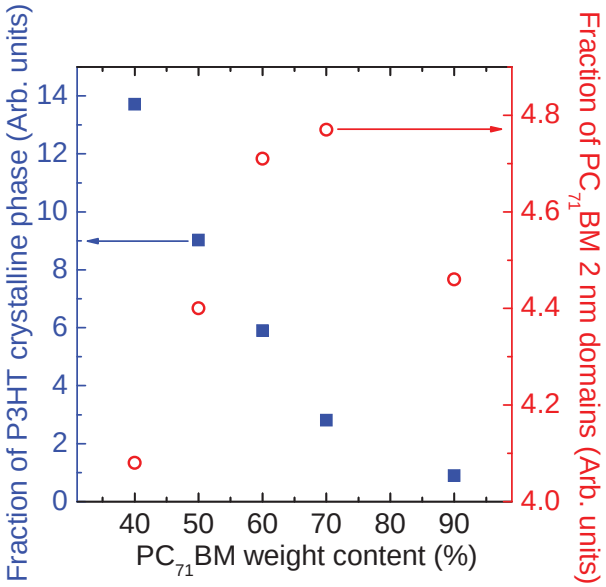

Figure S3.3 Relative fractions of the P3HT crystalline phase (black) and of the $PC_{71}BM$ 2 nm domain phase (red) as a function of the $PC_{71}BM$ content in the blend.

3.5.3 Monte-Carlo Modelling With the X-Ray Data as an Input

In the Main Text we model the mixed phase as small $PC_{71}BM$ domain with a single size spheres. According to the X-ray measurements, for the RRe-P3HT:$PC_{71}BM$ blends the mixed phase consists of domains with characteristic sizes of 2 nm and 15 nm with different shares (Table S3.1). In this case, the output of the simulations reflects the effective domain size which lies between 2 and 15 nm and depends on the participation ratio of the two domains (Figure 3.3c in the Main Text). We performed the MC simulations with mixed phase modelled as two spherical domains of 3 and 15 nm with different shares as the X-ray data suggest (3 nm size instead of 2 nm was chosen due to the limitation of MC simulations). The simulations perfectly describe the transients and show increasing of the fraction of 15 nm domains for higher $PC_{71}BM$

concentration (Figure S3.4). As the exact choice of the model does not affect the dynamics nor the exciton harvesting efficiency, it does not play any role for the solar cell operation.

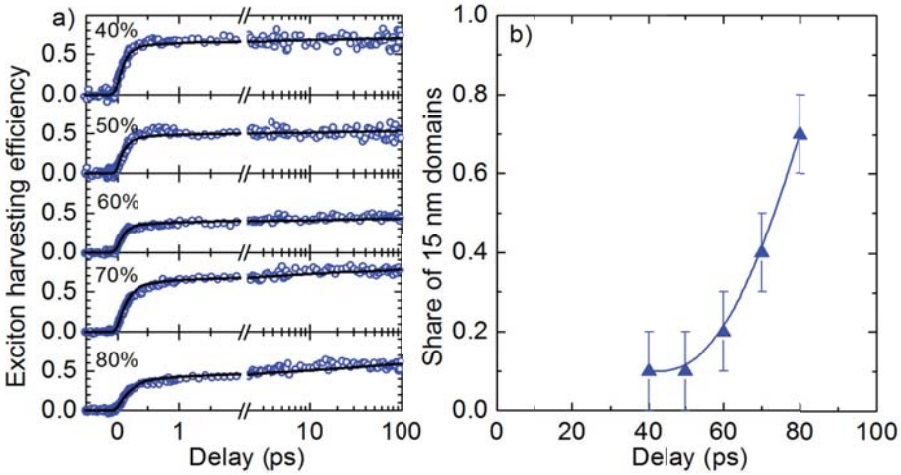

Figure S3.4 (a) MC simulations for RRe-P3HT:$PC_{71}BM$ blends with different $PC_{71}BM$ content (indicated) with mixed phase modelled as 3 nm and 15 nm spheres. The open symbols represent experimental data while the solid lines show simulated transients. (b) Share of 15 nm domains in the mixed phase as resulted from the MC modelling.

3.5.4 PL Quenching

The results of PIA measurements were independently verified by the PL quenching measurements. Representative time-integrated spectra of the samples based on three different polymers are shown in Figure S3.5. Generally, the spectra of the BHJ blends consist of three contributions: $PC_{71}BM$ PL, polymer PL, and PL of the charge-transfer (CT) state[18,74].

In RRa-P3HT-based blends, red flanks of PL spectra of RRa-P3HT and $PC_{71}BM$ are very close (Figure S3.5a). Besides, CT-state PL develops already at low $PC_{71}BM$ concentrations. However, high contrast of $PC_{71}BM$ excitation (Figure S3.1) and PL spectral filtering in the 680-710 region allow for extraction of the PL signal that is mainly assigned to $PC_{71}BM$ PL (Figure S3.6a). The transients clearly show that PL is strongly quenched, down to the width of the apparatus function at all $PC_{71}BM$ concentrations except 90% where slight elongation of the PL transient is observed. These results are in line with those derived from PIA (Figure 3.3 of the main text) where strong quenching is predicted because of fine intermixing of RRa-P3HT and $PC_{71}BM$ in the blends. Nonetheless, due to aforementioned reasons PL experiments provide no ground for deriving any qualitative information on the $PC_{71}BM$ domain size.

MDMO-PPV based blends suffer from the complications similar to the RRa-P3HT case (Figure S3.5b). However, because the $PC_{71}BM$ domains are much larger, time-resolved PL does provide some useful information (Figure S3.6b). PL transients demonstrate increased PL

quenching as $PC_{71}BM$ content decreases, in full correspondence to Figure 3.3 of the main text. Both PIA and PL quenching methods demonstrate similar exciton harvesting efficiencies (Figure S3.7) which proves the validity of the PIA measurements. Note that the initial amplitude of the transients decreases at lower $PC_{71}BM$ concentrations because the time-resolved PL measurements cannot catch PL originating from small $PC_{71}BM$ domains due to limited time resolution (~ 10 ps). This is in high contrast with the PIA measurements (Figure 3.2 of the main text) where all the times from 0.1 to 100 ps are readily captured.

Finally, for the RRe-P3HT-based blends, the PL spectra are also strongly contaminated by the polymer emission (Figure S3.5c, green lines). However, due to low contrast of $PC_{71}BM$ excitation, low $PC_{71}BM$ PL quantum yield (QY) but high PL QY of RRe-P3HT, it is virtually impossible to deconvolute $PC_{71}BM$ PL from the total PL. At blends with <60% $PC_{71}BM$ concentration, the PL is mainly originates from P3HT crystals (note increase of PL amplitude for those blends in Figure S3.6c). As a result, PL of the large $PC_{71}BM$ domains can barely be seen only at 90% $PC_{71}BM$ concentration. This excludes deriving any quantitative information of the $PC_{71}BM$ domain size, in contrast with the PIA measurements (see Figure 3.3 of the main text).

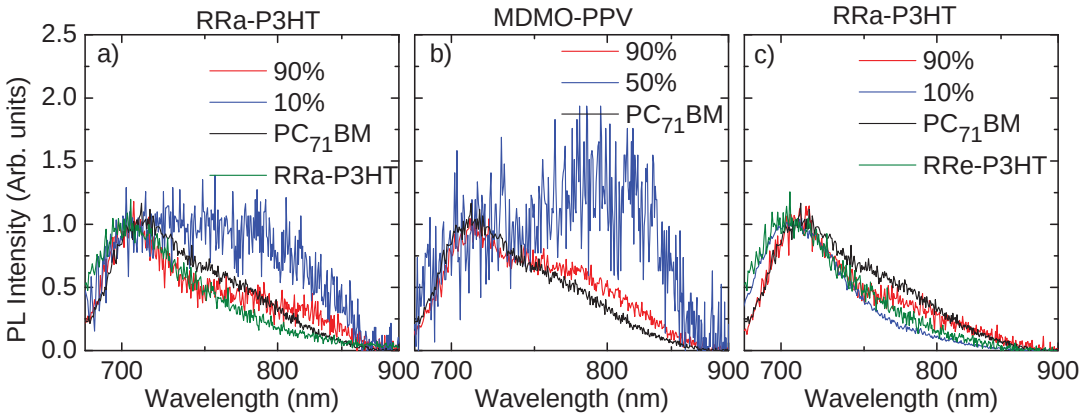

Figure S3.5 Representative PL spectra after 650 nm excitation for (a) RRa-P3HT, (b) MDMO-PPV and (c) RRe-P3HT based blends with different $PC_{71}BM$ concentrations (indicated). The spectra are normalized to $PC_{71}BM$ maximum at 710 nm. Blue flanks of the spectra are cut off by a long-pass RG695 filter placed before the polychromator to filter out the excitation light.

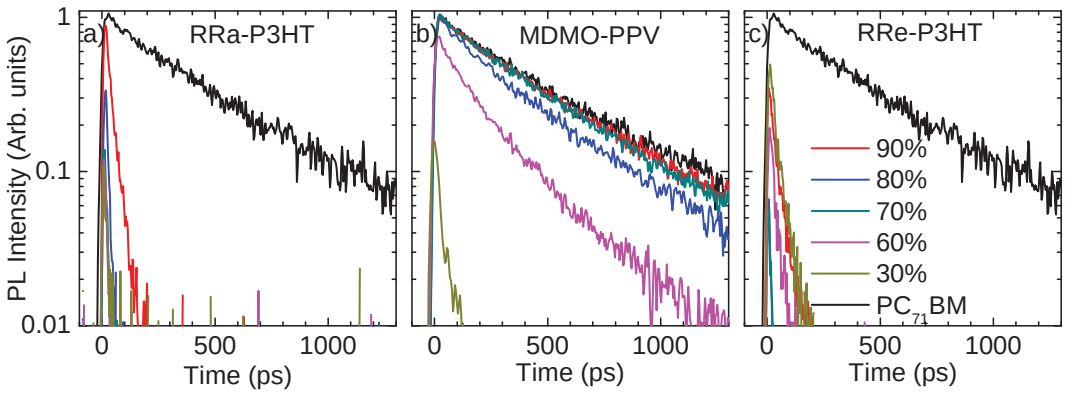

Figure S3.6 PL transients for (a) RRa-P3HT, (b) MDMO-PPV and (c) RRe-P3HT based blends with $PC_{71}BM$ after 650 nm excitation. Concentrations of $PC_{71}BM$ are indicated in the legend. Transients are integrated in the 680-710 (a,c) or 680-730 (b) nm spectral ranges and normalized by the blend absorption at the wavelength of excitation.

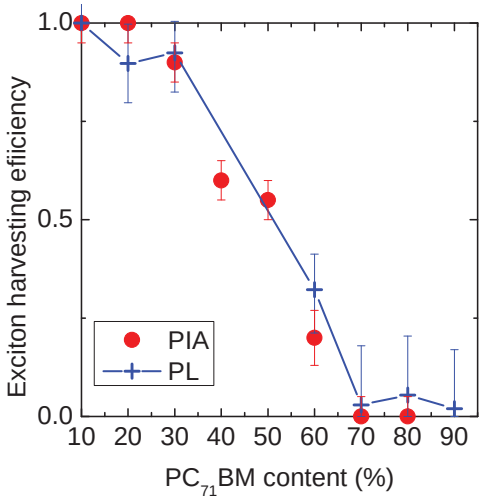

Figure S3.7 Exciton harvesting efficiency within first 100 ps as obtained from PIA (dots) and PL (crosses/line) measurements.

3.5.5 Influence of Energetic Disorder

The energetic disorder has a great influence on the exciton dynamics as it creates low-energy trap states which significantly slow exciton diffusion. Moreover, the presence of neighboring sites with different energies makes the probability of hopping to different directions unequal thereby effectively reducing the dimensionality of the diffusion process. As a reminder, the difference between diffusion coefficient in 3D and 1D is $\sqrt{3}$.

Figure S3.8 shows representative trajectories of the excitons with infinite lifetime in media with and without disorder obtained from the MC simulations (parameters of the simulations are given in the Main Text). Without energetic disorder, the diffusion process is uniform in time with each subsequent step bringing the exciton to the new site. In the disordered medium, plateaus are formed on the trajectories where the exciton spends more time in the low-energy sites from where it is hard to escape. This leads to shorter displacements and a wide distribution of the average hopping times (Figure S3.9) in contrast to the no-disorder case where the exciton spends identical times on each site.

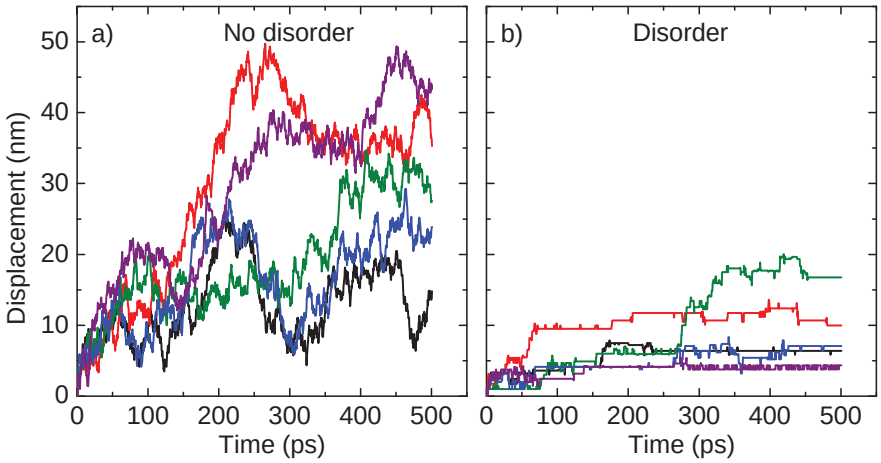

Figure S3.8 Simulated displacement of 5 different excitons without (a) and with (b) energetic disorder. Initial diffusion coefficient is $D=4.5\cdot10^{-3}$ cm^2/s, energetic disorder in (b) is σ=70 meV and the room temperature kT=26 meV.

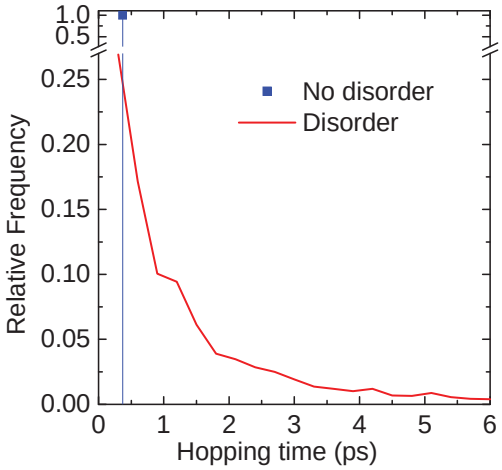

Figure S3.9 Distribution of average exciton hopping times with (red line) and without (blue dot) energetic disorder. Without the disorder, the distribution is a δ-function.

3.5.6 Hole transfer times

To reproduce the short-time part of the experimental data, the finite hole transfer (HT) time was set as free parameter for each sample in the MC simulations. The resulted dependence of the HT time on the $PC_{71}BM$ content is shown in Figure S3.10. The HT time gradually decreases from ~0.1 ps to ~0.5 ps with the increase of $PC_{71}BM$ concentration (and hence the domain size). We attribute this behavior to the long-range hole transfer [65,66,75] from next to the outer layer of $PC_{71}BM$ domains, which probability increases with increasing of the fullerene domain size (see Main Text). However, the effect of exciton screening in the large fullerene domains and/or exciton delocalization cannot be ruled out as also influencing the HT time. We emphasize that the ultrafast component of HT time in the 30-50 fs range [26,76] was clearly observed in these experiments but instead of treated separately was included in the apparatus function in the MC simulations for the sake of simplicity.

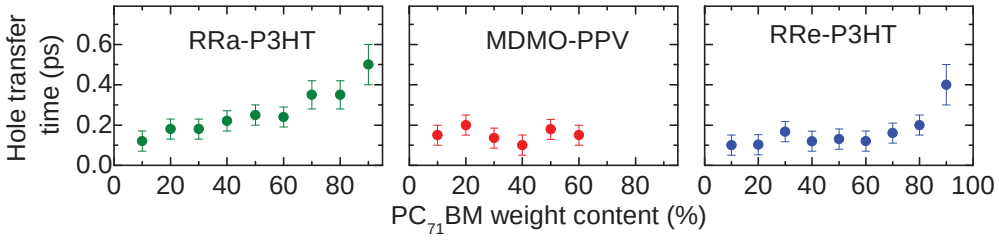

Figure S3.10 Hole transfer time as obtained from MC simulations

3.5.7 Accuracy of Domain Size Retrieval from the Monte-Carlo Simulations

Kinetic parameters of the MC simulations, i.e. energetic disorder, exciton lifetime and the hopping time were derived from time-resolved PL on pristine films of $PC_{71}BM$ (section 3.5.9 "Exciton Kinetic Parameters from Time-Resolved PL") and used for retrieval of the $PC_{71}BM$ domain size (Figure 3.3, Main Text). However, one can argue that these parameters may in turn depend on the $PC_{71}BM$ domain size, with the data derived from the pristine films being a limiting case of a very big $PC_{71}BM$ domain. As a consequence, the problem of size retrieval loses self-consistency and as such might lack a unique solution for the mixed polymer:$PC_{71}BM$ phase. Here we show, by examining the stability of the MC simulations with respect to those parameters, that this is not the case. In particular, we demonstrate the retrieved sizes do not change upon vast variations of the kinetic parameters thereby lifting the requirement of their precise determination for each particular blend (which would have been hardly feasible).

Figure S3.11 shows the MC simulations output for two mixed phase domain sizes: 6 nm (RRa-P3HT:$PC_{71}BM$ with 10% $PC_{71}BM$ concentration) and 8 nm (RRe-P3HT:$PC_{71}BM$ with 80% $PC_{71}BM$ concentration) taken as the representative cases, with the aforementioned

parameters varied in a wide range. As follows from the figure, the hopping time has very moderate influence on the dynamics. Only when the hopping time is increased by a factor of 3, the MC simulations begin to fail to reproduce the early-time experimental data for $PC_{71}BM$ concentration of 80%. This is due to the fact that the early-time part of the PIA transient is mainly determined by the excitons arrived from the interfacial and the next to the interfacial layers, i.e. when the exciton cooling has not occurred yet. In all other cases, the variations of the hopping time as much as a factor of 3 do not result in any appreciable deterioration of the fit quality, considering experimental noise.

Due to a similar reason, the energy disorder also has very little effect on the simulated curves. From the mixed phase, the excitons are mainly extracted before equilibration of the diffusion coefficient *D* (Figure S3.12) and, therefore, the variations in energy disorder do not have any serious influence on harvesting efficiency from the mixed phase. Perhaps, some effect could be observed in the dynamics for relatively large domains (>8 nm) but here the degree of freedom in hopping time is strongly confined by the fact that the 8-nm domains represent bulk material and therefore the values derived from PL quenching experiments, should be applied.

Finally, the exciton lifetime does not affect the early-time dynamics either because of the extraction of excitons from the mixed phase occurs in time that is much shorter than the exciton lifetime. The concern about the exciton lifetime is especially valid because the $PC_{71}BM$ lifetime changes, albeit very moderately - from 900 ps for non-interacting $PC_{71}BM$ molecules dissolved in a solid matrix of PMMA to 650 ps in the pristine $PC_{71}BM$ film (Figure S3.14). This reduction most probably results from PL self-quenching due to intermolecular interactions in the film of $PC_{71}BM$. Nonetheless, the dynamics for the mixed phase do not change with the exciton lifetime variation within this limit (Figure S3.11).

Therefore, we conclude that MC simulations are stable for domain sizes retrieval for both mixed phase and large domains with respect to the kinetic parameters that arguably may depend on the $PC_{71}BM$ domain size. This is attributed to extremely fast extraction of the excitons from the $PC_{71}BM$ domains. On the other hand, the large $PC_{71}BM$ domains behave as the bulk material so that the parameters derived from the PL measurements can be safely used.

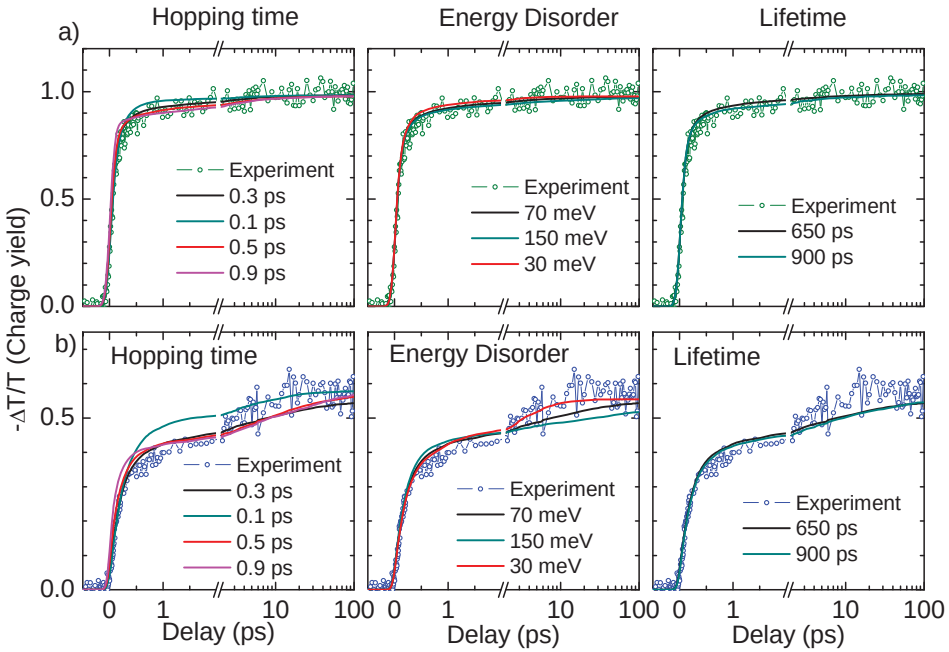

Figure S3.11 MC simulations for (a) RRa-P3HT:$PC_{71}BM$ with 10% $PC_{71}BM$ concentration (retrieved mixed phase domain size 6 nm) and (b) RRe-P3HT:$PC_{71}BM$ with 80% $PC_{71}BM$ concentration (retrieved mixed phase domain size 8 nm). The parameters of the MC simulations (hopping time τ, energy disorder σ and exciton lifetime T_1) were varied in wide range (indicated in the legend). The values deduced from the PL quenching measurements are τ=0.3 ps , σ=70 meV and T_1=650 ps.

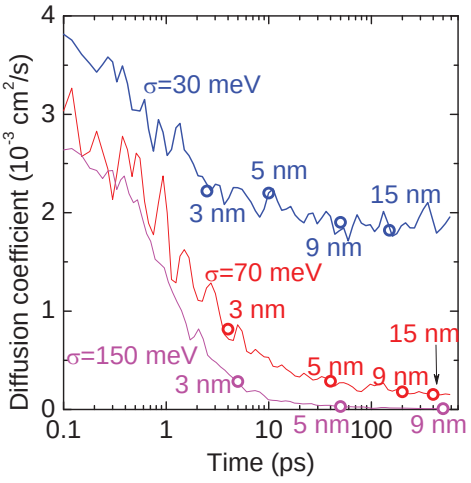

Figure S3.12 Simulated exciton diffusion coefficient dependence on time for energy disorder of σ=70 meV (red line; the value deduced from the PL quenching measurements), σ=150 meV (magenta line) and σ=30 meV (blue line). Open circles indicate the domain size from which the excitons are extracted at the given time.

3.5.8 Generalization of the proposed method to modern donor-acceptor systems

To demonstrate the applicability of the proposed technique to the modern donor-acceptor systems, we performed the analysis of photovoltaic blend based on a push-pull polymer PCPDTBT with different $PC_{71}BM$ content. The excitation wavelength was set to 480 nm; therefore, both donor and $PC_{71}BM$ are excited approximately equally. As excitons from PCPDTBT phase and interfacial $PC_{71}BM$ excitons dissociate within <200 fs[77], the respective PIA contributions can be considered as a step-like function at the timescale of $PC_{71}BM$ exciton diffusion (Figure S3.13a). By including this response into the MC simulations, we readily separate the PCPDTBT and diffusion-delayed $PC_{71}BM$ contributions. Using the same kinetic parameters for $PC_{71}BM$ as in the Main Text, the $PC_{71}BM$ domain size between 3 and 9 nm are obtained (Figure S3.13b). This clearly demonstrates that the high contrast between $PC_{71}BM$ and polymer/small molecule excitations is a convenient but not essential requirement.

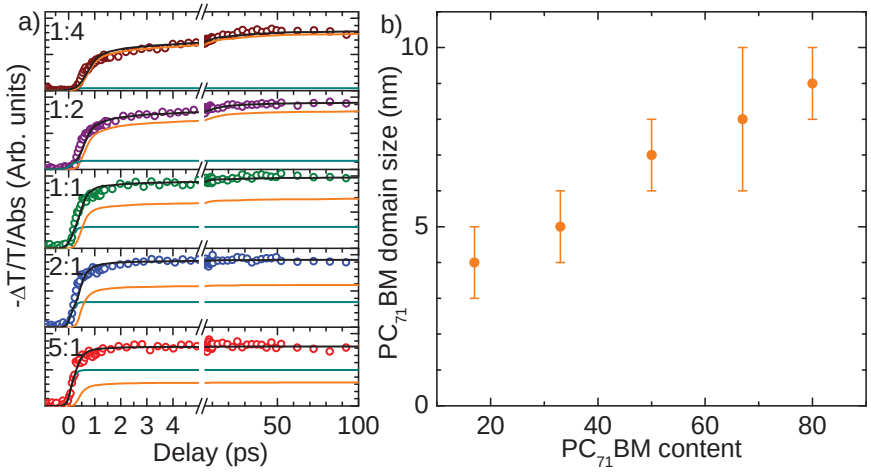

Figure S3.13 (a) Measured (open circles) and simulated (black lines) isotropy transients PCPDTBT-based blends with different $PC_{71}BM$ content (indicated) after 480 nm excitation. Cyan and orange lines represent polymer and $PC_{71}BM$ contribution to the simulated transients, respectively. (b) The sizes of $PC_{71}BM$ domains retrieved from MC simulations. For details see to Ref. [77].

3.5.9 Exciton Kinetic Parameters from Time-Resolved PL

The MC simulations require several parameters for the data modeling: i). $PC_{71}BM$ exciton lifetime; ii). energy disorder of excitons on different $PC_{71}BM$ molecules (which enters as the energy differences E_i - E_j in Eq. 3.1 of the main text); and iii). initial exciton hopping rate. All these parameters were obtained from independent measurements of PL quenching efficiency. $PC_{71}BM$ films mixed with TPTPA[16] quencher were manufactured under controlled TPTPA molar fractions of 50%, 25%, 12.8%, 3.2%, 0.8%, 0.1%, 0.0125%, and 0% (neat $PC_{71}BM$ film).

The materials were separately dissolved in ODCB at concentrations of 20 g/l, and then mixed to achieve given molar concentrations of TPTPA.

To examine the effect of intermolecular interactions, we also measured PL of the well-separated $PC_{71}BM$ molecules diluted in a PMMA matrix. For this, PMMA was dissolved in ODCB at concentrations of 150 g/l and then mixed with $PC_{71}BM$ solution to achieve the relative concentration of ~1 $PC_{71}BM$ molecule per 2000 PMMA monomers (the averaged inter$PC_{71}BM$ distance of ~7 nm). The samples were prepared by drop-casting of the resulted solutions.

For each sample, time-resolved PL transients were measured with a Hamamatsu C5680 streak-camera system after 560 nm excitation, with time resolution of ~10 ps. To obtain the PL dynamics, the red flank of $PC_{71}BM$ PL was integrated in the spectral region of 780-850 nm, which is the least affected by $PC_{71}BM$ exciton spectral dynamics (see below).

The resulted PL decay transients were globally fit with effective exciton lifetime T_1, hopping time τ and energy disorder σ as the global fit parameters, i.e. identical for all samples (Figure S3.14). The MC model was similar to that described above with exception of the grid size used. Here, the $PC_{71}BM$ film was modelled as a grid of 400x400x400 nods with periodic boundary conditions (i.e. if the exciton crosses the border it appears at the other side). TPTPA quenchers were placed randomly in the grid with the given molar fraction. At time zero, the pre-defined number of excitons (6400) was placed randomly in the $PC_{71}BM$ molecules in the grid. Once the exciton hops to the TPTPA quencher, it splits into the charges and is excluded from the simulations. As the output, the number of as-yet survived excitons is used.

PL dynamics at all concentrations were successfully simulated with a single set of parameters of T_1=650 ps, τ=0.3 ps and σ=70 meV; the obtained values are in line with those reported in the literature[27,78,79]. This suggests that the kinetic parameters obtained from the PL quenching measurements can be used to model the $PC_{71}BM$ domains of any size since low quencher concentrations represent bulk $PC_{71}BM$ while high quencher concentrations (50%) correspond dispersed $PC_{71}BM$ molecules in a TPTPA matrix. The fact that a single set of kinetic parameters is needed to describe as high range of quencher concentrations as 0.0125-50%, signifies similar exciton diffusion in $PC_{71}BM$ domains of different sizes.

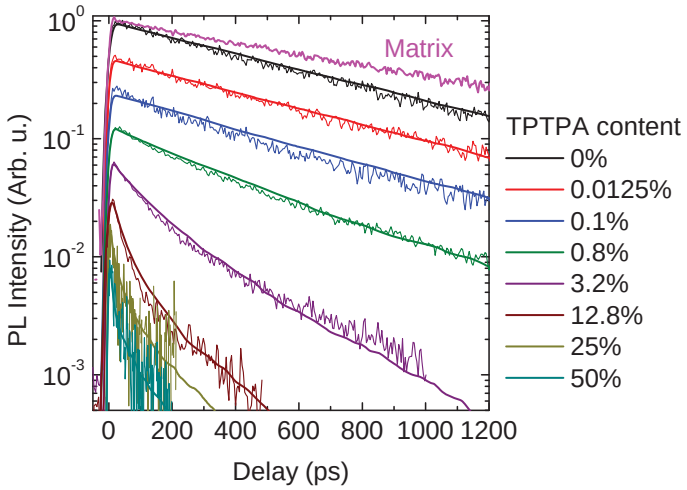

Figure S3.14 Experimental $PC_{71}BM$ PL transients (thin lines) and results of the MC simulations (thick lines). The PL transient for $PC_{71}BM$ molecules strongly diluted in the PMMA matrix is shown for comparison.

3.5.10 PL Energy Shift

One of the crucial parameters in the MC simulations, the energy disorder of 70 meV, was independently verified by direct comparison of the PL red-shift in the neat $PC_{71}BM$ film with results of the simulations (Figure S3.15a). The PL red shift is caused by exciton downhill hopping in the disordered medium[80,81], which results in dynamical decrease of exciton mobility (Figure 3.5b, Main Text). The fact that the energy relaxation is due to the downhill exciton migration is confirmed by the absence of a noticeable PL red-shift for the $PC_{71}BM$ molecules diluted in PMMA matrix, where no exciton migration occurs because of absence of intermolecular interactions (Figure S3.15b, red line).

To track the energy dynamics from the MC simulation, the mean energy of the whole exciton ensemble was calculated on each simulation step. As in the simulations the density of states is centered at 0 eV, the simulated values were shifted by 1.78 eV to match the experimental conditions. Experimental and simulated energy dynamics are compared in Figure S3.15b. Levelling-off of the experimental curve at short delays is due to limited streak-camera resolution of ~10 ps. The simulated energy shift matches the experiment perfectly both in amplitude and dynamics, which confirms the validity of disorder value quoted above.

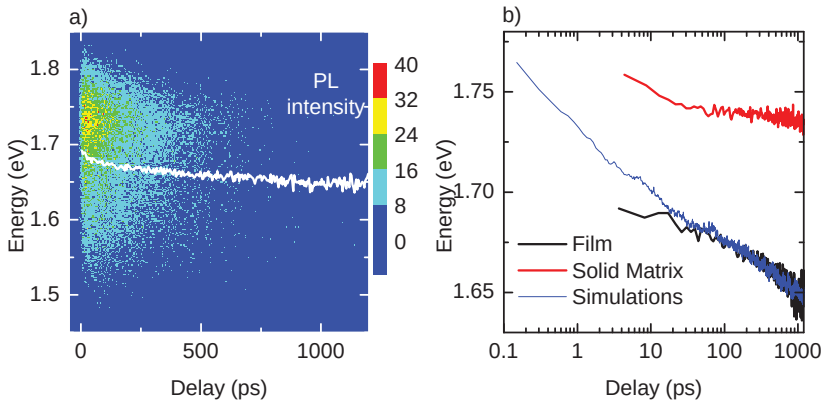

Figure S3.15 (a) PL map for the neat $PC_{71}BM$ film. The mean energy value at each time is shown by the white line. The mean energy does not coincide with the PL maximum due to an asymmetric shape of the $PC_{71}BM$ PL spectrum. (b) Measured in film (black line) and PMMA matrix (red line) and simulated (blue line) energy dynamics of the PL maximum. The simulated curve is shifted by 1.78 eV to match the experimental conditions.

Author Contributions

OVK performed PL measurements and Monte-Carlo analysis of the data; AS performed PIA and microscopic measurements; GP performed GIWAXS and GISAXS measurements, PHMvL and MSP conceived the concept and supervised the research.

References

1 Z. He, B. Xiao, F. Liu, H. Wu, Y. Yang, S. Xiao, C. Wang, T. P. Russell, and Y. Cao. Single-junction polymer solar cells with high efficiency and photovoltage. *Nat. Photonics* **9** no. 3, 2015, p. 174.

2 J. You, L. Dou, K. Yoshimura, T. Kato, K. Ohya, T. Moriarty, K. Emery, C.-C. Chen, J. Gao, G. Li *et al.* A Polymer Tandem Solar Cell with 10.6% Power Conversion Efficiency. *Nat. Commun.* **4**, 2013, p. 1446.

3 Y.-W. Su, S.-C. Lan, and K.-H. Wei. Organic Photovoltaics. *Mater. Today* **15** no. 12, 2012, p. 554.

4 S. M. Menke and R. J. Holmes. Exciton Diffusion in Organic Photovoltaic Cells. *Energy Environ. Sci.* **7** no. 2, 2014, p. 499.

5 O. V. Mikhnenko, P. W. M. Blom, and T.-Q. Nguyen. Exciton Diffusion in Organic Semiconductors. *Energy Environ. Sci.* **8**, 2015, p. 1867.

6 M. Hiramoto, H. Fujiwara, and M. Yokoyama. Three-Layered Organic Solar Cell with a Photoactive Interlayer of Codeposited Pigments. *Appl. Phys. Lett.* **58** no. 10, 1991, p. 1062.

7 J. J. M. Halls, C. A. Walsh, N. C. Greenham, E. A. Marseglia, R. H. Friend, S. C. Moratti, and A. B. Holmes. Efficient Photodiodes from Interpenetrating Polymer Networks. *Nature* **376** no. 6540, 1995, p. 498.

8 G. Yu, J. Gao, J. C. Hummelen, F. Wudl, and A. J. Heeger. Polymer Photovoltaic Cells: Enhanced Efficiencies via a Network of Internal Donor-Acceptor Heterojunctions. *Science* **270** no. 5243, 1995, p. 1789.

9 C. K. Lee, C. W. Pao, and C. W. Chu. Multiscale Molecular Simulations of The Nanoscale Morphologies of P3HT: PCBM Blends for Bulk Heterojunction Organic Photovoltaic Cells. *Energ. Environ. Sci.* **4** no. 10, 2011, p. 4124.

10 S. Kouijzer, J. J. Michels, M. van den Berg, V. S. Gevaerts, M. Turbiez, M. M. Wienk, and R. A. J. Janssen. Predicting Morphologies of Solution Processed Polymer:Fullerene Blends. *J. Am. Chem. Soc.* **135** no. 32, 2013, p. 12057.

11 B. V. Andersson, A. Herland, S. Masich, and O. Inganäs. Imaging of the 3D Nanostructure of a Polymer Solar Cell by Electron Tomography. *Nano Lett.* **9** no. 2, 2009, p. 853.

12 A. A. Herzing, L. J. Richter, and I. M. Anderson. 3D Nanoscale Characterization of Thin-Film Organic Photovoltaic Device Structures via Spectroscopic Contrast in the TEM. *J. Phys. Chem. C* **114** no. 41, 2010, p. 17501.

13 W. Chen, M. P. Nikiforov, and S. B. Darling. Morphology Characterization in Organic and Hybrid Solar Cells. *Energy Environ. Sci.* **5** no. 8, 2012, p. 8045.

14 R. C. Masters, A. J. Pearson, T. S. Glen, F.-C. Sasam, L. Li, M. Dapor, A. M. Donald, D. G. Lidzey, and C. Rodenburg. Sub-Nanometre Resolution Imaging of Polymer-Fullerene Photovoltaic Blends Using Energy-Filtered Scanning Electron Microscopy. *Nat. Commun.* **6**, 2015, p. 6928.

15 S. D. Dimitrov, C. B. Nielsen, S. Shoaee, P. Shakya Tuladhar, J. Du, I. McCulloch, and J. R. Durrant. Efficient Charge Photogeneration by the Dissociation of $PC_{70}BM$ Excitons in Polymer/Fullerene Solar Cells. *J. Phys. Chem. Lett.* **3** no. 1, 2012, p. 140.

16 F. S. U. Fischer, D. Trefz, J. Back, N. Kayunkid, B. Tornow, S. Albrecht, K. G. Yager, G. Singh, A. Karim, D. Neher *et al.* Highly Crystalline Films of PCPDTBT with Branched Side Chains by Solvent Vapor Crystallization: Influence on Opto-Electronic Properties. *Adv. Mater.* **27**, 2014, p. 1223.

17 X.-D. Dang, A. B. Tamayo, J. Seo, C. V. Hoven, B. Walker, and T.-Q. Nguyen. Nanostructure and Optoelectronic Characterization of Small Molecule Bulk Heterojunction Solar Cells by Photoconductive Atomic Force Microscopy. *Adv. Funct. Mater.* **20** no. 19, 2010, p. 3314.

18 D. Baran, N. Li, A.-C. Breton, A. Osvet, T. Ameri, M. Leclerc, and C. J. Brabec. Qualitative Analysis of Bulk-Heterojunction Solar Cells without Device Fabrication: An Elegant and Contactless Method. *J. Am. Chem. Soc.* **136** no. 31, 2014, p. 10949.

19 A. Ruseckas, P. E. Shaw, and I. D. W. Samuel. Probing the Nanoscale Phase Separation in Binary Photovoltaic Blends of Poly(3-hexylthiophene) and Methanofullerene by Energy Transfer. *Dalton Trans.* **45** no. 45, 2009, p. 10040.

20 G. Grancini, D. Polli, D. Fazzi, J. Cabanillas-Gonzalez, G. Cerullo, and G. Lanzani. Transient Absorption Imaging of P3HT:PCBM Photovoltaic Blend: Evidence For Interfacial Charge Transfer State. *J. Phys. Chem. Lett.* **2** no. 9, 2011, p. 1099.

21 S. Westenhoff, I. A. Howard, and R. H. Friend. Probing the Morphology and Energy Landscape of Blends of Conjugated Polymers with Sub-10 nm Resolution. *Phys. Rev. Lett.* **101** no. 1, 2008, p. 016102.

22 J. G. Muller, J. M. Lupton, J. Feldmann, U. Lemmer, M. C. Scharber, N. S. Sariciftci, C. J. Brabec, and U. Scherf. Ultrafast Dynamics of Charge Carrier Photogeneration and Geminate Recombination in Conjugated Polymer:Fullerene Solar Cells. *Physical Review B* **72** no. 19, 2005, p. 195208

23 L. G. Kaake, D. Moses, and A. J. Heeger. Coherence and Uncertainty in Nanostructured Organic Photovoltaics. *J. Phys. Chem. Lett.* **4** no. 14, 2013, p. 2264.

24 S. Mukamel. Comment on "Coherence and Uncertainty in Nanostructured Organic Photovoltaics". *J. Phys. Chem. A.* **117** no. 40, 2013, p. 10563.

25 D. Cheyns, M. Kim, B. Verreet, and B. P. Rand. Accurate Spectral Response Measurements of a Complementary Absorbing Organic Tandem Cell with Fill Factor Exceeding the Subcells. *Appl. Phys. Lett.* **104** no. 9, 2014, p. 093302.

26 A. A. Bakulin, J. C. Hummelen, M. S. Pshenichnikov, and P. H. M. van Loosdrecht. Ultrafast Hole-Transfer Dynamics in Polymer/PCBM Bulk Heterojunctions. *Adv. Funct. Mater.* **20** no. 10, 2010, p. 1653.

27 S. D. Dimitrov, Z. Huang, F. Deledalle, C. B. Nielsen, B. C. Schroeder, R. S. Ashraf, S. Shoaee, I. McCulloch, and J. R. Durrant. Towards Optimisation of Photocurrent from Fullerene Excitons in Organic Solar Cells. *Energy Environ. Sci.* **7** no. 3, 2014, p. 1037.

28 C. J. Brabec, S. Gowrisanker, J. J. M. Halls, D. Laird, S. Jia, and S. P. Williams. Polymer–Fullerene Bulk-Heterojunction Solar Cells. *Adv. Mater.* **22** no. 34, 2010, p. 3839.

29 G. J. Hedley, A. J. Ward, A. Alekseev, C. T. Howells, E. R. Martins, L. A. Serrano, G. Cooke, A. Ruseckas, and I. D. W. Samuel. Determining the Optimum Morphology in High-Performance Polymer-Fullerene Organic Photovoltaic Cells. *Nat. Commun.* **4**, 2013, p. 2867.

30 S. Cook, A. Furube, R. Katoh, and L. Han. Estimate of Singlet Diffusion Lengths in PCBM Films by Time-Resolved Emission Studies. *Chem. Phys. Lett.* **478** no. 1–3, 2009, p. 33.

31 A. Baumann, T. J. Savenije, D. H. K. Murthy, M. Heeney, V. Dyakonov, and C. Deibel. Influence of Phase Segregation on Recombination Dynamics in Organic Bulk-Heterojunction Solar Cells. *Adv. Funct. Mater.* **21** no. 9, 2011, p. 1687.

32 M. C. Scharber and N. S. Sariciftci. Efficiency of Bulk-Heterojunction Organic Solar Cells. *Prog. Polym. Sci.* **38** no. 12, 2013, p. 1929.

33 B. Bernardo, D. Cheyns, B. Verreet, R. D. Schaller, B. P. Rand, and N. C. Giebink. Delocalization and Dielectric Screening of Charge Transfer States in Organic Photovoltaic Cells. *Nat. Commun.* **5**, 2014, p. 3245.

34 O. V. Kozlov, F. de Haan, R. A. Kerner, B. P. Rand, D. Cheyns, and M. S. Pshenichnikov. Real-Time Tracking of Singlet Exciton Diffusion in Organic Semiconductors. *Phys. Rev. Lett.* **116** no. 5, 2016, p. 057402.

35 A.-M. Dowgiallo, K. S. Mistry, J. C. Johnson, O. G. Reid, and J. L. Blackburn. Probing Exciton Diffusion and Dissociation in Single-Walled Carbon Nanotube-C_{60} Heterojunctions. *J. Phys. Chem. Lett.* **7** no. 10, 2016, p. 1794.

36 X. Wei, Z. V. Vardeny, N. S. Sariciftci, and A. J. Heeger. Absorption-Detected Magnetic-Resonance Studies Of Photoexcitations In Conjugated-Polymer/C_{60} Composites. *Physical Review B* **53** no. 5, 1996, p. 2187.

37 S. Cook, R. Katoh, and A. Furube. Ultrafast Studies of Charge Generation in PCBM:P3HT Blend Films following Excitation of the Fullerene PCBM. *J. Phys. Chem. C* **113** no. 6, 2009, p. 2547.

38 Y. N. Luponosov, J. Min, A. N. Solodukhin, O. V. Kozlov, M. A. Obrezkova, S. M. Peregudova, T. Ameri, S. N. Chvalun, M. S. Pshenichnikov, C. J. Brabec *et al.* Effects of Electron-Withdrawing Group and Electron-Donating Core Combinations on Physical Properties and Photovoltaic Performance in D-π-A Star-Shaped Small Molecules. *Org. Electron.* **32**, 2016, p. 157.

39 O. V. Kozlov, Y. N. Luponosov, S. A. Ponomarenko, N. Kausch-Busies, D. Y. Paraschuk, Y. Olivier, D. Beljonne, J. Cornil, and M. S. Pshenichnikov. Ultrafast Charge Generation Pathways in Photovoltaic Blends Based on Novel Star-Shaped Conjugated Molecules. *Adv. Energy Mater.* **5** no. 7, 2015, p. 1401657.

40 A. V. Akkuratov, D. K. Susarova, O. V. Kozlov, D. V. Novikov, A. V. Chernyak, Y. L. Moskvin, L. A. Frolova, M. S. Pshenichnikov, and P. A. Troshin. Design of $(X\text{-}DADAD)_n$ Type Copolymers with Improved Optoelectronic Properties for Bulk Heterojunction Organic Solar Cells. *Macromolecules* **48** no. 7, 2015, p. 2013.

41 A. R. S. Kandada, G. Grancini, A. Petrozza, S. Perissinotto, D. Fazzi, S. S. K. Raavi, and G. Lanzani. Ultrafast Energy Transfer in Ultrathin Organic Donor/Acceptor Blend. *Sci. Rep.* **3**, 2013, p. 2073.

42 K. Fesser, A. R. Bishop, and D. K. Campbell. Optical-Absorption from Polarons in a Model of Polyacetylene. *Phys. Rev. B.* **27** no. 8, 1983, p. 4804.

43 R. Österbacka, C. P. An, X. M. Jiang, and Z. V. Vardeny. Two-Dimensional Electronic Excitations in Self-Assembled Conjugated Polymer Nanocrystals. *Science* **287** no. 5454, 2000, p. 839.

44 A. A. Bakulin, D. S. Martyanov, D. Y. Paraschuk, M. S. Pshenichnikov, and P. H. M. van Loosdrecht. Ultrafast Charge Photogeneration Dynamics in Ground-State Charge-Transfer Complexes Based on Conjugated Polymers. *J. Phys. Chem. B* **112** no. 44, 2008, p. 13730.

45 A. Serbenta, O. V. Kozlov, G. Portale, P. H. M. van Loosdrecht, and M. S. Pshenichnikov. Bulk Heterojunction Morphology of Polymer:Fullerene Blends Revealed by Ultrafast Spectroscopy. *Sci. Rep.* **6**, 2016, p. 36236.

46 I. W. Hwang, C. Soci, D. Moses, Z. Zhu, D. Waller, R. Gaudiana, C. J. Brabec, and A. J. Heeger. Ultrafast Electron Transfer and Decay Dynamics in a Small Band Gap Bulk Heterojunction Material. *Adv. Mater.* **19** no. 17, 2007, p. 2307.

47 A. A. Bakulin, S. D. Dimitrov, A. Rao, P. C. Y. Chow, C. B. Nielsen, B. C. Schroeder, I. McCulloch, H. J. Bakker, J. R. Durrant, and R. H. Friend. Charge-Transfer State Dynamics Following Hole and Electron Transfer in Organic Photovoltaic Devices. *J. Phys. Chem. Lett.* **4** no. 1, 2013, p. 209.

48 S. Shoaee, S. Subramaniyan, H. Xin, C. Keiderling, P. S. Tuladhar, F. Jamieson, S. A. Jenekhe, and J. R. Durrant. Charge Photogeneration for a Series of Thiazolo-Thiazole Donor Polymers Blended with the Fullerene Electron Acceptors PCBM and ICBA. *Adv. Funct. Mater.* **23** no. 26, 2013, p. 3286.

49 J. Guo, H. Ohkita, H. Benten, and S. Ito. Charge Generation and Recombination Dynamics in Poly(3-hexylthiophene)/Fullerene Blend Films with Different Regioregularities and Morphologies. *J. Am. Chem. Soc.* **132** no. 17, 2010, p. 6154.

50 G. Grancini, M. Maiuri, D. Fazzi, A. Petrozza, H. J. Egelhaaf, D. Brida, G. Cerullo, and G. Lanzani. Hot Exciton Dissociation in Polymer Solar Cells. *Nat. Mater.* **12** no. 1, 2013, p. 29.

51 D. Bartesaghi and L. J. A. Koster. The Effect of Large Compositional Inhomogeneities on the Performance of Organic Solar Cells: A Numerical Study. *Adv. Funct. Mater.* **25** no. 13, 2015, p. 2013.

52 H. Hoppe and N. S. Sariciftci. Morphology of Polymer/Fullerene Bulk Heterojunction Solar Cells. *J. Mater. Chem.* **16** no. 1, 2006, p. 45.

53 X. N. Yang, J. K. J. van Duren, R. A. J. Janssen, M. A. J. Michels, and J. Loos. Morphology and Thermal Stability of the Active Layer in poly(p-phenylenevinylene)/Methanofullerene Plastic Photovoltaic Devices. *Macromolecules* **37** no. 6, 2004, p. 2151.

54 T. Martens, J. D'Haen, T. Munters, Z. Beelen, L. Goris, J. Manca, M. D'Olieslaeger, D. Vanderzande, L. De Schepper, and R. Andriessen. Disclosure of the Nanostructure of MDMO-PPV:PCBM Bulk Hetero-Junction Organic Solar Cells by a Combination of SPM and TEM. *Synthetic Met.* **138** no. 1-2, 2003, p. 243.

55 B. Schmidt-Hansberg, M. Sanyal, M. F. G. Klein, M. Pfaff, N. Schnabel, S. Jaiser, A. Vorobiev, E. Muller, A. Colsmann, P. Scharfer *et al.* Moving Through the Phase Diagram: Morphology Formation in Solution Cast Polymer-Fullerene Blend Films for Organic Solar Cells. *Acs Nano* **5** no. 11, 2011, p. 8579.

56 M. A. Brady, G. M. Su, and M. L. Chabinyc. Recent Progress in The Morphology of Bulk Heterojunction Photovoltaics. *Soft Matter* **7** no. 23, 2011, p. 11065.

57 J. Y. Kim and D. Frisbie. Correlation of Phase Behavior and Charge Transport in Conjugated Polymer/Fullerene Blends. *J. Phys. Chem. C.* **112** no. 45, 2008, p. 17726.

58 V. Shrotriya, J. Ouyang, R. J. Tseng, G. Li, and Y. Yang. Absorption Spectra Modification in Poly(3-hexylthiophene):Methanofullerene Blend Thin Films. *Chem. Phys. Lett.* **411** no. 1-3, 2005, p. 138.

59 O. V. Mikhnenko, F. Cordella, A. B. Sieval, J. C. Hummelen, P. W. M. Blom, and M. A. Loi. Temperature Dependence of Exciton Diffusion in Conjugated Polymers. *The Journal of Physical Chemistry B* **112** no. 37, 2008, p. 11601.

60 G. M. Akselrod, F. Prins, L. V. Poulikakos, E. M. Y. Lee, M. C. Weidman, A. J. Mork, A. P. Willard, V. Bulović, and W. A. Tisdale. Subdiffusive Exciton Transport in Quantum Dot Solids. *Nano Lett.* **14** no. 6, 2014, p. 3556.

61 A. Kohler and H. Bassler. *Electronic Processes in Organic Semiconductors: An Introduction*. (Wiley-VCH Verlag GmbH & Co. KGaA, Weinheim, Germany, 2015).

62 W.-R. Wu, U. S. Jeng, C.-J. Su, K.-H. Wei, M.-S. Su, M.-Y. Chiu, C.-Y. Chen, W.-B. Su, C.-H. Su, and A.-C. Su. Competition between Fullerene Aggregation and Poly(3-hexylthiophene) Crystallization upon Annealing of Bulk Heterojunction Solar Cells. *ACS Nano* **5** no. 8, 2011, p. 6233.

63 W. Chen, T. Xu, F. He, W. Wang, C. Wang, J. Strzalka, Y. Liu, J. G. Wen, D. J. Miller, J. H. Chen *et al.* Hierarchical Nanomorphologies Promote Exciton Dissociation in Polymer/Fullerene Bulk Heterojunction Solar Cells. *Nano Lett.* **11** no. 9, 2011, p. 3707.

64 B. A. Collins, J. R. Tumbleston, and H. Ade. Miscibility, Crystallinity, and Phase Development in P3HT/PCBM Solar Cells: Toward an Enlightened Understanding of Device Morphology and Stability. *J. Phys. Chem. Lett.* **2** no. 24, 2011, p. 3135.

65 D. Caruso and A. Troisi. Long-Range Exciton Dissociation in Organic Solar Cells. *Proceedings of the National Academy of Sciences* **109** no. 34, 2012, p. 13498.

66 O. S. Wenger. How Donor−Bridge−Acceptor Energetics Influence Electron Tunneling Dynamics and Their Distance Dependences. *Acc. Chem. Res.* **44** no. 1, 2011, p. 25.

67 D. Moses, A. Dogariu, and A. J. Heeger. Ultrafast Photoinduced Charge Generation in Conjugated Polymers. *Chem. Phys. Lett.* **316** no. 5-6, 2000, p. 356.

68 C. Zhong, H. Choi, J. Y. Kim, H. Y. Woo, T. L. Nguyen, F. Huang, Y. Cao, and A. J. Heeger. Ultrafast Charge Transfer in Operating Bulk Heterojunction Solar Cells. *Adv. Mater.* **27** no. 12, 2015, p. 2036.

69 K. Kawashima, Y. Tamai, H. Ohkita, I. Osaka, and K. Takimiya. High-Efficiency Polymer Solar Cells With Small Photon Energy Loss. *Nat. Commun.* **6**, 2015, p. 10085.

70 J. Min, Y. N. Luponosov, A. Gerl, M. S. Polinskaya, S. M. Peregudova, P. V. Dmitryakov, A. V. Bakirov, M. A. Shcherbina, S. N. Chvalun, S. Grigorian *et al.* Alkyl Chain Engineering of Solution-Processable Star-Shaped Molecules for High-Performance Organic Solar Cells. *Adv. Energy Mater.* **4** no. 5, 2014, p. 1301234.

71 Y. Liu, C.-C. Chen, Z. Hong, J. Gao, Y. Yang, H. Zhou, L. Dou, G. Li, and Y. Yang. Solution-Processed Small-Molecule Solar Cells: Breaking the 10% Power Conversion Efficiency. *Sci. Rep.* **3**, 2013, p. 3356.

72 N. D. Treat and M. L. Chabinyc. Phase Separation in Bulk Heterojunctions of Semiconducting Polymers and Fullerenes for Photovoltaics. *Annu. Rev. Phys. Chem.* **65** no. 1, 2014, p. 59.

73 K. Feron, W. Belcher, C. Fell, and P. Dastoor. Organic Solar Cells: Understanding the Role of Förster Resonance Energy Transfer. *Int. J. Mol. Sci.* **13** no. 12, 2012, p. 17019.

74 M. Manca, C. Piliego, E. Wang, M. R. Andersson, A. Mura, and M. A. Loi. Tracing Charge Transfer States in Polymer:Fullerene Bulk-Heterojunctions. *J. Mater. Chem. A* **1** no. 25, 2013, p. 7321.

75 M. N. Paddon-Row. Investigating Long-Range Electron-Transfer Processes with Rigid, Covalently Linked Donor-(Norbornylogous Bridge)-Acceptor Systems. *Acc. Chem. Res.* **27** no. 1, 1994, p. 18.

76 A. Serbenta. *Organic Donor-Acceptor Systems: Charge Generation and Morphology* PhD thesis, University of Groningen, (2016).

77 O. V. Kozlov, V. G. Pavelyev, H. D. de Gier, R. W. A. Havenith, P. H. M. van Loosdrecht, J. C. Hummelen, and M. S. Pshenichnikov. Ultrafast Electron and Hole Transfer in Bulk Heterojunctions of Low-Bandgap Polymers. *Organic Photonics and Photovoltaics* **4** no. 1, 2016, p. 24.

78 A. Fedorova, M. N. Berberan-Santosa, J.-P. Lefèvreb, and B. Valeur. Picosecond Time-Resolved and Steady-State Studies of the Polarization of the Fluorescence of C_{60} and C_{70}. *Chem. Phys. Lett.* **267** no. 5-6, 1997, p. 467.

79 D. A. Vithanage, A. Devižis, V. Abramavičius, Y. Infahsaeng, D. Abramavičius, R. C. I. MacKenzie, P. E. Keivanidis, A. Yartsev, D. Hertel, J. Nelson *et al.* Visualizing Charge Separation in Bulk Heterojunction Organic Solar Cells. *Nat. Commun.* **4**, 2013, p. 2334

80 C. R. Kagan, C. B. Murray, and M. G. Bawendi. Long-Range Resonance Transfer of Electronic Excitations in Close-Packed CdSe Quantum-Dot Solids. *Physical Review B* **54** no. 12, 1996, p. 8633.

81 S. A. Crooker, J. A. Hollingsworth, S. Tretiak, and V. I. Klimov. Spectrally Resolved Dynamics of Energy Transfer in Quantum-Dot Assemblies: Towards Engineered Energy Flows in Artificial Materials. *Phys. Rev. Lett.* **89** no. 18, 2002, p. 186802.

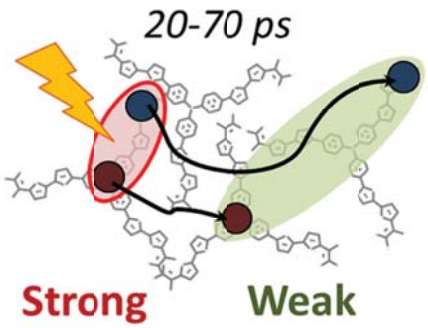

Chapter 4

Ultrafast Exciton-to-Polaron Conversion in Densely-Packed Small Organic Semiconducting Molecules

In the rapidly developing field of organic photovoltaics, the material design and device engineering are key factors that eventually determine the device efficiency. Design of the active layer material and intermolecular interactions largely determine the efficiency of organic solar cells (OSCs). In this Chapter, ultrafast photophysics of four star-shaped molecules (SSMs) as benchmark materials with time-resolved photoinduced absorption and photoluminescence spectroscopy as experimental tools are discussed. It is shown that efficient exciton-to-charge conversion occurs in SSM films even without an external acceptor. This results in the lowering of the Coulomb binding between intermolecular electron-hole polaron pairs which, in turn, could lead to an increased open-circuit voltage. These findings suggest that promoting intermolecular interactions in films of small organic molecules is one of the pathways to highly efficient organic solar cells.

This Chapter is based on the following publication:
Oleg V. Kozlov, Yuriy N. Luponosov, Alexander N. Solodukhin, Bruno Flament, Yoann Olivier, Roberto Lazzaroni, Jérôme Cornil, Sergei A. Ponomarenko and Maxim S. Pshenichnikov, *Adv Optical Mater* **5**(7), 1700024 (2017)

4.1 Introduction

The efficiency of organic optoelectronic devices essentially depends on two main factors: the photophysical and chemical properties of the materials[1-9] and the optimization of the device structure.[7,10-13] Even though both factors are of high importance, the properties of the materials might be considered as prevailing: it is impossible to make an efficient device out of poorly designed materials. Therefore, the optimization of the material design and understanding the structure-property relationship are burning issues in materials sciences.[14-16]

Nowadays, among the most popular donor materials for organic solar cells (OSCs) are push-pull small molecules (SMs).[7,10,17-23] Optimized devices based on SMs have already broken the 10% threshold in power conversion efficiency with a great potential for further improvement.[7,19,24,25] The best results of >10% efficiency for solution-processed OSCs were achieved using relatively complex and difficult to synthetize SMs as donors.[24,25] Alternatively, triple-layer vacuum-processed OSCs based on relatively simple SMs demonstrate outstanding efficiencies of >11% .[26]

The efficiency of OSCs is determined by three parameters:[27] the open-circuit voltage (V_{OC}), the short-circuit current (J_{SC}) and the fill factor (*FF*), which have to be maximized to achieve the best device performance. Short-circuit current is typically improved by maximizing the amount of collected photons, and maximal *FF* requires elaborate device engineering to reduce the recombination processes.[28] To maximize the V_{OC}, energy losses have to be minimized by e.g. matching at best the energy levels of the donor and acceptor materials,[29] lowering the exciton binding energy,[30] increasing state delocalization,[5] reducing energy disorder of the materials,[31] minimizing the recombination via interfacial CT states[32] etc.[33]

Recently, it was shown that simple SMs with a star-shaped architecture (SSMs) fulfil most requirements for high-efficiency solar cells, with efficiencies >5% demonstrated.[13] The donor core and acceptor end groups ensure broad absorption in the visible region, which results in J_{SC} of >8 mA cm^{-2}, while the star-shaped structure assists column-like self-assembling in the films, thereby enhancing charge transport properties and leading to FF >50%.[1,4,14,34-38] Finally, SSMs-based OSCs demonstrate high V_{OC} of >0.9 V[2,14] in mixture with $PC_{71}BM$, the reason of which is not yet understood. To put it in the perspective, V_{OC} of archetypical P3HT:$PC_{71}BM$ OSCs hardly exceeds 0.6 V[39-41] even though the SSMs have similar HOMO level with P3HT (ca. 5.2-5.3 eV). Therefore, V_{OC} losses (calculated as $(E_{LUMO}^{PC_{71}BM}-E_{HOMO}^{Donor})/e-V_{OC}$) amounts to <0.5 V in the OSCs based on the SSMs studied (with the energy level positions taken from Refs. [2,14]), while in P3HT-based OSCs they exceed 0.8 V. Altogether, high J_{SC} and V_{OC} make SSMs perfect benchmark materials for understanding the relations between fundamental photophysics of SM-based OSCs with their performance.

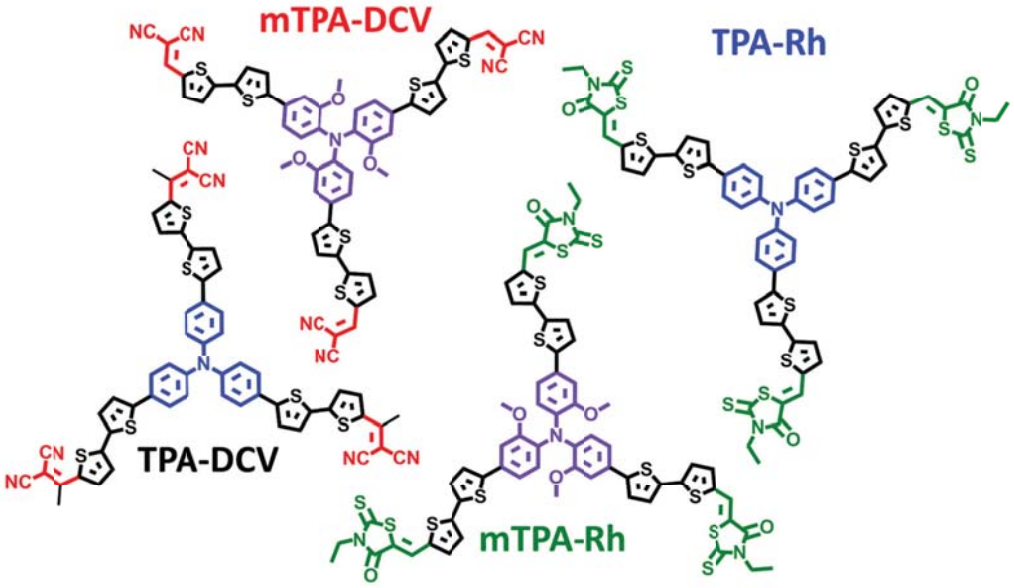

Figure 4.1 Chemical structures and notations of the SSMs studied.[14] The notations reflect the donor and acceptor units used: triphenylamine (TPA) or *tris*(2-methoxyphenyl)amine (mTPA) as donor core and dicyanovinyl or methyldicyanovinyl (both denoted as DCV) or rhodanine (Rh) as acceptor end groups.

In this work, we used four SSMs[2,14] (Figure 4.1) to understand the early-time photon-to-charge conversion processes in SM-based OCSs. These SSMs comprise different donor (triphenylamine or *tris*(2-methoxyphenyl)amine) and acceptor (dicyanovinyl, methyldicyanovinyl or rhodanine) units (Figure 4.1) and, therefore, possess different chemical and photophysical properties.[2,14] Despite these major differences in chemical structures, all molecules demonstrate low V_{OC} losses of <0.5 eV and J_{SC} of >8 mA cm^{-2} in BHJs with $PC_{71}BM$.[2,14] Using time-resolved photoinduced absorption (PIA) and time-resolved photoluminescence (PL) spectroscopies, we compare the photophysical properties of the molecules diluted in a PMMA matrix and strongly interacting molecules in a solid film. We demonstrate that in solid films efficient exciton-to-polaron conversion occurs within the first 100 ps, which leads to the population of the SSM phase with quasi-free charges (polaron pairs). The polaron pairs have lower binding energy compared to excitons and do not fill interfacial charge transfer states at the donor-acceptor interface, which leads to improved charge collection and lower geminate recombination. Our findings demonstrate that promoting a strong intermolecular coupling between molecules in films is a promising way to increase the OSC efficiency.

4.2 Experimental Results

4.2.1 Absorption Spectra

The absorption spectra of the SSMs studied in a PMMA matrix and solid films are shown in Figure 4.2. The low-energy absorption peak is mainly caused by an intramolecular charge transfer (CT)[3,42] and its position depends strongly on the particular donor-acceptor combination used. In the PMMA matrices, where the intermolecular interactions are absent, the absorption peak position varies from 499 nm (2.48 eV) for TPA-DCV to 526 nm (2.35 eV) for mTPA-DCV. The peak for mTPA-Rh molecule lies between the peaks for mTPA-DCV and TPA-Rh. These differences are explained by the fact that the absorption peak reflects the transition energy to an intramolecular CT[3] and therefore depends not on the donor and acceptor units *per se* but on their combination. The high-energy absorption shoulder has a mixed π-π^* and CT character[3] and also exhibits prominent dependence on the molecular structure. These trends in the absorption spectra are confirmed (even though to a smaller extent than observed experimentally) by the TD-DFT calculations (Figure 4.2, shaded contours[43]).

For all molecules, the absorption spectra in films are red-shifted and broadened compared to the spectra in the matrices. The shift varies from 0.12 eV for TPA-DCV to 0.20 eV for mTPA-DCV. As a result, in the films the absorption spectra for the different molecules peak almost at the same wavelength. The reason is two-fold: first, in the solid films, the effect of local dielectric environment[44-47] is more prominent compared to the isolated molecules in matrix as evidenced from the increased peak widths (~0.25 eV in PMMA matrix *vs.* ~0.3 eV in films). Second, the close packing in the solid allows for intermolecular charge separation which also affects the absorption properties. Overall, the complex behavior of absorption spectra suggests the importance of both the specific molecular structure and intermolecular interactions on the photophysical properties of the materials.

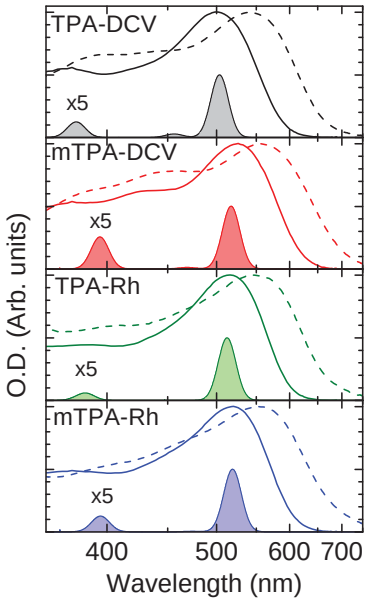

Figure 4.2 Absorption spectra of the SSMs measured in a PMMA matrix (lines) and in solid films (dashed lines) and calculated (shaded contours) at the TD-DFT level. The calculated spectra are systematically red-shifted by 0.3 eV to account for medium effects and/or the deficiencies of DFT when dealing with charge transfer states. Due to the strong difference in the amplitudes, the calculated intensities of the high-energy peaks were multiplied by 5 for representation purposes.

4.2.2 Photoinduced Absorption Spectra

To examine the early-time photophysics of exciton/charge generation, we performed time-resolved PIA experiments. In these measurements, the samples are excited by an ultrashort visible light and the photoinduced response is probed by the delayed IR probe pulse. The absorption of the probe pulse is proportional to the number of photogenerated species and therefore the photoinduced dynamics can be easily tracked with common pump-probe experiment.

It should be noted that the nature of the photoinduced species in the isolated molecules and in the films may be substantially different. For well-separated molecules in a neutral matrix (e.g. PMMA), there are no intermolecular interactions. Therefore, only intramolecular excited states (i.e. excitons and/or intramolecular CT-excitons in push-pull molecules as considered herein) are formed upon photon absorption. In the films, the molecules are interacting and, hence, additional pathways for the charge separation become open - e.g. intermolecular formation of polaron pairs.[6,48,49] The optical signatures of intramolecular CT-excitons and polarons are typically different and, therefore, the nature of the excited states can be spectrally identified.[6]

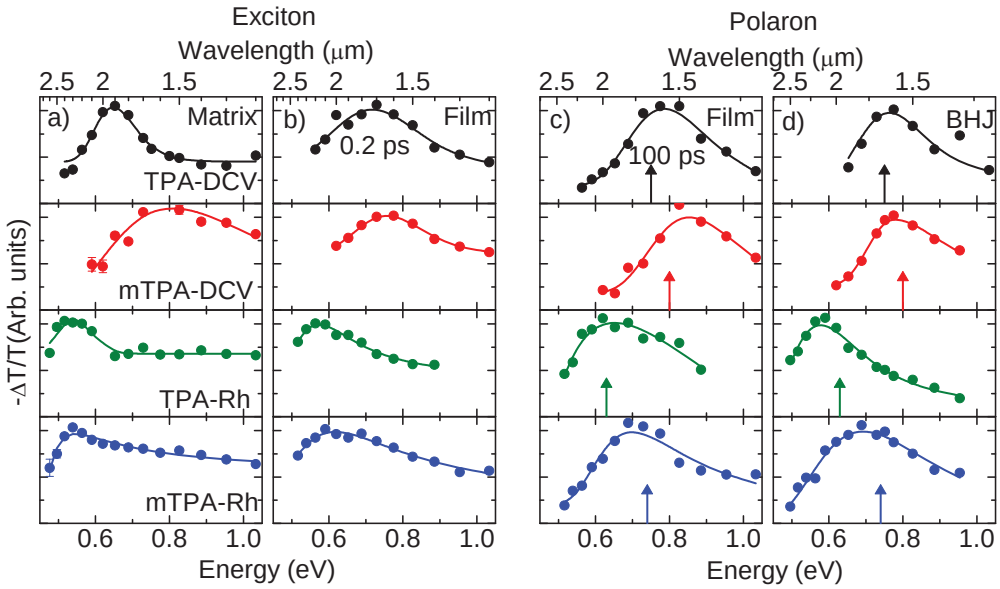

Figure 4.3 PIA spectra of the SSMs studied in (a) PMMA matrix, (b,c) solid films, and (d) 1:1 blends with $PC_{71}BM$ acceptor upon (a) 510 nm or (b-d) 550 nm excitation. Symbols represent the experimental data points while solid lines are the best fits with asymmetrical Gaussian functions. The spectra are reconstructed from the PIA transients measured at different wavelengths. The time delays are (a) 10 ps, (b) 0.2 ps, (c, d) 100 ps. Arrows in (c) and (d) show positions of the TD-DFT calculated polaron peaks, systematically red-shifted by 0.2 eV.

Figure 4.3a shows the PIA spectra of the SSMs in a PMMA matrix upon 510 nm excitation (i.e., near the absorption maximum). Since the molecules are well-separated, the spectra reflect the optical signatures of intramolecular excitations: due to the push-pull nature of the molecules, efficient intramolecular charge separation occurs which causes the electron density to be shifted from the donor core to the acceptor units (see e.g. Supporting Information, Figure S4.1[43]).

For all molecules, the PIA spectra in the PMMA matrices consist of an extremely broad background, with a more resolved IR peak (with exception of mTPA-DCV). The broad background is assigned to the excited state absorption as many transitions S_1-S_n are allowed from the first excited state to higher-lying excited states while the peak is likely due to the presence of transition(s) with significantly higher oscillator strength(s) compared to the rest of the manifold.

Figure 4.3b,c show the PIA spectra of the SSMs in solid films at early (0.2 ps) and late (100 ps) delay times. Surprisingly, the spectra are very different at the two delays, indicating a different nature of the photoexcited species. At 0.2 ps delay, the spectra in films resemble those in matrices, indicating photogeneration of intramolecular (CT-)excitons. At 100 ps, the spectra are blue-shifted while the background is significantly reduced in comparison to the 0.2 ps spectra. This is assigned to the formation of the so-called polaron pairs[6,48,49] in the film. The

electron and hole of the polaron pair are located on different SSMs (unlike intramolecular CT-excitons, where the electron and hole belong to the same molecule), which leads to a reduced Coulomb attraction. On the other hand, the polaron pair is essentially different from the charges located in an interfacial CT state (also called interfacial CT-exciton,[50] not to be confused with intramolecular CT-excitons), as in the case of the interfacial CT-exciton the electron and hole reside on different materials, while the polaron pair is located in the SSM phase. It should be noted that even though no apparent driving force for charge separation is present in the SSM film, the intermolecular charge separation between neighboring SMs is still possible[51,52] because of dense packing. If the donor unit of one molecule is in close proximity to the acceptor unit of the neighboring molecule, intermolecular charge transfer becomes energetically favorable,[3,53] and a polaron pair is formed upon photoexcitation.

Even though the polaron pairs have similar spectroscopic signatures with isolated polarons (charges),[6] they cannot be considered as free charges because (i) the electron and hole still belong to same material and (ii) Coulomb attraction is still significantly higher than kT. Spectroscopically, if the number of intermolecularly separated charges is high, the PIA response should follow the absorption spectra of polarons and not of the intramolecular (CT-)excitons.

To verify this assumption, we measured the PIA response of 1:1 bulk heterojunction (BHJ) films of the SSMs with the $PC_{71}BM$ electron acceptor, where complete charge separation is known to occur within first 100 ps (Figure 4.4d) and therefore the PIA response is caused solely by the positive hole polarons (the negative electron polarons on $PC_{71}BM$ do not produce a signal in near-IR). As there is a reasonable match between the two sets of spectra, one can conclude that the PIA response of the neat SSM films at long delays is mainly driven by polarons.

The positions of the polaron absorption peaks are different for the different SSMs: the Rh-based molecules exhibit red-shifted absorption compared to the DCV-based SSMs. This can be explained by a longer conjugation length of the Rh-based molecules and, therefore, by a larger delocalization of the charge and a weaker degree of local geometric distortions. In contrast, the methoxy substituents on the mTPA core do not change the conjugation length with respect to TPA; therefore, the polaron peak positions are expected to be similar for the TPA and mTPA-based molecules. This is, however, not the case: the polaron peak positions for the mTPA-based SSMs are in fact blue-shifted compared to the TPA-based molecules. This is attributed to an increased localization of the positive charge around the core in mTPA-based molecules, due to the dominant electron-donating character of the methoxy groups. As a result, the spectrum for the mTPA-Rh molecule is intermediate between the spectra for the TPA-Rh and mTPA-DCV molecules. This counterintuitive behavior is fully captured by the TD-DFT calculations (Figure 4.3c,d, vertical lines[43]) and highlights the major influence of the particular donor-acceptor combination on the photophysical properties of the material.

4.2.3 Photoinduced Dynamics

To examine the exciton and polaron dynamics, we studied the time-dependent PIA and PL of SSMs in PMMA matrices and neat films. The PL dynamics of the SSM molecules in PMMA matrices are shown in Figure 4.4a by solid symbols. For all molecules, the PL decays biexponentially: ~20% of the initial PL decays at hundreds ps timescale, while the rest of PL decays at >2 ns time. The slow decay reflects the radiative lifetime of the intramolecular (CT-)excitons. The fast decay is ascribed to torsional deformation of the molecules upon photoexcitation.[53] For mTPA-based molecules, the decay is considerably faster compared to the TPA-based derivatives due to the higher floppiness imparted by the methoxy groups: the calculated difference in angle between benzene ring in the donor core and the plane of the molecule in ground and charged state is ~6° for the mTPA-based molecules and only ~1° for the TPA-based compounds[43].

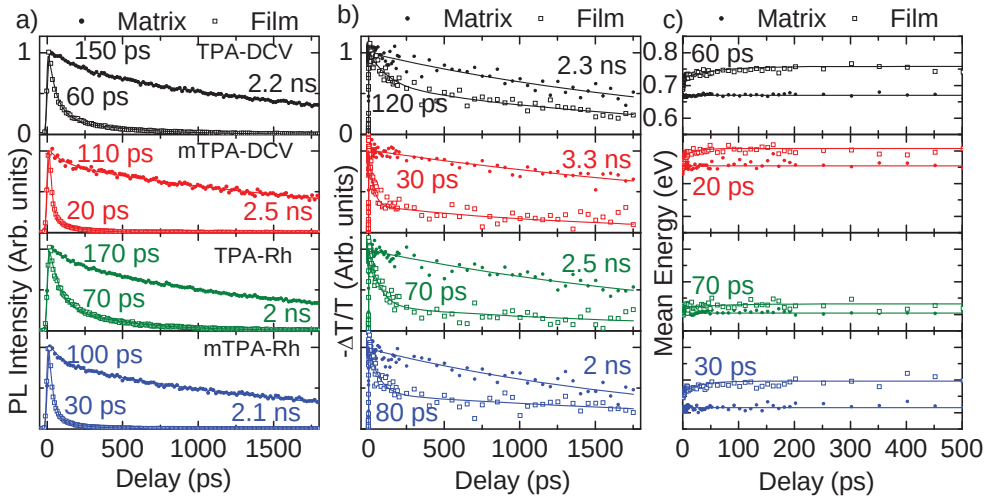

Figure 4.4 (a) PL and (b) PIA dynamics and (c) shift of the mean energy of the PIA spectra for SSMs in PMMA matrices (solid symbols) and films (open symbols). Experimental points are shown by symbols, solid lines are the best fits with (bi)exponential functions. Excitation wavelengths were 510 nm (matrices) and 550 nm (films), probe wavelengths were set to the maxima of the respective PIA responses (Figure 4.3a,c). The transients in (a,b) are normalized by their maxima. The numbers show the timescale of the respective processes. PL is integrated in 580-850 nm region (SI, Figure S4.3).

The PIA signals in all SSMs decay with a single exponential time of several nanoseconds: mTPA-DCV SSM produces the longest lifetime of 3.3 ns while the mTPA-Rh exhibits the shortest lifetime of 2 ns. Since the excited state lifetime depends on the transition energy and the transition dipole moment, it is not surprising that the lifetimes are different for different molecules. Note that even though the torsional deformation leads to some PL quenching, the

molecule remains in the excited state as no fast decay is observed in PIA measurements (Figure 4.4b, solid symbols).

In the solid films, both PL and PIA signals decay significantly faster compared to the isolated molecules (Figure 4.4a,b). 70-95% of PL decays within first 20-70 ps in the SSM films (Figure 4.4a, open symbols), indicating fast depletion of the exciton population either via decay to the ground state or dissociation into polarons. In contrast, the PIA signals last much longer and demonstrate biexponential dynamics with the fast part decaying within tens of ps and the slow part decaying on the nanosecond timescale (Figure 4.4b, open symbols). The fast component of the PIA signal is generally slower as compared to the PL decay time. This indicates interconversion of the initially photogenerated excitons to the polaron pairs, which slows down the decay of the PIA signals probed at the polaron response maxima.

To verify this assumption, we measured the dynamical shift of the PIA spectra (Figure 4.4c): since the response of intramolecular (CT-)excitons is red-shifted compared to the polaron response, a dynamical blue-shift of the spectrum is expected when the relative share of the polaron pairs increases. This is indeed the case: the PIA spectra gradually shift to higher energies in all studied films, and the shift is more prominent for the molecules where polaron and exciton responses are better separated (e.g. for TPA-DCV and mTPA-Rh). The spectral dynamics at the timescale of tens of ps perfectly match the PL decay times in films, which is in line with the assumption of exciton-to-polaron conversion. Note that the magnitude of spectral diffusion is correlated with the PIA decay times probed at polaron absorption maxima: for the compounds with prominent energy shift (i.e. TPA-DCV and mTPA-Rh) the PIA decay is considerably slower compared to the PL decay (Figure 4.4a,b). This is due to the interplay between exciton and polaron responses in the PIA signal. As the exciton PIA response is red-shifted compared to the polaron response (Figure 4.3), at the early timescales the maximum of PIA spectra is blue-shifted relative to the probe wavelength, i.e. the probe wavelength is detuned from the precise resonance. At the later timescales, the exciton response decreases in amplitude, and the polaron response becomes prevailing. The maximum of the PIA spectrum shifts toward the probe wavelength making it on-resonance. Therefore, the decay times of PIA signal probed at the polaron maximum is determined by two factors: (i) depopulation of the excited state (be it polarons or excitons) and (ii) dynamical spectral response due to the exciton-to-polaron conversion.

The exciton-to-polaron conversion is further supported by the fast decay of the photoinduced anisotropy in SSM films (SI, Figure S4.2) as the transition dipole moments of the polaron pairs are not necessary correlated with the polarization of the excitation light. Furthermore, in the solid films the excitation migrates within the material, herewith losing the correlation with the polarization of the incident light.

From the PL and PIA measurements, we conclude that after 20-70 ps, the SSM films are populated mainly by polaron pairs and not by excitons. Moreover, high amplitude of fast PL decay and similarity of PIA spectra of neat films and BHJ blends suggest very high (>70%) exciton-to-polaron conversion efficiency. This is beneficial for the OSC operation as the binding energy of intermolecular polaron pairs is lower compared to the exciton binding energy due to the larger separation of the electron and the hole. This echoes the previously proposed scenario that relies on the importance of wavefunction delocalization (to increase the electron-hole separation) for efficient charge separation.[5] We further speculate that the formation of polaron pair instead of excitons likely leads to reduced filling of the interfacial CT states in the BHJs. In the case of an intermolecular polaron pair, the electron and hole belong to different donor molecules in the donor phase and, therefore, after electron transfer to an acceptor (e.g. $PC_{71}BM$) the electron and hole are well-separated spatially. This effectively prevents formation of interfacial CT-excitons where electron and hole are located at the adjusting donor and acceptor molecules at the interface. Consequently, the high V_{OC} (>0.5 eV) and J_{SC} (>8 A cm^{-2}) in SSM-based OSCs[14] may be attributed both to the decreased Coulomb attraction between electron and hole (and, therefore, increased charge collection) and reduced CT state recombination.

4.3 Conclusions

In this work, we studied the early time charge photogeneration in conjugated small molecules. As benchmark systems, four star-shaped molecules (SSMs) with two different donor cores: triphenylamine (TPA) and methoxy-triphenylamine (mTPA), and dicyanovinyl or methyldicyanovinyl (DCV) and rhodanine (Rh) acceptor groups were selected. To separate the intrinsic properties of the molecules and the collective effects, the photophysical responses of molecules isolated in a PMMA matrix and closely-packed in solid films were compared.

The linear absorption of the separated molecules depends on the particular donor-acceptor combination used: the absorption peak position varies from 499 nm to 526 nm, which is rationalized by the TD-DFT calculations. In the solid films, however, the absorption properties of the different molecules are almost similar and, therefore, are highly determined by collective effects.

For the isolated molecules, the excited state lifetime varies from 2 ns (mTPA-Rh-based molecule) to 3.5 ns (mTPA-DCV-based molecule), which is mainly determined by the radiative lifetime of the excitons. In the films, the radiative lifetime shortens significantly due to dissociation of the excitons into polaron pairs. The formation of polaron pairs is beneficial for the OSC operation as the Coulomb attraction between intermolecular electron-hole pair is significantly lower compared to the intramolecular exciton. In addition, as the electron and hole in the polaron pair are located at different molecules (although of the same donor phase), a

reduced amount of interfacial CT-excitons is expected to be formed after electron transfer to the acceptor. These lead to improved charge collection and reduced recombination in SMs-based solar cells. Therefore, enhancing the intermolecular interactions to promote exciton-to-polaron conversion appears to be a promising way towards efficiency optimization.

4.4 Methods

Sample preparation

The SSMs were synthesized as described previously in Ref. [2] for TPA-DCV, in Ref. [14] for TPA-Rh and m-TPA-Rh, and in Ref. [54] for m-TPA-DCV. All SSMs were separately dissolved in ortho-dichlorobenzene at a concentration of 10 g/l, PMMA (Sigma-Aldrich, Mw=120000 g/mol) was dissolved in ortho-dichlorobenzene at a concentration of 150 g/l. All solutions were stirred on a magnetic stirrer for at least 12 hours at 50°C. To prepare the separated SSMs in PMMA matrix, PMMA was mixed with the SSMs to achieve 1:50 SSM:PMMA molar ratio (1 SSM per 60000 PMMA monomer units, ~20 nm separation between SSMs). Matrix samples and neat films were prepared by drop-casting of 150 μl of the solution on microscope cover glass slips. Preparation of the BHJ samples is described elsewhere.[14]

Optical

Absorption spectra were measured with a Lambda-900 spectrometer. The PIA measurements were performed with a setup based on Spectra-Physics Hurricane Ti:Sapphire system and two Light Conversion TOPAS OPAs, which were used to generate excitation and probe pulses. More detailed description of the PIA setup is given elsewhere.

The isotropic PIA signal and photoinduced anisotropy were recalculated from parallel and perpendicular to the polarization of the excitation pulse PIA components as:[55]

$$\Delta T_{iso}(t) = \frac{\Delta T_{\parallel}(t) + 2 \times \Delta T_{\perp}(t)}{3} \tag{4.1}$$

$$r(t) = \frac{\Delta T_{\parallel}(t) - \Delta T_{\perp}(t)}{3 \times \Delta T_{iso}} \tag{4.2}$$

The angle α between polarization of excitation pulse and photoinduced dipole moment was calculated from the anisotropy value *r*:[55]

$$r = r_0(1 - \frac{3}{2} sin^2(\alpha)) \tag{4.3}$$

Time-resolved PL was measured at a Hamamatsu C5680 streak-camera. The excitation wavelengths of 510 and 550 nm were selected from the white light supercontinuum generated from a Mira Ti:sapphire laser output in a Newport SCG-800 hollow fiber.

4.5 Supporting Information

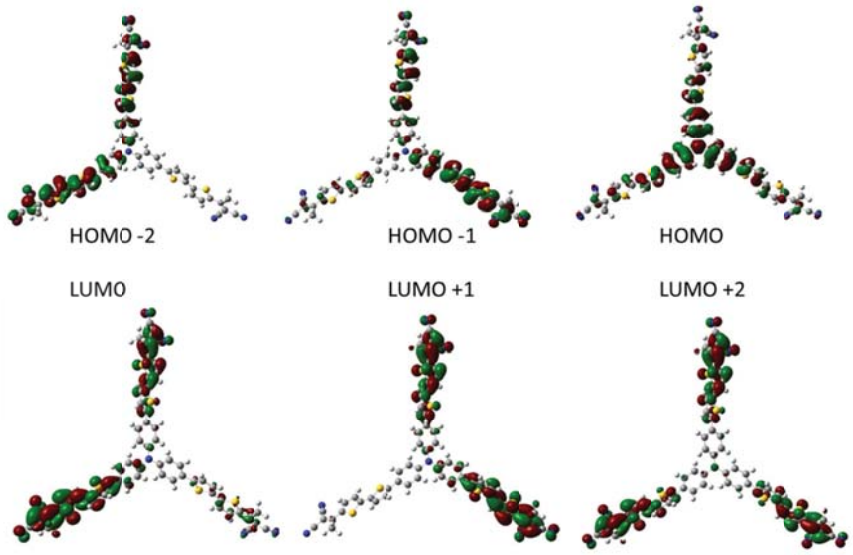

Figure S4.1 Shape of the frontier molecular orbitals (indicated) for TPA-DCV as derived from the DFT calculations. For other molecules, refer to Ref. [43].

4.5.1 Anisotropy dynamics

To gain more information about the excited state dynamics, we measured the photoinduced anisotropy. The photoinduced anisotropy provides valuable information on intra- *vs.* intermolecular dynamics of the photoexcited species[3,56-58] as it depends on the mutual orientation of the polarization of the incoming light and the transition dipole moment of the excited state. In an isotropic system of non-interacting dipoles, the maximal anisotropy is 0.4 if the transition dipoles for ground-state absorption and photoinduced absorption are parallel.[55]

In the PMMA matrix, the anisotropy is much lower than its maximum value of 0.4 for all SSMs (~0.1 for TPA-based and ~0.05 for mTPA-based molecules). This indicates instantaneous change in the direction of the transition dipole moment of the excited state by 45-50°. Due to the high symmetry of the SSMs, the lowest excited state is doubly degenerate and the two states are characterized by different distribution of the electron densities[43] and by orthogonal transition dipole moments.[3] Therefore, upon photoexcitation of the molecule to one of the excited state,

ultrafast interconversion occurs between the degenerate states which leads to the twist of the transition dipole moment.

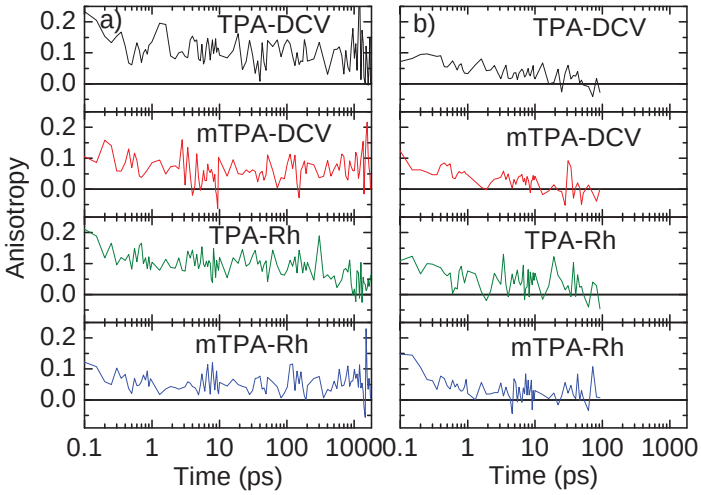

Figure S4.2 Anisotropy dynamics for SSMs in (a) PMMA matrix and (b) solid films. Excitation wavelengths were (a) 510 nm and (b) 550 nm, probe wavelengths were set to the maxima of the respective PIA responses (Figure 4.3a,d).

In the films, the anisotropy is systematically lower and decays to zero within ~10 ps timescale for all SSMs studied. The reason of the fast anisotropy decay is two-fold. First, as discussed earlier, due to the close packing of the molecules, the polaron pairs are formed whose transition dipole moments are not necessary correlated with the polarization of the excitation light. Second, in the solid film, the excitations migrate within the material, losing the correlation with the polarization of the incident light. Therefore, in the solid films, the anisotropy reflects the *inter*molecular dynamics of the excitons/polarons and do not provide any information about the *intra*molecular processes.

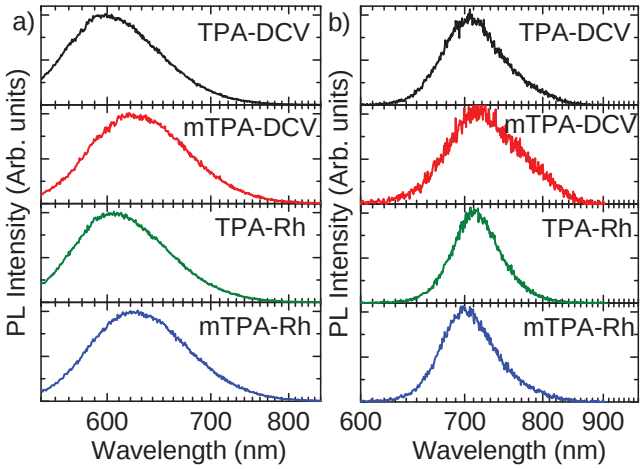

Figure S4.3 PL spectra for SSMs in (a) PMMA matrices after 510 nm excitation and (b) films after 550 nm excitation.

Author Contributions

OVK prepared the samples, performed linear absorption, PIA and PL measurements and analyzed the data; YNL, ANS and SAP synthetized the molecules; BF, YO, RL and JC performed (TD-)DFT calculations (see Ref. [43] for details), MSP supervised the research.

References

1 S. Ponomarenko, Y. Luponosov, J. Min, A. N. Solodukhin, N. Surin, M. Shcherbina, S. N. Chvalun, T. Ameri, and C. J. Brabec. Design of Donor-Acceptor Star-Shaped Oligomers for Efficient Solution-Processible Organic Photovoltaics. *Faraday Discuss.* no. 174, 2014, p. 313.

2 J. Min, Y. N. Luponosov, A. Gerl, M. S. Polinskaya, S. M. Peregudova, P. V. Dmitryakov, A. V. Bakirov, M. A. Shcherbina, S. N. Chvalun, S. Grigorian *et al.* Alkyl Chain Engineering of Solution-Processable Star-Shaped Molecules for High-Performance Organic Solar Cells. *Adv. Energy Mater.* **4** no. 5, 2014, p. 1301234.

3 O. V. Kozlov, Y. N. Luponosov, S. A. Ponomarenko, N. Kausch-Busies, D. Y. Paraschuk, Y. Olivier, D. Beljonne, J. Cornil, and M. S. Pshenichnikov. Ultrafast Charge Generation Pathways in Photovoltaic Blends Based on Novel Star-Shaped Conjugated Molecules. *Adv. Energy Mater.* **5** no. 7, 2015, p. 1401657.

4 Z. M. Tang, T. Lei, J. L. Wang, Y. G. Ma, and J. Pei. Star-Shaped Donor-π-Acceptor Conjugated Molecules: Synthesis, Properties, and Modification of Their Absorptions Features. *J. Org. Chem.* **75** no. 11, 2010, p. 3644.

5 A. A. Bakulin, A. Rao, V. G. Pavelyev, P. H. M. van Loosdrecht, M. S. Pshenichnikov, D. Niedzialek, J. Cornil, D. Beljonne, and R. H. Friend. The Role of Driving Energy and Delocalized States for Charge Separation in Organic Semiconductors. *Science* **335** no. 6074, 2012, p. 1340.

6 R. Tautz, E. Da Como, T. Limmer, J. Feldmann, H.-J. Egelhaaf, E. von Hauff, V. Lemaur, D. Beljonne, S. Yilmaz, I. Dumsch *et al.* Structural Correlations in the Generation of Polaron Pairs in Low-Bandgap Polymers for Photovoltaics. *Nat. Commun.* **3**, 2012, p. 970.

7 Q. Zhang, B. Kan, F. Liu, G. Long, X. Wan, X. Chen, Y. Zuo, W. Ni, H. Zhang, M. Li *et al.* Small-Molecule Solar Cells with Efficiency over 9%. *Nat. Photonics* **9** no. 1, 2015, p. 35.

8 W. Ni, M. Li, F. Liu, X. Wan, H. Feng, B. Kan, Q. Zhang, H. Zhang, and Y. Chen. Dithienosilole-Based Small-Molecule Organic Solar Cells with an Efficiency over 8%: Investigation of the Relationship between the Molecular Structure and Photovoltaic Performance. *Chem. Mater.* **27** no. 17, 2015, p. 6077.

9 K. Kawashima, Y. Tamai, H. Ohkita, I. Osaka, and K. Takimiya. High-Efficiency Polymer Solar Cells With Small Photon Energy Loss. *Nat. Commun.* **6**, 2015, p. 10085.

10 Q. An, F. Zhang, Q. Sun, J. Wang, L. Li, J. Zhang, W. Tang, and Z. Deng. Efficient Small Molecular Ternary Solar Cells by Synergistically Optimized Photon Harvesting and Phase Separation. *J. Mater. Chem. A* **3** no. 32, 2015, p. 16653.

11 G. J. Hedley, A. J. Ward, A. Alekseev, C. T. Howells, E. R. Martins, L. A. Serrano, G. Cooke, A. Ruseckas, and I. D. W. Samuel. Determining the Optimum Morphology in High-Performance Polymer-Fullerene Organic Photovoltaic Cells. *Nat. Commun.* **4**, 2013, p. 2867.

12 M. S. Siraj. Improvement of Power Conversion Efficiency of P3HT/PCBM Polymer Solar Cell Systems by Optimization of the Process Steps. *Synth. Commun.* **42** no. 13, 2012, p. 1922.

13 J. Min, Y. N. Luponosov, Z.-G. Zhang, S. A. Ponomarenko, T. Ameri, Y. Li, and C. J. Brabec. Interface Design to Improve the Performance and Stability of Solution-Processed Small Molecule Conventional Solar Cells. *Adv. Energy Mater.* **4** no. 16, 2014, p. 1400816.

14 Y. N. Luponosov, J. Min, A. N. Solodukhin, O. V. Kozlov, M. A. Obrezkova, S. M. Peregudova, T. Ameri, S. N. Chvalun, M. S. Pshenichnikov, C. J. Brabec *et al.* Effects of Electron-Withdrawing Group and Electron-Donating Core Combinations on Physical Properties and Photovoltaic Performance in D-π-A Star-Shaped Small Molecules. *Org. Electron.* **32**, 2016, p. 157.

15 M. Schwarze, W. Tress, B. Beyer, F. Gao, R. Scholz, C. Poelking, K. Ortstein, A. A. Günther, D. Kasemann, D. Andrienko *et al.* Band Structure Engineering in Organic Semiconductors. *Science* **352** no. 6292, 2016, p. 1446.

16 S. Torabi, F. Jahani, I. Van Severen, C. Kanimozhi, S. Patil, R. W. A. Havenith, R. C. Chiechi, L. Lutsen, D. J. M. Vanderzande, T. J. Cleij *et al.* Strategy for Enhancing the Dielectric Constant of Organic Semiconductors Without Sacrificing Charge Carrier Mobility and Solubility. *Adv. Funct. Mater.* **25** no. 1, 2015, p. 150.

17 J. Roncali, P. Leriche, and P. Blanchard. Molecular Materials for Organic Photovoltaics: Small is Beautiful. *Adv. Mater.* **26** no. 23, 2014, p. 3821.

18 Y. Liu, Y. M. Yang, C. C. Chen, Q. Chen, L. Dou, Z. Hong, G. Li, and Y. Yang. Solution-Processed Small Molecules Using Different Electron Linkers for High-Performance Solar Cells. *Adv. Mater.* **25** no. 33, 2013, p. 4657.

19 L. Li, L. Xiao, H. Qin, K. Gao, J. Peng, Y. Cao, F. Liu, T. P. Russell, and X. Peng. High-Efficiency Small Molecule-Based Bulk-Heterojunction Solar Cells Enhanced by Additive Annealing. *ACS Appl. Mater. Interfaces* **7** no. 38, 2015, p. 21495.

20 B. Walker, C. Kim, and T.-Q. Nguyen. Small Molecule Solution-Processed Bulk Heterojunction Solar Cells. *Chem. Mater.* **23** no. 3, 2010, p. 470.

21 Y. Lin, Y. Li, and X. Zhan. Small Molecule Semiconductors for High-Efficiency Organic Photovoltaics. *Chem. Soc. Rev.* **41** no. 11, 2012, p. 4245.

22 K. Do, C. Kim, K. Song, S. J. Yun, J. K. Lee, and J. Ko. Efficient Planar Organic Semiconductors Containing Fused Triphenylamine for Solution Processed Small Molecule Organic Solar Cells. *Sol. Energy Mater. Sol. Cells* **115**, 2013, p. 52.

23 J. W. Choi, C.-H. Kim, J. Pison, A. Oyedele, D. Tondelier, A. Leliege, E. Kirchner, P. Blanchard, J. Roncali, and B. Geffroy. Exploiting the Potential of 2-((5-(4-(diphenylamino)phenyl)thiophen-2-yl)methylene)malononitrile as an Efficient Donor Molecule in Vacuum-Processed Bulk-Heterojunction Organic Solar Cells. *RSC Adv.* **4** no. 10, 2014, p. 5236.

24 B. Kan, M. Li, Q. Zhang, F. Liu, X. Wan, Y. Wang, W. Ni, G. Long, X. Yang, H. Feng *et al.* A Series of Simple Oligomer-like Small Molecules Based on Oligothiophenes for Solution-Processed Solar Cells with High Efficiency. *J. Am. Chem. Soc.* **137** no. 11, 2015, p. 3886.

25 Y. Liu, C.-C. Chen, Z. Hong, J. Gao, Y. Yang, H. Zhou, L. Dou, G. Li, and Y. Yang. Solution-Processed Small-Molecule Solar Cells: Breaking the 10% Power Conversion Efficiency. *Sci. Rep.* **3**, 2013, p. 3356.

26 X. Che, X. Xiao, J. D. Zimmerman, D. Fan, and S. R. Forrest. High-Efficiency, Vacuum-Deposited, Small-Molecule Organic Tandem and Triple-Junction Photovoltaic Cells. *Adv. Energy Mater.* **4** no. 18, 2014, p. 1400568.

27 Y.-W. Su, S.-C. Lan, and K.-H. Wei. Organic Photovoltaics. *Mater. Today* **15** no. 12, 2012, p. 554.

28 M.-H. Jao, H.-C. Liao, and W.-F. Su. Achieving a High Fill Factor for Organic Solar Cells. *J. Mater. Chem. A* **4** no. 16, 2016, p. 5784.

29 I. Lange, J. Kniepert, P. Pingel, I. Dumsch, S. Allard, S. Janietz, U. Scherf, and D. Neher. Correlation Between the Open Circuit Voltage and the Energetics of Organic Bulk Heterojunction Solar Cells. *J. Phys. Chem. Lett.* **4** no. 22, 2013, p. 3865.

30 S. Y. Leblebici, T. L. Chen, P. Olalde-Velasco, W. Yang, and B. Ma. Reducing Exciton Binding Energy by Increasing Thin Film Permittivity: An Effective Approach To Enhance Exciton Separation Efficiency in Organic Solar Cells. *ACS Appl. Mater. Interfaces* **5** no. 20, 2013, p. 10105.

31 J. C. Blakesley and D. Neher. Relationship Between Energetic Disorder and Open-Circuit Voltage in Bulk Heterojunction Organic Solar Cells. *Physical Review B* **84** no. 7, 2011, p. 075210.

32 K. Vandewal, K. Tvingstedt, A. Gadisa, O. Inganas, and J. V. Manca. On the Origin of the Open-Circuit Voltage of Polymer-Fullerene Solar Cells. *Nat. Mater.* **8** no. 11, 2009, p. 904.

33 N. K. Elumalai and A. Uddin. Open Circuit Voltage of Organic Solar Cells: An in-depth Review. *Energy Environ. Sci.* **9** no. 2, 2016, p. 391.

34 D. Dan, S. Suling, Z. Jing, H. Chang, Z. Zhanjun, and L. Yongfang. Solution-Processable Star-Shaped Photovoltaic Organic Molecule with Triphenylamine Core and Thieno[3,2-b]thiophene–dicyanovinyl Arms. *Org. Electron.* **13**, 2012, p. 2546.

35 J. Zhang, D. Deng, C. He, Y. He, M. Zhang, Z.-G. Zhang, Z. Zhang, and Y. Li. Solution-Processable Star-Shaped Molecules with Triphenylamine Core and Dicyanovinyl Endgroups for Organic Solar Cells. *Chem. Mater.* **23** no. 3, 2011, p. 817.

36 H. X. Shang, H. J. Fan, Y. Liu, W. P. Hu, Y. F. Li, and X. W. Zhan. A Solution-Processable Star-Shaped Molecule for High-Performance Organic Solar Cells. *Adv. Mater.* **23** no. 13, 2011, p. 1554.

37 Z. H. Lin, J. Bjorgaard, A. G. Yavuz, and M. E. Kose. Low Band Gap Star-Shaped Molecules Based on Benzothia(oxa)diazole for Organic Photovoltaics. *J. Phys. Chem. C* **115** no. 30, 2011, p. 15097.

38 N. Metri, X. Sallenave, L. Beouch, C. Plesse, F. Goubard, and C. Chevrot. New Star-Shaped Molecules Derived from Thieno 3,2-b thiophene Unit and Triphenylamine. *Tetrahedron Lett.* **51** no. 50, 2010, p. 6673.

39 F. Zhang, Z. Zhuo, J. Zhang, X. Wang, X. Xu, Z. Wang, Y. Xin, J. Wang, J. Wang, W. Tang *et al.* Influence of $PC_{60}BM$ or $PC_{70}BM$ as Electron Acceptor on the Performance of Polymer Solar Cells. *Sol. Energy Mater. Sol. Cells* **97**, 2012, p. 71.

40 C.-W. Chu, H. Yang, W.-J. Hou, J. Huang, G. Li, and Y. Yang. Control of the Nanoscale Crystallinity and Phase Separation in Polymer Solar Cells. *Appl. Phys. Lett.* **92** no. 10, 2008, p. 103306.

41 Y. Toshihiro, T. Tetsuya, S. Jun, and S. Kazuhiro. Highly Efficient Organic Thin-Film Solar Cells Based on Poly(3-hexylthiophene) and Soluble C_{70} Fullerene Derivative. *Japanese Journal of Applied Physics* **47** no. 2S, 2008, p. 1230.

42 E. Ripaud, Y. Olivier, P. Leriche, J. Cornil, and J. Roncali. Polarizability and Internal Charge Transfer in Thiophene-Triphenylamine Hybrid π-Conjugated Systems. *J. Phys. Chem. B* **115** no. 30, 2011, p. 9379.

43 O. V. Kozlov, Y. N. Luponosov, A. N. Solodukhin, B. Flament, Y. Olivier, R. Lazzaroni, J. Cornil, S. A. Ponomarenko, and M. S. Pshenichnikov. Ultrafast Exciton-to-Polaron Conversion in Densely-Packed Small Organic Semiconducting Molecules. *Advanced Optical Materials* **5** no. 7, 2017, p. 1700024.

44 H. van Eersel, R. A. J. Janssen, and M. Kemerink. Mechanism for Efficient Photoinduced Charge Separation at Disordered Organic Heterointerfaces. *Adv. Funct. Mater.* **22** no. 13, 2012, p. 2700.

45 L. Goris, A. Poruba, L. Hod'akova, M. Vanecek, K. Haenen, M. Nesladek, P. Wagner, D. Vanderzande, L. De Schepper, and J. V. Manca. Observation of the Subgap Optical Absorption in Polymer-Fullerene Blend Solar Cells. *Appl. Phys. Lett.* **88** no. 5, 2006, p. 052113

46 R. Coehoorn, W. F. Pasveer, P. A. Bobbert, and M. A. J. Michels. Charge-Carrier Concentration Dependence of The Hopping Mobility in Organic Materials with Gaussian Disorder. *Physical Review B* **72** no. 15, 2005, p. 155206.

47 G. M. Akselrod, F. Prins, L. V. Poulikakos, E. M. Y. Lee, M. C. Weidman, A. J. Mork, A. P. Willard, V. Bulović, and W. A. Tisdale. Subdiffusive Exciton Transport in Quantum Dot Solids. *Nano Lett.* **14** no. 6, 2014, p. 3556.

48 J. G. Muller, J. M. Lupton, J. Feldmann, U. Lemmer, M. C. Scharber, N. S. Sariciftci, C. J. Brabec, and U. Scherf. Ultrafast Dynamics of Charge Carrier Photogeneration and Geminate Recombination in Conjugated Polymer:Fullerene Solar Cells. *Physical Review B* **72** no. 19, 2005, p. 195208

49 Z. Xu and B. Hu. Photovoltaic Processes of Singlet and Triplet Excited States in Organic Solar Cells. *Adv. Funct. Mater.* **18** no. 17, 2008, p. 2611.

50 A. E. Jailaubekov, A. P. Willard, J. R. Tritsch, W.-L. Chan, N. Sai, R. Gearba, L. G. Kaake, K. J. Williams, K. Leung, P. J. Rossky *et al.* Hot Charge-Transfer Excitons Set the Time Limit for Charge Separation at Donor/Acceptor Interfaces in Organic Photovoltaics. *Nat. Mater.* **12** no. 1, 2013, p. 66.

51 U. B. Cappel, D. Moia, A. Bruno, V. Vaissier, S. A. Haque, and P. R. F. Barnes. Evidence for Photo-Induced Charge Separation Between Dye Molecules Adsorbed to Aluminium Oxide Surfaces. *Sci. Rep.* **6**, 2016, p. 21276.

52 X. He, G. Zhu, J. Yang, H. Chang, Q. Meng, H. Zhao, X. Zhou, S. Yue, Z. Wang, J. Shi *et al.* Photogenerated Intrinsic Free Carriers in Small-molecule Organic Semiconductors Visualized by Ultrafast Spectroscopy. *Sci. Rep.* **5**, 2015, p. 17076.

53 E. Salamatova, O. V. Kozlov, Y. N. Luponosov, A. N. Solodukhin, V. Y. Toropynina, S. A. Ponomarenko, and M. S. Pshenichnikov. Visualization of Molecular Excitons Diffusion. *Proc. SPIE* **9923**, 2016, p. 99230K.

54 Y. N. Luponosov, J. Min, A. N. Solodukhin, A. V. Bakirov, P. V. Dmitryakov, M. A. Shcherbina, S. M. Peregudova, G. V. Cherkaev, S. N. Chvalun, C. J. Brabec *et al.* Star-Shaped D-π-A Oligothiophenes with a Tris(2-methoxyphenyl)amine Core and Alkyldicyanovinyl Groups: Synthesis and Physical and Photovoltaic Properties. *J. Mater. Chem. C* **4** no. 29, 2016, p. 7061.

55 R. G. Gordon. Molecular Collisions and Depolarization of Fluorescence in Gases. *J. Chem. Phys.* **45** no. 5, 1966, p. 1643.

56 O. Kozlov, Y. Luponosov, S. Ponomarenko, D. Paraschuk, N. Kausch-Busies, and M. Pshenichnikov. in *Ultrafast Dynamics in Molecules, Nanostructures and Interfaces Optics and Photonics* (eds G. G. Gurzadyan, G. Lanzani, C. Soci, & T. C Sum) 169 (World Scientific Publishing Co. Pte. Ltd., Singapore, 2014).

57 L. G. Kaake, J. J. Jasieniak, R. C. Bakus, G. C. Welch, D. Moses, G. C. Bazan, and A. J. Heeger. Photoinduced Charge Generation in a Molecular Bulk Heterojunction Material. *J. Am. Chem. Soc.* **134** no. 48, 2012, p. 19828.

58 A. A. Bakulin, D. S. Martyanov, D. Y. Paraschuk, M. S. Pshenichnikov, and P. H. M. van Loosdrecht. Ultrafast Charge Photogeneration Dynamics in Ground-State Charge-Transfer Complexes Based on Conjugated Polymers. *J. Phys. Chem. B* **112** no. 44, 2008, p. 13730.

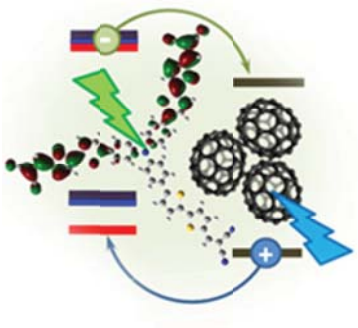

Chapter 5

Ultrafast Charge Generation Pathways in Photovoltaic Blends Based on Novel Star-Shaped Conjugated Molecules

The quest for new materials is one of the main factors propelling recent advances in organic photovoltaics. Star-shaped small molecules (SSMs) have been proven promising candidates as perspective donor material due to the increase in numbers of excitation pathways caused by the degeneracy of the LUMO level. In order to unravel the pathways of the initial photon-to-charge conversion, the photovoltaic blends based on three different SSMs with a generic structure of N(Phenylene-*n*Thiophene-Dicyanovinyl-Alkyl)$_3$ (*n*=1-3), and [6,6]-phenyl-C_{71}-butyric acid methyl ester ($PC_{71}BM$) acceptor are investigated by ultrafast photoinduced absorption spectroscopy assisted by Density Functional Theory calculations. It is shown that both electron transfer from SSMs to $PC_{71}BM$ and hole transfer from $PC_{71}BM$ to SSMs are equally significant for generation of long-lived charges. In contrast, intramolecular (intraSSM) charge separation results in geminate recombination and therefore constitutes a loss channel. Overall, up to 60% of long-lived separated charges are generated at the optimal $PC_{71}BM$ concentrations. The obtained results suggest that further improvement of the SSM-based solar cells is feasible via optimization of blend morphology and by suppressing the intraSSM recombination channel.

This Chapter is based on the following publication:
Oleg V. Kozlov, Yuriy N. Luponosov, Sergei A. Ponomarenko, Nina Kausch-Busies, Dmitry Yu. Paraschuk, Yoann Olivier, David Beljonne, Jérôme Cornil, and Maxim S. Pshenichnikov, *Adv. Energy Mater.* **5**(7), 1401657 (2015)

5.1 Introduction

Bulk-heterojunction (BHJ) organic solar cells (OSC) based on solution-processable small molecules (SM) donors have recently attracted much interest as an alternative to more conventional polymer-based OSCs.[1-8] SM-based OSCs combine advantages of polymers - flexibility, solution processability, ease of manufacturing etc., with benefits of small molecules such as high purity, batch-to-batch reproducibility, well-defined molecular structure and molecular weight, and easy mass-scale production.[9-14] Nowadays, both linear and star-shaped SMs are successfully used as donors in OSCs.[15-24] OSCs based on linear SMs have been studied more thoroughly,[15,16] and recently demonstrated power conversion efficiency (PCE) as high as 10%.[17] OSCs based on star-shaped molecules (SSMs) have also shown impressive results of PCE exceeding 5%.[18] SSMs have a number of attractive advantages over linear conjugated oligomers since the LUMO orbital degeneracy increases the number of pathways for light conversion.[19] Furthermore, the SSMs have a propensity to stack in films, thereby providing enhanced π-π interactions between neighboring molecules to form pathways for hole transport.[20,25] Finally, high solubility and low anisotropy of optical and electrochemical properties[21-24] represent another attractive feature of SSMs.

The most common SSMs are push-pull materials with triphenylamine (TPA) core as a donor, benzothiazole[5,9,14] or dicyanovinyl (DCV)[12,13,19,26-29] as acceptor units, and oligothiophene arms as π-bridges.[30] Such SSMs have been thoroughly investigated by Roncali and coworkers, who demonstrated PCE of ~2% in planar heterojunction SSM:C_{60} OSC.[19,26,31-33] Recently, a number of TPA-based SSMs with different lengths of the solubilizing alkyl chain ends and thiophene arms were proposed and synthesized.[20,28] Such SSMs demonstrated enhanced solubility in organic solvents, high stability, good hole mobility (>10^{-3} $cm^2/V{\cdot}s$),[20] broad absorption spectrum in the visible region, and homogeneous packing in film. Additionally, ultrafast exciton-to polaron conversion occurs in SSM phase which is beneficial for the OSC operation[34] (see Chapter 4 for details). Altogether, these developments have led to a PCE increase to more than 5% for bulk heterojunction (BHJ) based devices,[18] which put such structures at the frontline of perspective materials for OSCs.[9,13,19,27]

One of the key processes occurring in the OSC BHJ active layer is the photogeneration of free charges, which includes the following steps: photoexcitation of the donor (acceptor), exciton formation, and its subsequent dissociation at the donor-acceptor interface.[35] These processes take place at a wide range of ultrafast time scales (from tens of fs to ns's), and their efficiency directly influences the final PCE of the OSC.[36] Efficient charge generation is counterbalanced by loss processes such as exciton annihilation, geminate and non-geminate charge recombination, charge-transfer (CT) state trapping etc.[36] These losses lead to reduced photocurrent, voltage, and

fill factor of the OSC and subsequently to reduced PCE.[37] Optimization of the active layer to minimize the losses calls for understanding of pathways to efficient long-lived charge generation. Insofar, this fundamental issue has been very little addressed for BHJ active layers based on SSMs.

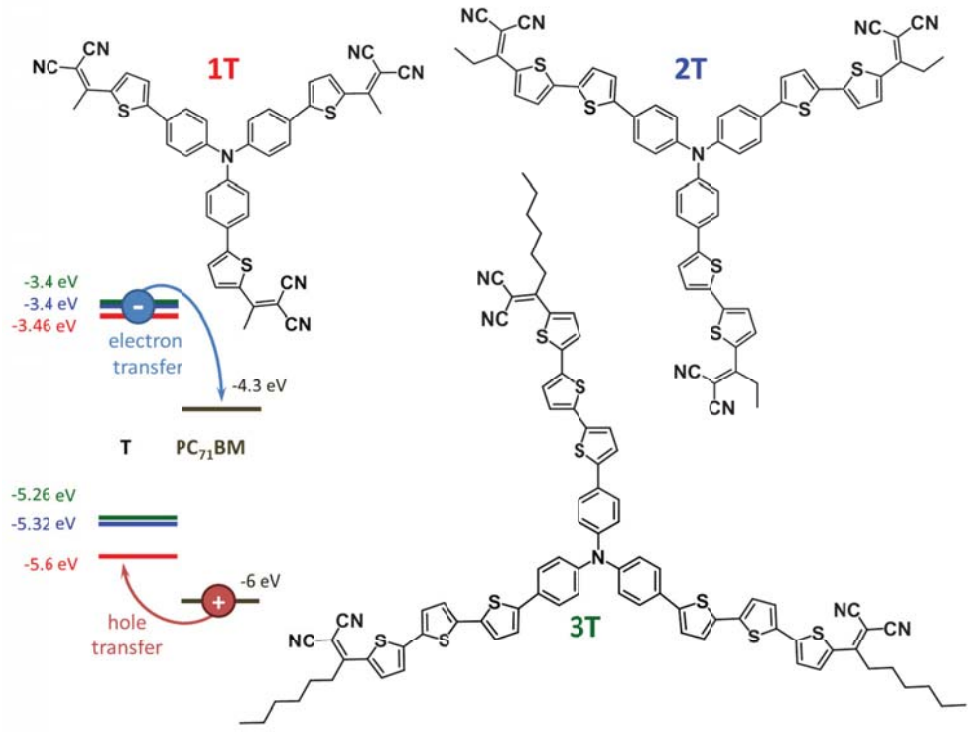

Figure 5.1 Chemical structure of the SSMs. Notations 1T (in red), 2T (in blue) and 3T (in green) refer to the number of thiophene rings in the star arm. The inset shows the frontier energy levels for the SSMs[20,28] and $PC_{71}BM$,[38] as obtained from cyclic voltammetry.

In this Chapter, charge generation and recombination processes are studied in thin films of three different SSMs with N(Phenylene-*n*Thiophene-Dicyanovinyl-Alkyl)$_3$ structure (Figure 5.1), as well as in their blends with [6,6]-phenyl-C_{71}-butyric acid methyl ester ($PC_{71}BM$) acceptor. The molecules mainly differ from each other by the length of the conjugated arm (*n* = 1, 2 or 3 thiophene rings). Charge dynamics are probed by ultrafast polarization-sensitive visible-pump – IR-probe photoinduced absorption spectroscopy (PIA). The experimental results are further supported by quantum-chemical calculations at the (Time-Dependent) Density Functional Theory (TD-DFT) level to characterize the absorption spectra of neutral and singly positively charged SSMs. From the PIA transients we conclude that the long-lived charges in the blends are

produced via *inter*molecular channel on the timescale up to 10's ps. Charges separated within the same SSM and/or trapped in the interfacial SSM:$PC_{71}BM$ CT states recombine via *intra*molecular channel on the timescale of 100's ps, providing the main loss pathway. For the blends with optimal $PC_{71}BM$ concentration, up to 30% of the long-lived charges are generated via hole transfer upon $PC_{71}BM$ photoexcitation, underlining the significance of this pathway. The efficiency of hole harvesting is limited by the exciton diffusion length in $PC_{71}BM$ domains which calls for blend morphology optimization. For each star-shaped donor molecule, the optimal SSM:$PC_{71}BM$ concentration in the blend is assessed that allows generation of up to 60% of long-lived charges.

In a broader context, the results presented herein demonstrate how ultrafast spectroscopy combined with quantum-chemistry calculations can be used to reveal pathways of charge generation and losses, thereby providing an efficient means for optimization of OSCs materials. We envision that this approach is not limited by OPV but can also be extended to emerging fields of hybrid[39,40] and perovskite-based[41] photovoltaics.

5.2 Experimental Results

5.2.1 UV-VIS Absorption

Thin films of neat SSMs exhibit strong absorption in the visible region (Figure 5.2a), with two absorption bands centered at ~400 nm and ~530 nm. From time-dependent Density Functional Theory (TD-DFT) calculations (see Ref. [42] for details) both transition are ascribed to intramolecular charge transfer (CT).[9,13,19] The high-energy band is red-shifted with the elongation of the conjugated arm, while the position of the low-energy band remains almost unchanged for 2T and 3T molecules most probably due to intramolecular distortions. Moreover, the band at higher energy gains oscillator strength compared to the lowest absorption peak. The presence of *two* intense absorption bands in the visible extends the light harvesting capacities of the chromophores.

The absorption spectra calculated for the neutral molecules with an imposed C_3 symmetry do not match well the corresponding experimental spectra (Figure 5.2b; calculations were performed by Y. Olivier and J. Cornil, University of Mons, Belgium). While the calculations yield a red shift for the two bands with elongation of the conjugated arm going from 1T to 2T in consistency with the experimental spectra, this effect is exaggerated for the low-energy absorption band, and the calculated ratio between the intensities of the two bands is largely overestimated. The origin of this discrepancy is rooted in the conformational disorder present in the thin films due to the relative floppiness of the interring torsions. To illustrate this effect, TD-DFT calculations on multiple conformations were performed with intentionally-introduced

disorder in the interring torsion angles (by selecting randomly for the phenyl-thiophene and thiophene-thiophene torsion angles a value ranging from 0 to 60 degrees) in the three arms of the molecules. The averaged absorption spectrum is shown in Figure 5.2b. The comparison with experiment is here significantly improved (when accounting for a rigid shift of 0.5 eV which most probably arises from intermolecular interactions in the solid state as well as solid-state polarization effects linked to the stabilization of the local permanent dipole in the excited state via induced dipoles in the neighboring molecules). These calculations also allow capturing the large spectral widths measured for the two absorption bands.

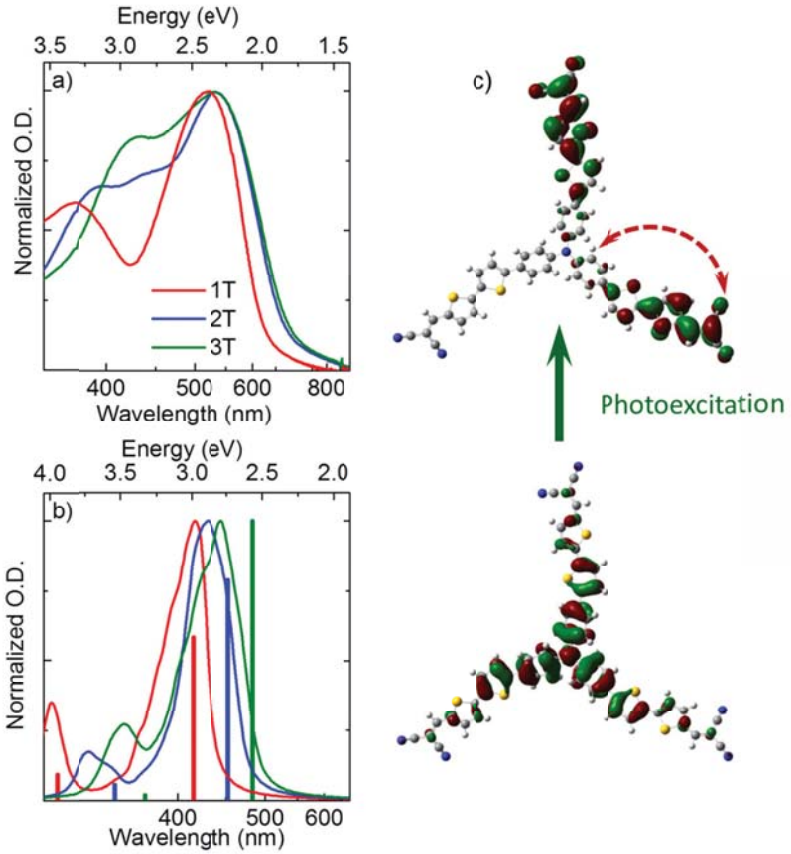

Figure 5.2 (a) Normalized absorption spectra of neat SSM films. (b) Calculated absorption spectra for SSMs. Vertical bars show the transition energies for the 1T, 2T, and 3T SSMs obtained from a TD-DFT calculation with the functional BHHLYP and the 6-31G(d,p) basis set, on the basis of a geometry optimized with the C3 symmetry at the DFT level. The solid curves show absorption spectra for the 1T, 2T, and 3T SSMs calculated from averaging TD-DFT spectra obtained for geometries where the interring torsion angles are varied randomly between 0 and 60 degrees. Note the rigid blue shift of 0.5 eV of the calculated spectra compared to the experimental data. (c) Distribution of the electron density in the HOMO and LUMO levels for the 2T SSM, as derived from the DFT calculations. Note the charge-transfer character of the transition.

Without loss in generality, we analyzed the nature of the two bands on the basis of the results obtained for the molecule with an imposed C_3 symmetry. Since the three branches of the molecule are interacting via the central core, the molecular levels are not triply degenerate, as it might have been intuitively expected. The low-energy absorption band of the three SSMs originates from two degenerate excited states mostly described by a HOMO to LUMO or LUMO[+1] transition, respectively.[42] In view of the shape of the orbitals, there is a clear reshuffling of the electronic density upon excitation, thus leading to an intramolecular charge-transfer character of the absorption band[42]. This situation is illustrated in Figure 5.2c for the HOMO-LUMO transition in 2T (see also Chapter 4, Figure S4.1 for exemplary charge density distributions in 2T molecule). Indeed, the HOMO is principally localized around the center of the molecule and over the three donor branches while the LUMO or LUMO+1 have large weights at the outer parts, over one or two acceptor units. The high-energy absorption band is described by a larger mixing of one-electron excitations (with their weighting factor depending on the actual torsion angles in non-planar structures).[42] Thus, based on these TD-DFT results, we question the usual assignment of these two bands as being π-π^* *vs.* CT.[9,13,19] In fact, both electronic excitations have a mixed character and, remarkably, the intensity of the high-energy absorption feature is a direct measure of the degree of conformational disorder in the SSMs.

5.2.2 Polaron Absorption

The time-dependent concentration of photogenerated charges in the blends has been evaluated via the polaron absorption of the SSMs.[43] Photogenerated charges on a conjugated molecule lead to the appearance of additional absorption bands in the near-IR region (Figure 5.a) with intensity proportional to the amount of generated charges.[43,44] This provides a simple and convenient means for tracking charge dynamics in a pump-probe arrangement. For conjugated polymers, these bands are usually located at ~1 μm (the so-called high-energy polaron band) and at ~3 μm (the low-energy band).[45,46] However, in the SSMs the band positions are expected to be different because of shorter conjugation lengths as compared to polymers. In order to localize these energetic positions, polaron spectra (i.e. dependences of the photoinduced IR response on the probe wavelength)[43] were measured. Note that in diluted solutions of SSMs and partly in their neat films, CT excitons (i.e. bound electron-hole pair residing at the same molecule) rather than polarons (i.e. a hole on a particular SSM with an electron located on another molecule) are generated upon photoexcitation (see also Chapter 4 for more detailed discussion of exciton and polaron formation and their interconversion in SSMs).

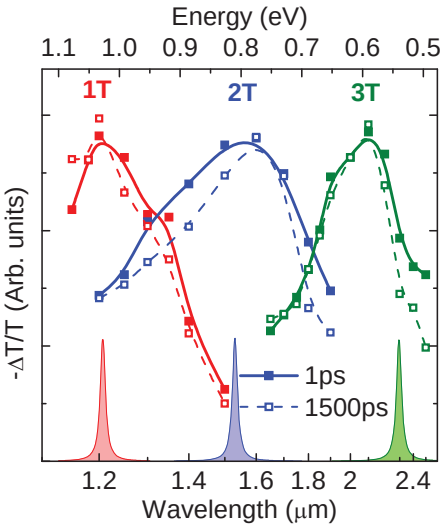

Figure 5. Normalized measured polaron spectra of the 1:1 SSM:$PC_{71}BM$ blends at 1 ps (solid symbols) and 1.5 ns (open symbols) delays, and calculated polaron peak positions broadened by a lorentzian function with a width of 0.02 eV (shaded contours). The positions of the calculated peaks are red-shifted by 0.1 eV.

The photoinduced IR absorption spectra of the 1:1 SSM:$PC_{71}BM$ blends obtained at 1 ps and 1.5 ns pump-probe delays are presented in Figure 5.b. The spectra were reconstructed from the transients taken at several probe wavelengths. All spectra show a broad intense peak in the near-IR region (below 2.6 μm); no other spectral peaks except for vibrational modes were observed in the 3-10 μm region (Supporting Information (SI), Figure S5.10) making the observed peaks lowest in energy. The peak is red-shifted with elongation of the conjugated length, i.e. with increase in the number of thiophene rings. The positions of the IR peaks are also well predicted by DFT calculations (Figure 5.b, shaded contours), providing their assignment as low-energy polaron absorption bands (as opposed to e.g. exciton absorption). Interestingly, these calculations had been performed well before the experimental spectra were measured experimentally thereby illustrating predictive power of calculations.

The lowest-energy absorption band is mostly described by a transition between the HOMO and SOMO levels (see Figure 1.2 in Chapter 1). The red shift can be intuitively understood from the fact that the HOMO level raises up with the extent of delocalization in contrast to the SOMO level which is more localized. The ~0.1 eV shift between the theoretical and experimental spectra most probably originates from the fact that the molecules are not fully symmetric in the thin films, as assumed in the calculations, and/or solid-state polarization effects.

The positions of the absorption peaks in the blends remain unchanged with the pump-probe delay which indicates no spectral relaxation due to, for instance, transient polarisability of the

environment. This is in sharp contrast with neat films of the SSMs where blue shift of ~0.5 eV was observed (SI, Figure S5.1) within ~100 ps. This blue shift is due to exciton-to-polaron conversion occurring in the neat SSM films (see Chapter 4 for detailed discussion). The minor but persistent narrowing of the polaron spectra for the blends of all three SSMs was also detected at long time delays (Figure 5.b). Most probably, it originates from the superposition of polaron and CT exciton responses with different time dynamics; in any case, this does not affect the positions of the peaks. Therefore, we selected a single probe wavelength near the respective polaron absorption maxima at 1.2, 1.7 and 2.1 μm for 1T, 2T and 3T SSMs, respectively, and consider the amplitude of the PIA response proportional to the concentration of photogenerated charges.

5.2.3 Photoinduced Absorption Dynamics

Figure 5.3 shows isotropic PIA transients for blends of all three SSMs with different fullerene content. Since the absorption of blends with different composition is not a constant (SI, Figure S5.2), the transient amplitudes were normalized by the number of absorbed photons to yield the (relative) amount of generated charges per absorbed photon. This allows for direct comparison between not only the transient dynamics but also the amount of charges generated in different blends.

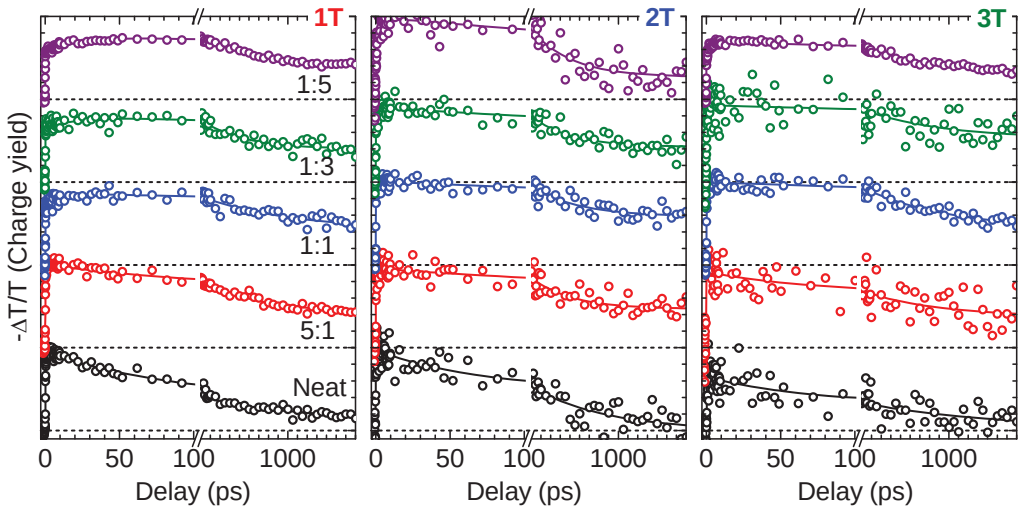

Figure 5.3 PIA isotropic transients for SSM:$PC_{71}BM$ blends at different $PC_{71}BM$ contents as indicated next to the transients. Circles represent the experimental data points while solid lines show best fits according to Equation (5.1). All transients are normalized to the number of absorbed excitation photons to allow direct comparison of their amplitudes.

For all neat films, a fast build-up of the pump-probe signal occurs around zero pump-probe delay within the apparatus function raise time. Since the amplitude of the signal is proportional to the amount of generated charges, we conclude that initial charge separation occurs within 100 fs timescale. This is consistent with instantaneous separation of photogenerated charges in ground-state charge transfer complexes.[46,47] Further evolution of the transients is quite complex, featuring both decaying and growing components. In order to quantify the dynamics, the experimental data were fitted with a multiexponential function:

$$\Delta T_{ISO} = A_0 + A_1 \exp(-t/\tau_1) + A_2 \exp(-t/\tau_2) + A_3(1-\exp(-t/\tau_3)) \quad (5.1)$$

convoluted with a Gaussian apparatus function with standard deviation of σ~100 fs. Here, A_i stands for the amplitude of the terms with the respective lifetimes τ_i. The fit parameters are listed in Table 5.1.

An initial decay at a timescale of ~60-100 ps takes place for films of neat SSMs and 5:1 blends. The amplitude of this component diminishes with decreasing donor content in the blend until it totally vanishes for the 1:1 blend, so that it cannot be ascribed to the back electron transfer from $PC_{71}BM$ to SSM. Furthermore, no similar decay component was observed in diluted solutions (SI, Figure S5.3) where the SSMs are well separated and therefore noninteracting. All these make us attribute this channel to *inter*molecular recombination of charges initially separated between neighboring SSMs. Additionaly, exciton-to-polaron conversion at the given timescales may contribute to the PIA decay (see Chapter 4 for details) as polarons and initially generated exciton likely have different absorption cross-section at the probe wavelength.

For $PC_{71}BM$ concentrations higher than 1:1, the initial decay changes into a growing component with a characteristic timescale of ~10-20 ps for 1T and ~2 ps for 2T and 3T. Both amplitude and time of this component increase with increasing $PC_{71}BM$ content so it cannot be ascribed to exciton diffusion in the SSM-rich domains. On the other hand, the $PC_{71}BM$ absorption at the excitation wavelength of 550 nm amounts to 20-25% in 1:1 blends, and further increases to ~50% at the highest fullerene concentration (SI, Figure S5.4). Therefore, it is reasonable to assign the increasing component to the hole transfer process[48] which is preceded by exciton photogeneration in the fullerene phase and its diffusion to the donor-acceptor interface (see Chapter 3 for details). This process leads to a gradual increase in the amount of holes at the donor phase, which in turn leads to the signal growth. To check the consistency of this assignment, we substituted $PC_{71}BM$ with [6,6]-phenyl-C_{61}-butyric acid methyl ester ($PC_{61}BM$), which optical absorption is noticeably lower. Indeed, no initial growing was observed in SSM blends with $PC_{61}BM$ (SI, Figure S5.7), which strengthens the argument on the hole-transfer origin of the process.

Table 5.1 Fit parameters (Equation (5.1)) for all blends of SSMs with $PC_{71}BM$

		A_0	A_1	τ_1 [ns]	A_2	τ_2 [ps]	A_3	τ_3 [ps]	ΣA_i
1T	Neat	0	0.36±0.03	2.3±2	0.58±0.03	100±10	-	-	0.94±0.06
	5:1	0.38±0.06	0.44±0.05	0.8±0.3	0.18±0.07	85±40			1.0±0.2
	1:1	0.26±0.06	0.45±0.06	0.9±0.3			0.16±0.02	9±3	0.87±0.14
	1:3	0.19±0.03	0.46±0.03	0.8±0.1	-	-	0.13±0.02	15±11	0.78±0.08
	1:5	0.15±0.01	0.42±0.02	0.8±0.1			0.20±0.01	23±3	0.77±0.04
2T	Neat	0.15±0.02	0.41±0.03	0.5±0.1	0.41±0.03	40±10	-	-	0.96±0.08
	5:1	0.46±0.02	0.48±0.06	0.4±0.1	0.02±0.01	60±40			0.96±0.09
	1:1	0.47±0.04	0.43±0.03	0.5±0.1			0.10±0.03	2±1	1.0±0.1
	1:3	0.30±0.02	0.48±0.02	0.4±0.1	-	-	0.12±0.02	3±2	0.90±0.06
	1:5	0.20±0.02	0.60±0.04	0.4±0.1			0.20±0.03	7±5	1.0±0.1
3T	Neat	0.18±0.03	0.30±0.06	0.4±0.2	0.48±0.06	45±15	-	-	0.96±0.15
	5:1	0.37±0.03	0.43±0.04	0.8±0.2	0.09±0.02	60±30			0.9±0.1
	1:1	0.34±0.06	0.57±0.06	0.9±0.2			0.10±0.03	1.6±0.5	1.0±0.1
	1:3	0.33±0.03	0.42±0.02	0.6±0.1	-	-	0.17±0.02	2±0.7	0.92±0.07
	1:5	0.1±0.02	0.38±0.02	0.7±0.1			0.20±0.01	2 ±0.3	0.68±0.05

The fact that the time scale of the hole-transfer processes is limited to ~2-7 ps for 2T and 3T SSMs, indicates short diffusion distance of the fullerene excitons, and therefore a small size of the $PC_{71}BM$ clusters even at the highest fullerene concentrations. In contrast, in 1T-based blends hole transfer occurs at longer timescales, which is indicative of larger $PC_{71}BM$ domain sizes. It is known from X-ray diffraction (XRD) experiments[20] that 1T molecules, unlike 2T and 3T, tend to form crystalline domains in films thereby enhancing phase segregation. Furthermore, the time constant associated with the hole transfer process in 1T (and in 2T albeit to lower extent) increases with a growing $PC_{71}BM$ concentration (Table 5.1) which points to longer diffusion times and therefore larger $PC_{71}BM$ domains. Nonetheless, the fastest time of ~10 ps obtained in 1T exceeds by far respective times for 2T and 3T molecules (~3 ps). This is consistent with the less favorable HOMO-HOMO energy offset for 1T (Figure 5.1, inset) which results in a lower rate of the hole transfer process compared to 2T and 3T molecules. Therefore, 2T and 3T-based films possess a two-fold advantage over 1T for production of the long-lived charges: first, they create a finer domain structure for maximizing the interfacial area where charge separation occurs, and, second, they feature a larger HOMO-HOMO energy offset for making hole transfer more efficient.

It is important to note that the peak amplitude of the transients decreases with increase of the $PC_{71}BM$ content in the blends of all SSMs (Figure 5.3, last row in Table 5.1). This means that

not all $PC_{71}BM$ excitons are harvested which points towards co-existing small and large $PC_{71}BM$ domains, where the bulk excitons simply cannot reach the interface within their lifetime (see Chapter 3 for detailed discussion). Our estimations show that these losses are as high as ~60% of all $PC_{71}BM$ excitons in the 3T-based 1:5 blend. As approximately half of the blend absorption is due to $PC_{71}BM$ (see SI, Figure S5.4), the hole transfer process becomes of utmost importance for device functionality and hence a special attention has to be paid to its optimization. For instance, it has been demonstrated that a small amount of 4-Bromoanisole (BrAni) solvent additive leads to increase in the short-circuit current and fill factor of the 2T-based device.[27] No difference in the PIA transients from 2T:$PC_{71}BM$ 1:2 blends prepared with and without the BrAni additive (see SI, Figure S5.11) was observed at the experimental timescale. This most probably indicates that the additive rather affects microscopic parameters like hole mobility[27] than ultrafast charge dynamics and nanomorphology.

Finally, for all blends, the transients decay was found at a longer time scale of ~ 0.5-0.8 ns. Similar timescales were also observed in diluted solutions of SSMs, i.e. in a system of non-interacting molecules (SI, Figure S5.3).[49] This allows us to assign this part of the transients to intramolecular recombination of charges initially separated within the same molecule (i.e. to CT excitons recombination). The share of this channel changes very little in blends with different $PC_{71}BM$ content implying that such charges are not involved in the further (electron) transfer to e.g. $PC_{71}BM$. It is plausible to suggest that the electron after being transferred to the end DCV group is trapped in a local potential energy well which results in recombination times that are much longer than typically observed for push-pull architectures (10-100 ps).[50,51] Such an assignment makes the intramolecular electron transfer a waste channel in the charge generation process, through which ~40% of overall generated charges are lost in investigated blends (see Table 1). It is also possible that back electron transfer from $PC_{71}BM$ to SSMs (i.e. interfacial CT state recombination) occurs at a similar timescale and therefore cannot be clearly disentangled from the intramolecular process.

The transients similar to those in Figure 5.3 were also observed for 2T SSM with 6 carbon atoms in the alkyl chain N(Ph-2T-DCN-Hex)$_3$ (SI, Figure S5.5). This shows that small variations in the alkyl chain do not affect ultrafast charge generation (having nevertheless strong influence on the hole mobility).[28] Moreover, transients after photoexcitation of the high-energy absorption peak at 400 nm (SI, Figure S5.6) are almost identical to those with 550 nm excitation (Figure 5.3). This points towards wavelength-independence of the origin of photogenerated charges and is consistent with the EQE spectral response following the blend absorption of the OSC based on 2T SSM.[27]

5.2.4 Efficiency of Long-Lived Charge Generation

For a good-working OSC, the photovoltaic blend should provide a sufficient amount of long-lived separated charges. The amount of long-lived charges is determined by both the amount of the initially generated charges and the efficiency of the back recombination processes. Amongst blends with the same SSM, the efficiencies of long-lived charge generation can be compared straightforwardly because all transients are normalized to the number of absorbed photons. Comparison of charge generation efficiencies for blends based on different SSMs is more challenging since signal amplitudes depend not only on the amount of generated charges per absorbed photon, but also on the polaron absorption cross-section which is not identical for different SSMs. We circumvent this problem by assigning tentatively a unity polaronic yield to the maximal amplitude amongst all blends of the same SSM. After this normalization, the signal amplitudes at delays of 1.5-1.7 ns (where most of the ultrafast dynamic processes are completed) directly provide the share of long-lived charges (Figure 5.4).

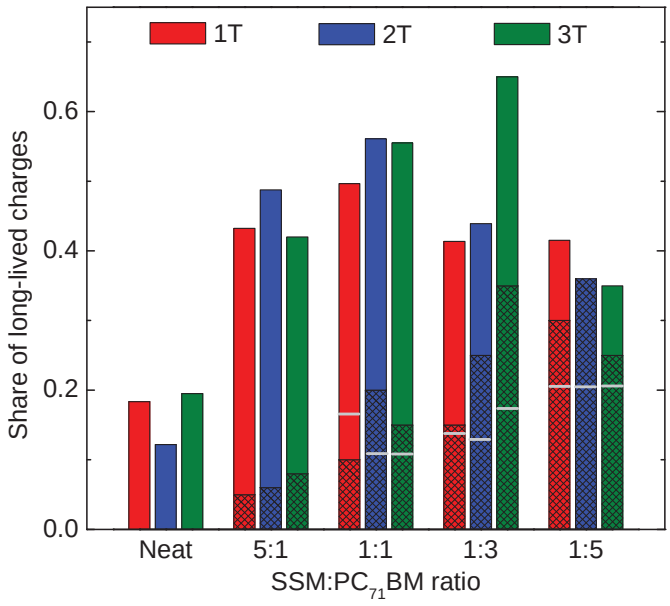

Figure 5.4 Share of long-lived charges in SSM:$PC_{71}BM$ blends *vs* $PC_{71}BM$ content (colored bars). The patterned areas inside the colored bars indicate the $PC_{71}BM$ share in the long-lived charges via the hole-transfer process. The horizontal grey lines show the $PC_{71}BM$ share in the long-lived charges derived directly from the fits of the PIA transients (i.e. A_3 column in Table 1).

In order to estimate the $PC_{71}BM$ contribution to the long-lived charges, we used the amplitude of the growing component in Equation (5.1), that is A_3 in Table 5.1 (Figure 5.4, grey horizontal lines). For example, for 1:5 1T:$PC_{71}BM$ blend the contribution of $PC_{71}BM$ charges can be

estimated as 20%. However, this approach underestimates the yield of $PC_{71}BM$ excitons because only the bulk $PC_{71}BM$ excitons, i.e. photogenerated within the $PC_{71}BM$ clusters and delayed by diffusion to the SSM/$PC_{71}BM$ interface, are counted. In contrast, the interfacial excitons that are photogenerated at the interface and delayed by the hole transfer time (which falls within the apparatus function) are fully omitted. To evaluate the integral interface and bulk contribution, we have developed a complementary method to account for the both types of $PC_{71}BM$ excitons.

We assume that the only factor for the decreasing maximal amplitudes of the transients at high $PC_{71}BM$ concentrations (Figure 5.3) is exciton losses within large $PC_{71}BM$ domains. Thus, the contribution of $PC_{71}BM$ to charge generation may be calculated as a difference between $PC_{71}BM$ contribution to blend absorption (SI, Figure S5.4) and the share of lost charges. For example, in the 1:5 1T:$PC_{71}BM$ blend, $PC_{71}BM$ absorbs ~53% of the incoming photons (SI, Figure S5.4). Since ~23% of the overall charges are lost (last row in Table 5.1), the share of $PC_{71}BM$-related charges amounts to ~30%; these values are shown in Figure 5.4 by crossed pattern.

For all the films of neat SSMs, the amount of surviving charges is extremely low, <20%. This is consistent with electron transfer upon optical excitation within the same SSM or between adjacent SSMs. The initially separated charges can hardly escape their short-time locations because the energy landscape provides no gradient for further charge separation,[52] and therefore the electron is bound to recombine eventually with the hole. This situation changes dramatically with addition of a small amount of $PC_{71}BM$ (Figure 5.4, 5:1) because a new pathway opens up for electron transfer to the fullerene. As a result, the share of long-lived charges increases to ~40%. This increase grows for the 1:1 blends although for heavier $PC_{71}BM$ loading the number of long-lived charges diminishes because of two counterbalancing factors. On the one hand, the recombination losses (i.e. the ratio between the long-time and maximal amplitudes of the particular transient) keep on decreasing due to the higher fullerene content and therefore the more efficient charge separation. On the other hand, the maximal amplitude of the 1:1 transient for 1T and 2T falls down to 80% at higher $PC_{71}BM$ content because not all $PC_{71}BM$ excitons can reach the interfaces to dissociate onto charges. The second trend becomes prevalent at the 1:3 ratio, with the exception of 3T where most probably finer (smaller) $PC_{71}BM$ domains help balancing both the electron and hole transfer processes. At the highest $PC_{71}BM$ content, when its absorption amounts to about 50% of all absorbed photons, large fullerene domains do not allow the fullerene excitons to escape, thereby leading to an even lower share of the surviving charges.

Figure 5.4 demonstrates that for all SSMs the optimal donor:acceptor ratio is between 1:1 and 1:3, where the blends provide more than 50% of long-lived charges. This is consistent with Refs. [20,28] where an external quantum efficiency of ~50% was observed for OSCs based on the SSMs. The highest short-circuit current was observed for the 1:2 blend of 2T molecule[28] with

~30% $PC_{71}BM$ absorbance (SI, Figure S5.4) which is in line with the described interplay between $PC_{71}BM$ cluster sizes and their absorption. Moreover, from the dependence of signal amplitude on acceptor concentration and efficiency of the hole transfer process, we conclude that the holes generated from $PC_{71}BM$ excitons play a significant role in device operation. Thus, the size of $PC_{71}BM$ clusters has to be optimized in order to achieve both efficient exciton splitting at the donor-acceptor interface and electron transport to the electrodes.

5.2.5 Charge Generation and Recombination

Figure 5.5 summarizes charge separation pathways and their dynamics in donor:acceptor blends of SSMs in an artist representation. After absorption of a photon from the incoming light, charge separation processes occur via three independent channels.

The first channel is an intramolecular charge separation with CT exciton formation within the molecule that has absorbed a photon. This process occurs for blends with any acceptor concentration, and is followed by CT exciton recombination, which takes place at a timescale of about 0.5-0.8 ns. The share of this channel is comparable for all blends and neat-molecule films, which prompts us to conclude that intramolecular charge separation does not yield a subsequent electron transfer to $PC_{71}BM$.

The second channel is intermolecular (interSSMs) charge separation. In this case, the charges are separated not within the same SSM, but between two (or more) neighboring molecules. To make this process possible, a dense packing of the SSMs is required. The herein separated charges recombine with a characteristic time of ~60-100 ps. Upon adding $PC_{71}BM$ into the blend, the share of this channel decreases, approaching zero at 1:1 concentration. We assign this decrease to fast (much faster than the charge recombination time) electron transfer from the SSM to $PC_{71}BM$, resulting in a pair of long-lived free charges.

In films with high acceptor concentration (more than 50%), $PC_{71}BM$ absorption becomes substantial, and initial excitons are also generated within the fullerene phase. Such excitons diffuse within the $PC_{71}BM$ cluster, reach the interface and dissociate into charges, creating a hole on the SSM. The exciton diffusion process takes place at timescales up to 20 ps depending on the size of the $PC_{71}BM$ clusters and the particular SSM. With the increase of the $PC_{71}BM$ concentration (and, as a consequence, of the clusters size), the efficiency of the exciton harvesting through this channel decreases because of limited exciton diffusion length in the $PC_{71}BM$ domains.

Finally, the separated charges are likely trapped in the interfacial CT states an can recombine within sub-ns timescale. The interplay between charge generation and recombination processes result in up to 60% of long-lived separated charges.

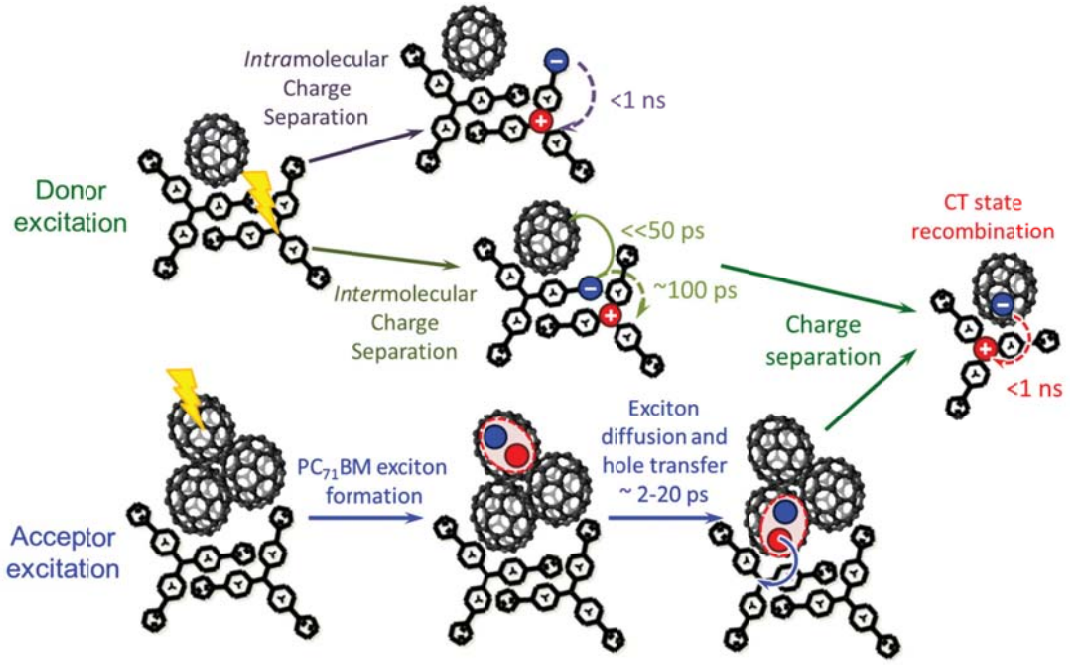

Figure 5.5 Artist representation of charge generation and recombination pathways in SSM:$PC_{71}BM$ blends.

5.3 Conclusions

Using time-resolved visible pump – IR probe technique, charge dynamics in films of donor-acceptor blends based on three novel star-shaped molecules (SSMs) with a generic structure of N(Phenylene-*n*Thiophene-Dicyanovinyl-Alkyl)$_3$ (*n*=1-3, notated as *n*T) as donors and [6,6]-phenyl-C_{71}-butyric acid methyl ester ($PC_{71}BM$) as an acceptor, have been studied. Donors differ from each other mainly by the length of the conjugated arm (1 to 3 thiophene rings) which spectroscopically results in the red-shift of the optical bandgap and the polaron absorption band.

For all blends intramolecularly separated charges recombine with a characteristic timescale of about 0.5-0.8 ns. The efficiency of this process is almost independent of the acceptor concentration thereby providing very few long-lived (i.e., at the timescale of a few ns) charges. For the blends with low $PC_{71}BM$ concentration, intermolecular (i.e. amongst SSMs) charge separation occurs as well, with a recombination timescale of ~60-100 ps. This recombination channel vanishes completely in the blends with a ratio higher than 1:1 $PC_{71}BM$ content thereby not causing charge losses. For the blend with a $PC_{71}BM$ concentration larger than 50%, the hole transfer process with a characteristic time of 2-20 ps has been identified as yielding up to 50-70% (for 1:5 blends) of the overall long-lived charges. However, up to a half of initially

generated $PC_{71}BM$ excitons are lost because of too large sizes of the $PC_{71}BM$ domains. Additionally, in blends with $PC_{71}BM$, geminate recombination of charges trapped in interfacial CT states take place at sub-ns timescale.

The amount of long-lived charges which are available to contribute to the organic solar cell photocurrent has been obtained from the transient dynamics for all blends. The optimal SSM:$PC_{71}BM$ ratio in the blends is estimated as ranging from 1:1 to 1:3 where up to 60% of long-lived charges are produced via both electron transfer (40-20%) and hole transfer (20-25%) pathways (for 2T).

Summarizing, triphenylamine-based SSMs with oligothiophene arms and electron-accepting dicyanovinyl substituents provide efficient charge separation in blends with $PC_{71}BM$, which makes them attractive donor material for organic solar cells. Amongst this series, 1T molecule appears the least promising because of blue-shifted absorption and too coarse phase separation between the donor and acceptor phases. On the other hand, 2T and 3T molecules have more favorable absorption spectra and provide efficient long-time charge separation (Figure 5). However, hole mobility in 3T-based blends[20] is typically lower in comparison with 2T,[28] which makes the latter molecule the most promising donor amongst the three. We believe that further optimization of the molecular structures and blend morphology will result in increase of ~5% efficiency already achieved for 2T:$PC_{71}BM$ blends.[28]

5.4 Methods

Samples Preparation

For the films preparation, each SSM and $PC_{71}BM$ (Solenne BV) were dissolved separately in *o*-dichlorobenzene at a concentration of 25 g/l (2T and 3T molecules) or 15 g/l (1T molecule). Solutions were stirred on a magnetic stirrer for at least 12 hours at 50°C. For neat SSMs the respective solutions were used as is; for blends, each donor solution was mixed with $PC_{71}BM$ with weight ratio of 5:1, 1:1, 1:3, and 1:5. Mixed solutions were again stirred for at least 1 hour at 50°C. Films were spin-coated from solutions (1000 rpm, 2 min) on microscope cover-glass substrates. This procedure resulted in the maximal optical density (OD) of ~0.4.

Optical

Absorption spectra of the samples were recorded with a Perkin-Elmer Lambda 900 spectrophotometer. Polarization-sensitive ultrafast PIA measurements were performed at a VIS-pump, IR-probe setup based on a Spectra-Physics Hurricane system (~120 fs, 800 nm, 1 KHz repetition rate) and two optical parametrical amplifiers (Light Conversion TOPAS) operating in the visible (400-800 nm) and IR (1.2-12 μm) regions.

The wavelength of the pump pulse was chosen near the absorption maxima of the blends at 550 nm or 400 nm (see SI, Figure S5.2). The wavelength of the IR probe pulse was varied in the range between 1.2-10 μm to record complete polaron spectra[43] of the blends. The polarization of the probe pulse was rotated by 45° with respect to the polarization of the pump pulse, and after the sample signal components with parallel and perpendicular to the pump polarizations were selected by two orthogonal polarizers and detected by nitrogen-cooled MCT detectors. The energy density of the pump pulse was as low as ~35 μJ/cm^2 (~5·10^{-3} absorbed photons per 1 nm^3, i.e. 1 photon per ~6 nm distance) to insure linearity of the detected signal with pump intensity and to prevent exciton annihilation and/or non-geminate recombination of photogenerated charges in blends (see SI, Figure S5.8).

The population isotropic signal was calculated using the following standard relation[53] to ensure that polarization-dependent effects do not interfere with the isotropic signal:

$$\Delta T_{ISO}(t) = \frac{\Delta T_{||}(t) + 2\Delta T_{\perp}(t)}{3}, \tag{5.2}$$

where $\Delta T_{||}$ and $\Delta T_{\perp}$ are the relative transmission changes with the pump open/closed for the parallel and perpendicular components of the probe, respectively. Due to molecular symmetry (see DFT calculations), depolarization (also known as anisotropy dynamics)[53] decayed at the time scale of ~1-10 ps regardless the blend (see SI, Figure S5.9) and therefore does not contain any information of, for instance, hole dynamics.[48]

For details of synthesis and DFT calculations, refer to Ref. [42]

5.5 Supporting Information

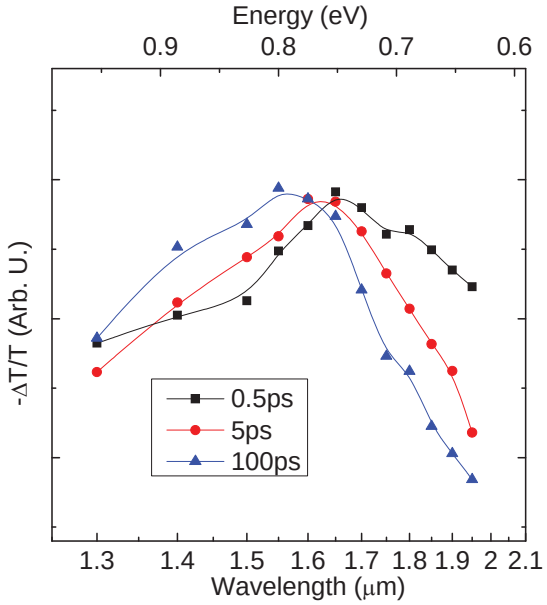

Figure S5.1 Normalized charge-transfer (CT) exciton absorption spectra for the neat 2T film at different delays (indicated). The spectra were reconstructed from the transients measured at different probe wavelengths. Excitation wavelength is 550 nm. The CT exciton absorption spectra demonstrate apparent spectral dynamics. The blue spectral shift of ~0.5 eV occurs within ~100 ps while the low-energy wing of the spectrum steepens within first 5 ps. The spectral shift and narrowing are assigned to exciton-to-polaron conversion in the films and interplay between exciton response at early times and polaron response at later times (see Chapter 4 for details). Such dynamics do not show up in the SSM:$PC_{71}BM$ blends (Figure 5.b of the main text) because of further electron transfer to $PC_{71}BM$ molecules and/or lower medium polarizability due to dilution of SSMs with $PC_{71}BM$. Note that the spectral dynamics have very little effect on the transients at the probe wavelength of 1.65 μm because of its proximity to the spectrum peak.

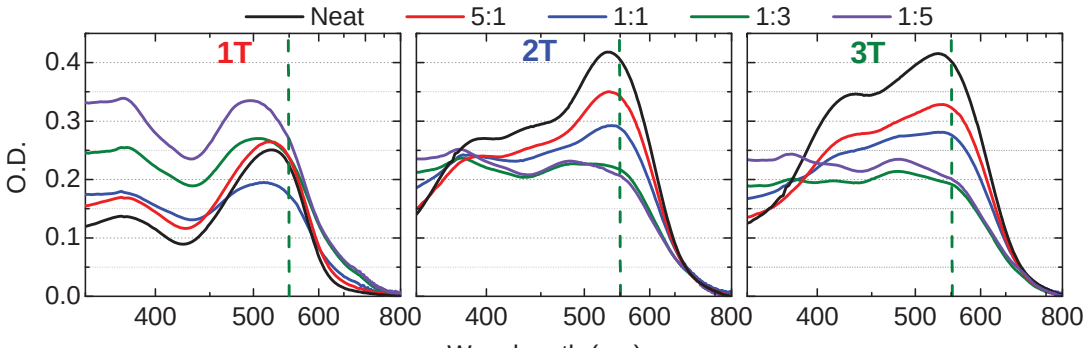

Figure S5.2 Absorption spectra of the investigated films of SSM:$PC_{71}BM$ blends. Vertical dashed lines show the wavelength of the excitation pulse.

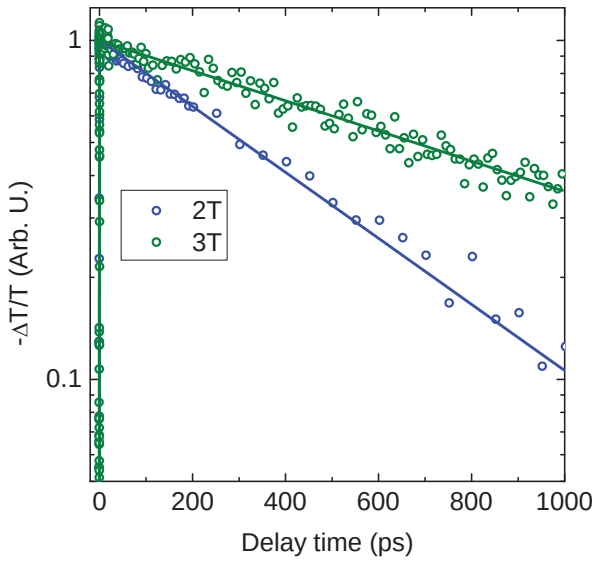

Figure S5.3 PIA transients for the 2T and 3T SSMs diluted in toluene. The pump wavelengths are 520 and 550 nm for 2T and 3T, respectively; the probe wavelengths are 2 μm and 3 μm for 2T and 3T, respectively. The signals decay monoexponentially with times of ~0.4 ns for 2T and ~0.9 ns for 3T. Note logarithmic scale of the Y-axis.

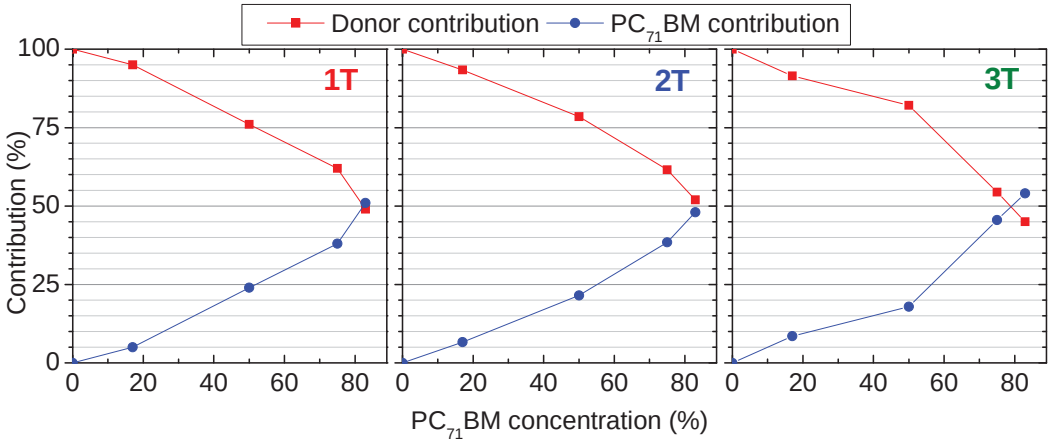

Figure S5.4 Contributions of SSMs (red line) and $PC_{71}BM$ (blue line) absorption into the overall blend absorption at the pump wavelength of 550 nm as derived from decomposition of the absorption spectra to SSM and $PC_{71}BM$ contributions (not shown). Note substantial (~50%) $PC_{71}BM$ contribution to the overall absorption at high concentrations.

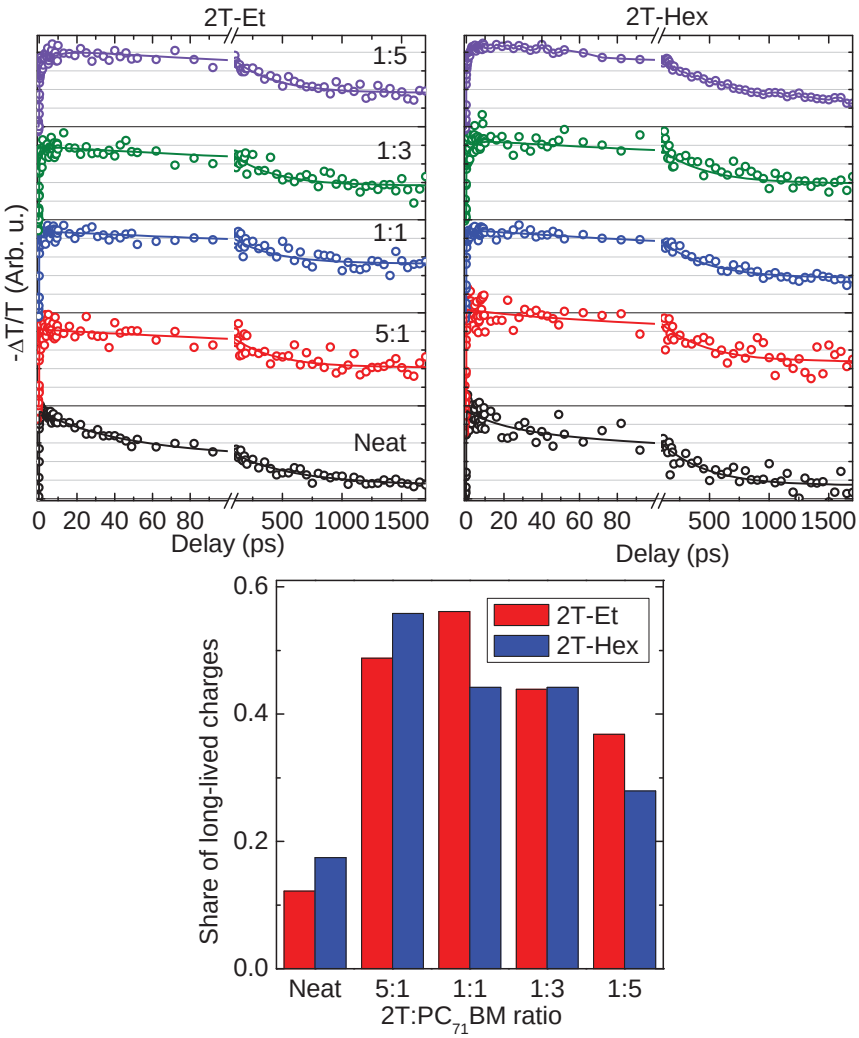

Figure S5.5 (top) PIA transients for blends of 2T SSMs with 2 (2T-Et, left) or 6 (2T-Hex, right) carbon atoms in the alkyl chain with $PC_{71}BM$ at different $PC_{71}BM$ contents (indicated next to the transients). Circles represent the experimental data points while solid lines show best fits according Equation (5.1) (see the main text). All transients are normalized to the number of absorbed excitation photons to allow direct comparison of their amplitudes. Unity polaronic yield is assigned to the maximal amplitude amongst all blends of the same SSM. (bottom) Share of long-lived charges at 1.5-1.7 ns delay.

The transients are similar for both molecules, which indicates minor influence of the alkyl chain on the charge generation and recombination processes. Nonetheless, the amount of long-lived charges for the 2T-Hex:$PC_{71}BM$ 1:1 blend is slightly lower compared to 2T-Et based blend. This is most probably related to less efficient “interstar” charge separation (which leads to generation of long-lived charges, see the main text) due to weaker intermolecular interactions because of the longer alkyl chain.

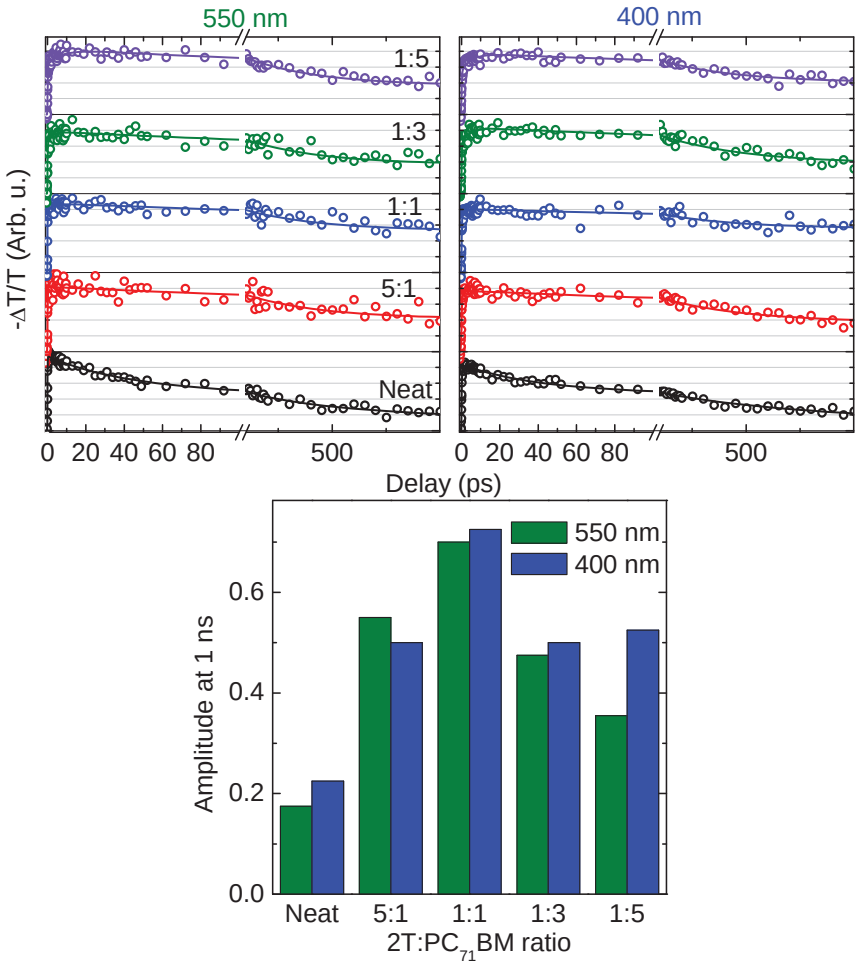

Figure S5.6 (top) PIA transients for the 2T:$PC_{71}BM$ blends at different $PC_{71}BM$ contents (indicated) after excitation of the low-energy absorption band at 550 nm (left panel) and the high-energy absorption band at 400 nm (right panel). Circles represent the experimental data points while the solid lines show best fits according to Equation (5.1) (see main text). All transients are normalized to the number of absorbed excitation photons to allow direct comparison of their amplitudes. Unity polaronic yield is assigned to the maximal amplitude amongst all blends. (bottom) Transient amplitude at 1 ns delay.

Similarity of the transients for both excitation wavelengths strongly suggests that the origin of charge generation and recombination processes is the same in both cases. This also confirms the charge-transfer character of both 400 nm and 550 nm absorption bands. The only noticeable difference is for the 1:5 blend where the 400-nm excitation is more efficient than the 550-nm one. This is because of stronger $PC_{71}BM$ absorption (~70% *vs* ~50) and, therefore, lower share of the waste channel associated with intramolecular charge generation and recombination processes.

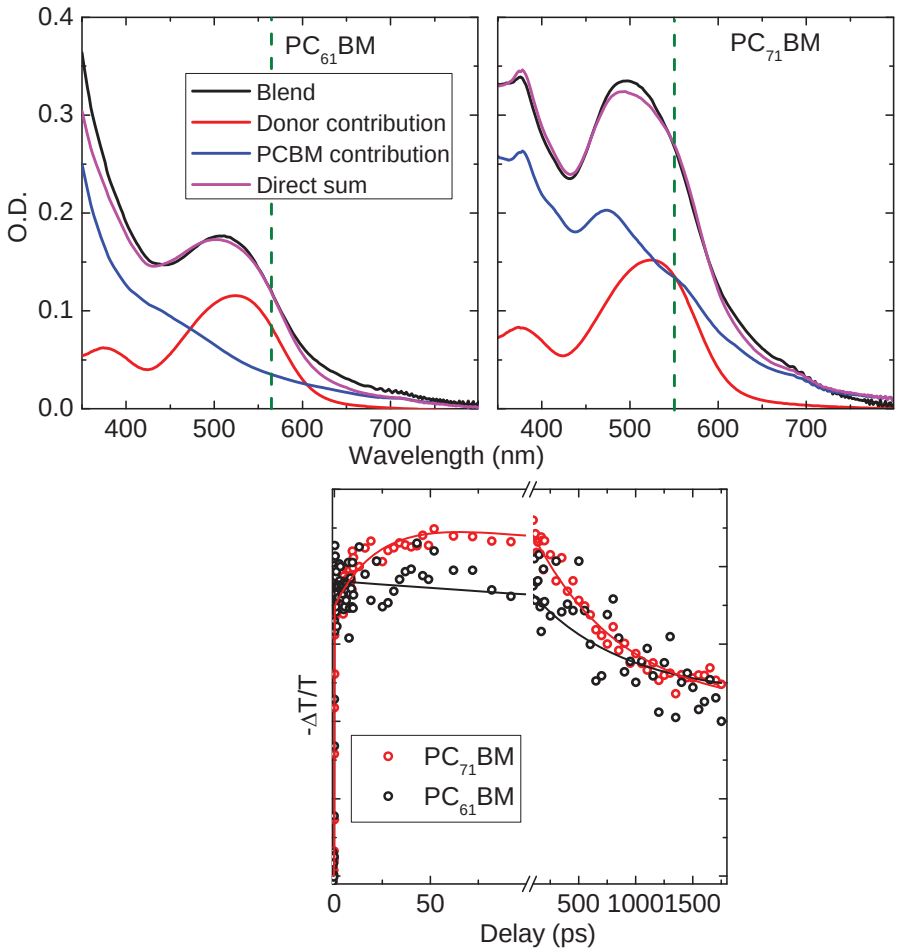

Figure S5.7 (top) Decomposition of absorption spectra and (bottom) PIA transients for 1T:$PC_{61}BM$ and 1T:$PC_{71}BM$ 1:5 blends. Circles represent the experimental data points while solid lines show best fits according Equation (5.1) (see main text). The signal amplitudes are normalized by SSM absorption (note: not blend absorption). The recombination timescales were set identical for both blends. The blend with $PC_{61}BM$ was prepared with the standard procedure, and measured under similar conditions to the $PC_{71}BM$-based blend (see main text). For the $PC_{71}BM$-based blend a noticeable increase of the signal occurs within first 50 ps while for the $PC_{61}BM$-based blend no growing signal is observed. Since at 550 nm pump wavelength, share of $PC_{61}BM$ absorption is considerably lower that the $PC_{71}BM$ share (~30% and ~50%, respectively), we conclude that the signal growth for the 1T:$PC_{71}BM$ case is caused by the hole-transfer process.

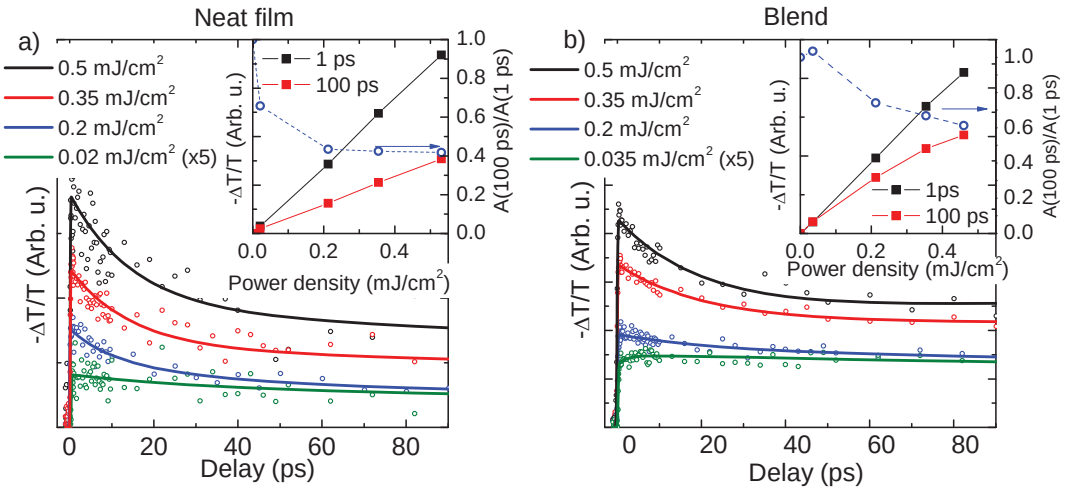

Figure S5.8 Pump intensity dependences of transients for (a) neat 3T and (b) 1:1 3T:$PC_{71}BM$ films. Excitation and probe wavelengths are 550 nm and 2.1 μm, respectively. Open circles represent the experimental data points while solid lines show best fits according Equation (5.1). Insets show signal amplitudes at 1 ps (black symbols) and 100 ps (red symbols), and their ratio (blue symbols, the right axis). For neat films (a), the initial decay at high power densities is (partially) caused by exciton-exciton annihilation; its amplitude decreases with decrease of pump intensity (see inset, blue symbols). In 1:1 blends (b) the initial decay is replaced by growth for lower pump intensities. For both cases, extrapolation to zero pump intensities results in no more than 5% of residual share of bi-exciton annihilation, which is lower than experimental uncertainty.

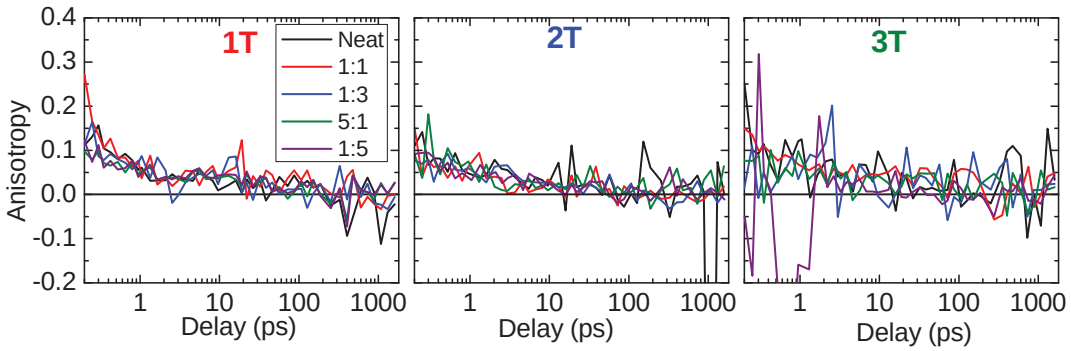

Figure S5.9 Anisotropy dynamics for all investigated blends. The anisotropy was calculated from parallel and perpendicular components of the probe using the following equation[53]: $r(t) = \frac{\Delta T_{\parallel}(t) - \Delta T_{\perp}(t)}{\Delta T_{\parallel}(t) + 2\Delta T_{\perp}(t)}$. The anisotropy dynamics does not depend on the SSM structure and/or $PC_{71}BM$ concentration which is assigned to intramolecular mixing of the excited states due to C3 symmetry of the molecules. The low anisotropy values and its ~1-ps decay time precludes using anisotropy as a contrast parameter[48] for e.g. distinguishing processes of electron and hole transfer.

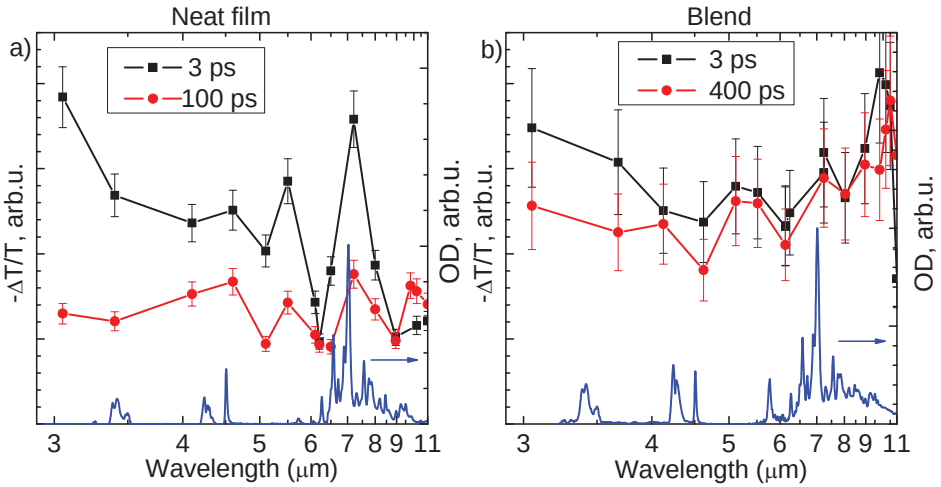

Figure S5.10 Transient spectra responses in the 3-11 μm probe region (black and red symbols) and IR absorption (blue lines) of (a) the neat 3T film and (b) 1:1 3T:$PC_{71}BM$ blend. The transient spectra were obtained at delays of 3 ps (black symbols) and 100 ps (a) and 400 ps (b) (red symbols). Note that the peak around 7.5 μm in the transient spectra in (a) matches positions of IR absorption peaks of 3T which suggests that this peak originates from altering of amplitudes or/and frequencies of the vibrational modes. The peak in IR absorption at ~5.7 μm in 1:1 blend in (b) is assigned to the fullerene carbonyl mode. Increase of the spectral response above 9 μm of the 3T:$PC_{71}BM$ blend (b) could be a high-frequency tail of the far-IR response of quasi-free charges that do not exist in the neat 3T film.

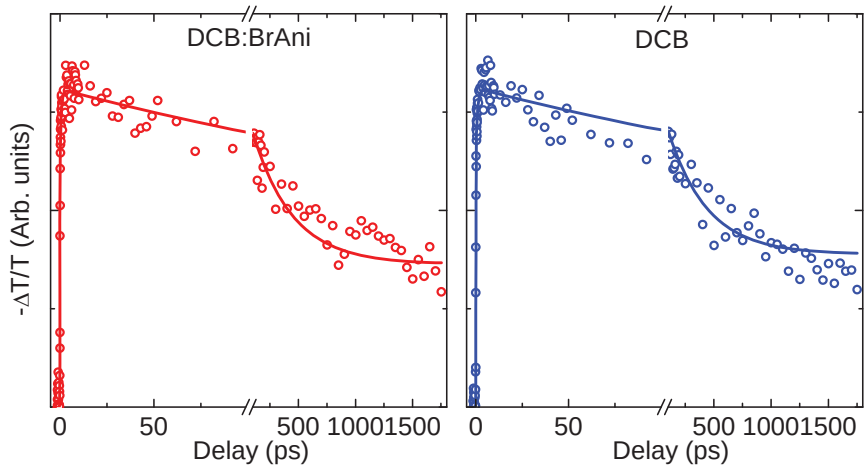

Figure S5.11 PIA transients for 2T:$PC_{71}BM$ 1:2 blends with (left, red) and without (right, blue) BrAni additive. For the blend with the additive, 2 vol% of BrAni were added to oDCB before dissolving the materials. The blends were measured under similar conditions to the other blends (see main text). Note that no noticeable difference is observed for both transients within experimental accuracy.

5.5.1 Influence of Donor and Acceptor Units[1]

To complement the study presented herein, influence of donor and acceptor units on ultrafast dynamics was investigated (for the chemical structures and notations of respective molecules refer to Chapter 4, for details of the experiment and sample preparation see Ref. [54]). Note that the TPA-DCV molecules studied in this section does not have any alkyl chain attached to the DCV group.

Representative PIA transients for the studied blends are shown in Figure S5.12. All star-shaped donors in blends with $PC_{70}BM$ demonstrate similar behavior, which is consistent with our previous findings described in this Chapter. For all blends, a fast build-up of the signal occurs due to immediate formation of charge-transfer (CT) excitons and/or separated charges. At later times, the PIA signal grows with timescale of ~2 ps, which is attributed to the hole-transfer process from $PC_{70}BM$ to the star-shaped donor molecule. Finally, the signals decay at ~500 ps timescale due to the intramolecular recombination of the CT excitons and/or geminate recombination of the charges trapped in CT states. Both processes lead to a decrease of the amount of the long-lived separated charges thereby impeding the maximal attaining PCE. Note

[1] *This Section is based on the following publication:*
Yuriy N. Luponosov , Jie Min , Alexander N. Solodukhin, Oleg V. Kozlov, Marina A. Obrezkova, Svetlana M. Peregudova, Tayebeh Ameri, Sergei N. Chvalun, Maxim S. Pshenichnikov, Christoph J. Brabec, Sergei A. Ponomarenko, "Effects of electron-withdrawing group and electron-donating core combinations on physical properties and photovoltaic performance in D-π-A star-shaped small molecules", Organic Electronics **32**, 157 (2016)

that at higher excitation densities (>20 μJ/cm^2) substantial non-geminate exciton-exciton annihilation was observed which prompted us to limit excitation intensities is such a way to ensure the exciton density of ~3·10^{-3} nm^{-3}.

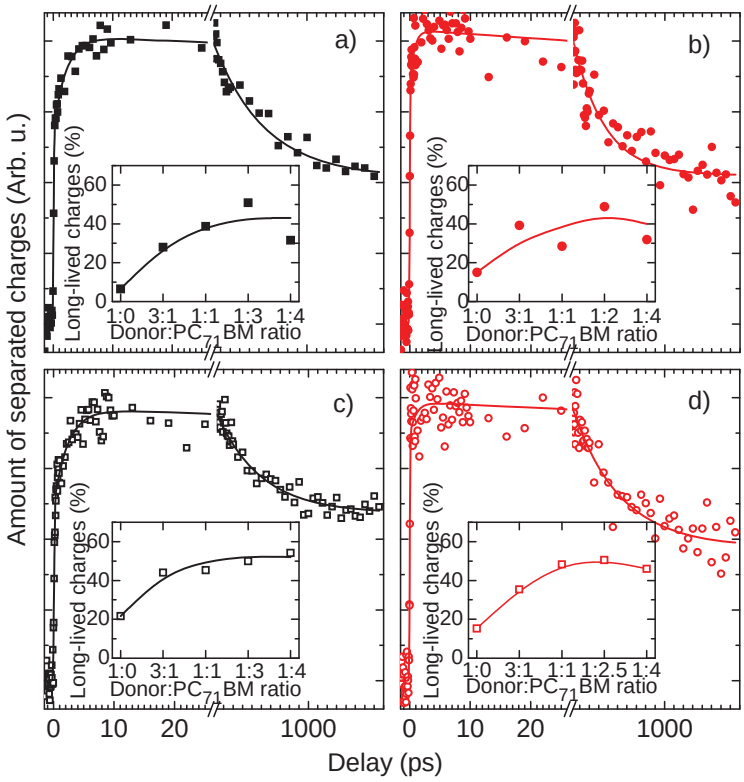

Figure S5.12 PIA transients for (a) TPA-Rh:PC$_{71}$BM (1:3, wt%), (b) TPA-DCV:PC$_{71}$BM (1:2, wt%), (c) mTPA-Rh:PC$_{71}$BM (1:4, wt%), (d) mTPA-DCV:PC$_{71}$BM (1:2.5, wt%), respectively, after excitation at the wavelengths of 550 nm. Open circles represent the experimental data while solid lines show the best multiexponential fits (Equation (5.1)), with the fit parameters given in Table S5.1. The insets show the dependence of the efficiency of generation of long-lived charges on PC$_{70}$BM concentration.

Maximizing the amount of long-lived separated charges is important for the optimization of a good-working device. Insets in Figure S5.12 show the efficiency of charge separation as a function of the PC$_{71}$BM content. Efficiencies were calculated as a ratio of the amount of the long-lived charges (i.e. the signal amplitude at 1.5-1.8 ns delays) to a maximal amount of charges which is provided by the given molecule. The efficiency of charge separation for all donor molecules depends strongly on both PC$_{71}$BM content and the particular donor molecule structure. At the optimal PC$_{71}$BM contents the blends provide up to 60% of long-lived separated charges, which perfectly matches the values of external quantum efficiencies (EQE) for the OSCs (see Ref. [54]). Importantly, for all donor molecules, the optimal PC$_{71}$BM content for

ultrafast charge separation directly correlates with the optimal blend composition for the OSCs (see Ref. [54]). This indicates optimized performance at both the ultrafast sub-ns timescale (i.e. maximized amount of the long-lived charges) and the ultraslow timescale at which the device operates.

At the optimal $PC_{71}BM$ concentration, the blends behave quite similarly at the ultrafast timescales, providing about 50-60% of long-lived charges. However, there are some important differences in the initial growth of the PIA signal. Noticeably, for the TPA-Rh and mTPA-Rh molecules that demonstrate the best performance in devices, there is a prominent delayed build-up of the transients at a ps timescale that is more suppressed at the other two transients. This initial growth is attributed to the diffusion-delayed splitting of $PC_{71}BM$ excitons, so that in blends based on TPA-DCV and mTPA-DCV: no $PC_{71}BM$ exciton diffusion is observed. The absence of such exciton diffusion may be caused by either of the two scenarios. First, the $PC_{71}BM$ domains in BHJ blends are too large (larger than the exciton diffusion length of ~10 nm) so that the excitons cannot make it to the interface and therefore produce no charges. Second, intermixing of the donor and $PC_{71}BM$ phases is too fine, with the typical scale that is much lower than exciton diffusion length, which leads to almost instantaneous dissociation of the $PC_{71}BM$ excitons. Large $PC_{71}BM$ domains cause decreased contribution of the $PC_{71}BM$ excitons to the overall photocurrent. However, no signs of this are observed in the EQE spectra (see Ref. [54] for details) which shapes look essentially similar for all blends. Therefore, contributions of the donor and $PC_{71}BM$ to the photocurrent are comparable for all molecules.

Fine intermixing, in turn, would not affect the EQE shape, since both donor and $PC_{71}BM$ excitons split with high efficiency. However, very small domain sizes imply extremely large interfacial area in the BHJ films and, most probably, lack of intercalated pathways to the corresponding electrodes. Such nanomorphology leads to the increased non-geminate recombination and decreased charge extraction, which explains low FF and J_{sc} values of the devices based on the TPA-DCV and mTPA-DCV molecules (see Ref. [54] for details). In contrast, in the well-performing blends based on TPA-Rh and mTPA-Rh the $PC_{71}BM$ cluster sizes seem to be more optimal, i.e. close to ~10 nm. In this case the clusters are hardly detectable by standard AFM due to its limited spatial resolution and/or poor contrast between the donor and $PC_{71}BM$ domains.

Table S5.1 Fit parameters (Equation (5.1)) for the studied blends.

	A_0	A_1	A_2	τ_2 [ps]	A_3	τ_3 [ps]
TPA-Rh	0.17	-	0.49	530±60	0.34	1±0.7
TPA-DCV	0.3		0.53	430±60	0.17	0.7±0.6
mTPA-Rh	0.24		0.34	500±50	0.31	2.3±0.3
mTPA-DCV	0.48		0.5	550±70	0.02	1±1

Author Contributions

OVK performed linear absorption and PIA measurements and analyzed the data; YNL and SAP synthetized the molecules; JK and YO performed (TD-)DFT calculations, MSP conceived the concept and supervised the research.

References

1 B. Walker, C. Kim, and T.-Q. Nguyen. Small Molecule Solution-Processed Bulk Heterojunction Solar Cells. *Chem. Mater.* **23** no. 3, 2010, p. 470.

2 G. D. Sharma, J. A. Mikroyannidis, S. S. Sharma, M. S. Roy, and K. R. J. Thomas. Efficient Bulk Heterojunction Photovoltaic Devices Based on Diketopyrrolopyrrole Containing Small Molecule as Donor and Modified PCBM Derivatives as Electron Acceptors. *Org. Electron.* **13** no. 4, 2012, p. 652.

3 S. Seulgi, C. Hyunbong, K. Haye Min, K. Chulwoo, P. Sanghyun, N. Cho, S. Kihyung, L. Jae Kwan, and K. Jaejung. Novel Unsymmetrical Push-Pull Squaraine Chromophores for Solution Processed Small Molecule Bulk Heterojunction Solar Cells. *Sol. Energy Mater. Sol. Cells* **98**, 2012, p. 224.

4 Z. Li, G. R. He, X. J. Wan, Y. S. Liu, J. Y. Zhou, G. K. Long, Y. Zuo, M. T. Zhang, and Y. S. Chen. Solution Processable Rhodanine-Based Small Molecule Organic Photovoltaic Cells with a Power Conversion Efficiency of 6.1%. *Adv. Energy Mater.* **2** no. 1, 2012, p. 74.

5 H. X. Shang, H. J. Fan, Y. Liu, W. P. Hu, Y. F. Li, and X. W. Zhan. A Solution-Processable Star-Shaped Molecule for High-Performance Organic Solar Cells. *Adv. Mater.* **23** no. 13, 2011, p. 1554.

6 B. Yin, L. Y. Yang, Y. S. Liu, Y. S. Chen, Q. J. Qi, F. L. Zhang, and S. G. Yin. Solution-Processed Bulk Heterojunction Organic Solar Cells Based on an Oligothiophene Derivative. *Appl. Phys. Lett.* **97** no. 2, 2010, p. 023303

7 A. B. Tamayo, B. Walker, and T. Q. Nguyen. A Low Band Gap, Solution Processable Oligothiophene with a Diketopyrrolopyrrole Core For Use in Organic Solar Cells. *J. Phys. Chem. C* **112** no. 30, 2008, p. 11545.

8 J. Roncali, P. Leriche, and P. Blanchard. Molecular Materials for Organic Photovoltaics: Small is Beautiful. *Adv. Mater.* **26** no. 23, 2014, p. 3821.

9 J. Zhang, J. Yu, C. He, D. Deng, Z.-G. Zhang, M. Zhang, Z. Li, and Y. Li. Solution-Processable Star-Shaped Photovoltaic Organic Molecules Based on Triphenylamine and Benzothiadiazole with Longer π-Bridge. *Org. Electron.* **13** no. 1, 2012, p. 166.

10 Y. Z. Lin, P. Cheng, Y. F. Li, and X. W. Zhan. A 3D Star-Shaped Non-Fullerene Acceptor for Solution-Processed Organic Solar Cells with a High Open-Circuit Voltage of 1.18 V. *Chemical Communications* **48** no. 39, 2012, p. 4773.

11 Y. Lin, Z.-G. Zhang, H. Bai, Y. Li, and X. Zhan. A Star-Shaped Oligothiophene End-Capped with Alkyl Cyanoacetate Groups for Solution-Processed Organic Solar Cells. *Chemical Communications* **48** no. 77, 2012, p. 9655.

12 J. Zhang, D. Deng, C. He, Y. He, M. Zhang, Z.-G. Zhang, Z. Zhang, and Y. Li. Solution-Processable Star-Shaped Molecules with Triphenylamine Core and Dicyanovinyl Endgroups for Organic Solar Cells. *Chem. Mater.* **23** no. 3, 2011, p. 817.

13 D. Dan, S. Suling, Z. Jing, H. Chang, Z. Zhanjun, and L. Yongfang. Solution-Processable Star-Shaped Photovoltaic Organic Molecule with Triphenylamine Core and Thieno[3,2-b]thiophene–dicyanovinyl Arms. *Org. Electron.* **13**, 2012, p. 2546.

14 Z. H. Lin, J. Bjorgaard, A. G. Yavuz, and M. E. Kose. Low Band Gap Star-Shaped Molecules Based on Benzothia(oxa)diazole for Organic Photovoltaics. *J. Phys. Chem. C* **115** no. 30, 2011, p. 15097.

15 Y. Sun, G. C. Welch, W. L. Leong, C. J. Takacs, G. C. Bazan, and A. J. Heeger. Solution-Processed Small-Molecule Solar Cells with 6.7% Efficiency. *Nat. Mater.* **11** no. 1, 2012, p. 44.

16 T. S. van der Poll, J. A. Love, T. Q. Nguyen, and G. C. Bazan. Non-Basic High-Performance Molecules for Solution-Processed Organic Solar Cells. *Adv. Mater.* **24** no. 27, 2012, p. 3646.

17 Y. Liu, C.-C. Chen, Z. Hong, J. Gao, Y. Yang, H. Zhou, L. Dou, G. Li, and Y. Yang. Solution-Processed Small-Molecule Solar Cells: Breaking the 10% Power Conversion Efficiency. *Sci. Rep.* **3**, 2013, p. 3356.

18 J. Min, Y. N. Luponosov, Z.-G. Zhang, S. A. Ponomarenko, T. Ameri, Y. Li, and C. J. Brabec. Interface Design to Improve the Performance and Stability of Solution-Processed Small Molecule Conventional Solar Cells. *Adv. Energy Mater.* **4** no. 16, 2014, p. 1400816.

19 E. Ripaud, Y. Olivier, P. Leriche, J. Cornil, and J. Roncali. Polarizability and Internal Charge Transfer in Thiophene-Triphenylamine Hybrid π-Conjugated Systems. *J. Phys. Chem. B* **115** no. 30, 2011, p. 9379.

20 J. Min, Y. N. Luponosov, D. Baran, S. N. Chvalun, M. A. Shcherbina, A. V. Bakirov, P. V. Dmitryakov, S. M. Peregudova, N. Kausch-Busies, S. A. Ponomarenko *et al.* Effects of Oligothiophene π-Bridge Length on Physical and Photovoltaic Properties of Star-Shaped Molecules for Bulk Heterojunction Solar Cells. *J. Mater. Chem. A* **2**, 2014, p. 16135.

21 J. Luo, B. Zhao, H. S. On Chan, and C. Chi. Synthesis, Physical Properties and Self-Assembly of Star-Shaped Oligothiophenes-Substituted and Fused Triphenylenes. *J. Mater. Chem.* **20** no. 10, 2010, p. 1932.

22 K. H. Kim, Z. Chi, M. J. Cho, J.-I. Jin, M. Y. Cho, S. J. Kim, J. S. Joo, and D. H. Choi. Soluble Star-Shaped Molecules Based on Thiophene Derivatives as Organic Semiconductors for Field-Effect Transistor Applications. *Chem. Mater.* **19** no. 20, 2007, p. 4925.

23 E. A. Kleymyuk, P. A. Troshin, E. A. Khakina, Y. N. Luponosov, Y. L. Moskvin, S. M. Peregudova, S. D. Babenko, T. Meyer-Friedrichsen, and S. A. Ponomarenko. 3D Quater- and Quinquethiophenesilanes as Promising Electron-Donor Materials for BHJ Photovoltaic Cells and Photodetectors. *Energy Environ. Sci.* **3** no. 12, 2010, p. 1941.

24 J. Roncali, P. Leriche, and A. Cravino. From One- to Three-Dimensional Organic Semiconductors: In Search of the Organic Silicon? *Adv. Mater.* **19** no. 16, 2007, p. 2045.

25 D. Cheyns, M. Kim, B. Verreet, and B. P. Rand. Accurate Spectral Response Measurements of a Complementary Absorbing Organic Tandem Cell with Fill Factor Exceeding the Subcells. *Appl. Phys. Lett.* **104** no. 9, 2014, p. 093302.

26 A. Cravino, S. Roquet, P. Leriche, O. Aleveque, P. Frere, and J. Roncali. A Star-Shaped Triphenylamine π-Conjugated System with Internal Charge-Transfer as Donor Material for Hetero-Junction Solar Cells. *Chemical Communications* no. 13, 2006, p. 1416.

27 J. Min, T. Ameri, A. Elschner, Y. Luponosov, S. Peregudova, D. Baran, T. Heumuller, N. Li, S. Ponomarenko, and C. J. Brabec. A Solution-Processable Star-Shaped Molecule for High-Performance Organic Solar Cells via Alkyl Chain Engineering and Solvent Additive *Org. Electron.* **14** no. 1, 2013, p. 219.

28 J. Min, Y. N. Luponosov, A. Gerl, M. S. Polinskaya, S. M. Peregudova, P. V. Dmitryakov, A. V. Bakirov, M. A. Shcherbina, S. N. Chvalun, S. Grigorian *et al.* Alkyl Chain Engineering of Solution-Processable Star-Shaped Molecules for High-Performance Organic Solar Cells. *Adv. Energy Mater.* **4** no. 5, 2014, p. 1301234.

29 D. Demeter, V. Jeux, P. Leriche, P. Blanchard, Y. Olivier, J. Cornil, R. Po, and J. Roncali. Tuning of the Photovoltaic Parameters of Molecular Donors by Covalent Bridging. *Adv. Funct. Mater.* **23** no. 38, 2013, p. 4854.

30 Y. N. Luponosov, A. N. Solodukhin, and S. A. Ponomarenko. Branched Triphenylamine-Based Oligomers for Organic Electronics. *Polymer Science, Ser. C* **56** no. 1, 2014, p. 104.

31 A. Cravino, P. Leriche, O. Alévêque, S. Roquet, and J. Roncali. Light-Emitting Organic Solar Cells Based on a 3D Conjugated System with Internal Charge Transfer. *Adv. Mater.* **18** no. 22, 2006, p. 3033.

32 P. Leriche, P. Frère, A. Cravino, O. Alévêque, and J. Roncali. Molecular Engineering of the Internal Charge Transfer in Thiophene−Triphenylamine Hybrid π-Conjugated Systems. *The Journal of Organic Chemistry* **72** no. 22, 2007, p. 8332.

33 S. Roquet, A. Cravino, P. Leriche, O. Aleveque, P. Frere, and J. Roncali. Triphenylamine-Thienylenevinylene Hybrid Systems with Internal Charge Transfer as Donor Materials for Heterojunction Solar Cells. *J. Am. Chem. Soc.* **128** no. 10, 2006, p. 3459.

34 O. V. Kozlov, Y. N. Luponosov, A. N. Solodukhin, B. Flament, Y. Olivier, R. Lazzaroni, J. Cornil, S. A. Ponomarenko, and M. S. Pshenichnikov. Ultrafast Exciton-to-Polaron Conversion in Densely-Packed Small Organic Semiconducting Molecules. *Advanced Optical Materials* **5** no. 7, 2017, p. 1700024.

35 S. Günes, H. Neugebauer, and N. S. Sariciftci. Conjugated Polymer-Based Organic Solar Cells. *Chemical Reviews* **107** no. 4, 2007, p. 1324.

36 S. R. Cowan, N. Banerji, W. L. Leong, and A. J. Heeger. Charge Formation, Recombination, and Sweep-Out Dynamics in Organic Solar Cells. *Adv. Funct. Mater.* **22** no. 6, 2012, p. 1116.

37 D. Veldman, S. C. J. Meskers, and R. A. J. Janssen. The Energy of Charge-Transfer States in Electron Donor-Acceptor Blends: Insight into the Energy Losses in Organic Solar Cells. *Adv. Funct. Mater.* **19** no. 12, 2009, p. 1939.

38 S. H. Park, A. Roy, S. Beaupre, S. Cho, N. Coates, J. S. Moon, D. Moses, M. Leclerc, K. Lee, and A. J. Heeger. Bulk Heterojunction Solar Cells with Internal Quantum Efficiency Approaching 100%. *Nat. Photonics* **3** no. 5, 2009, p. 297.

39 E. Stratakis and E. Kymakis. Nanoparticle-Based Plasmonic Organic Photovoltaic Devices. *Mater. Today* **16** no. 4, 2013, p. 133.

40 W. C. H. Choy. The Emerging Multiple Metal Nanostructures for Enhancing the Light Trapping of Thin Film Organic Photovoltaic Cells. *Chemical Communications* **50** no. 81, 2014, p. 11984.

41 M. A. Green, A. Ho-Baillie, and H. J. Snaith. The Emergence of Perovskite Solar Cells. *Nat. Photonics* **8** no. 7, 2014, p. 506.

42 O. V. Kozlov, Y. N. Luponosov, S. A. Ponomarenko, N. Kausch-Busies, D. Y. Paraschuk, Y. Olivier, D. Beljonne, J. Cornil, and M. S. Pshenichnikov. Ultrafast Charge Generation Pathways in Photovoltaic Blends Based on Novel Star-Shaped Conjugated Molecules. *Adv. Energy Mater.* **5** no. 7, 2015, p. 1401657.

43 X. Wei, Z. V. Vardeny, N. S. Sariciftci, and A. J. Heeger. Absorption-Detected Magnetic-Resonance Studies Of Photoexcitations In Conjugated-Polymer/C_{60} Composites. *Physical Review B* **53** no. 5, 1996, p. 2187.

44 G. Lanzani. *The Photophysics behind Photovoltaics and Photonics.* (Wiley-VCH, Weinheim, Germany, 2012).

45 C. X. Sheng, M. Tong, S. Singh, and Z. V. Vardeny. Experimental Determination of the Charge/Neutral Branching Ratio η in the Photoexcitation of π-Conjugated Polymers by Broadband Ultrafast Spectroscopy. *Physical Review B* **75** no. 8, 2007, p. 085206.

46 A. A. Bakulin, D. S. Martyanov, D. Y. Paraschuk, M. S. Pshenichnikov, and P. H. M. van Loosdrecht. Ultrafast Charge Photogeneration Dynamics in Ground-State Charge-Transfer Complexes Based on Conjugated Polymers. *J. Phys. Chem. B* **112** no. 44, 2008, p. 13730.

47 A. A. Bakulin, S. A. Zapunidy, M. S. Pshenichnikov, P. H. M. van Loosdrecht, and D. Y. Paraschuk. Efficient Two-Step Photogeneration of Long-Lived Charges in Ground-State Charge-Transfer Complexes of Conjugated Polymer Doped With Fullerene. *Phys. Chem. Chem. Phys.* **11** no. 33, 2009, p. 7324.

48 A. A. Bakulin, J. C. Hummelen, M. S. Pshenichnikov, and P. H. M. van Loosdrecht. Ultrafast Hole-Transfer Dynamics in Polymer/PCBM Bulk Heterojunctions. *Adv. Funct. Mater.* **20** no. 10, 2010, p. 1653.

49 O. Kozlov, Y. Luponosov, S. Ponomarenko, D. Paraschuk, N. Kausch-Busies, and M. Pshenichnikov. in *Ultrafast Dynamics in Molecules, Nanostructures and Interfaces Optics and Photonics* (eds G. G. Gurzadyan, G. Lanzani, C. Soci, & T. C Sum) 169 (World Scientific Publishing Co. Pte. Ltd., Singapore, 2014).

50 R. Tautz, E. Da Como, T. Limmer, J. Feldmann, H.-J. Egelhaaf, E. von Hauff, V. Lemaur, D. Beljonne, S. Yilmaz, I. Dumsch *et al.* Structural Correlations in the Generation of Polaron Pairs in Low-Bandgap Polymers for Photovoltaics. *Nat. Commun.* **3**, 2012, p. 970.

51 S. D. Dimitrov, A. A. Bakulin, C. B. Nielsen, B. C. Schroeder, J. Du, H. Bronstein, I. McCulloch, R. H. Friend, and J. R. Durrant. On the Energetic Dependence of Charge Separation in Low-Band-Gap Polymer/Fullerene Blends. *J. Am. Chem. Soc.* **134** no. 44, 2012, p. 18189.

52 M. C. Scharber and N. S. Sariciftci. Efficiency of Bulk-Heterojunction Organic Solar Cells. *Prog. Polym. Sci.* **38** no. 12, 2013, p. 1929.

53 R. G. Gordon. Molecular Collisions and Depolarization of Fluorescence in Gases. *J. Chem. Phys.* **45** no. 5, 1966, p. 1643.

54 Y. N. Luponosov, J. Min, A. N. Solodukhin, O. V. Kozlov, M. A. Obrezkova, S. M. Peregudova, T. Ameri, S. N. Chvalun, M. S. Pshenichnikov, C. J. Brabec *et al.* Effects of Electron-Withdrawing Group and Electron-Donating Core Combinations on Physical Properties and Photovoltaic Performance in D-π-A Star-Shaped Small Molecules. *Org. Electron.* **32**, 2016, p. 157.

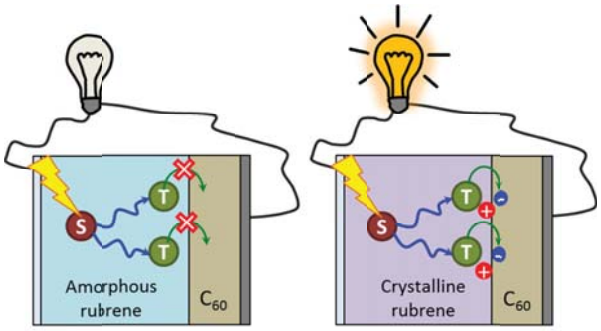

Chapter 6

Triplet Exciton Harvesting in Singlet Fission Solar Cells

In singlet fission solar cells, one absorbed photon produces two triplet excitons, and therefore internal quantum efficiencies up to 200% can be achieved. However, collecting the triplets is challenging and possible only in selected donor-acceptor systems. Here we demonstrate how the morphology of the singlet fission material (rubrene) affects the triplet collection in rubrene/C_{60} bilayers. The dynamics of the triplets are tracked by delayed photoluminescence caused by triplet-triplet annihilation events. In amorphous rubrene/C_{60} bilayer, no triplet excitons are collected at the interface. This is in sharp contrast with rubrene/C_{60} bilayer, where efficient triplet dissociation is observed due to the favorable energy alignment. The difference between the two systems clearly indicates the effect of the singlet fission layer morphology on the triplet exciton harvesting. This, together with the extremely fast singlet fission, makes crystalline rubrene-based solar cells essentially triplet-driven.

This Chapter is based on the following publication:
YunHui L. Lin, Michael A. Fusella, Oleg V. Kozlov, Xin Lin, Antoine Kahn, Maxim S. Pshenichnikov and Barry P. Rand, *Adv. Funct. Mater.* **26**(35), 6489 (2016)

6.1 Introduction

Solar cells are the devices that are capable of converting the incoming solar photons into electricity. Typically, one absorbed photon creates one electron-hole pair which (if no loses occurs) is collected as the electron and the hole at the electrodes. Not all photons are converted to the electron-hole pairs with similar efficiency: the photons with energies lower than the bandgap of the material, are not harvested at all while excessive energy of high-energetic photons is lost in the thermalization process. The interplay between photon collection and thermalization losses results in intrinsic limitation of power conversion efficiency of a single-bandgap solar cell: the famous Shockley-Queisser limit.[1] According to this limit, maximal possible efficiency which can be achieved with single-junction solar cell is ~32% with the optimal bandgap of the absorbing semiconductor of 1.34 eV.[1]

One of the possibilities to overcome this limit is more effective management of high-energy photons: if a photon with energy twice as high as the band gap produced two electron-hole pairs, the maximal possible efficiency increases to ~42%.[2] Among a number of mechanisms which allow for such a process to occur, one is singlet fission in organic molecular crystals.[3-8] In singlet fission materials, absorbed photon creates a singlet exciton which is further converted to a triplet pair (see Chapter 1, Section 1.2.2 “Triplet excitons” for details) which is further to be separated into two electron-hole pairs.

Efficient singlet fission is known to occur in family of polyacene materials (e.g. tetracene, pentacene and their derivatives).[4,9,10] However, the ability to produce a triplet pair from a single photon is not the only requirement for the efficiency enhancing: the triplets are also must be able to dissociate to the electron-hole pair at the donor-acceptor interface. For this, elaborate material and device engineering is needed in order to ensure property energy alignment. Additionally, the morphology of singlet fission material may affect both singlet fission efficiency and energies of the excitons.[11] Recently it was shown that rubrene obtained in crystalline and amorphous forms exhibit highly different energetics which can affect the singlet fission process and exciton harvesting efficiency.[12]

Here we use time-resolved photoluminescence (PL) to track the exciton dynamics in amorphous and crystalline rubrene layers of rubrene/C_{60} planar heterojunctions. We show that in both crystalline and amorphous rubrene fast singlet fission occurs populating the rubrene layer with triplet excitons. The dynamics of the triplets are monitored by delayed PL caused by triplet-triplet annihilation (TTA) events. In the amorphous system, dramatic quenching of prompt singlet PL is observed in rubrene/C_{60} bilayer, while delayed PL dynamics are unchanged. Therefore, only singlet excitons undergo dissociation at the amorphous rubrene/C_{60} interface, while the triplet excitons cannot be harvested. This is in sharp contrast with the crystalline

samples, where delayed PL dynamics are noticeably different in the bilayer because the triplet excitons dissociate at the interface. The experimental data are successfully described by the analytical model which confirms the triplet quenching in crystalline rubrene-based bilayers.

6.2 Experimental Results

6.2.1 Absorption and PL Spectra

For transient PL experiments, 17 nm of amorphous and crystalline rubrene were fabricated on glass, with and without a 5 nm C_{60} quenching layer (Figure 6.1a).

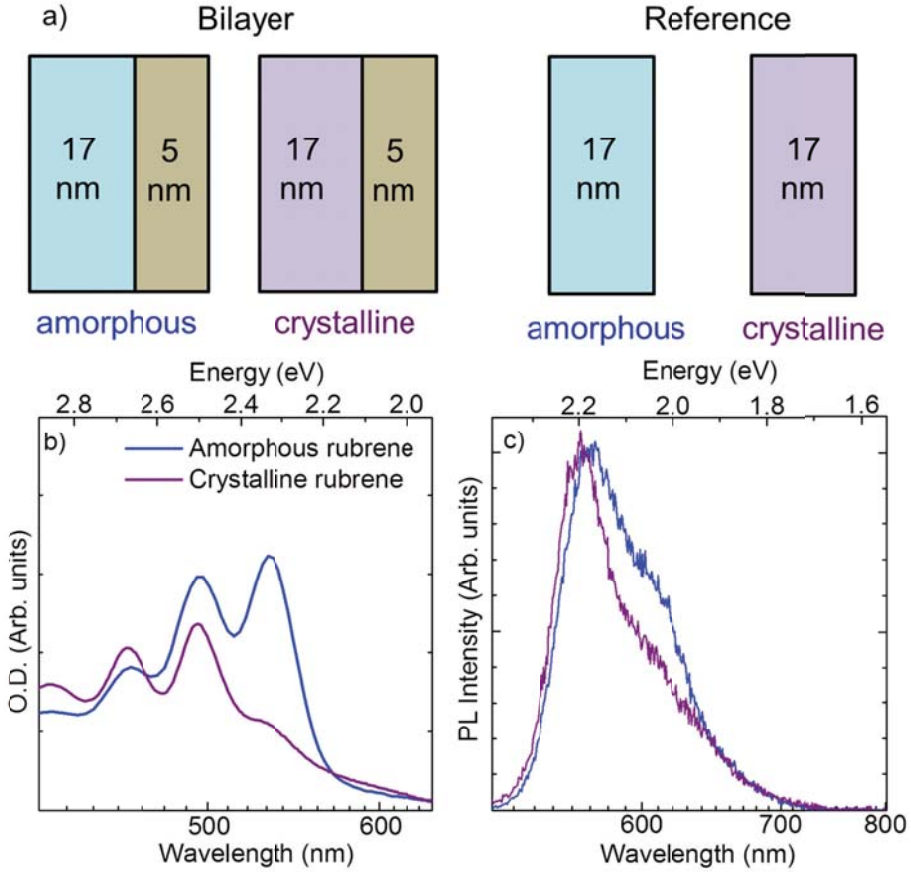

Figure 6.1 (a) Schematic drawing of the samples studied (manufactured by M. Fusella, Princeton, US); (b) absorption and (c) PL spectra of amorphous (blue) and crystalline (purple) rubrene layers. PL spectra are obtained by integrating the PL dynamics measured after 440 nm excitation over first 2 ns.

Figure 6.1b shows the absorption spectra for amorphous and crystalline rubrene layers. Both spectra exhibit strong vibrational structure; however, the spectrum of crystalline rubrene is

noticeably blue-shifted due to the stronger aggregation of the rubrene molecules in the crystal. To ensure similar excitation of the two samples and simplify the data analysis, the excitation wavelength of 440 nm was chosen where the optical densities of both samples are comparable.

Photoluminescence spectra for amorphous and crystalline rubrene layers are shown in Figure 6.1c. Both samples exhibit strong PL in the 550-700 nm region; the PL spectrum of amorphous rubrene is slightly broader due to the higher orientational disorder of the rubrene molecules in amorphous phase.

6.2.2 PL Dynamics

The PL dynamics of all samples exhibit a fast initial drop in the signal followed by slower decay (Figure 6.2). This can be understood as follows: at early timescales, a decay process rapidly removes emissive singlets from the system after which, at late timescales, a slower singlet generation mechanism is present that results in a lower rate of decay. Previous studies have reported negligible yields of intersystem crossing and internal conversion for isolated rubrene molecules in polystyrene, along with a fluorescence lifetime of 16 ns.[13] Therefore, singlet fission, occurring in bulk rubrene on the order of 1-2 ns (amorphous)[13,14] and 50-100 ps (crystalline)[6,15] is the fastest decay mechanism present which dominates the early-time PL dynamics of each sample. Thus, the rubrene layer becomes populated with triplet excitons and the PL at late timescales is assigned to delayed fluorescence due to TTA.[13,16]

Triplet population dynamics are described by the following equation:[17]

$$\frac{\partial T}{\partial t} = 2f_s\frac{S}{\tau_s} - \frac{T}{\tau_T} - \gamma T^2, \tag{6.1}$$

where S and T are singlet and triplet concentrations, respectively, τ_s and τ_T are singlet and triplet lifetimes, f_s is the probability of singlet fission and γ is bimolecular triplet interaction rate (depends on the diffusivity of triplets, probability of TTA etc.). Note that if the quenching interface is present, τ_s and τ_T represent effective lifetimes which also account for the quenching process.

If the singlet lifetime is short ($\tau_s << T^{-1}\gamma^{-1}$ and $\tau_s << \tau_T$),[17] the singlet population remains low compared to the triplet density, and the first singlet-related term in Equation (6.1) can be omitted. In this case, the tripled density is calculated as:

$$T(t) = \frac{T_0}{(1 + T_0\gamma\tau_T)e^{\frac{t}{\tau_T}} - T_0\gamma\tau_T}, \tag{6.2}$$

where T_0 is the initial triplet concentration. The delayed PL caused by TTA events is proportional to the squared triplet density:

$$PL(t) \sim \left(\frac{T_0}{(1 + T_0\gamma\tau_T)e^{\frac{t}{\tau_T}} - T_0\gamma\tau_T} \right)^2 \tag{6.3}$$

As the timescales of singlet fission and TTA events are significantly different, the total PL dynamics are described as

$$PL(t) = \sum_i A_i e^{-t/\tau_i} + A_T \left(\frac{T_0}{(1 + T_0\gamma\tau_T)e^{\frac{t}{\tau_T}} - T_0\gamma\tau_T} \right)^2, \tag{6.4}$$

where the first multiexponential term accounts for the singlet fission process. Equation (6.4) was used to fit the PL dynamics with A_i, τ_i, A_T, T_0, γ and τ_T as fit parameters. As γ depends on the material properties and does not depend on the presence of the quenching interface, it was set as global fit parameter for each pair (amorphous or crystalline) of samples.

In the neat amorphous rubrene film, the early-time PL dynamics follow triexponential decay with timescales of 40 ps, 450 ps, and 1 ns (Figure 6.2a, inset; Table 6.1). Similar time constants, 226 ps and 2.2 ns, were identified in a previous work on solution-processed amorphous rubrene, with the conclusion that the slower component reflects the majority of fission events.[13] In our measurements, the slow component was not as prominent as the fast components and the timescale was somehow faster than in Ref. [13] (1 ns *vs* 2.2 ns), but variations in film preparation, morphology, and the temporal resolution of the PL apparatus are likely to account for differences in PL decay dynamics.

In contrast to the amorphous rubrene, in the crystalline rubrene film the initial PL dynamics are dominated by a 50 ps decay (Figure 6.2b inset; Table 6.1) which has been previously attributed to the extremely efficient singlet fission in this system.[3,6] Because fission is so fast, emission beyond 1 ns is unlikely to originate from the initial pool of optically excited singlets, but rather from the process of TTA. In crystalline rubrene, direct quenching of triplets is favored via the CT state[12]; therefore, the TTA rates (and, consequently, PL dynamics) after 1 ns are expected to be substantially different for crystalline rubrene films fabricated with and without the C_{60} quenching layer.

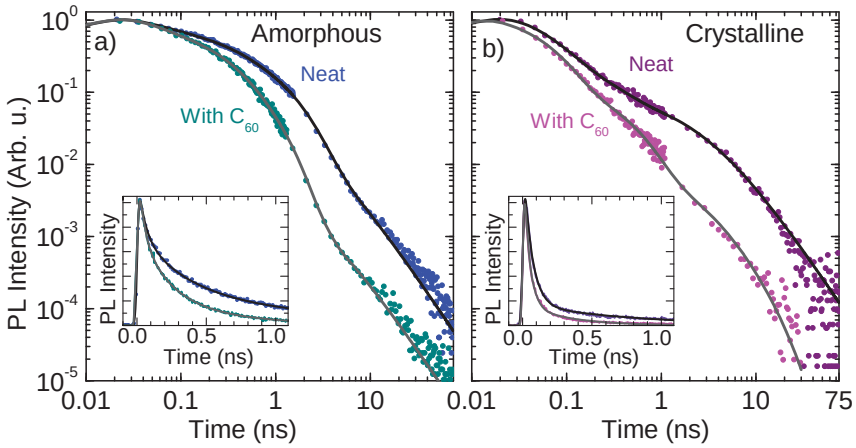

Figure 6.2 The log-log plots of PL dynamics for amorphous (a) and crystalline (b) rubrene samples. The experimental data are shown as the dots. The fits to PL transients according to Equation (6.4),(6.3) convoluted with the apparatus function, are shown by the thick lines. The insets show the early-time dynamics in the linear scale. Excitation wavelength is 440 nm; rubrene PL was integrated between 500 and 800 nm; all transients are normalized to maximum intensity. The abrupt decrease in noise level around 1 ns is due to the data stitching.

Table 6.1 Fit parameters for all samples. t_i and A_i stand for the timescales and amplitudes of exponent decay functions in the multiexponential fit of the early-time PL dynamics, A_T is the amplitude of TTA-related delayed PL and τ_T is the effective triplet lifetime.

	t_1 [ps] (A_1)	t_2 [ps] (A_2)	t_3 [ps] (A_3)	τ_T [ns] (A_T)	γ [ns^{-1}]
Amorphous	40 (0.36)	450 (0.31)	1000 (0.28)	∞ (0.05)	0.5
Amorphous/C_{60}	40 (0.42)	200 (0.4)	550 (0.18)	∞ (0.005)	
Crystalline	50 (0.79)	200 (0.15)	-	∞ (0.06)	0.35
Crystalline/C_{60}	50 (0.9)	350 (0.1)	-	20 (0.008)	

When the amorphous rubrene is paired with C_{60}, as shown in Figure 6.2a, dramatic quenching is observed within 1 ns. The fact that the singlet fission process in amorphous rubrene is relatively slow[13,14] implies that the significant amount of optically excited singlets is able to diffuse to the C_{60} interface before undergoing fission. Therefore, we attribute the initial acceleration of PL to the quenching of the singlet excitons at the rubrene/C_{60} interface. Some singlets, however, do undergo fission, and the resulting triplets then have an opportunity to annihilate and produce emissive singlets at late timescales, which is reflected in the late-time PL dynamics. However, because the process of direct triplet transfer from amorphous rubrene to C_{60} is energetically blocked, as established previously by EQE measurements[12], we expect the late-time TTA rates in the amorphous rubrene layer with and without C_{60} to be similar. This is indeed

the case, as seen in the region beyond 5 ns in Figure 6.2a: in the amorphous rubrene samples with and without C_{60}, the fitting curves are essentially similar (see Table 6.1 for the parameters) with the effective triplet lifetimes being much longer compared to the experimental timescale.

In the case of crystalline rubrene, PL behavior at short timescales are similar to the ones in amorphous rubrene: the PL decays mainly due to the singlet fission events, which in crystalline rubrene are somehow faster compared to the amorphous one (see Table 6.1). Note that even though the "slow" decay time seems to be somehow slower in C_{60}-covered sample, the respective amplitude is also lower which most probably reflects quenching of the singlet excitons at the interface. The delayed PL at late timescales are noticeably different for the two samples (Figure 6.2). For the rubrene layer without C_{60}, the effective triplet lifetime obtained from the fit is still much longer compared to the experimental timescale which points towards PL originated solely from the TTA process (this is confirmed by the power-dependence measurements; see Section 6.2.3 "PL Intensity Dependence on the Excitation Power"). In the sample paired with C_{60}, the effective lifetime amounts to ~20 ns, which is consistent with the presence of a competing cannel that depopulates diffusive triplets through charge transfer at the interface, thereby reducing the effective triplet lifetime. This is clearly seen as acceleration of the delayed PL decay in the C_{60}-covered sample, especially in the 3-10 ns region where the decay is dominated by the triplet quenching (Figure 6.2b).

6.2.3 PL Intensity Dependence on the Excitation Power

Following Akselrod and coworkers[18], we analyzed PL intensity of the samples as a function of excitation power. Such a study provides valuable insights into the origin of the emitting species at different points in time. For example, if PL originates directly from singlets generated by the excitation pulse, a linear PL intensity dependence on excitation power is observed. In contrast, if the emission is delayed fluorescence due to annihilation of two diffusing triplets, a quadratic dependence is expected, since the probability of bimolecular annihilation scales linearly with the population of each species involved (assuming the likelihood of singlet fission is not affected by the density of singlet excitons).

To investigate the intensity dependence of the PL decays, we measured the PL decay transients in amorphous and crystalline neat samples at different excitation powers (Figure 6.3). Then we plot the dependence of PL intensity on excitation power averaged over different time delays (Figure 6.4) and fit the resulting curves with the power law function.

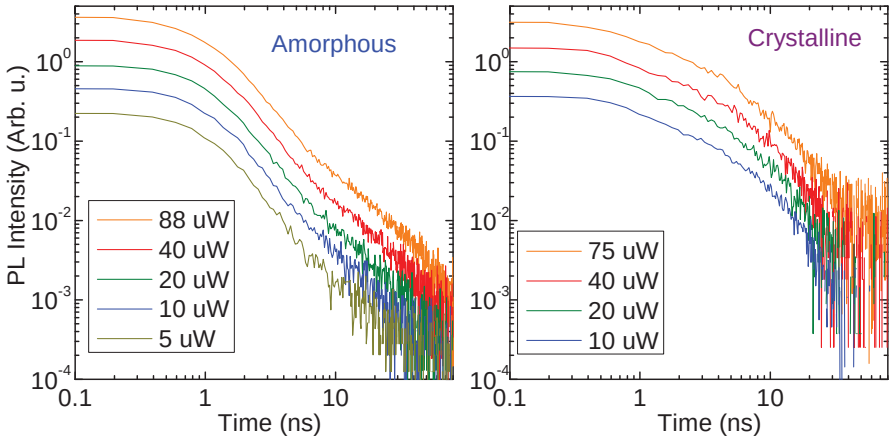

Figure 6.3 The PL dynamics for neat amorphous (left) and crystalline (right) rubrene samples at different excitation powers under 440 nm excitation. The PL dynamics are integrated in the 500-800 nm spectral range.

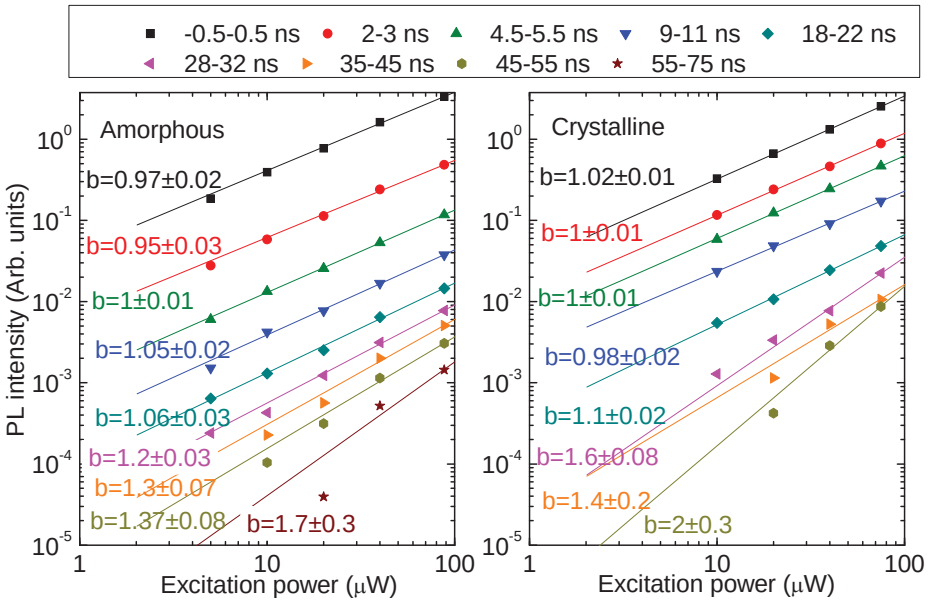

Figure 6.4 Dependence of PL intensity on excitation power at different time delays (indicated in legend) for neat amorphous (left) and crystalline (right) rubrene samples. The dependences at each time delay were fitted independently with a power law function $PL=A*I^b$, where PL is the PL intensity, A is a scaling factor, I is the excitation power, and b is the fitting parameter. The fitted values of b are shown next to each curve and summarized in Figure 6.5.

Figure 6.5 summarizes the PL intensity dependence on the pulse power. For the amorphous sample, the power law slope is 1 at early timescales because fission is relatively slow, such that

fluorescence at this timescale arises mainly from optically excited singlets. After around 20 ns, the power law slope increases due to the enhanced population of triplet excitons that can contribute to TTA to produce PL. This is independently verified by a log-log slope analysis of the PL transients (Figure 6.2): at late timescales (>10 ns) the PL decay is linear with a slope close to -2, confirming that delayed fluorescence of singlets generated by bimolecular TTA is the primary mechanism at this timescale.

For crystalline rubrene, however, in the PL-to-pulse-power plot (Figure 6.5), the power law slope remains at 1 for long after the initially excited singlets have undergone fission (up to ~20 ns). The origin of fluorescence at these intermediate time points can be understood if we consider the evolution of the rubrene PL spectrum over time.

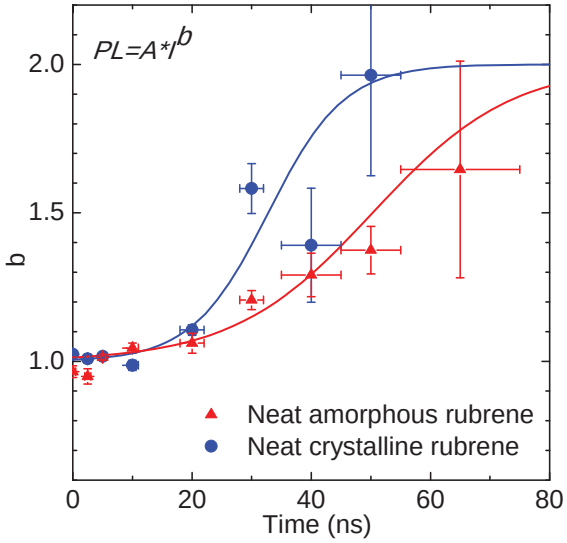

Figure 6.5 Photoluminescence (PL) intensity dependence on pulse power for the neat amorphous and crystalline rubrene at different time delays. The PL transients under excitation powers of 5-90 μW (Figure 6.3) were averaged over a particular time range (horizontal bars) and fitted as a function of excitation power according to the power law function $PL = A*I^b$, where PL is the PL intensity, A is an arbitrary scaling factor, I is the excitation power, and b is the fitting parameter. Symbols represent fitting parameters while solid lines are guides for the eye. Horizontal bars at the symbols show the time delays ranges in Figure 6.3.

6.2.4 PL Spectra Time Dependence

Figure 6.6 shows the evolution of neat amorphous and crystalline rubrene PL spectra at different times. For the amorphous sample, no spectral dynamics are observed, which implies that in all three time windows, emission stems from a single species, namely the rubrene singlets generated by either the excitation pulse or by TTA. The close-to-one power-law slope in this case may be

explained by competition between the TTA process and other processes that are not quadratic with triplet concentration (e.g. singlet fluorescence and/or geminate triplet-triplet fusion).[13]

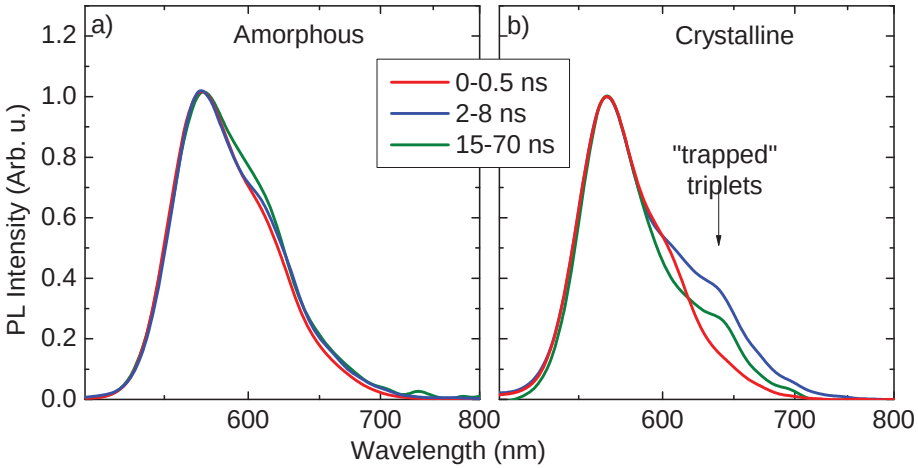

Figure 6.6 PL spectra integrated in different delay ranges (indicated) for amorphous (a) and crystalline (b) neat rubrene layers. Spectra are normalized by their maxima and digitally smoothened with a Gaussian filter with sd=5 nm.

In the crystalline sample a noticeable change in spectral shape is observed with time. At the earliest time window, singlet fission is not yet complete, and the spectrum is equivalent to that seen in the amorphous rubrene, indicating emission from identical species (the optically excited rubrene singlets). PL spectrum demonstrates intense peak around 565 nm which was earlier attributed to PL from the *bc* facet of the rubrene crystal.[19] In the intermediate time window, a prominent shoulder emerges in the spectrum around 650 nm. This 650 nm feature has been investigated in a previous work, with the conclusion that it arises due to fluorescence from low energy singlets formed by annihilation of a free rubrene triplet with a slightly lower energy triplet trapped in amorphous pockets of the otherwise crystalline film.[16]

This explains the linear dependence on excitation power: the probability of TTA scales linearly with the *mobile* triplet population (assuming the traps are prefilled). After around 20 ns the power law slope rapidly increases to 2, which is indicative of mobile TTA, and we can assume that the majority of trapped triplets have been exhausted. Indeed, at late timescales in the PL spectrum shown in Figure 6.6, the 650 nm feature has receded and the spectral line shape approaches that seen at early times.

Taken together, the analysis of PL decay (Figure 6.2) and the power dependent analysis (Figure 6.5) establish the time scales at which singlet fission and TTA represent the dominant mechanisms of singlet depopulation and population, respectively. As following from the PL

dynamics, amorphous rubrene/C_{60} interface is singlet dissociating and triplet blocking. In contrast, triplet dissociation is observed at crystalline rubrene/C_{60} interface. This behavior, when coupled with extremely fast singlet fission, makes crystalline rubrene-based devices essentially triplet-driven.

6.3 Conclusions

In this Chapter, we demonstrate how the morphology of singlet fission material (rubrene) affects the triplet harvesting in rubrene/C_{60} solar cells. In the amorphous rubrene/C_{60} system, where the energetics at the interface does not allow for triplet dissociation, only singlet excitons are quenched with high efficiency which results in similar dynamics of delayed photoluminescence caused by triplet-triplet annihilation events. In contrast, in the crystalline rubrene/C_{60} bilayer, photoluminescence dynamics suggest that both singlet and triplet excitons are quenched because of the favorable energy alignment. Therefore, morphology of the singlet fission material has strong impact on the functioning of singlet-fission solar cells, and achieving optimal morphology which ensures both efficient singlet fission and triplet harvesting is a prospective way to increase the efficiency of organic solar cells.

6.4 Methods

Samples preparation

The samples were prepared by vacuum evaporation technique by M. Fusella (Princeton, US). For the details of sample preparation, refer to Ref. [12].

Optical

Absorption spectra of the samples were recorded with a Perkin-Elmer Lambda 900 spectrophotometer. Transient photoluminescence measurements were performed using a Hamamatsu C5680 streak-camera system. The 440 nm excitation wavelength was produced by doubling of the output from a Mira Titanium:Sapphire laser. Unless otherwise specified, PL transients were measured with a 40 μW excitation power, which corresponds to an estimated initial singlet exciton density of 4×10^{-5} nm^{-3}, or one exciton per 30 nm. The emission signal was collected at a 90° geometry with respect to the excitation beam. The wavelength range from 500 to 800 nm was detected.

Because of strongly different timescales of the processes observed (fast singlet fission and slow TTA), the experiments were performed at two repetition rates of the laser (2 MHz and 76 MHz) to adequately resolve the relevant timescales. At both repetition rates, the effects of the

nonequilibrium triplet population buildup can affect the measurements due to the extremely long triplet lifetime (~100 μs [17]).

Singlet fission processes were observed at the 76 MHz repetition rate with high temporal resolution (~10 ps) in the time region up to ~1.5 ns. In this case, the PL observed is caused by singlet emission. As the triplet population does not affect the PL dynamics because of the extreme difference in the timescales (0.1-1 ns *vs.* 100's μs), the PL from TTA was directly subtracted as a constant baseline.

The delayed PL caused by the TTA events was studied at the 2 MHz repetition rate as a compromise between the triplet lifetime and signal-to-noise ratio with resolution of ~200 ps. The time window of 75 ns was limited by the extremely low signal at long delays and ultimately by the streak camera dynamic range. The TTA-based PL first of all depends on triplet concentration and triplet diffusion constant but not the triplets' lifetime. Taking into account quadratic dependence of PL dynamics on excitation power (Figure 6.5), we conclude that only few triplets contribute to the TTA process after 500 ns (i.e, the time interval between the adjacent pulses) and therefore the PL dynamics are not affected by the build-up of the triplet population.

After the correction for triplet build-up, the data measured with high and low repetition rates were stitched at 1 ns.

Data analysis

The PL dynamics were fitted with Equation (6.4) using A_i, τ_i, A_T, γ and τ_T as fit parameters; γ was set as global fit parameters for each (amorphous or crystalline) pair of samples; T_0 was set to unity to avoid interference with A_T. The Poisson statistics was assumed to account for five decimal orders dynamical range. The final fit parameters are summarized in Table 6.1.

Author Contributions

OVK performed PL measurements and analysis, MAF manufactured the samples, BPR and MSP conceived the project and supervised the research.

References

1 W. Shockley and H. J. Queisser. Detailed Balance Limit of Efficiency of p-n Junction Solar Cells. *J. Appl. Phys.* **32** no. 3, 1961, p. 510.

2 M. C. Hanna and A. J. Nozik. Solar Conversion Efficiency of Photovoltaic and Photoelectrolysis Cells with Carrier Multiplication Absorbers. *J. Appl. Phys.* **100** no. 7, 2006, p. 074510.

3 D. N. Congreve, J. Lee, N. J. Thompson, E. Hontz, S. R. Yost, P. D. Reusswig, M. E. Bahlke, S. Reineke, T. Van Voorhis, and M. A. Baldo. External Quantum Efficiency Above 100% in a Singlet-Exciton-Fission–Based Organic Photovoltaic Cell. *Science* **340** no. 6130, 2013, p. 334.

4 P. D. Reusswig, D. N. Congreve, N. J. Thompson, and M. A. Baldo. Enhanced External Quantum Efficiency in an Organic Photovoltaic Cell via Singlet Fission Exciton Sensitizer. *Appl. Phys. Lett.* **101** no. 11, 2012, p. 113304.

5 M. B. Smith and J. Michl. Singlet Fission. *Chemical Reviews* **110** no. 11, 2010, p. 6891.

6 L. Ma, K. Zhang, C. Kloc, H. Sun, M. E. Michel-Beyerle, and G. G. Gurzadyan. Singlet Fission in Rubrene Single Crystal: Direct Observation by Femtosecond Pump-Probe Spectroscopy. *Phys. Chem. Chem. Phys.* **14** no. 23, 2012, p. 8307.

7 Y. Kasai, Y. Tamai, H. Ohkita, H. Benten, and S. Ito. Ultrafast Singlet Fission in a Push–Pull Low-Bandgap Polymer Film. *J. Am. Chem. Soc.* **137** no. 51, 2015, p. 15980.

8 A. Köhler and H. Bässler. Triplet States in Organic Semiconductors. *Materials Science and Engineering: R: Reports* **66** no. 4–6, 2009, p. 71.

9 P. J. Jadhav, A. Mohanty, J. Sussman, J. Lee, and M. A. Baldo. Singlet Exciton Fission in Nanostructured Organic Solar Cells. *Nano Lett.* **11** no. 4, 2011, p. 1495.

10 M. Tabachnyk, B. Ehrler, S. Bayliss, R. H. Friend, and N. C. Greenham. Triplet Diffusion in Singlet Exciton Fission Sensitized Pentacene Solar Cells. *Appl. Phys. Lett.* **103** no. 15, 2013, p. 153302.

11 Y. Nakayama, S. Machida, T. Minari, K. Tsukagishi, Y. Noguchi, and H. Ishii. Direct Observation of the Electronic States of Single Crystalline Rubrene under Ambient Condition by Photoelectron Yield Spectroscopy. *Appl. Phys. Lett.* **93** no. 17, 2008, p. 173305.

12 Y. L. Lin, M. A. Fusella, O. V. Kozlov, X. Lin, A. Kahn, M. S. Pshenichnikov, and B. P. Rand. Morphological Tuning of the Energetics in Singlet Fission Organic Solar Cells. *Adv. Funct. Mater.* **26** no. 35, 2016, p. 6489.

13 G. B. Piland, J. J. Burdett, D. Kurunthu, and C. J. Bardeen. Magnetic Field Effects on Singlet Fission and Fluorescence Decay Dynamics in Amorphous Rubrene. *J. Phys. Chem. C* **117** no. 3, 2013, p. 1224.

14 M. Ullah, S. D. Yambem, E. G. Moore, E. B. Namdas, and A. K. Pandey. Singlet Fission and Triplet Exciton Dynamics in Rubrene/Fullerene Heterojunctions: Implications for Electroluminescence. *Advanced Electronic Materials* **1** no. 12, 2015, p. n/a.

15 S. R. Yost, J. Lee, M. W. B. Wilson, T. Wu, D. P. McMahon, R. R. Parkhurst, N. J. Thompson, D. N. Congreve, A. Rao, K. Johnson *et al*. A Transferable Model for Singlet-Fission Kinetics. *Nat Chem* **6** no. 6, 2014, p. 492.

16 H. Najafov, B. Lee, Q. Zhou, L. C. Feldman, and V. Podzorov. Observation of Long-Range Exciton Diffusion in Highly Ordered Organic Semiconductors. *Nat. Mater.* **9** no. 11, 2010, p. 938.

17 A. Ryasnyanskiy and I. Biaggio. Triplet Exciton Dynamics in Rubrene Single Crystals. *Physical Review B* **84** no. 19, 2011, p. 193203.

18 G. M. Akselrod, P. B. Deotare, N. J. Thompson, J. Lee, W. A. Tisdale, M. A. Baldo, V. M. Menon, and V. Bulović. Visualization of Exciton Transport in Ordered and Disordered Molecular Solids. *Nat. Commun.* **5**, 2014, p. 3646

19 P. Irkhin, A. Ryasnyanskiy, M. Koehler, and I. Biaggio. Absorption and Photoluminescence Spectroscopy of Rubrene Single Crystals. *Physical Review B* **86** no. 8, 2012, p. 085143.

Summary

Organic photovoltaics is an emerging technology which aims to supplement conventional inorganic (e.g. silicon-based) solar cells. Because of unique features of organic devices such as light weight, possible semitransparency, flexibility, strong absorption in the visible and near-infrared regions etc., the possible application area of organic solar cells seems to be endless. The main difference between organic solar cells and their inorganic counterparts is the physics of photon-to-charge conversion. In the conventional inorganic solar cells, the absorbed photon generates a pair of free charges which are further collected at the electrodes. In contrast, in organic semiconductors the charges which are generated after photoexcitation are not free – they are bound in a neutral quasiparticle called an "exciton". In order to be dissociated into free charges, the exciton needs to be "shaken", i.e. extra energy needs to be provided. Typically, this is achieved by bringing two materials with different energy levels in close proximity, i.e. creating an interface. At such an interface, one material acts as electron donor while the other plays role of electron acceptor. Often the donor and the acceptor materials are mixed together and form a self-organized network, the so-called bulk heterojunction. After being generated within the donor or acceptor phase, the exciton needs to diffuse to the interface to have the possibility to dissociate into the separated charges. Finally, the separated charges need to travel to the electrodes to be extracted there producing photocurrent. Thus, the photon-to-charge conversion process in organic solar cells is complex, with the intermediate quasi-particle – the exciton – involved.

Such important steps of photon-to-charge conversion process as exciton photogeneration, its diffusion to the interface and dissociation occur at nanosecond and sub-nanosecond timescales, i.e. faster than one billionth of a second. Even at such incredibly short times, there might be losses which cannot be recovered later. Thus, each process of early-time photon-to-charge conversion needs to be carefully monitored and controlled. This Thesis aims to address this issue step-by-step using time-resolved ultrafast spectroscopy as a tool. Each chapter of the Thesis addresses a particular process of exciton or/and charge dynamics, explains its physics and suggests possible ways to maximize the efficiency of this process.

The very first step of photon-to-charge conversion is the photon absorption and exciton formation, i.e. the exciton photogeneration. After photogeneration, the exciton needs to reach the interface between the donor and the acceptor. To prevent any losses at this step, it is a must to understand how the exciton reaches the donor-acceptor interface. In **Chapter 2**, we present a new spectroscopic technique which allows for tracking of the exciton motion in real time. The

donor (acceptor) material is populated by excitons with the excitation laser pulse, and the dynamics of the exciton dissociation at the interface is monitored by the delayed probe pulse. With this technique, it is readily possible to measure how fast the exciton reaches the interface and to estimate the exciton harvesting efficiency for any donor-acceptor system.

The ability to monitor the exciton harvesting is especially important for the bulk heterojunction organic solar cells. The efficiency of exciton dissociation in the bulk heterojunction active layer strongly depends on the particular configuration of the blend, mainly on the spatial separation of donor and acceptor phases (the so-called morphology). Bulk heterojunction morphology is of utmost importance for the organic solar cell operation; however, it is extremely difficult to characterize the morphology due to the nanometer-scale phase separation. In **Chapter 3**, we demonstrate how the morphology of donor-acceptor blends can be characterized by spectroscopic means. Combining the exciton-tracking technique (Chapter 2) with extensive computer simulations, we are able to identify the length scale of donor-acceptor phase separation with nanometer precision. As the technique is non-invasive, it can be applied to the operating organic solar cells without any special preparation thus paving a new way for device optimization.

In the organic solar cell active layer, not all photogenerated excitons reach the interface and dissociate into the charges. In the classical picture, the photogenerated exciton can also relax to the ground state due to its limited lifetime. In **Chapter 4**, we demonstrate that this dual behavior of the exciton is not always guaranteed. We study the exciton dynamics in thin films of organic semiconductors without the external acceptor using push-pull star-shaped molecules as benchmark materials. We show that in such films the exciton can spontaneously dissociate into separated (quasi-)free charges even without presence of external acceptor. In this case, no energy gradient is needed anymore to separate the charges. This is extremely beneficial for the organic solar cell design as the second material may only be used as a charge transport layer. We envision this mechanism of intrinsic exciton-to-charge conversion to play a crucial role in the forthcoming device design.

Chapter 5 summarizes the whole early-time photon-to-charge conversion processes. Using photovoltaic blends based on push-pull star-shaped molecules as benchmark systems, we demonstrate that the early-time charge generation can be broken down to a series of consequent substeps. After photon absorption, the excitons are generated both in donor and acceptor phases. The photogenerated excitons are dissociated either almost instantaneously (from the donor phase) or after delayed transport to the interface (from the acceptor phase). The separated charges, however, are not free but are trapped in the interfacial charge-transfer state. Due to the relatively high Coulomb attraction between negative electron and positive hole in the charge-transfer state, up to a half of the initially separated charges recombine. Thus, we demonstrate that

geminate charge recombination is the main loss mechanism at early timescales and that it needs to be suppressed in order to maximize the charge generation efficiency.

We further discuss a possibility to fundamentally improve the efficiency of solar cells by efficient utilizing the high-energy photons. In organic materials, this can be done via a singlet fission process – splitting high-energy singlet exciton into two triplet excitons with lower energies. If both triplet excitons are collected, one absorbed photon results in two electron-hole pairs, i.e. the internal quantum efficiency reaches 200%. In **Chapter 6**, we demonstrate that in organic solar cells based on a singlet fission material – rubrene – the efficiency of triplet exciton dissociation highly depends on morphology of the rubrene layer. In crystalline rubrene:C_{60} devices, the triplets are collected due to the favorable energetics. In contrast, if the rubrene layer is amorphous, the rubrene triplets are blocked at the interface with C_{60}. This highlights the importance of morphology control for the device optimization not only in the bulk heterojunction solar cells but also in the next-generation photovoltaics.

Overall, the Thesis covers all initial steps of photon-to-charge conversion in both singlet- and triplet- driven modern organic photovoltaics revealing the ultrafast processes which eventually lead to the generation of photocurrent. Charge generation processes and loss mechanisms are thoroughly examined by ultrafast spectroscopy, which provides a powerful and indispensable tool for understanding the photophysics of organic optoelectronic devices. We envision the results presented in this Thesis to be of great value for understanding the fundamental photophysics of organic solar cells, which will eventually lead to improved device efficiency.

Samenvatting

Organische fotovoltaïca is een opkomende technologie die beoogt verder te gaan dan de technologie van de conventionele anorganische (bv op silicium gebaseerde) zonnecellen. Door de unieke eigenschappen van organische ‘devices’, zoals het lichte gewicht, mogelijke semitransparantie, flexibiliteit, sterke absorptie in het zichtbare en bijna infrarode spectrum, lijkt het toepassingsgebied voor organische zonnecellen bijna eindeloos groot. Het belangrijkste verschil tussen organische zonnecellen en hun anorganische tegenhangers is de fysica van de foton-naar-lading conversie. In conventionele, anorganische zonnecellen genereert een ingevangen foton een paar (twee) vrije ladingen, die vervolgens bij de electroden worden verzameld. Echter, in organische zonnecellen zijn de gemaakte ladingen niet vrij - ze zijn gebonden in een neutraal quasi-deeltje: het ‘exciton’. Om het exciton te splitsen in twee vrije ladingen, moet het als het ware worden ‘opgeschud’ : er is extra energie nodig. Dit wordt typisch gedaan door twee materialen met verschillende energie niveaus dicht bij elkaar te brengen, zodat een grensvlak wordt gecreëerd. Bij zo’n grensvlak fungeert het ene materiaal als elektron donor en het andere als elektron acceptor. Vaak worden de twee materialen door elkaar gemengd en vormen zo een zelf-georganiseerd netwerk: de zogenaamde ‘bulk-heterojunction’. Nadat een exciton is gegenereerd in ofwel het donor gedeelte ofwel in het acceptor gedeelte, moet het naar het grensvlak toe diffunderen, om daar eventueel te worden gesplitst in twee afzonderlijke ladingen. Deze ladingen moeten vervolgens naar de electroden gaan om daar de elektrische stroom te vormen. Het is duidelijk dat de foton-naar-lading conversie in organische zonnecellen (met het quasi -deeltje ’exciton’ als intermediair) een complexe zaak is.

De belangrijke stappen in de foton-naar-lading conversie, zoals het maken van een exciton door een foton, de diffusie van het exciton naar het grensvlak en de splitsing aldaar, gebeuren op nanoseconde en sub-nanoseconde tijdschalen, dat wil zeggen, sneller dan een miljardste van een seconde. En zelfs met zulke ongelofelijk snelle tijden, kunnen er verliezen optreden, die later niet meer ongedaan kunnen worden gemaakt. En dus moet elk proces in het eerste begin van de foton-naar-lading conversie zorgvuldig worden bekeken en gecontroleerd. Dit proefschrift streeft ernaar om dit stap voor stap aan te pakken, met als gereedschap de tijd opgeloste ultrasnelle spectroscopie. Elk hoofdstuk van dit proefschrift behandelt een bepaald proces van de exciton

en/of lading dynamica, verklaart de fysica ervan en geeft suggesties voor mogelijke manieren om de efficiëntie van dat proces te maximaliseren.

De allereerste stap in de foton-naar-lading conversie is de absorptie van het foton en het maken van het exciton : de exciton fotogeneratie. Na gemaakt te zijn moet het exciton het grensvlak tussen donor en acceptor bereiken. Om verliezen te voorkomen in deze stap, is het essentieel om te begrijpen hoe het exciton het donor-acceptor grensvlak bereikt. In **hoofdstuk 2** presenteren we een nieuwe techniek die het mogelijk maakt om de exciton beweging in real-time te volgen. Het donor (acceptor) materiaal wordt bevolkt met excitonen met de excitatie laserpuls en de dynamica van de exciton splitsing aan het grensvlak wordt gevolgd met de in tijd vertraagde 'probe' pulse. Met deze techniek is het gemakkelijk mogelijk te meten hoe snel het exciton het grensvlak bereikt en een schatting te maken van de exciton 'oogst'-efficiëntie van elk donor-acceptor systeem.

De mogelijkheid om het exciton oogsten te monitoren is vooral belangrijk voor de bulk-heterojunction organische zonnecellen. De efficiëntie van de exciton splitsing in de actieve laag van de bulk-heterojunction hangt sterk af van de specifieke configuratie van het donor-acceptor mengsel en dan vooral van de ruimtelijke scheiding van de donor en acceptor fasen (de zogenaamde morfologie). De bulk-heterojunction morfologie is van het grootste belang voor de werking van een organische zonnecel; het is echter extreem moeilijk om de morfologie te karakteriseren vanwege de nanometer schaal van de afstand van de fasen. In **hoofdstuk 3** laten we zien hoe de morfologie van donor-acceptor mengsels kan worden gekarakteriseerd door middel van spectroscopie. Door de techniek van het volgen van de excitonbeweging (hoofdstuk 2) te combineren met uitgebreide computer simulaties kunnen we de lengte schaal van de donor-acceptor fase scheiding bepalen met nanometer precisie. Aangezien deze techniek niet invasief is, kan het worden toegepast op werkende zonnecellen, zonder speciale voorbereidingen, en maakt zo de weg vrij voor een nieuwe manier om deze devices te optimaliseren.

Niet alle door licht gegenereerde excitonen in de actieve laag van een organische zonnecel bereiken het grensvlak en worden daar gesplitst in ladingen. In het klassieke verhaal kan een exciton ook terugvallen naar de grondtoestand vanwege zijn eindige levensduur. In **hoofdstuk 4** laten we zien dat dit tweevoudige gedrag niet altijd gebeurt. We bestuderen de exciton dynamica in dunne lagen van organische halfgeleiders zonder een externe acceptor, door gebruik te maken van push-pull stervormige moleculen als benchmark materiaal. We laten zien dat dat in zulke

dunne lagen een exciton ook spontaan kan worden gesplitst in afzonderlijke (quasi-) vrije ladingen, zelfs zonder de aanwezigheid van een externe acceptor. In dit geval is er geen energie gradiënt meer nodig om de ladingen te scheiden. Dit is zeer gunstig voor het ontwerpen van organische zonnecellen, omdat het tweede materiaal nu alleen nog maar hoeft te worden gebruikt voor de verplaatsing van de ladingen. We denken dat dit mechanisme van intrinsieke exciton-naar-lading conversie een cruciale rol gaat spelen in toekomstige device ontwerpen.

Hoofdstuk 5 geeft een samenvatting van alle eerste stappen in de foton-naar-lading conversie. We gebruiken fotovoltaïsche mengsels met push-pull stervormige moleculen als benchmarks en laten zo zien dat het eerste begin van de ladingsgeneratie opgedeeld kan worden in een reeks van consistente, afzonderlijke stappen. Na absorptie van een foton worden excitonen gegenereerd in zowel de donor als de acceptor fase. Deze excitonen worden ofwel vrijwel meteen gesplitst (donor fase) of even later, na transport naar het grensvlak (acceptor fase). Deze gescheiden ladingen zijn echter niet vrij, maar zitten vast in een ‘charge-transfer’ toestand van het grensvlak. Door de relatief hoge Coulomb aantrekkingskracht tussen het negatief geladen elektron en het positief geladen gat in de ‘charge-transfer’ toestand, worden tot vijftig procent van de gescheiden ladingen weer samengevoegd. We laten dus zien dat deze recombinatie van ladingen het belangrijkste verliesmechanisme is in het begin en dat het onderdrukt moet worden om de efficiëntie van het genereren van lading te maximaliseren.

Verder bespreken we een mogelijkheid om de efficiëntie van zonnecellen fundamenteel te verhogen door gebruik te maken hoog energetisch fotonen. In organische materialen kan dit gebeuren door het splitsen van een singlet aangeslagen toestand: het splitsen van een hoog energetische singlet toestand in 2 triplet excitonen met een lagere energie. Als beide excitonen worden benut dan resulteert één geabsorbeerd foton in twéé elektron-gat paren: de interne kwantum efficiëntie bereikt dan de 200%. In **hoofdstuk 6** laten we zien dat in organische zonnecellen die gebaseerd zijn op materialen met singlet splitsing - rubreen - de efficiëntie van de splitsing van de triplet excitonen zeer sterk afhangt van de morfologie van de rubreen laag. In kristallijne rubreen:C_{60} devices worden de excitonen benut dankzij de gunstige energieën. Als de rubreen laag daarentegen amorf is, dan worden de rubreen triplet excitonen geblokkeerd aan de grens met C_{60}. Dit illustreert het belang van de controle over de morfologie voor het optimaliseren van een device, niet alleen bij bulk-heterojunction zonnecellen, maar ook bij fotovoltaïsche devices van een volgende generatie.

Samenvattend: dit proefschrift behandeld alle eerste stappen van de foton-naar-lading conversie in zowel door singlet als door triplet gedreven moderne organische fotovoltaïca en laat de ultrasnelle processen zien die uiteindelijk leiden tot het genereren van stroom door licht. Ladingsgeneratie processen en verliesmechanismes zijn grondig onderzocht door middel van ultrasnelle spectroscopie, wat een krachtig en onontbeerlijk hulpmiddel verschaft voor het begrijpen van de fotofysica van organische opto-elektronische devices. We denken dat de resultaten die in dit proefschrift zijn gepresenteerd van grote waarde zullen zijn voor het begrijpen van de fundamentele fotofysica van organische zonnecellen, wat uiteindelijk zal leiden tot een betere efficiëntie van deze devices.

Summary for General Public

Imagine a world with free energy everywhere. You don't need to take a phone charger with you – your backpack generates energy. You don't need to electrify your house – the energy is produced by the walls and windows. Even though this sounds like science fiction, this world is much closer to reality than you might think: our Sun provides more than enough energy to cover mankind's needs.

Already now, people successfully use solar energy by converting it to electricity with silicon solar cells. However, these devices are quite heavy and bulky which essentially limits their application area. Alternatively, solar cells can be made of special plastics – and those solar cells can be foldable, semi-transparent, light-weight, shape-customizable, wearable – so that their potential application areas seem unlimited. However, to date the efficiencies of such solar cells are still twice as low as the efficiencies of their silicon analogues.

To promote the efficiency of plastic solar cells, we should understand all the photophysics behind light-to-electricity conversion. Many crucial processes occur faster than one billionth of a second but still have a great influence on overall device performance. In this Thesis, we use laser spectroscopy to reveal main processes which contribute to the photocurrent of the solar cells at such incredibly short timescales, along with possible losses which decrease the efficiency of the overall device. Armed with this understanding, we propose the pathways to maximize the efficiency of light-to-electricity conversion which we believe will make the Dream World a bit closer to us!

List of Journal Publications

1. Elena Agina, Artur Mannanov, Alexey Sizov, Olga Vechter, Oleg Borshchev, Artem Bakirov, Maxim Shcherbina, Sergey Chvalun, Vladislav Konstantinov, Vladimir Bruevich, Oleg V. Kozlov, Maxim S. Pshenichnikov, Dmitry Yu. Paraschuk, and Sergei A. Ponomarenko, "Luminescent Organic Semiconducting Langmuir Monolayers", *ACS Applied Materials & Interfaces*, 2017, 9(21), 18078 (DOI: 10.1021/acsami.7b01919)
2. Oleg V. Kozlov*, Xiaomeng Liu*, Yuriy N Luponosov, Alexander N. Solodukhin, Victoria Y. Toropynina, Jie Min, Mikhail I. Buzin, Svetlana M Peregudova, Christoph J. Brabec, Sergei A. Ponomarenko, and Maxim S. Pshenichnikov, "Triphenylamine-Based Push-Pull Molecule for Photovoltaic Applications: from Synthesis to Ultrafast Device Photophysics", *Journal of Physical Chemistry C*, 2017, 121(12). 6424 (DOI: 10.1021/acs.jpcc.6b12068)
3. ✓ Oleg V. Kozlov, Yuriy N. Luponosov, Alexander N. Solodukhin, Bruno Flament, Yoann Olivier, Roberto Lazzaroni, Jérôme Cornil, Sergei A. Ponomarenko, and Maxim S. Pshenichnikov, "Ultrafast Exciton-to-Polaron Conversion in Densely-Packed Small Organic Semiconducting Molecules", *Advanced Optical Materials*, 2017, 5(7), 1700024 (DOI: 10.1002/adom.201700024)
4. Oleg V. Kozlov, Vlad G. Pavelyev, Hilde D. de Gier, Remco W. A. Havenith, Paul H.M. van Loosdrecht, Jan C. Hummelen, and Maxim S. Pshenichnikov, "Ultrafast electron and hole transfer in bulk heterojunctions of low-bandgap polymers", *Organic Photonics and Photovoltaics*, 2016, 4(1), 24 (DOI: 10.1515/oph-2016-0003)
5. ✓ Almis Serbenta*, Oleg V. Kozlov*, Giuseppe Portale, Paul H. M. van Loosdrecht, and Maxim S. Pshenichnikov, "Bulk heterojunction morphology of polymer:fullerene blends revealed by ultrafast spectroscopy", *Scientific Reports*, 2016, 6, 36236 (DOI: 10.1038/srep36236)
6. Evgeniia Salamatova, Oleg V. Kozlov, Yuriy N. Luponosov, Alexander N. Solodukhin, Viktoria Y. Toropynina, Sergei A. Ponomarenko, Maxim S. Pshenichnikov, "Visualization of molecular excitons diffusion", *Proc. SPIE 9923*, Physical Chemistry of Interfaces and Nanomaterials XV, 99230K (September 26, 2016); (DOI:10.1117/12.2237620)
7. ✓ YunHui L. Lin, Michael A. Fusella, Oleg V. Kozlov, Xin Lin, Antoine Kahn, Maxim S. Pshenichnikov and Barry P. Rand, "Morphological Tuning of the Energetics in Singlet Fission Organic Solar Cells", *Advanced Functional Materials*, 2016, 26(35), 6489 (DOI: 10.1002/adfm.201601125)

8. ✓ Yuriy N. Luponosov , Jie Min , Alexander N. Solodukhin, Oleg V. Kozlov, Marina A. Obrezkova, Svetlana M. Peregudova, Tayebeh Ameri, Sergei N. Chvalun, Maxim S. Pshenichnikov, Christoph J. Brabec, Sergei A. Ponomarenko, "Effects of electron-withdrawing group and electron-donating core combinations on physical properties and photovoltaic performance in D-π-A star-shaped small molecules", *Organic Electronics*, 2016, 32, 157 (DOI: 10.1016/j.orgel.2016.02.027)
9. ✓ Oleg V. Kozlov, Foppe de Haan, Ross A. Kerner, Barry P. Rand, David Cheyns, and Maxim S. Pshenichnikov, "Real-Time Tracking of Singlet Exciton Diffusion in Organic Semiconductors", *PRL*, 2016, 116(5), 057402 (DOI: 10.1103/PhysRevLett.116.057402)
10. Alexander V. Akkuratov, Diana K. Susarova, Oleg V. Kozlov, Alexander V. Chernyak, Yury L. Moskvin, Lyubov A. Frolova, Maxim S. Pshenichnikov, and Pavel A. Troshin, "Design of $(X\text{-}DADAD)_N$ Type Copolymers for Efficient Bulk Heterojunction Organic Solar Cells", *Macromolecules*, 2015, 48(7), 2013 (DOI: 10.1021/ma5023956)
11. ✓ Oleg V. Kozlov, Yuriy N. Luponosov, Sergei A. Ponomarenko, Dmitry Yu. Paraschuk, Yoann Olivier, David Beljonne, Jérôme Cornil, Nina Kausch-Busies and Maxim S. Pshenichnikov, "Ultrafast Charge Generation Pathways in Photovoltaic Blends Based on Novel Star-Shaped Conjugated Molecules", *Advanced Energy Materials*, 2015, 5(7), 1401657 (DOI: 10.1002/aenm.201401657)

* Authors contributed equally

✓ Publication or a part of it is included in this Thesis

Acknowledgements

For the first time, I visited a small city of Groningen in the fall of 2012 for a short master research project. After three months spent, I returned back to Moscow with a strong feeling that I definitely want to come to Groningen for a longer period of time. I was really impressed first of all by extremely productive working environment but at the same time the relaxed atmosphere of the city and its kind people. A year later, in the winter of 2013, I won the “Aurora - Towards Modern and Innovative Higher Education” grant that allowed me to move to Groningen for my PhD studies. Ever since, I did not regret for a second about my decision. I spent wonderful and productive four years here that culminated in this thesis, so that I would like to thank many people who supported and helped me on my way to become a Doctor of Science.

First of all, I would like to thank my promoters, Kees Hummelen and Maxim Pshenichnikov, for providing me an opportunity to work in the University of Groningen. Without your support during these four years, this book would not have been existent.

Kees, you were very kind and welcoming while accepting me, a physicist, to your group which mainly deals with chemistry. It was fun to look at the word of organic electronics from the other perspective and learn a bit about the chemistry involved. I am grateful for this opportunity and hope that the little knowledge of chemistry I earned in your group will help me a lot in my further career.

Maxim, I cannot even fully express how much I have learned and inherited from you. Pretty much everything I know about conducting the research, making and delivering scientific presentations, writing, publishing and reviewing the papers, I have mastered under your supervision with your endless support. You always had time to discuss all possible issues I faced and answer all my questions. I am certain that these long and frequent discussions played the most crucial role in my development as a scientist. You were the best supervisor I could imagine, and I will miss working with you a lot. Hopefully, we will have a chance to work together again in the future.

I also would like to thank Paul van Loosdrecht for welcoming me into his group during my short visit in 2012 which was my first (and very important) step towards the PhD study in Groningen.

Next, I would like to thank people who developed and promoted my interest in science in the first place, the supervisors of my master project from the side of Faculty of Physics of the Moscow State University, Dmitry Paraschuk and Sergey Zapunidi. Dmitry Yurievich, thank you for creating the impressive research environment in the Laboratory of Organic Electronics which gave, gives and I hope will give a lot of opportunities for the professional development of the

young scientists. Sergey, you were not only excellent supervisor but also a good friend, I really enjoyed working with you and I guess you were the one who influenced my initial decision to go after the PhD study.

Next, I would like to greatly acknowledge the members of the Reading Committee: Maria Loi, Laurens Siebbeles, and Vladimir Dyakonov. Thank you very much for your time and efforts spent on reading and reviewing my thesis.

In science, you never work alone, and this book would not have been written without many, many collaborators of mine. I would like to thank Sergei Ponomarenko and his research group at the Institute of Synthetic Polymeric Materials, Moscow, Russia (special thanks for Dr. Yuriy Luponosov) for the whole zoo of molecules which I was honored to study.

I also acknowledge the group of David Beljonne and Jérôme Cornil from the University of Mons, Belgium for their theoretical support and their unique ability to deliver the exact results we were looking for. I would also like to thank the experimental team from Materia Nova R&D Center, Mons for providing us the samples to study. The joined workshop on small organic molecules organized by the Mons groups made it an unforgettable event!

My next acknowledge goes to Barry Rand and his group (especially Mike Fusella and Lisa Lin) from the Princeton University, US. Barry, I am honored that I had an opportunity to work with you and I am really proud of the output of our joint projects. I enjoyed my visit to Princeton, and I am looking forward to further collaborations with you, which hopefully promote more visits. Here I also would like to thank David Cheyns (IMEC, Belgium) for manufacturing unique multi-layered samples without which one of our joint projects with Barry would not have been possible.

I also would like to thank my other collaborators: Pavel Troshin (Institute of Problems of Chemical Physics, Russia) for providing us new polymers, Christoph Brabec and Jie Min (i-MEET, Germany) for assistance with making the solution-processed devices, Giuseppe Portale (University of Gronigen) for measuring the X-ray scattering to characterize the morphology of our samples which eventually resulted in publishing of one of my major papers, and Remco Havenith and Hilde de Gier (University of Groningen) for theoretical support. I enjoyed every single project I worked on with you.

Life of a PhD student is not extremely easy, so that I would like to thank the people who made it a lot simpler. Ben Hesp and Foppe de Haan, thank you very much for your technical support. Ben, lasers definitely love you and when you are around, all of us are sure that nothing really bad could happen to the equipment. Foppe, your software is just amazing, I am not sure if one can find something more convenient for the data processing. I am deeply grateful for Jeannette de Boer, Renate Hekkema and Henriet van Mil-Boddeveld for their administrative support and all the paperwork they helped me with.

During this for years I was a part of not one, but two research groups. I thank the group of Chemistry of (Bio)Organic Materials and Devices for adopting me. Having such a number of great chemists around definitely helped me to broaden my knowledge, and now I can say that I am not a stranger in the world of organic chemistry anymore. Additionally, it was always useful to have a feedback on my work from the community of chemists; I especially acknowledge prof. Ryan Chiechi for his sometimes harsh but always relevant comments and remarks during the group meeting discussions. Also I would like to thank here the whole FOM focus group which meetings I attended with a great pleasure and interest.

Most of the time I spent in the Optical Condensed Matter Science group. It was a pleasure to work here and I thank all the group members who made my stay in Groningen unforgettable. Maxim, Paul, Ron, Foppe, Ben, Jeannette, Zhenya, Artur, Julius, Almis, Vlad, Björn, Kevin, Toni, Keisuke, Matteo, Katja, Anna, Michiel, Nilesh, Chia-Lin, Qi, Sonya and all the others – it was great to have you around. I enjoyed lunches and coffee breaks with all the discussions and rare but still fun group activities. I am sure that the daily working process was enjoyable greatly due to the wonderful people who surrounded me. This friendly and kind atmosphere really made the basement of building 5117 like a second home for me.

Kevin, it was a great pleasure working with you. You were not only a good student, but also a good friend; I wish you all the best in your future career and personal life. Björn, we had great time in Santa Fe, let's repeat.

Almis and Vlad, I am glad that you were here during my first visit to Groningen. You showed me around, supported me a lot and made that trip even more fun. Almis, I miss that uncountable number of evenings spent on climbing, watching movies, playing games and just hanging around. It's a pity that our time overlap here in Groningen was that short.

Zhenia, Julius, Anya, Artur – every evening spent with you was like a little celebration. Barbeques, pool games, board games, movie nights, travelling or just sitting somewhere – it didn't matter what exactly we did, just gathering together meant a lot for me. I am happy that I had such great friends here in Groningen. I hope that one day we will meet all together again like in good old times. I will miss all of you a lot.

Zhenia, I cannot find enough words to describe how glad I am that you were here during my whole stay in Groningen. We started at the same date, so in a way we walked through the PhD journey together side by side. You were always very kind and supportive; you have been a real friend. I knew that if I had any problems or just wanted to chat a bit I could go to you pretty much any time. Julius, you always had a lot of ingenious and crazy ideas. Building a potato gun with you was extremely fun; hopefully one day we will finally launch a rocket. You also was a great sports buddy, we spend enormous amount of hours climbing higher and higher. Anya, you were always extremely cheerful and extremely active, you were a little engine of our group.

Thank you for all your initiatives, even though sometimes I was lazy to accept them. Artur, when you were here I knew that it was impossible to have a boring evening. You were always up to everything. You were the one with whom I spent the most Friday evenings and I really appreciate this. I wish you could spend more time in Groningen.

I also would like to thank other people who supported me during my stay in the Netherlands. Alexander, you were a great neighbor and a great friend. After you moved I still enjoyed visiting you in Rotterdam and Haarlem talking about everything until the late night. Sergey E., you have been my friend for many years. Unfortunately, I didn't have an opportunity to meet you as often as I wanted during my stay here, but I enjoyed all my visits to Geneva and all your visits to Groningen. Sergey D., as you have been living literally on the other side of the world I had a chance to meet you only a couple of times but each time was really precious. Thank you for showing me Kyoto. Sergey L., it was nice to have an old friend here in the Netherlands, I was really happy for you when you got your position. Sardar, our climbing weekends with GSAC were fun, thank you for sharing this experience with me. Vlad, you are the only film director I know in person, I wish you to become famous and invite me for all your premieres. Edvards, thank you for all the remote discussions we had.

Alexey, Andrey and Petr, I was happy meeting you every time I visited Russia. Those rare moments with old friends were really special. I am proud that I have such great friends for many years and hope that our friendship will last no matter where we are.

Finally, I would like to acknowledge the most special people in my life. Dear Sveta, you have made my last months in the Netherlands even more happy and meaningful then all the previous years. I cannot express how grateful I am to the city of Amsterdam for that day when we met. I feel you close to me even when you are physically far away. Thank you for supporting me in the home stretch to graduation which is probably emotionally the most difficult part of the whole PhD run.

Мои дорогие родители, Мама и Папа. Спасибо вам большое за огромную поддержку и содействие, что вы оказывали мне на протяжении этого долгого пути. Вы всегда верили в меня и мягко, но настойчиво подталкивали меня в нужном направлении, когда это было необходимо. С каждым разом я уезжаю все дальше и дальше, но по-прежнему чувствую ваше тепло и поддержку и знаю: что бы ни случилось, есть место, где мне всегда будут рады. Спасибо вам за все.

Oleg Kozlov
Groningen
August 2017